Advances in Material Research and Technology

J. Radhakrishnan
Sunil Pathak *Editors*

Advanced Engineering of Materials Through Lasers

Springer

Advances in Material Research and Technology

This Series covers the advances and developments in a wide range of materials such as energy materials, optoelectronic materials, minerals, composites, alloys and compounds, polymers, green materials, semiconductors, polymers, glasses, nanomaterials, magnetic materials, superconducting materials, high temperature materials, environmental materials, Piezoelectric Materials, ceramics, and fibers.

More information about this series at https://link.springer.com/bookseries/16426

J. Radhakrishnan · Sunil Pathak
Editors

Advanced Engineering of Materials Through Lasers

Springer

Editors
J. Radhakrishnan
Departamento de Física Aplicada e
Ingeniería de Materiales
E.T.S. de Ingenieros Industriales
Universidad Politécnica de Madrid
Madrid, Spain

Sunil Pathak
HiLase Centre, Institute of Physics
Czech Academy of Sciences
Dolni Brezany, Czech Republic

ISSN 2662-4761 ISSN 2662-477X (electronic)
Advances in Material Research and Technology
ISBN 978-3-031-03829-7 ISBN 978-3-031-03830-3 (eBook)
https://doi.org/10.1007/978-3-031-03830-3

This Springer imprint is published by the registered company Springer Nature Switzerland AG
The registered company address is: Gewerbestrasse 11, 6330 Cham, Switzerland

Preface

The 4th industrial revolution urges all sectors, including manufacturing to develop sustainable and advanced manufacturing processes with a solution to process the parts after manufacturing. This required intelligent methods and techniques in order to stay competitive in the global economy. Laser in recent times has been one of the most significant contributors in the world economy, always helping industry by latest development in promoting research and innovations to meet the accelerated demand for productivity, quality, and sustainability. The development of lasers in applications of additive manufacturing (AM) and post processing of AM parts and composite structures has been a challenging work in the current and future scenario of worlds manufacturing economy. The book will cover the process fundamentals of different laser-based manufacturing and processing, namely: laser shock peening, laser micromachining, laser cutting, re-melting, and several other aspects related to this field. Laser interaction with different materials is aim to be part of the book.

This book will help in providing fundamental understanding and advanced research insights on laser materials interaction and their applications in a wide range of conventional and advanced manufacturing.

This book consists of eight chapters on fundamentals to advanced use of lasers in manufacturing. Chapter "Introduction to Lasers and Processing's of Materials" presents a detailed overview of laser materials interaction. Chapter "Introduction to Gas and Solid State Laser Techniques in Cutting Process" sheds lights on the gas and solid state laser techniques in cutting process. Chapter "Laser Cutting of Ceramic Matrix Composites" presents details on laser cutting of ceramic matrix composites. Chapter "Laser Shock Peening: A Walkthrough" highlights the use of laser shock peening (LSP) in a detailed manner to discuss the effects of LSP on materials properties and fatigue life. Chapter "Laser Re-Melting of Atmospheric Plasma Sprayed High Entropy Alloy" describes laser re-melting of atmospheric plasma sprayed high entropy alloy. Chapter "Surface Morphology of Nimonic Alloy 263™ in Nanosecond Pulsed Laser Ablation" presents insights on surface morphology of Nimonic Alloy 263™ in nanosecond pulsed laser ablation. Chapter "Laser-Based Post-processing of Metal Additive Manufactured Components" sheds highlights on laser-based post-processing of metal additive manufactured components. The book ends with Chapter

"Advances in Superhydrophobic Surfaces: Biology to Biomimetic" highlighting the advances in superhydrophobic surfaces: biology to biomimetic.

I sincerely acknowledge Springer for this opportunity and their professional support. I am also thankful to all the chapter contributors for their availability and valuable contributions.

Madrid, Spain — J. Radhakrishnan
Dolni Brezany, Czech Republic — Sunil Pathak

Contents

Introduction to Lasers and Processing's of Materials

Ashish K. Shukla, Achyuth Kulkarni, Shalini Singh, S. Jayachandran, Anshu Sahu, and I. A. Palani

1 Introduction

The materials processing from nano to micro and bulk level for various commercial applications such as Texturing, engraving, and peening dedicated to commercial applications can be substantiated employing a Laser system [1–4]. The material processing employing laser system is chosen depending on the demand of processing capability and its real-life application [5, 6]. The outlining of a laser system depends on laser parameters, Laser wavelength, Pulse duration, Laser Power, and Repetition rate [7, 8]. Besides, Identifying the absorption coefficient of range of laser wavelength (225 nm to 1064 nm) with sample material before real-time interaction with laser plays a significant role in outlining the experimental system and window for experimental parameters [9, 10].

Figure 1 shows the application of lasers in actuation, forming, peening, honing, nitriding, patterning, and additive manufacturing [11]. In the field of actuation, a laser can be used to actuate smart bi-morph materials [12]. The smart bi-morph material is thin film of Ni–Ti-based smart material over the pre-strained flexible polyimide substrate. A smart bimorph is different from a conventional bimorph [13]. The Ni–Ti is heat-sensitive material; therefore, its bimorph can be actuated with a different medium of heat input such as electrical heating (Joule heating) [14].

The outlined window entirely depends on the absorption coefficient of material for the different wavelengths. The influence of varying laser wavelengths can be

A. K. Shukla (✉)
School of Design and Innovations, ATLAS SKILLTECH UNIVERSITY, Mumbai 400070, M.P., India
e-mail: ashish.shukla@atlasuniversity.edu.in

A. Kulkarni · S. Singh · S. Jayachandran · A. Sahu · I. A. Palani
Mechatronics and Instrumentation Lab, Indian Institute of Technology Indore, Indore 453552, M.P, India

J. Radhakrishnan and S. Pathak (eds.), *Advanced Engineering of Materials Through Lasers*, Advances in Material Research and Technology,
https://doi.org/10.1007/978-3-031-03830-3_1

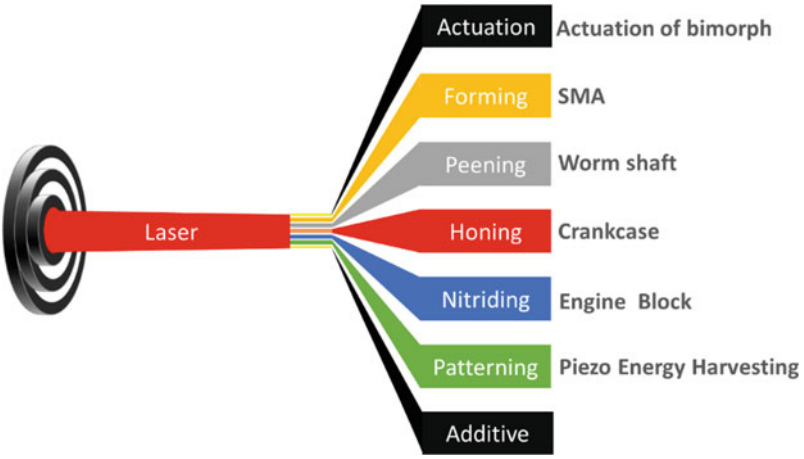

Fig. 1 Laser processing of different materials and their application in various fields

observed in the graph represented in Fig. 2 [15]. The selected material is complex in its lattice characteristics, such as polycrystalline polyimide flexible substrates [16]. Figure 2 Demonstrates the influence of laser wavelength ranging from 225 to 1086 nm over flexible polymeric substrates [16]. Figure 2 Illustrates the absorption of PI substrate is started reducing at 450 nm straight up to 550 nm [17]. Further, after 600 nm, it should decay straight, which is not happening due to the polycrystalline nature of the substrate [18]. In addition, the percentage increase in absorption for PI substrate because of 355 nm laser processing compared to 1064 nm of laser processing is considered as absorption of 50% in simulation and subsequently 25%

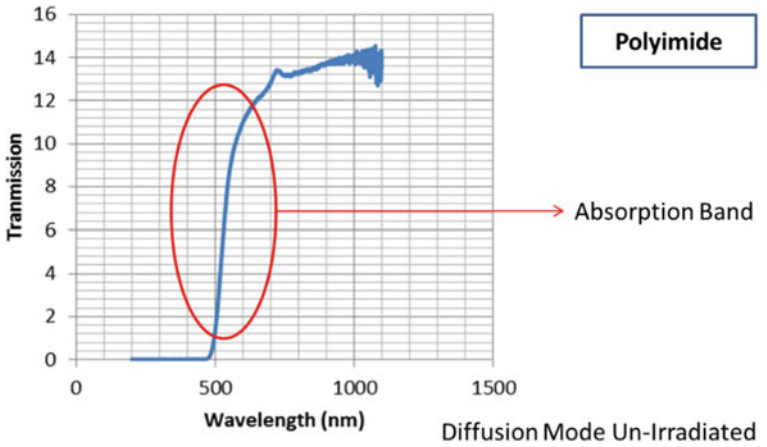

Fig. 2 Primary survey for the determination of transition band and highly absorbing region of incident laser wavelength; UV–Vis Transmission spectroscopy of pristine polyimide

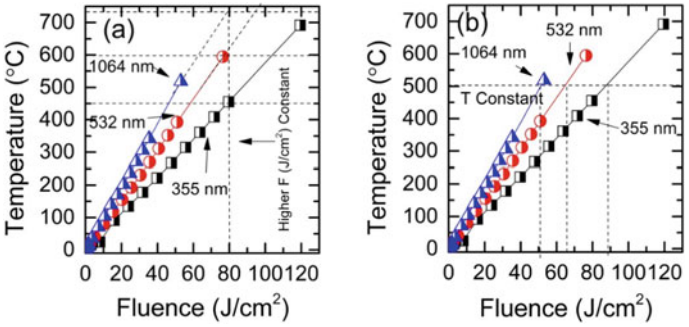

Fig. 3 Comparison of two constant parameters of Temperature versus fluence diagram for 355 nm, 532 nm, and 1064 nm wavelengths; **a** Interpolation of processing temperature at constant higher fluence (F) J/cm^2 and **b** Interpolation of different fluence which depends upon the wavelength of laser; constant temperature, which is melting point temperature of PI is presented

for 532 nm wavelength and 10% using 355 nm wavelengths [19]. The other two (532 and 1064 nm) wavelengths such as 532 nm and 1064 nm demonstrated the lower absorption [20, 21].

Figure 3a shows the selection of higher fluence J/cm^2 (constant at 80 J/cm^2 (dotted line). Black half-square line shows the simulated fluence for 355 nm laser wavelength. Red half-circle represents simulated fluence for 532 nm laser wavelength [22, 23]. Blue half-triangle shows the simulated fluence for 1064 nm. The constant higher fluence line intersects the 355 nm fluence line at 450 °C, 532 nm fluence line intersects at 600 °C, and 1064 nm fluence line intersects at 740 °C [24–30]. The fluence intersection for 1064 nm is at the projected dotted line, in line with the 1064 nm existing plot [31]. Whereas Fig. 3b illustrates the intersection of all three laser wavelengths such as 355, 532, and 1064 nm and fluence (J/cm^2) line by constant temperature line, which is marked at 500 °C [32]. As the melting temperature of materials remains constant [33].

2 Mathematical Modelling

The mathematical modeling and simulation were carried to identify the parameter's process window [35–37]. Figure 4 shows the parameters of laser materials interaction which is required for precise control of ablation process. The process is governed by means of ambient condition, laser beam parameters and thermo optical characteristics of the substrate materials. While processing Multiphysics parameters. In observation its having three different such as (i) laser-solid interactions, (ii) Vapor/Plasma formation and Expansion and (iii) Laser plasma interaction. In order to quantify and roundup the involved physics we need fundamental equations which are presented below as Eqs. 1 and 2.

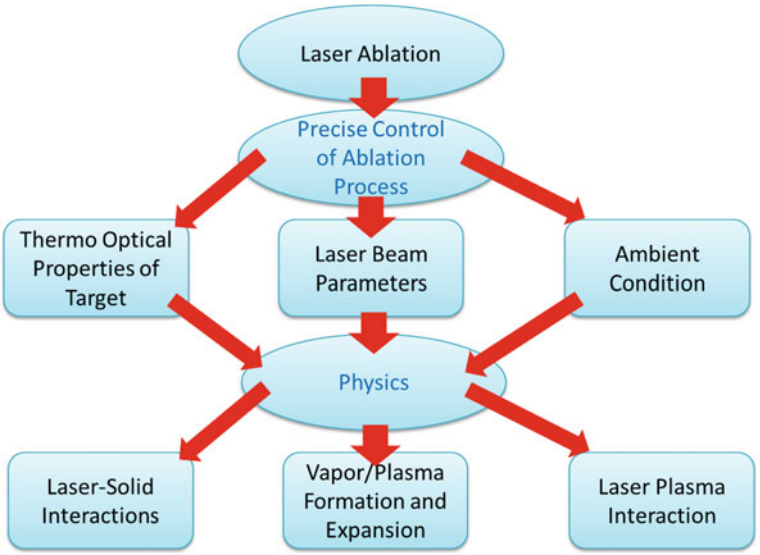

Fig. 4 Flow chart of Laser Materials Interactions [Publish with permission from springer Nature, 1996, 66]

$$C_e \frac{\partial T_e}{\partial t} = \frac{\partial}{\partial z}\left(k_e \frac{\partial T_e}{\partial z}\right) - \Gamma_{e-p}(Te - T) + (1 - R)\alpha I(t)\exp(-\alpha z) \quad [66] \qquad (1)$$

$$C \frac{\partial T}{\partial t} = \Gamma_{e-p}(Te - T) \quad [66] \qquad (2)$$

T_e = Electron Temperature, T = Lattice Temperature, K_e = Electron thermal conductivity, C_e = Electron Volumetric Heat Capacity, C = Lattice Volumetric Heat Capacity, α = Target attenuation coefficient, Γ_{e-p} = Electron lattice energy transfer Coefficient, R = Reflectivity, I(t) = laser Intensity, Characteristic Time Scale, τ_e = Electron Cooling Time, τ_p = Lattice Heating Time, τ_l = Pulse Duration, [34]. The simplified and derived equations with certain assumption arrived to direct equations which are tabulated in Table 1.

The first significant challenge is the heat input effect on surrounding material [38]. Second major challenge is the post-processing result associated with energy interaction with ITO-PET flexible substrate material, which is prone to forming a high heat-affected zone (HAZ) [39]. To minimize HAZ pulsed laser energy is used due to its distinguished property of focused area heating and not affecting surrounding material [40]. The second challenge was overcome using LIWE processing using nanosecond laser and a highly finished surface pattern [41]. Although surrounding material unaffected plasma needs to be quenched to minimize further processed material's heat affected zone (HAZ) [42]. Minimizing HAZ leads to achieving a high surface finish; hence using nanosecond laser in LIWE highly surface finished pattern can be achieved [43]. With the motive to minimize heat-affected zone onto

Table 1 Derived Assumptions and ablation per pulse equation for three different laser pulse duration [Publish with permission from springer Nature, 1996, 66]

τ_l(s) laser pulse duration	Assumption	Surface phase behavior	Ablation per pulse
Femtosecond	No. conduction to lattice	Solid to vapor	$\Delta h = \alpha^{-1} \ln \frac{F}{F_{th}}$
Picosecond	Lattice temp do not affect T_e	Solid to vapor Some melting	$\Delta h = \alpha^{-1} \ln \frac{F}{F_{th}}$
Nanosecond	Thermal equilibrium ($T_e = T$)	Melting Vaporization	$\Delta h = l_t = \sqrt{D\tau_l}$

the surface of the sample, Snell's law followed for wet etching in Laser Induced Wet Etching (LIWE) [44, 45]. The propagated Gaussian wave is converged towards the surface in wet etching process, which is demonstrated in Fig. 5. Laser absorption of the material is the key parameter to identify ablated zone and the heat-affected zone [46]. Figure 5 shows the Gaussian beam's convergence is seen after passing through liquid surrounding the substrate and the nature of the transverse Gaussian beam [62]. The effective energy transfer zone is the W_d spot diameter on the work surface [63].

The depth of the trench is a function of laser wavelength, fluence and pulse duration, and mode of pulse incident. [47] According to Beer-Lambert's law, the

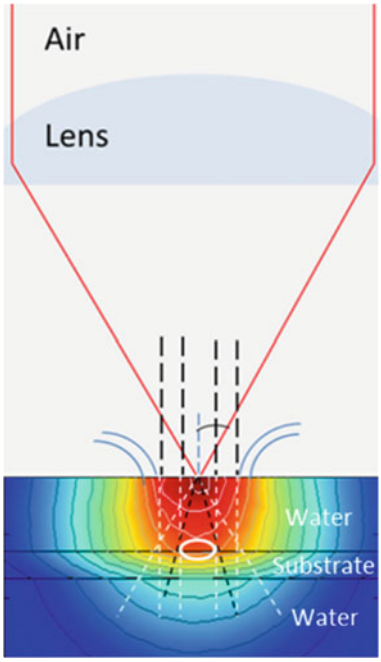

Fig. 5 Convergence of propagated Gaussian profile laser beam while passing through first air then water and absorbed at liquid substrate interface [Publish with permission from Elsevier, 2017, 35]

Laser energy interaction with material determines the amount of energy absorbed by the substrate. [48] The diffused absorbed energy is the cause of the temperature rise. This temperature rises according to lattice collision and electron excitation due to the thermal conductivity of material and induced thermal gradient. [49] Thermal diffusion length indicates pulse duration scaling, which plays a vital role in mapping HAZ dimensions w.r.t. processing parameters [50].

The thermal diffusion length is $l_{th} = 2\sqrt{D\tau_p}$, where D is thermal diffusivity $D = k/(\rho C_p)$. The complete penetration length l completely dependent on l_{th} thermal and l_α optical penetration depth $= l_{th} + l_\alpha$ [51]. The quantitative estimation for the depth determination in which material is molten or vaporized mainly depends on the laser spot energy density, i.e., fluence and interacted with the liquid and then further propagated to the interface of liquid and substrate [52]. While propagation laser converges towards interface; hence in case of laterally oriented samples, the coinciding of ablated zone diameter (W_d) with laser incident diameter of the ablated zone is unobserved [53]. The long-pulse laser ablation at interface $D\tau_p\alpha^2 \gg 1$ is usually to be fulfilled [54]. For the Gaussian beam propagating through liquid (water) via ambient atmosphere ablated diameter d_{abl} depends on the optimized fluence F whereas F depends on W_d and calculated threshold fluence F_{th} [54].

$$d_{abl} = W_d\sqrt{\frac{1}{2}}\ln\left(\frac{F}{F_{th}}\right) \quad [56] \tag{3}$$

And for calculating laser beam diameter at the interface of the liquid and substrate using Snell's law [56].

$$Wd = \frac{2 * \lambda * M^2}{\pi \mathrm{Tan}\theta_w}\left\{1 + \left(\frac{(W_t)\left(\left(\frac{b_d}{2f}\right) - \mathrm{Tan}\theta_w\right)}{Zr\,\mathrm{Tan}\theta_w}\right)^2\right\}^{1/2} \quad [58] \tag{4}$$

where λ, M^2, θ_w, b_d, f, Z_r, W_t are wavelength, laser beam quality, Refractive angle of the laser beam in water, the diameter of the collimated beam entering a focusing lens, the focal length of focusing lenses, Rayleigh length, the thickness of the water layer [57]. The value of $S_{int}(x,t)$ changes due to its convergence at the interface and due to change in reflectivity of water to laser and reflectivity of liquid substrate interface and the substrate itself, which is incorporated in $I_{int}(x,t)$ Eq. (6) [59].

$$S_{\mathrm{int}}(x,t) = \alpha(T) I_{\mathrm{int}}(x,t) \quad [58] \tag{5}$$

$$I_{\mathrm{int}}(x,t) = I_0(t)(1 - R(T)_w - R(T)_{\mathrm{int}})\exp(-\alpha(T)x) \quad [58] \tag{6}$$

$$F_{\mathrm{int}} \geq F_{th} \approx \rho H_v l_{th} \quad [58] \tag{7}$$

where, H_v is the latent heat of vaporization and l_{th} is identified as the depth of ablation in LIWE [58]. The following assumptions were used to solve the equation: (i) The heat conduction is coplanar and its gradient generated in parallel to laser incident plane, (ii) No re-radiation of energy from incident surface due to convergence of Gaussian beam and quenching of propagated and generated plasma, negligible heat conduction to liquid surrounds the substrate, (iii) Negligible convection from interface and surrounded liquid, (iv) Substrates surface evaporates at the melting point (v) Laser intensity is single pulse-based (vi) Thermal conductivity and specific heat capacity and optical absorption is considered homogenous in liquid medium, liquid substrate interface and in substrate also, (vii) As one dimensional two-temperature model is considered then its legitimate to consider it for one dimensional thermal problem and non-radial heat transfer (viii) Temperature and pressure of liquid is maintained at ambient temperature and pressure (ix) liquid is in stationary state due to quasi-static movement of translational stage [59]. The Linear homogeneous equation's transformation system solved by considering initial condition as T (x, 0) = 0 and final boundary condition T (x, t) = 0 at $x = l$ [60]. It is expected that the Marangoni effect will persist below the strong heating region below the interface [61]. The Eqs. 5–7 was used to simulate using COMSOL Multiphysics to outline the laser induced temperature in material that is specifically with assigned materials property, waveform, power, wavelength, and time duration of laser irradiated on material [87]. According the assigned fluence value we obtained the temperature induced and further segregated the temperature based on materials property into two different classes such as ablation and crystallization temperature [88]. The temperature above the secondary glass transition temperature i.e., above 450 °C, in present case is termed as ablation temperature and temperature below the start of secondary glass temperature i.e., 350 °C [89, 90]. In addition, in case of chosen material PI the melting temperature is higher than decomposition temperature and its decomposition starts after 500 °C that can be evidenced using thermogravimetric analysis (TGA) [91–94]. Explanation of TGA is out of scope of this book chapter.

Figure 6a shows the maximum interface temperature is probed around 700 °C with spot diameter 400 μm, fluence 120 J/cm^2 using wavelength 355 nm [72]. Figure 6b: shows Maximum temperature 300 °C with spot diameter 400 μm, fluence 120 J/cm^2 using wavelength 532 nm [73]. In case of wavelength 355 nm, the required laser fluence to raise the interface temperature about 200 °C was below 40 J/cm^2 at a spot diameter 400 μm [74]. The estimated interface temperature is 217 °C [75]. In 532 nm wavelength value of fluence for interface temperature, 200 °C was above 40 J/cm^2 [76]. At constant spot diameter and fluence as in 355 nm wavelength simulation, the probed temperature at interface is about 100 °C [77]. The estimated temperature in 532 nm is lower than 355 nm [78]. The fluence to attain 200 °C in 532 nm is interpolated at about 95 J/cm^2, significantly higher than estimated at lower wavelength 355 nm [79]. In addition, the substrate temperature was estimated to be 280 °C at 120 J/cm^2, keeping spot diameter 400 μm, which is even higher than the melting temperature of the substrate, also from 355 nm wavelength [80]. The semicrystalline nature of substrate underwater absorbs less energy and nonlinearly, resulting in significantly higher fluence requirement than 355 nm wavelength [81].

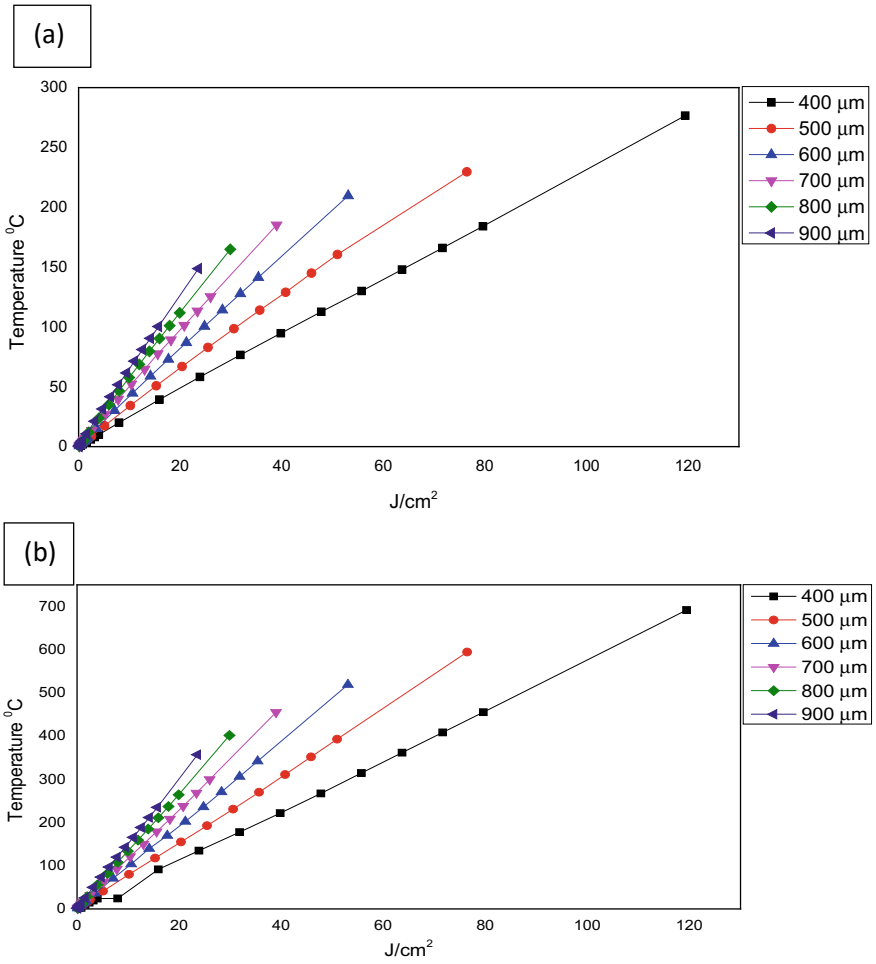

Fig. 6 Fluence (J/cm^2) versus Temperature (°C) plot of **a** 355 nm Single pulse mode for spot diameter from 400 to 900 um and **b** 532 nm Single pulse mode for spot diameter from 400 um to 900 µm

The nonlinear absorbance allows a higher penetration depth at the point of interaction apart from the non-interacting domain [82]. Figure 7 shows the average interface temperature and the penetration of the centrally overlapped spot [83]. To maintain surface temperature below the melting temperature, the average interface temperature line was identified [84]. Minimizing the heat-affected zone and heat transfer into the substrate, however at half of the substrate thickness maintaining the substrate temperature is essential to mark below the lowest crystallization temperature range [85].

Figure 8a, b, shows the temperature obtained at the selective employed probe position in simulation. The maximum temperature obtained using 355 nm wavelength is

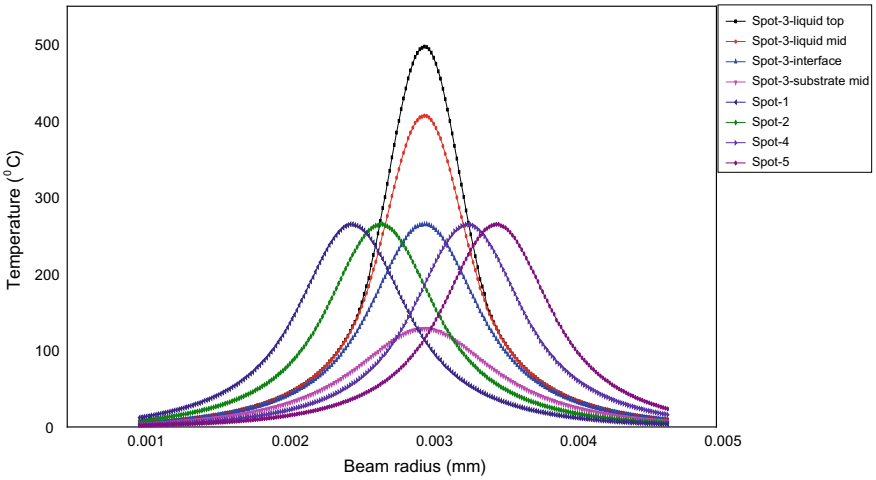

Fig. 7 Temperature distribution of overlapped spot and average temperature distribution, mid of substrate temperature distribution as well as central spot region from the top of water surface to mid of substrate thickness

1100 °C, 120 J/cm^2, and 400 μm spot diameter, whereas 550 °C was obtained using 532 nm wavelength. Experiments were performed with this simulation window information, and further experimental setup details and characterization were discussed [86].

Threshold fluence for the phase transformation was calculated by considering that crystallization of amorphous ITO coated PET flexible substrate starts above 97–240 °C [64]. When the temperature in W_d exceeds and reaches the melting point temperature, the process is treated as an ablation [65]. The above-described model was simulated using COMSOL multi-physics version (5.1) software to investigate the convergence of Gaussian beam and temperature level at the $r = 0$ in the W_d where the maximum intensity is transferred [66]. Thermal conductivity $k(T)$ is invariant with temperature and $C_p(T)$ which is considered invariant with temperature to avoid the heat generation inside substrate, interface, and liquid [67]. Surrounding liquid brings substrate to equilibrium condition by conduction, conductive, and radiation mode of heat transfer [68]. The absorption coefficient is laser wavelength dependent. In the simulation, laser spot size is considered 400–900 μm for the Gaussian beam [69]. The COMSOL simulation results presented in Fig. 8 shows temperature obtained at the interface of liquid and substrate with incident Gaussian laser beam [70]. The range of fluence and spot diameter is theoretically simulated to decide the working range, power between 0.005 W to 1.5 W, spot diameter 400–900 um the obtained fluence range is 78–120 J/cm^2 which is dependent on the absorption coefficient of material to the respective wavelength [71].

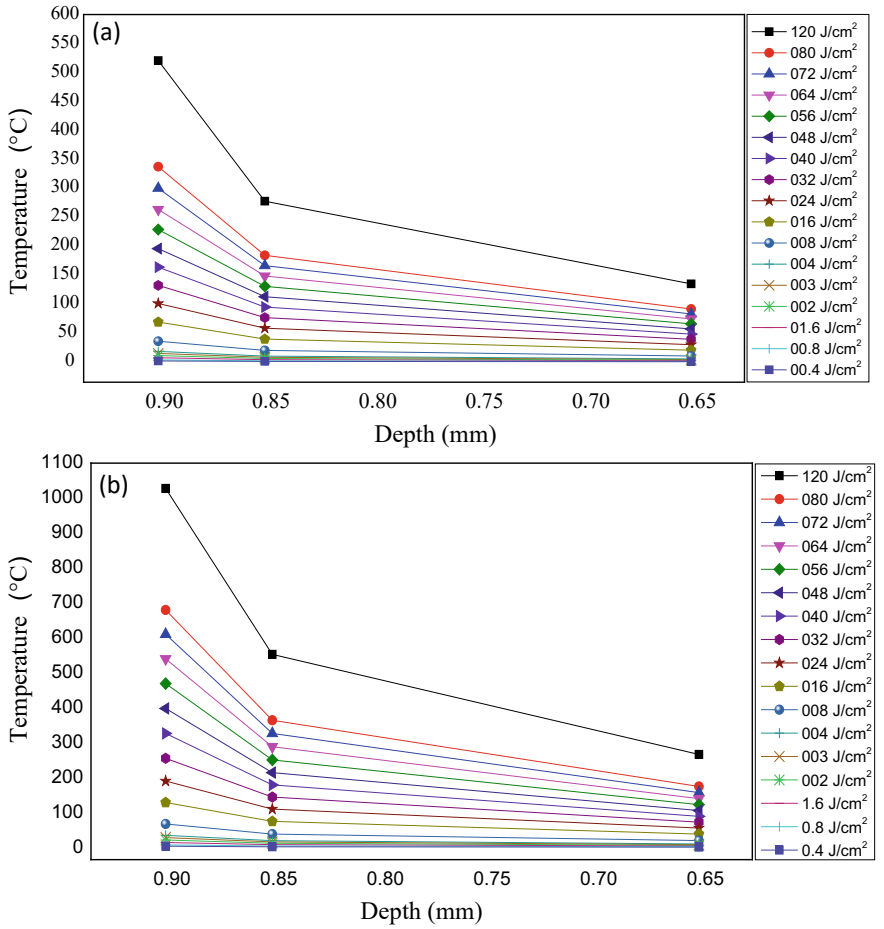

Fig. 8 Depth (mm) versus Temperature (°C) plot of **a** 355 nm Single pulse mode for spot diameter 400 μm and **b** 532 nm Single pulse mode for spot diameter 400 μm

3 Experimental Parameters and Setups

3.1 Influence of Laser Processing Parameters

The cumulative response of laser material interaction is important for end effect analysis as demonstrated in Fig. 9, however the response of material against each varying parameters are important for analytical analysis to derive the better insight. In this regard, the factors influencing the results and response are the following [103].

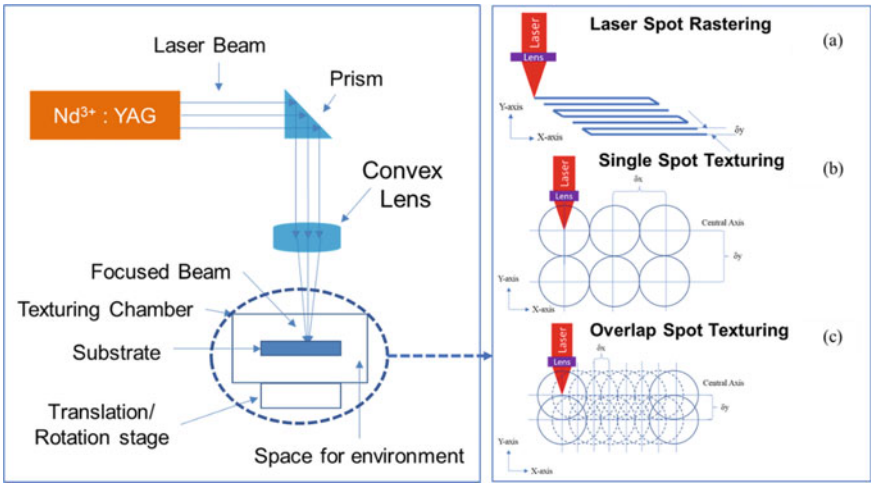

Fig. 9 Schematic of the laser system and beam steering to substrate. The beam steering plays important role in laser-base processig of different materials. The laser based processing is having a small chamber to make a it a closed system. The enlarged view respresnts the three different spot mapping over the substrate. **a** Continuous laser rastering, **b** Single spot based laser rastering and **c** overlapping of laser rastering in X and Y axis [Publish with permission from IOP, 2018, 67]

i. **Laser Fluence (J/cm^2)**

The individual material of specified thickness, with outlined parameters such as laser fluence (J/cm^2) which is calculated by laser energy and spot diameter marked on photographic sheet, and laser pulse duration governs the direction [100]. The chosen specimen for discussion is AL 1060 alloy of thickness 0.75, 1.0, and 1.75 mm [101]. The obtained laser intensity against laser energy 0.25, 0.35, 0.45 and 0.55 J are 1.25, 2.0, 2.5, and 3.0 GW/cm^2, respectively [84, 102, 103]. With the outlined parametric window both type of bend concave and convex curvature was achieved at above mentioned laser intensity [104]. The transition range for bending threshold from concave to convex is lying in between 1.2 and 1.8 GW/cm^2 and the critical thickness found to be 1.0 mm [105]. The laser intensity increases with an increase in thickness and threshold ranging from 2.5 to 3.0 GW/cm^2 for changing from Concave to Convex bend profile. [106]

ii. **Material Thickness**

The influence of material's thickness on bend angle investigated systematically and stated the observation by keeping fixed laser energy and varying the thickness of the material i.e., Aluminium Alloy 1060 [107]. The sequential raster of the line by 5 times and spot overlap 70% percentage demonstrated the critical thickness in the range of 0.7–0.9 mm, in between that inversion from concave to convex occurs [108]. Interestingly it is found that the thoroughly strained workpiece affine to deformation towards concave structure by analyzing the

measurement of perturbation by means of plastic deformation with respect to thickness of the workpiece. If the ratio found to be less than unity (<1.0) then bending in convex arc dominates [109].

4 Applications

4.1 Laser Forming

Laser-assisted forming is an advanced technique using which elastic, pseudo-elastic sheets of metal and smart materials formed under influence of continuous laser materials interactions [95]. The laser material interaction induces thermal stresses along the laser beam incident direction, which in turn leads to plastic deformation to bend the free flange to a desired shape [96]. The laser-assisted forming technique possesses the flexibility to create 3D curved and mixed with flat bends on wide range of heat sensitive, and hard materials are advantages over other forming techniques [97]. The heat sensitiveness and materials characteristics of the SMA materials are well explained by three well classified mechanism such as temperature gradient, buckling, and upsetting mechanism [98–100]. However, influential mechanism depending upon selection of process parameters [101]. The continuous laser irradiation over the SMA sheet surface generates thermal gradient along the cross-section along with thermal expansion imparts counter bending away from the laser material interaction [84]. Concurrently, the bottom surface of the sheet is under compression [102]. Once the laser heating cycle over the heated zone starts cooling and due to volume shrinkage, it contracts towards the center, which causes the bending of the sheet [103]. The concurrent process of out bending and in-bending tends to cancel out the effect of the spring back effect [104].

The mechanism is basically depending on the focal point of the laser beam which is demonstrated with the schematics and actual/3D model experimental setup in Fig. 10. The adjustment of laser beam projection is dependent on the Z-axis moment of worktable demonstrated in Fig. 10c. The focused beam projecting the low beam spot over the substrate or workpiece depicted in Fig. 10a. Further there are two possibilities of changing the spot diameter i.e., pre and post focal pot. The projection before focus is called pre-focus and post focus is termed as defocus beam over the substrate used for large area heating over the workpiece depicted in Fig. 10b, c.

Figure 11 The laser-assisted forming induces the instantaneously change in temperature, which leading in thermal stresses in material [105]. The induced thermal stresses generating permanent plastic deformation which is altogether different phenomena in comparison to conventional forming technique [106]. The laser-assisted forming techniques driven by two mechanism such as Temperature Gradient Mechanism (TGM) and Buckling Mechanism (BM) [107]. Figure 11a, b TGM works on high-speed laser raster over the surface to prevent the heat propagation along the thickness (Vertical) in laser material interacting zone [108]. This principle allows only surfaces to expand whereas other part of the material remains unaffected substantiates

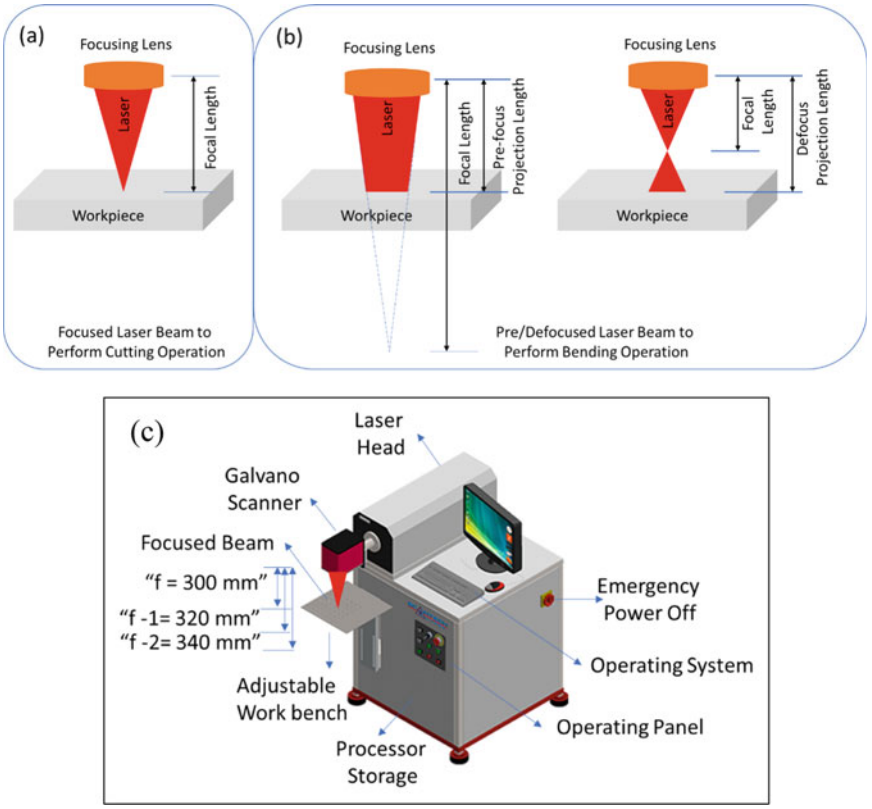

Fig. 10 Schematics to distinguish the laser focus position to mark the focal point and z-position such as standoff distance of substrate material with respect to focal point position of laser beam

in bending away from the top plane [109]. The bending away from laser material interacting plane is termed as counter-bending [110]. Simultaneously, the cooler mater of the material acting as a constraint for the expansion, the constraint is an agent to develop compressive stresses, demonstrated in Fig. 11a [111]. However, during cooling contraction occurs and developing bending back [112]. In TGM contraction during cooling process is dominating, which in turn demonstrates actual bending towards the laser material interacting plane i.e., towards the incident normal of laser beam [113]. Figure 11c–e The Buckling mechanism phenomena is working on delayed time (more time) interaction of laser energy with material [114]. The laser beam is rastered slowly over the surface. The slow rastering is leading to conduction of heat along the thickness i.e., in vertical direction of the sheet generates the temperature gradient, shown in Fig. 11c [115]. The heat confined region in heat gradient zone venture to expand laterally however due to constraint, generating a development of compressive stresses [116]. The developed stresses once attain the critical limit, an instability induced tends to be buckling, shown in Fig. 11d [117]. With the traverse

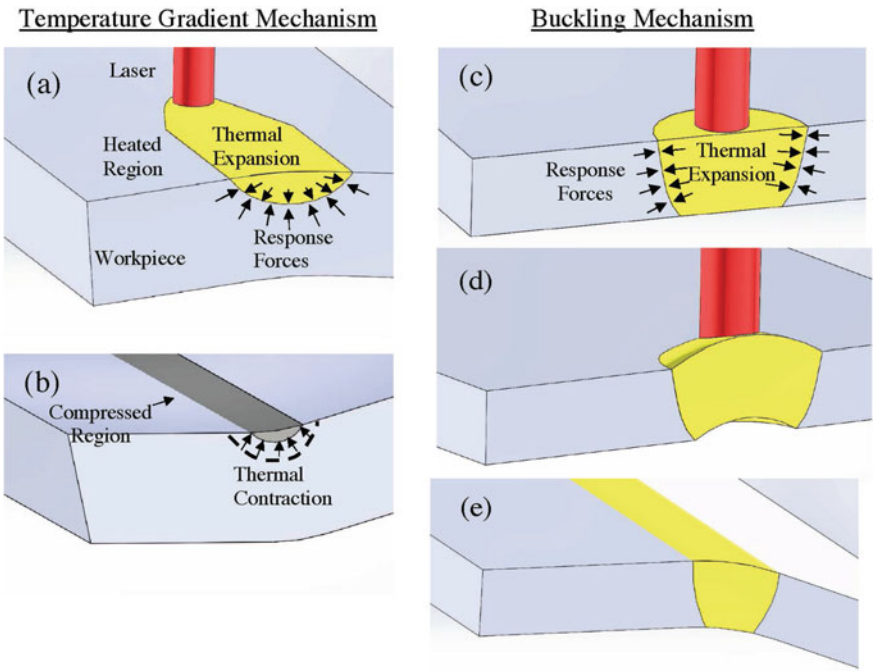

Fig. 11 Laser-assisted forming mechanism by means of temperature gradient **a** heating induced by laser material interaction resulting in outward expansion, b while cooling of the material it experiences the contraction force, **c** buckling mechanism by means of laser is demonstrated, **d** represents the induced buckling and **e** shows the growth of buckle intended for bending [Publish with permission from Elsevier, 2002, 68]

of the laser beam across the laser material interaction zone buckle is progressing over the surface, the process terminating as bending away from plane, depicted in Fig. 11e [117]. Other constraints if not present in the laser exposed region tends to buckle either towards or away from laser material interacting plane depending on influencing parameters such as rolling direction of sheet, residual stresses, and other applicable forces [118]. To formulate controlled laser-assisted forming technique potentiated by buckling in predefined direction [119]. The propensity of buckling can be done employing pre-bending before fixing flat, introducing an air stream or by means of gravity to bring about downside buckling [120].

The critical points for applicability of the laser based free form forming in the industry is influenced by cost, reliability, and rate of production demonstrate in Fig. 12 [121]. The critical parameter in bending angle in Laser based freeform forming is number of laser pulse interaction or irradiations [122]. The experiments performed in underwater environment is not counting any response of the material due to cooling time [123]. The cooling time is neglected due to rapid heat dissipation in H_2O environment [124]. However, in open-air environment the cooling time plays significant role in case of bending angle output [125].

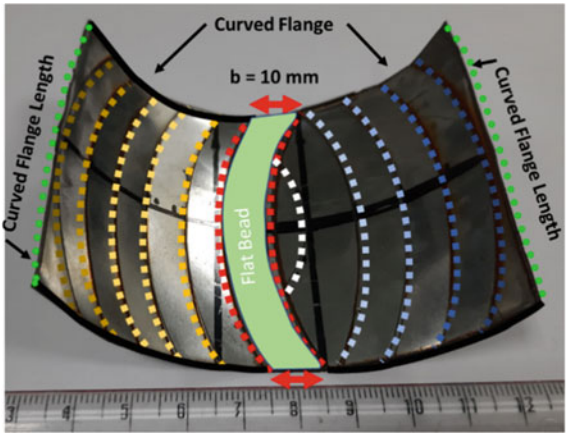

Fig. 12 Demonstration of Laser based freeform forming of the SS sheet metal using CW laser beam

The influence of 60 s cooling time in open air environment laser assisted freeform bending is demonstrated in Fig. 13 [126]. Interesting fact demonstrated that at following parameters such as Laser Power 200 ± 5 W, Laser scanning speed 4 ± 5% mm/s and laser beam diameter 0.5 ± 5% substantiated the maximum bending angle of 55° [127]. The fact is that in open-air environment it requires a smaller number of laser materials interaction i.e., 30, however in underwater environment it requires a greater number of laser materials interactions, i.e., 250 [128]. The quenching of laser induced heat in material in underwater environment resulting in approximate difference of 10 times in bending rate of same material in open-air environment in comparison to underwater environment such as 1.77 and 0.21 (Average bend angle/interaction), respectively [128]. To precisely control the laser-based forming requires less number low bending rate and that is advantageous in case of laser based freeform forming in underwater environment [129]. This advantageous function (low

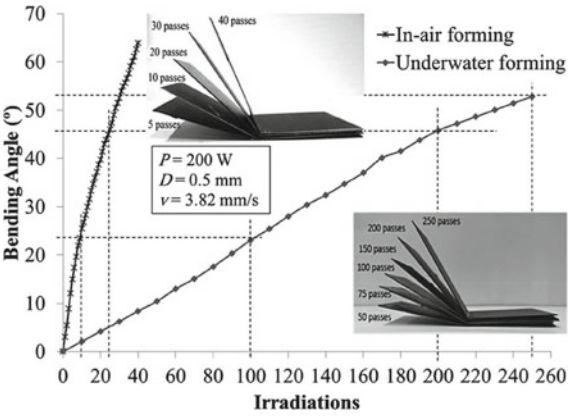

Fig. 13 Laser angle estimation in the field of laser-based sheet metal forming in two different environment such as open-air and understeer forming [Publish with permission from Elsevier, 2018, 139]

bending rate) of underwater laser forming in turn leading as an option for selectively laser bending to precisely achieve given bending angle [130].

4.2 *Laser Peen Forming*

The Laser Peen Forming (LP-f) demonstrated in Fig. 14 is an extended part of Laser Shock Peening, this method resembles with die—punch-based mechanical forming [132]. The major difference in LSP and LPF is of thickness of the specimen materials and secondly the bottom support of the material [133]. In LSP material can be circular or any gear profile [134]. However, in LPF material should be in form of sheet [135]. In case of LSP material should be at least constrained from two end [136]. In LPF should be its constrained from one end. [136] Free end of the sheet in LPF leads to elasto—plastic formation in turn generated the bend formation [136].

Hereby, target is to modify the curvature of specimen by means of coupling laser energy to the sample scripted in Fig. 15 [104]. In this method sample assembly is important because it requires three layer such as laser confining medium, ablative layer, and specimen material [137]. The confining medium should fulfill the condition of higher refractive index such as N2 > N1 [138]. The H_2O is most chosen confining liquid. Also, the assembled sample's translation is controlled by computer-controlled X–Y stage [138]. A laser of wavelength 1064 nm and nanosecond pulse duration is suitable for peening experiments [139]. In this technology the confining act as a hydrodynamic/dynamic arrest layer, which is used as refocusing the laser beam and

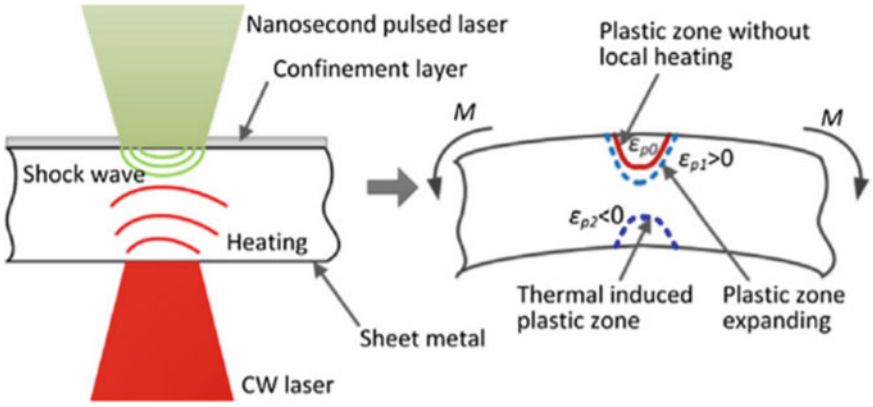

Fig. 14 Schematic representation of counter heat-assisted pulsed laser peen forming. The confinement layer is used from top side where pulsed laser is employed and continuous wave laser is aligned opposite to shock producing laser. The explored view is demonstrating the plastically deformed zone without localized heating and the expansion is revealed as plastic zone. The CW laser interacted zone depicts the thermal induced plastic zone [Publish with permission from Elsevier, 2014, 140]

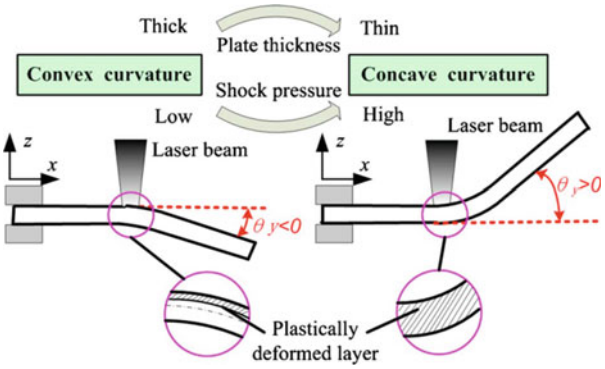

Fig. 15 Influence of materials thickness on generating different bend profiles [Publish with permission from Elsevier, 2006, 141]

eluding the plasma induced by laser material interaction demonstrated in previous Fig. 14 [140]. The temporary layer i.e., ablative layer coating, which is used to absorb the thermal energy carried by laser beam to prevent the pristine material from detrimental effect [141]. The ablative material can be black tape, black paint, graphite, and aluminum foil [142].

The forming of high strength and light weight alloy is challenging job. The high strength titanium material can be formed by means of laser-based peen forming (LPF) [143]. The efficiency of LPF can be improved by means of localized counter heating employing continuous wave laser beam [144]. The forming of high strength material requires high localized temperature as well as pulsating shock wave [145]. The counter localized heating induces adequate temperature, which subsequently decreases the materials strength, in turn leading to plastically deformed film while dynamic loading phases of LPF [146]. The counter heat dependent LPF tends to reduce the bend radius because of regional heating [147]. Inadvertently, counter heating with shock induces the defects such as cracks and porosity below the surface are harmful to fatigue and ductility [148]. Therefore, tuning of influence of temperature to reduce the damage is important in counter heat-assisted pulsed laser peen forming [149].

The bend induced by LPF is distinguished by four modes and that is governed by plastically deformed zone in laser interacted zone shown in Fig. 15 [150]. The tuning of experimental practice parameters affects the bending curvature in—turn leading to change in bending direction [151]. In LPF process high laser fluence of nanosecond pulse duration is coupled on to the interface of confining medium and ablating surface [152]. The coating material is influencing sublimation which leads to vaporization and subsequently ionization [153]. The sublimation process is generating high-pressure plasma and propagates speedily away from the surface of the pristine sheet metal [154]. The confining medium like H_2O traps the speedily propagating plasma and reflecting towards the sheet metal [155]. The reflected plasma hits back to surface and getting burst violently [156]. The burst of reflected plasma

generates pressure in the range of 10 s GPa, which is transferred to sheet metal [157]. The shockwave from Laser/Electromagnetic beam coupled to workpiece induces the compressive residual stresses over the surface [158]. The shockwave coupled to specimen generates plastic deformation, moreover it should over pass the Hugonjot Elastic Limit (HEL) of the sample [159]. The plastic deformation of the sheet metal irrespective of the dominant bending curvature is linearly varying with an increase in shock wave pressure within the range of 1–2 HEL that is outlined window for the working condition of LPF [160].

4.3 3D Laser Forming

The precise control of bending angle and position by employing laser marking machine corroborates the pathways as an opportunity to interact with numerous parts and components without any human mediation [128]. To experiment, we observed at one crucial challenge i.e., underside marking inside the complex structure of the sheet metal is viable without additional conditioning such as overturning the object under fabrication shown in Fig. 16 [129]. The simplified procedure to make 3D pattern or fold the MS sheet metal to fold up out of plane is demonstrated in Figs. 16 and 17 [130]. Figure 14 demonstrates the procedure of making 3D duct using only underside marking [131]. Whereas Fig. 15 demonstrates the marking of 3D channel

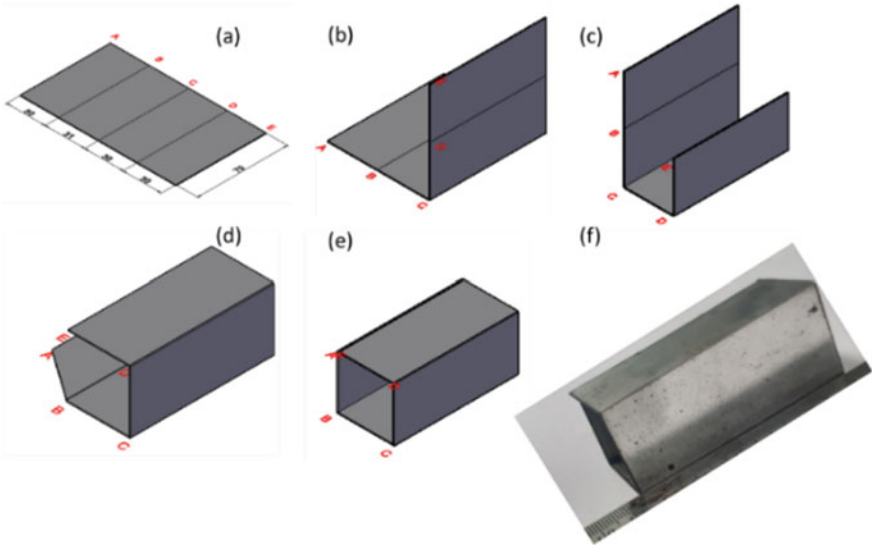

Fig. 16 Schematic of folding procedure for 3D duct out of MS sheet metal. **a** Marking over the sheet metal, **b** position of the first bend, **c** position of the second bend, **d** partial position of the third bend and **e** underside marking as a final bending procedure to make it 3D duct using laser forming

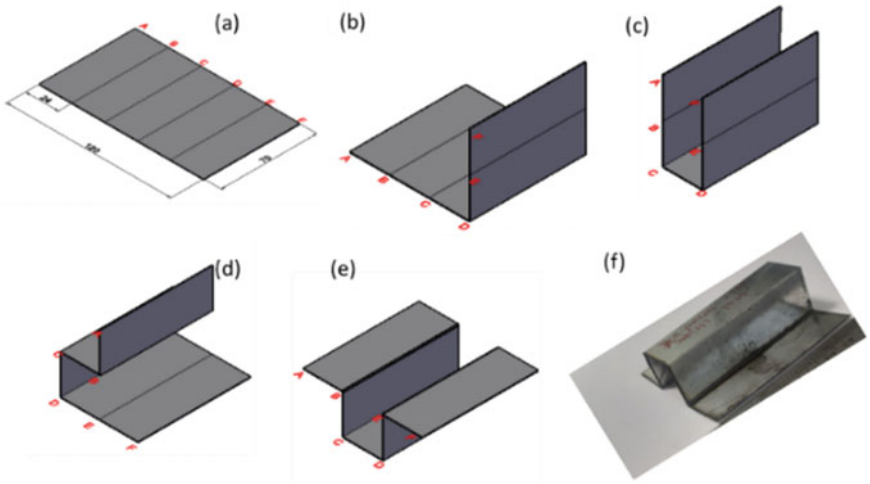

Fig. 17 Schematic of folding procedure for 3D channel out of MS sheet metal. **a** Marking over the sheet metal, **b** position of the first bend i.e., at mark position "d", **c** position of the second bend, at mark position "c" **d** first flange, outward bend by manual flipping of the object and (**d**) outside marking as a final flange bending procedure to make it 3D duct using laser forming

deploying similar procedures but few changes i.e., two undersides marking and two outside marking [132]. In this marking Galvano scanner-based laser marking system was employed. The laser processed parts and components can be taken for further assembly [133].

4.4 Advance Application of Laser Based Forming

Laser-forming based laser origami is a quick technique to turn idea into products demonstrated in Fig. 18 [161]. Laser origami delivers 3D components using cutting and heating [103]. The origami technique is faster than tradition 3D fabrication techniques such as different type and class of 3D printing [104]. Figure 18 demonstrates the conditional time requirement for the fabrication of the cover by three different technique such as 3D Printing, Manual fitment, and Laser-origami. Laser-origami is basically requiring no human intervention for assembly [105–107]. The prime though behind the origami is achieving 3D conformity by bending and lateral elongation of the parent material rather joining, by this means abolishing the labor-intensive product assembly [99]. Laser-origami attains the conformity in structure by inducing heat in the localized zone of the workpiece [100]. During the heating bending takes place by means of gravitational force and self-weight as well [101]. In this process laser-based heating is carried by defocusing the laser beam [103]. The defocus leading to the distribution of laser fluence (J/cm^2) over the large surface area [104]. This process is the best suitable example of cutting and forming, employing

Fig. 18 Advance and commercial application of laser-based forming. Despite 3D printing is an advance solution for making numerous conventional and unconventional objects the time taken to generate origami using laser it takes substantially less time in comparison to 3D printing system

a single system by close loop control of workbench movement [161]. Cooper and Ayers [161] Moreover, at the end of the process the pristine workpiece is found to be fully assembled [162].

4.5 Laser-Assisted Shock-Peening

There is a demand for lighter, more complex, yet strong components for machines [67]. The wear and tear of components is a major loss to the industry both economically and in terms of efficiency and productivity [68, 69]. Therefore, researchers have found many ways to increase the life of a component in both contact and non-contact way, among which one is Laser Shock Peening shown in Fig. 19 [163]. Laser shock Peening is an emerging surface treatment technique [164]. The technique of continuously inducing residual compressive stress in an object originally with the pin of the hammer is known as peening [165]. The process resulted in an increase is life of the object against cyclic loading and unloading. Many methods of peening have come up since the beginning [166].

One among which is shot peening [166]. Shot peening is a cold working process used to produce a compressive residual stress layer and modify mechanical properties of metals and composites [166]. It entails impacting a surface with shot (round

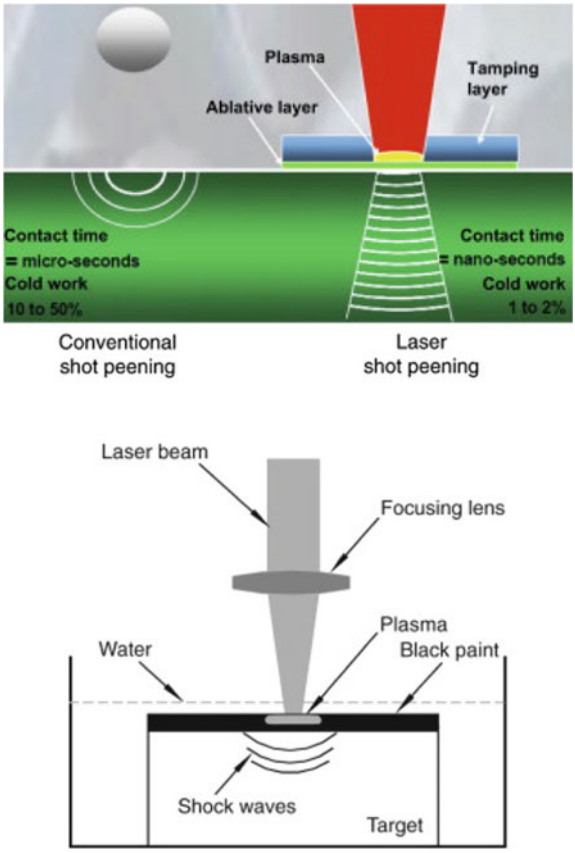

Fig. 19 Schematic of Laser Shock Peening Principle [with permission 145, 146]

metallic, glass, or ceramic particles) with force sufficient to create plastic deformation. Inducing the same impact using a laser instead of shots is known as laser shock peening [167].

The LSP is a distinguished surface characteristics modifying technique in commercial machine components as depicted in Fig. 20 [167]. The LSP technique on specified workpiece can induce significant compressive residual stress (CRS) under the laser interacted surfaces up to certain depth of the processed metallic elements [168]. The introduced CRS by means of LSP in turn enhances the Mechanical characteristics of the machine elements [169]. The characteristics are crack origination resistance and expansion through enhanced fatigue cycle and strength. [170] However, to understand the mechanism in detail simulation can be one of the effective tools [170]. The complexity in recording the response of material is due to shock wave discrimination along the vertical direction i.e., thickness of the alloyed machine elements [169]. To overcome such difficulty appropriate simulation can be carried out through appropriate computing platform [170].

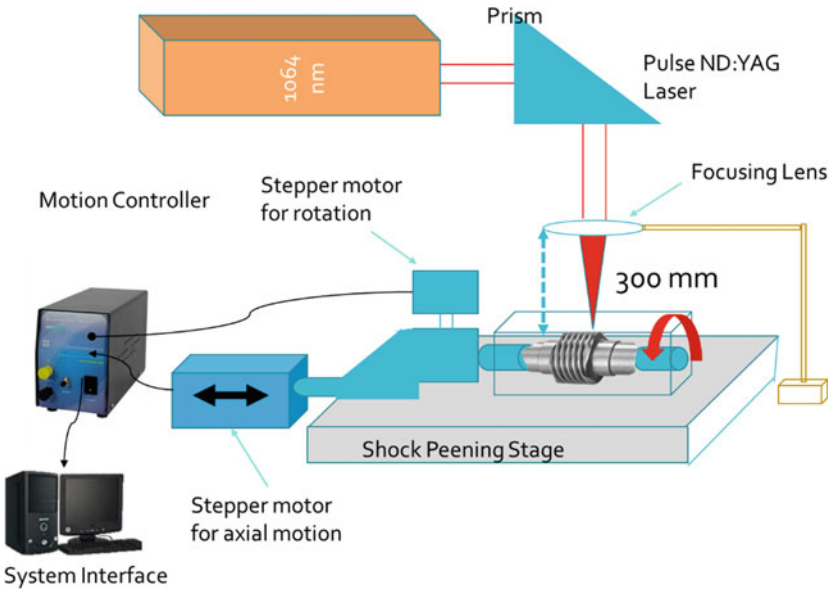

Fig. 20 Schematics of Laser assisted shock peening in underwater environment

4.6 Laser Assisted Crystallization

The melting characteristics of the PET polymer are not identical because of its dependency on the thermal history of materials [84]. Therefore, the melting characteristics o the complexly structured polymer that possesses the phase transition range between T_g and Tm are important to define the maximum working temperature of the amorphous polymer [101]. The laser processing close to the melting or above the melting temperature consistently resulting in phase, morphology, crystallinity, as well as alterations in physical and mechanical properties [100]. Also, measurement of effective melting temperature at equilibrium is important to outline the requirement of the crystallization process, and the reliance of 'phase's transition by employing Laser assisted crystallization of PET [100]. Many research groups conducted the investigations related to the it is melting performances and claimed complex melting behavior. The endotherms of the PET are attributed to the different lamella thickness distributions [103]. The lamella thickness produced upon cooling from (i) laser-induced crystallization temperature; (ii) laser-assisted annealing while inducing heat up to melting temperature, and (iii) extent up to laser-assisted primary (crystallization) and secondary (ablation) crystallization [104]. The melting ¬of lamellae produced during different laser-assisted crystallization, the process is of interest to carry out the differential scale calorimetric (DSC) measurement [105]. The rate of heating influences the melting temperature of the PET due to working temperature ranging between T_g (Glass Transition Temperature) and T_m (Melting Temperature), annealing during the process of melting, and most important is thermal lag [106].

The thermal history of thermal lag due to the time difference between one-incident laser pulses to another incident laser pulse [107]. Also, it persists due to heat re-generated or restored inside the materials is important to determine the shape of melting endotherms and maximum melting temperature [108]. In most of the cases, the change in color (physical properties) and brittleness (mechanical property) is due to accumulation of heat due to thermal lag in the laser-assisted crystallization process [109].

The LPF has demonstrated the outstanding features and numerous advantages for scaled up commercial applications. Furthermore, research and development in LPF is crucial to address the significant challenges of process manufacturing and system development. The output of system is limited to its capability for materials forming in micrometer scale. The size limiting condition leading to micro size plastic deformation due to reduced thickness: grain ratio. The limiting condition is applicable for high strength alloys. In case of ultrathin sheet thickness of alloys, the high flux of coupled shockwave's influence in turn leading to concave shape forming. However, convex bending is crucially challenging. The criticality of its application restricting its design of experiments because of temporary coating (ablative layer) and H_2O based transparent entrapment layer. The basic difficulty in case of using multiple passes i.e., using same layer continuously before attending the required bending angle i.e., inadequate procedure. The process is inadequate due to frequent redeposition of ablative layer during the process of the bending for high strength alloys. This process complexity leading to in-effectiveness. In this process light entrapment is required for the nanosecond time duration, which familiarizes the additional complexity. For industrial LPF process, constant water supply is required from nozzle for confinement. The reduction in ablative layer material's quantity during the process, leading to detrimental effect, whereas the flowing water level could substantially counterfeit the detrimental effect due to low volume of ablative material. Here we envisage the detailed and systematic attempt to address the shortcoming of the processes with optimum manufacturability and simple design of experiments, lead to wide range of scaled up commercial applications.

5 Conclusions

The laser-assisted heating to induce plastic strain to fine tune the bending, termed as laser-assisted forming. The laser-assisted forming is a rapid forming technology for generating 3D profiles stimulated by origami principles. The origami is first time employed beyond laser cutting and forming from flat non-structured sheet metal to finished conformity of the product, which includes vertically up and down folding patterns without involving any manual bending sequences. The bending orientation is tuned by experimenting the optimum laser beam rastering speed and subsequent bending angle by inducing thermal gradient across the cross-section or across the horizontal surface in the workpiece. The bending mechanism can be verified using thermal gradient modelling and simulations to map the critical point between bending

towards or away from the incident normal of the laser beam interacting over the flat specimen. The outlined laser beam parameters corroborate the pathway to demonstrate the numerous 3D folded complex profile of different automobile and components of medical gadgets. The laser origami employed the laser forming for precise alignment of two different components such as optical reflectors in order to guide the laser beam and make laser-based pattern over a specified segment of the sheet critically inaccessible on the underneath. This technological representation can be carried out using commercially available laser systems suitable for desired material without any accessories or optical arrangements.

References

1. Altıparmak, S.C., Yardley, V.A., Shi, Z., Lin, J.: Challenges in additive manufacturing of high-strength aluminium alloys and current developments in hybrid additive manufacturing. Int. J. Light. Mater. Manuf. **4**, 246–261 (2020)
2. Gao, W., Zhang, Y., Ramanujan, D., Ramani, K., Chen, Y., Williams, C., Wang, C.C., Shin, Y.C., Zhang, S., Zavattieri, P.: The status, challenges, and future of additive manufacturing in engineering. Comput.-Aided Des. **69**, 65–89 (2015)
3. Ngo, T., Kashani, A., Imbalzano, G., Nguyen, K.T., Hui, D.: Additive manufacturing (3D printing): a review of materials, methods, applications and challenges. Compos. Part B Eng. **143**, 172–196 (2018)
4. Mede, T., Kocjan, A., Paulin, I., Godec, M.: Numerical mesoscale modelling of microstructure evolution during selective laser melting. Metals **10**, 800 (2020)
5. Sunil Pathak Dutta, B., Froes, F.H.: The additive manufacturing (AM) of titanium alloys. In: Qian, M., Froes, F.H., (eds.) Titanium Powder Metallurgy, pp. 447–468. Butterworth-Heinemann, Boston, MA, USA (2015)
6. Siwick, B.J., Arslan, I., Wang, X.: Frontier nonequilibrium materials science enabled by ultrafast electron methods. MRS Bull. (2021)
7. Tan, J.H.K., Sing, S.L., Yeong, W.Y.: Microstructure modelling for metallic additive manufacturing: a review. Virtual Phys. Prototyp. **15**, 87–105 (2019)
8. Yang, M., Wang, L., Yan, W.: Phase-field modeling of grain evolutions in additive manufacturing from nucleation, growth, to coarsening. NPJ Comput. Mater. **7**, 56 (2021)
9. Hoppius, J.S., Kukreja, L.M., Knyazeva, M., Pohl, F.: On femtosecond laser shock peening of stainless steel AISI 316. Appl. Surf. Sci. **435**,1120–1124 (2018)
10. Duff W.H., Zhigilei, L.V.: Computational study of cooling rates and recrystallization kinetics in short pulse laser quenching of metal targets. J. Phys.: Conf. Series **59**, 413–417 (2007)
11. Noack, J., Hammer, D.X., Noojin, G.D., Rockwell, B.A., Vogel, A.: Influence of pulse duration on mechanical effects after laser-induced breakdown in water. J. Appl. Phys. **83**(12), 7488–7495 (1998)
12. Lee, D., Kannatey-Asibu, E.: Experimental investigation of laser shock peening using femtosecond laser pulses. J. Laser Appl. **23**(2), 022004 (2011)
13. Fabbro, R., Fournier, J., Ballard, P., Devaux, D., Virmont, J.: Physical study of laser-produced plasma in confined geometry. J. Appl. Phys. **68**(2), 775–784 (1990)
14. Takata, T., Enoki, M., Chivavibul, P., Matsui, A., Kobayashi, Y.: Effect of confinement layer on laser ablation and cavitation bubble during laser shock peening. Mater. Trans. **57**(10), 1776–1783 (2016)
15. Takata, T., Enoki, M., Chivavibul, P., Matsui, A., Kobayashi, Y.: Acoustic emission monitoring of laser shock peening by detection of underwater acoustic wave. Mater. Trans. **57**(5), 674–680 (2016)

16. Barker, L.M., Hollenbach, R.E.: Laser interferometer for measuring high velocities of any reflecting surface. J. Appl. Phys. **43**(11), 4669–4675 (1972)
17. Takemoto, M., Nakamura, M., Masano, S., Ueno, S.: Effect of shot peening on the delayed fracture using the almen strip and ae technique. J. Acoustic Emission **27** (2009); Segur J.B., Oberstar, H.E.: Ind. Eng. Chem. **43** 2117–2120 (1951)
18. Ito, K., Enoki, M.: Acquisition and analysis of continuous acoustic emission waveform for classification of damage sources in ceramic fiber mat. Mater. Trans. **48**(6), 1221–1226 (2007)
19. Montross, C.S., Wei, T., Ye, L., Clark, G., Mai, Y.-W.: Laser shock processing and its effects on microstructure and properties of metal alloys: a review. Int. J. Fatigue 1021–1036 (2002)
20. Niehoff, H.S., Vollertson, F.: Laser induced shock waves in deformation processing. Metalurgija-J. Metall. 183–194 (2005)
21. Wang, Y., Fan, Y., Vukelic, S., Yao, Y.L.: Energy-level effects on the deformation mechanism in microscale laser peen forming. J. Manuf. Process. 1–12 (2007)
22. Kannatey-Asibu, E., Jr., Lathia, B.: Laser forming by shock peening. Trans. NAMRI **35**, 401–407 (2007)
23. Hackel, L., Harris, F.: Contour forming of metals by laser peening. U.S. Patent No. 6,410,884 (2002)
24. Hackel, L., Harris, F.: Pre-loading of components during laser peen forming. U.S. Patent No. 6,670,578 (2002)
25. Ocaña, J.L., Morales, M., García-Ballesterosa, J.J., Porro, J.A., García, O., Molpeceres, C.: Laser shock microforming of thin metal sheets. Appl. Surf. Sci. **255**, 5633–5636 (2009)
26. Wang, Y., Fan, Y., Kysar, J.W., Vukelic, S., Yao, Y.L.: Microscale laser peen forming of single crystal. J. Appl. Phys. **103**(6), 063525 (2008)
27. Ding, K., Ye, L.: Three-dimensional dynamic finite element analysis of multiple laser shock peening processes. Surf. Eng. **19**(5), 351–358 (2003)
28. Hu, Y.X., Yao, Z.Q., Hu, J.: 3-D fem simulation of laser shock processing. Surf. Coat. Technol. **201**(3–4), 1426–1435 (2006)
29. Amarchinta, H.K., Grandhi, R.V., Langer, K., Stargel, D.S.: Material model validation for laser shock peening process simulation. Modell. Simul. Mater. Sci. Eng. **17**(1), 015010 (2009)
30. Hu, Y.X., Yao, Z.Q.: Numerical simulation and experimentation of overlapping laser shock processing with symmetry Cell. Int. J. Mach. Tools Manuf. **48**(2), 152–162 (2008)
31. Ocaña, J.L., Moralesa, M., Molpeceresa, C., García, O., Porro, J.A., García-Ballesteros, J.J.: Short pulse laser microforming of thin metal sheets for MEMS manufacturing. Appl. Surf. Sci. **254**(4), 997–1001 (2007)
32. Geiger, M., Kleiner, M., Eckstein, R., Tiesler, N., Engel, U.: Microforming. CIRP Ann. Manuf. Technol. **50**(2), 445–462 (2001)
33. Johnson, G., Cook, W.: A constitutive model and data for metals subjected to large strains, high strain rates and high temperatures. In: Michael, J.M., Joseph, E.B. (eds.) Proceedings of the 7th International Symposium on Ballistics, International Ballistics Committee, pp. 541–547. The Hague, Netherlands (1983)
34. Peyre, P., Chaieb, A.I., Braham, A.C.: Fem calculation of residual stresses induced by laser shock processing in stainless steels. Modell. Simul. Mater. Sci. Eng. **15**(3), 205–221 (2007)
35. Shukla, A.K., Akash, K., Palani, I.A., Manivannan, A.: Laser assisted wet texturing of flexible polyethylene terephthalate substrate using Nd3+: YAG laser for photovoltaics devices. Mater. Sci. Eng.: B **226**, 78–85 (2017)
36. Berthe, L., Fabbro, R., Peyre, P., Tollier, L., Bartnicki, E.: Shock waves from a water-confined laser-generated plasma. J. Appl. Phys. **82**(6), 2826–2832 (1997)
37. Zhang, W., Yao, Y.L., Noyan, I.C.: Microscale laser shock peening of thin films, part 1: experiment, modeling and simulation. ASME J. Manuf. Sci. Eng. **126**(1), 10–17 (2004)
38. Meyers, M.A., Benson, D.J., Voringer, O., Kad, B.K., Xue, Q., Fu, H.-H.: Constitutive description of dynamic deformation: physically-based mechanisms. Mater. Sci. Eng., A, **322**(1–2), 194–216 (2002)
39. Gilman, J.J.: Dislocation dynamics and the response of materials to impact. Appl. Mech. Rev. **218**, 767–783 (1968)

40. Leu, D.-K.: Modeling of size effect on tensile flow stress of sheet metal in micro forming. ASME J. Manuf. Sci. Eng. **131**(1), 011002 (2009)
41. Engel, U., Eckstein, R.: Micro forming—from basic research to its realization. J. Mater. Process. Technol. **125–126**, 35–44 (2002)
42. Kennedy, D., Rockwell, H.B.: Laser-Induced Breakdown In Aqueous Media, vol. 21, pp. 155–248. Elsevier Science Ltd.
43. Martí-López, L., Ocaña, R., Piñeiro, E., Asensio, A.: Laser peening induced shock waves and cavitation bubbles in water studied by optical schlieren visualization. Phys. Procedia **12**, 442–451 (2011)
44. H. Lee, A. Gojani, T. Han, J. Yoh. Dynamics of laser-induced bubble collapse visualized by time-resolved optical shadowgraph. Journal of Visualization, 14, 331–337.
45. Vogel, A., Busch, S., Parlitz, U.: J. Acoustical Soc. Am. **100**, 148; Cole, R.H.: Underwater Explosions. Princeton University Press
46. Segur, J.B., Oberstar, H.E.: Viscosity of glycerol and its aqueous solutions. Indus. Eng. Chem. **43**(9), 2117–2120 (1951); Ito, K., Enoki, M.: Mater. Trans. **48**, 1221–1226 (2007)
47. Sause, M.G.R.: Investigation of pencil-lead breaks as acoustic emission sources (2011)
48. Buttle, D.J., Scruby, C.B.: Characterization of particle impact by quantitative acoustic emission. Wear **137**(1), 63–90 (1990)
49. Philipp, A., Lauterborn, W.: Cavitation erosion by single laser-produced bubbles. J. Fluid Mech. **361**, 75–116 (1998)
50. Ma, C., Wang, C., Gao, B., Adams, J., Wu, G., Zhang, H.: Recent progress in ultrafast lasers based on 2D materials as a saturable absorber. Appl. Phys. Rev. **6**(4), 041304 (2019)
51. Ohl, C.D.: Cavitation incep221tion following shock wave passage. Phys. Fluids **14**(10), 3512–3521 (2002)
52. Ouyang, P., Li, P., Leksina, E.G., Michurin, S.V., He, L.: Effect of liquid properties on laser ablation of aluminum and titanium alloys. Appl. Surf. Sci. **360**, 880–888 (2016)
53. Mukai, N., Aoki, N., Obata, M., Ito, A., Sano, Y., Konagai, C.: Proceedings of 3rd JSME/ASME International Conference on Nuclear Engineering (ICONE-3), p. III-1489. Kyoto (1995)
54. Ochi, Y., Masaki, K., Matsumura, T., Wakabayashi, Y., Sano, Y., Kubo, T.: Proceedings of 12th International Conference on Experimental Mechanics (ICEM12). Bari (2004).
55. Altenberger, I., Sano, Y., Nikitin, I., Scholtes, B.: Proceedings of 9th International Fatigue Congress (FATIGUE 2006). Atlanta (2006)
56. Ochi, Y., Masaki, K., Matsumura, T., Kumagai, Y., Hamaguchi, T., Sano, Y.: Proceedings of International Conference on Advanced Materials Development and Performance (AMDP2005). Auckland (2005)
57. Sano, Y., Obata, M., Kubo, T., Mukai, N., Yoda, M., Masaki, K., Ochi, Y.: Mater. Sci. Eng. A **417**, 334 (2006)
58. Sano, Y., Kimura, M., Sato, K., Obata, M., Sudo, A., Hamamoto, Y., Shima, S., Ichikawa, Y., Yamazaki, H., Naruse, M., Hida, S., Watanabe, T., Oono, Y.: Proceedings of 8th International Conference on Nuclear Engineering (ICONE-8). Baltimore (2000)
59. Delloro, F., Zagouri, D., Boustie, M., Jeandin, M.: A laser shock approach to cold spray. In: Materials Science Forum, vol. 941, pp. 1833–1840. Trans Tech Publications Ltd (2018)
60. Fabbro, R., Peyre, P., Berthe, L., Scherpereel, X.: Physics and applications of laser-shock processing. J. Laser Appl. **10**(6), 265–279 (1998)
61. Masaki, K., Ochi, Y., Matsumura, T.: Initiation and propagation behaviour of fatigue cracks in hard-shot peened type 316L steel in high cycle fatigue. Fatigue Fract. Eng. Mater. Struct. **27**(12), 1137–1145 (2004)
62. Nalla, R.K., Altenberger, I., Noster, U., Liu, G.Y., Scholtes, B., Ritchie, R.O.: On the influence of mechanical surface treatments—deep rolling and laser shock peening—on the fatigue behavior of Ti–6Al–4V at ambient and elevated temperatures. Mater. Sci. Eng., A **355**(1–2), 216–230 (2003)
63. Sathyajith, S., Kalainathan, S.: Effect of laser shot peening on precipitation hardened aluminum alloy 6061–T6 using low energy laser. Opt. Lasers Eng. **50**(3), 345–348 (2012)

64. Sathyajith, S., Kalainathan, S., Swaroop, S.: Laser shot peening of 304 austenitic stainless steel without protective coating. In: Materials Science Forum, vol. 699, pp. 131–140. Trans Tech Publications Ltd. (2012)
65. Schmidt-Uhlig, T., Karlitschek, P., Yoda, M., Sano, Y., Marowsky, G.: Laser shock processing with 20 MW laser pulses delivered by optical fibers. Euro. Phys. J. Appl. Phys. **9**(3), 235–238 (2000)
66. Chichkov, B.N., Momma, C., Nolte, S., Von Alvensleben, F., Tünnermann, A.: Femtosecond, picosecond and nanosecond laser ablation of solids. Appl. Phys; A **63**(2), 109–115 (1996)
67. Shukla, A.K., Yadav, V.M., Kumar, A., Palani, I.A., Manivannan, A.: Investigations on effect of laser-induced self-assembled patterning on optical properties of flexible polyimide substrates for solar cell applications. J. Phys. D: Appl. Phys. **51**(4), 045502 (2018)
68. Lazarus, N., Smith, G.L.: Laser forming for complex 3D folding. Adv. Mater. Technol. **2**(10), 1700109 (2017)
69. Johnson, G.R.: A constitutive model and data for materials subjected to large strains, high strain rates, and high temperatures. In: Proceedings of the 7th International Symposium on Ballistics, pp. 541–547. The Hague, The Netherlands (1983)
70. Hfaiedh, N., Peyre, P., Song, H., Popa, I., Ji, V., Vignal, V.: Finite element analysis of laser shock peening of 2050–T8 aluminum alloy. Int. J. Fatigue **70**, 480–489 (2015)
71. Cuq-Lelandais, J.P.: Etude du Comportement Dynamique de Matériaux Sous Choc Laser Subpicoseconde. Ph.D. Thesis, ISAE-ENSMA Ecole Nationale Supérieure de Mécanique et d'Aérotechique, Poitiers, France (2010)
72. Fabbro, R., Fournier, J., Ballard, P., Devaux, D., Virmont, J.: Physical study of laser-produced plasma in confined geometry. J. Appl. Phys. **68**, 775–784 (1990)
73. Peyre, P., Berthe, L., Scherpereel, X., Fabbro, R., Bartnicki, E.: Experimental study of laser-driven shock waves in stainless steels. J. Appl. Phys. **84**, 5985–5992 (1998)
74. Pope, R.M., Fry, E.S.: Absorption spectrum (380–700 nm) of pure water. II. Integr. Cavity Meas. Appl. Opt. **36**, 8710–8723 (1997)
75. Peyre, P., Berthe, L., Vignal, V., Popa, I., Baudin, T.: Analysis of laser shock waves and resulting surface deformations in an Al–Cu–Li aluminum alloy. J. Phys. D Appl. Phys. **45**, 335304 (2012)
76. Boustie, M., Cuq-Lelandais, J., Bolis, C., Berthe, L., Barradas, S., Arrigoni, M., De Resseguier, T., Jeandin, M.: Study of damage phenomena induced by edge effects into materials under laser driven shocks. J. Phys. D Appl. Phys. **40**, 7103 (2007)
77. Sano, Y., Kimura, M., Yoda, M., Mukai, N., Sato, K., Uehara, T., Ito, T., Shimamura, M., Sudo, A., Suezono, N.: Development of fiber-delivered laser peening system to prevent stress corrosion cracking of reactor components (2001)
78. Nie, X., He, W., Zang, S., Wang, X., Zhao, J.: Effect study and application to improve high cycle fatigue resistance of TC11 titanium alloy by laser shock peening with multiple impacts. Surf. Coat. Technol. **253**, 68–75 (2014)
79. Ren, X.D., Zhou, W.F., Liu, F.F., Ren, Y.P., Yuan, S.Q., Ren, N.F., Xu, S.D., Yang, T.: Microstructure evolution and grain refinement of Ti-6Al-4V alloy by laser shock processing. Appl. Surf. Sci. **363**, 44–49 (2016)
80. Lou, S., Li, Y., Zhou, L., Nie, X., He, G., He, W.: Surface nanocrystallization of metallic alloys with different stacking fault energy induced by laser shock processing. Mater. Des. **104**, 320–326 (2016)
81. Hongchao, Q.: Experimental investigation of laser peening on Ti17 titanium alloy for rotor blade applications. Appl. Surf. Sci. **351**, 524–530 (2015)
82. Tong, Z., Ren, X., Ren, Y., Dai, F., Ye, Y., Zhou, W., Chen, L., Ye, Z.: Effect of laser shock peening on microstructure and hot corrosion of TC11 alloy. Surf. Coat. Technol. **335**, 32–40 (2018)
83. Sollier, A., Berthe, L., Fabbro, R.: Numerical modeling of the transmission of breakdown plasma generated in water during laser shock processing. EPJ Appl. Phys. **16**, 131–139 (2001)
84. Wu, B., Shin, Y.C.: A self-closed thermal model for laser shock peening under the water confinement regime configuration and comparisons to experiments. J. Appl. Phys. **97**, 113517 (2005)

85. Askar'yan, G.A., Moroz, E.M.: Pressure on evaporation of matter in a radiation beam. Sov. J. Exp. Theor. Phys. **16**, 1638 (1963)
86. Anderholm, N.C.: Laser-generated stress waves. Appl. Phys. Lett. **16**(3), 113–115 (1970)
87. Fairand, B.P., Wilcox, B.A., Gallagher, W.J., Williams, D.N.: Laser shock-induced microstructural and mechanical property changes in 7075 aluminums. J. Appl. Phys. **43**, 3893–3895 (1972)
88. Peyre, P., Fabbro, R., Merrien, P., Lieurade, H.: Laser shock processing of aluminum alloys. Application to high cycle fatigue behaviour. Mater. Sci. Eng. A **210**, 102–113 (1996)
89. Pavan, M., Furfari, D., Ahmad, B., Gharghouri, M., Fitzpatrick, M.: Fatigue crack growth in a laser shock peened residual stress field. Int. J. Fatigue **123**, 157–167 (2019)
90. Dhakal, B., Swaroop, S.: Review: laser shock peening as post welding treatment technique. J. Manuf. Process. **32**, 721–733 (2018)
91. Sun, R., Li, L., Guo, W., Peng, P., Zhai, T., Che, Z., Li, B., Guo, C., Zhu, Y.: Laser shock peening induced fatigue crack retardation in Ti-17 titanium alloy. Mater. Sci. Eng. A **737**, 94–104 (2018)
92. Peyre, P., Scherpereel, X., Berthe, L., Carboni, C., Fabbro, R., Béranger, G., Lemaitre, C.: Surface modifications induced in 316L steel by laser peening and shot peening. Influence on pitting corrosion resistance. Mater. Sci. Eng. A **280**, 294–302 (2000)
93. Devaux, D., Fabbro, R., Virmont, J.: Generation of shock-waves by laser-matter interaction in confined geometries. J. Phys. Iv **1**, 179–182 (1991)
94. Peyre, P., Fabbro, R.: Laser shock processing: a review of the physics and applications. Opt. Quantum Electron. **27**, 1213–1229 (1995)
95. Berthe, L., Fabbro, R., Peyre, P., Tollier, L., Bartnicki, E.: Shock waves from a waterconfined laser-generated plasma. J. Appl. Phys. **82**, 2826–2832 (1997)
96. Fabbro, R., Peyre, P., Berthe, L., Scherpereel, X.: Physics and applications of lasershock processing. J. Laser Appl. **10**, 265–279 (1998)
97. O'keefe, J., Skeen, C.: Laser-induced stress-wave and impulse augmentation, Appl. Phys. Lett. **21**, 464–466 (1972)
98. Yang, L.C.: Stress waves generated in thin metallic-films by a Q-switched rubylaser. J. Appl. Phys. **45**, 2601–2608 (1974)
99. Anderholm, N.: Laser-generated stress waves. Appl. Phys. Lett. **16**, 113–115 (1970)
100. Anderholm, N., Boade, R.: Laser-induced stress waves in quartz phenolic. J. Appl. Phys. **43**, 434–436 (1972)
101. Anderholm, N.: Fast gas switch for characterizing laser output pulses. Appl. Opt. **11**, 2057–2059 (1972)
102. Wu, B.: Numerical modeling and analysis of laser-matter interactions in laser based manufacturing and materials processing with short and ultrashort lasers Ph.D. Thesis, Purdue University, West Lafayette (IN) (2007)
103. Gladush, G.G., Smurov, I.: Physics of laser materials processing: theory and experiment, vol. 146. Springer Science & Business Media (2011)
104. Yocom, C.J., Zhang, X., Liao, Y.: Research and development status of laser peen forming: a review. Opt. Laser Technol. **108**, 32–45 (2018)
105. Gusarov, A.V., Smurov, I.: Thermal model of nanosecond pulsed laser ablation: analysis of energy and mass transfer. J. Appl. Phys. **97**, 014307 (2005)
106. Mazhukin, V.I., Nossov, V.V., Smurov, I., Flamant, G.: Modelling of radiation transfer in low temperature nanosecond laser-induced plasma of Al vapour. J. Phys. D Appl. Phys. **37**, 185–199 (2004)
107. Mazhukin, V.I., Smurov, I., Flamant, G.: 2D-simulation of the system: laser beamplus laser plasma plus target. Appl. Surf. Sci. **96–8**, 89–96 (1996)
108. Zeldovich, Y.B., Raizer, Y.P.: Physics of Shock Waves and High-temperature Hydrodynamic Phenomena. Academic Press Inc., New York (1966)
109. More, R.M., Warren, K.H., Young, D.A., Zimmerman, G.B.: A new quotidian equation of state (Qeos) for hot dense matter. Phys. Fluids **31**, 3059–3078 (1988)

110. Hu, Y.X., Yao, Z.Q.: Overlapping rate effect on laser shock processing 1045 of steel by small spots with Nd:YAG pulsed laser. Surf. Coat. Technol. **202**, 1517–1525 (2008)
111. Ocaña, J., Morales, M., Molpeceres, C., García, O., Porro, J., García-Ballesteros, J.: Short pulse laser microforming of thin metal sheets for MEMS manufacturing. Appl. Surf. Sci. **254**, 997–1001 (2007)
112. Sagisaka, Y., Kamiya, M., Matsuda, M., Ohta, Y.: Thin-sheet-metal bending by laser peen forming with femtosecond laser. J. Mater. Process. Technol. **210**, 2304–2309 (2010)
113. Hu, Y., Luo, M., Yao, Z.: Increasing the capability of laser peen forming to bend titanium alloy sheets with laser-assisted local heating. Mater. Des. **90**, 364–372 (2016)
114. Shen, H., Vollertsen, F.: Modelling of laser forming—an review. Comput. Mater. Sci. **46**, 834–840 (2009)
115. Umapathi, A., Swaroop, S.: Residual stress distribution in a laser peened Ti-2.5 Cu alloy. Surf. Coat. Technol. **307**, 38–46 (2016)
116. Sihai, L., Xiangfan, N., Liucheng, Z., Xi, Y., Weifeng, H., Yinghong, L.: Thermal stability of surface nanostructure produced by laser shock peening in a Ni-based superalloy. Surf. Coat. Technol. **311**, 337–343 (2017)
117. Xiao, Y., Peng, C.: Influence of laser shock peening on fatigue life of transmission gears in aeroengine. In: 2016 Prognostics and System Health Management Conference (PHM-Chengdu), pp. 1–4. IEEE (2016)
118. Gheisari, R., Lan, P., Polycarpou, A.A.: Efficacy of surface microtexturing in enhancing the tribological performance of polymeric surfaces under starved lubricated conditions. Wear **444**, 203162 (2020)
119. Zhu, R., Zhang, Y., Zhang, C.: Surface residual stress, micro-hardness and geometry of TC6 titanium alloy thin-wall parts processed by multiple oblique laser shock peening. Mater. Res. Exp. **7**(10), 106526 (2020)
120. Ganesh, P., Sundar, R., Kumar, H., Kaul, R., Ranganathan, K., Hedaoo, P., Raghavendra, G. et al.: Studies on fatigue life enhancement of pre-fatigued spring steel specimens using laser shock peening. Mater. Design (1980–2015) **54**, 734–741 (2014)
121. Gujba, A.K., Medraj, M.: Laser peening process and its impact on materials properties in comparison with shot peening and ultrasonic impact peening. Materials **7**(12), 7925–7974 (2014)
122. Guarino, S., Barletta, M., Afilal, A.: High Power Diode Laser (HPDL) surface hardening of low carbon steel: Fatigue life improvement analysis. J. Manuf. Process. **28**, 266–271 (2017)
123. Prabhakaran, S., Kalainathan, S., Shukla, P., Vasudevan, V.K.: Residual stress, phase, microstructure and mechanical property studies of ultrafine bainitic steel through laser shock peening. Optics Laser Technol. **115**, 447–458 (2019)
124. Schaaf, P. (ed.): Laser Processing of Materials: Fundamentals, Applications and Developments, vol. 139. Springer Science & Business Media (2010)
125. Malinauskas, M., Žukauskas, A., Hasegawa, S., Hayasaki, Y., Mizeikis, V., Buividas, R., Juodkazis, S.: Ultrafast laser processing of materials: from science to industry. Light: Sci. Appl. **5**(8), e16133–e16133 (2016)
126. Steen, W.M.: Arc augmented laser processing of materials. J. Appl. Phys. **51**(11), 5636–5641 (1980)
127. Perrière, J., Millon, E., Fogarassy, E. (eds).: Recent advances in laser processing of materials (2006)
128. Chien, C.Y., Gupta, M.C.: Pulse width effect in ultrafast laser processing of materials. Appl. Phys. A **81**(6), 1257–1263 (2005)
129. Duley, W.W.: Laser Processing and Analysis of Materials. Springer Science & Business Media (2012)
130. Weber, R., Hafner, M., Michalowski, A., Graf, T.: Minimum damage in CFRP laser processing. Phys. Procedia **12**, 302–307 (2011)
131. Bartkowiak, K., Ullrich, S., Frick, T., Schmidt, M.: New developments of laser processing aluminium alloys via additive manufacturing technique. Phys. Procedia **12**, 393–401 (2011)
132. Kruusing, A.: Handbook of Liquids-Assisted Laser Processing. Elsevier (2010)

133. Kreimeyer, M., Wagner, F., Vollertsen, F.: Laser processing of aluminum–titanium-tailored blanks. Opt. Lasers Eng. **43**(9), 1021–1035 (2005)
134. Fan, C.-H., Longtin, J.P.: Modeling optical breakdown in dielectrics during ultrafast laser processing. Appl. Opt. **40**(18), 3124–3131 (2001)
135. Besner, S., Degorce, J.-Y., Kabashin, A.V., Meunier, M.: Influence of ambient medium on femtosecond laser processing of silicon. Appl. Surface Sci. **247**(1–4), 163–168 (2005)
136. Seyedkashi, S.M.H., Cho, J.R., Lee, S.H., Moon, Y.H.: Feasibility of underwater laser forming of laminated metal composites. Mater. Manuf. Process. **33**(5), 546–551 (2018)
137. Hu, Y., Han, Y., Yao, Z., Hu, J.: Three-dimensional numerical simulation and experimental study of sheet metal bending by laser peen forming. J. Manuf. Sci. Eng. **132**(6) (2010)
138. Zohdi, T.I.: Ultra-fast laser-patterning computation for advanced manufacturing of powdered materials exploiting knowledge-based heat-kernels. Comput. Methods Appl. Mech. Eng. **343**, 234–248 (2019)
139. Turkyilmazoglu, M.: An analytic parametric study of rounded laser pulse heating. Optik **240**, 167001 (2021)
140. Bode, T.: Simulation of the Particle Distribution and Resulting Laser Processing of Selective Laser Melting Processes. Master's thesis, Gottfried Wilhelm Leibniz Universität, Hannover (2017)
141. Ding, K., Ye, L.: 1—General introduction. In: Woodhead Publishing Series in Metals and Surface Engineering, Laser Shock Peening, pp. 1–6. Woodhead Publishing (2006)
142. Gariépy, A., Miao, H., Lévesque, M.: Peen forming. In: Hashmi, S., Batalha, G.F., Van Tyne, C.J., Yilbas, B. (eds.) Comprehensive Materials Processing, pp. 295–329. Elsevier (2014)
143. Demir, K., Zhang, Z., Ben-Artzy, A., Hosemann, P., Gu, G.X.: Laser scan strategy descriptor for defect prognosis in metal additive manufacturing using neural networks. J. Manuf. Process. **67**, 628–634 (2021)
144. Radziemski, L.J.: Lasers-Induced Plasmas and Applications. CRC Press (2020)
145. Scruby, C.B., Dewhurst, R.J., Hutchins, D.A., Palmer, S.B.: Quantitative studies of thermally generated elastic waves in laser-irradiated metals. J. Appl. Phys. **51**(12), 6210–6216 (1980)
146. Hutchins, D.A.: Ultrasonic generation by pulsed lasers. Phys. Acoustics **18**, 21–123 (1988)
147. Fox, J.A.: Effect of water and paint coatings on laser-irradiated targets. Appl. Phys. Lett. **24**(10), 461–464 (1974)
148. Yeung, H., Hutchinson, K., Lin, D.: Design and implementation of laser powder bed fusion additive manufacturing testbed control software. In: 2021 International Solid Freeform Fabrication Symposium. University of Texas at Austin (2021)
149. Yang, Y., Ragnvaldsen, O., Bai, Y., Yi, M., Xu, B.-X.: Three-dimensional non-isothermal phase-field modeling of microstructure evolution during selective laser sintering (2019). arXiv:1902.04519
150. Xu, B.-X., Min, Y., Yang, Y.: Phase-field simulation on process-microstructure-property relation in power bed fusion additive manufactured metals.
151. Zohdi, T.I.: DEM extensions: higher-fidelity laser modeling. In: Modeling and Simulation of Functionalized Materials for Additive Manufacturing and 3D Printing: Continuous and Discrete Media, pp. 171–196. Springer, Cham (2018)
152. Apostolou, P.: High Performance Matrix-Fee Method for Large-Scale Finite Element Analysis on Graphics Processing Units. University of Pittsburgh, PhD diss. (2020)
153. Kim, D.H., Zohdi, T.I.: Tool path optimization of selective laser sintering processes using deep learning. Comput. Mech. 1–19 (2021)
154. Yu, T., Zhao, J.: Semi-coupled resolved CFD–DEM simulation of powder-based selective laser melting for additive manufacturing. Comput. Methods Appl. Mech. Eng. **377**, 113707 (2021)
155. Prabhakaran, S., Kalainathan, S.: Compound technology of manufacturing and multiple laser peening on microstructure and fatigue life of dual-phase spring steel. Mater. Sci. Eng., A **674**, 634–645 (2016)
156. Kumar, D., Idapalapati, S., Wang, W., Narasimalu, S.: Effect of surface mechanical treatments on the microstructure-property-performance of engineering alloys. Materials **12**(16), 2503 (2019)

157. Brenner, A., Bornschlegel, B., Finger, J.: Increasing productivity of ultrashort pulsed laser ablation in advance for a combination process with ns-laser. J. Laser Micro Nanoeng. **14**(1), 100–107 (2019)
158. Pawlowski, L.: Thick laser coatings: a review. J. Therm. Spray Technol. **8**(2), 279–295 (1999)
159. Draper, C.W., Ewing, C.A.: Laser surface alloying: a bibliography. J. Mater. Sci. **19**(12), 3815–3825 (1984)
160. Riabkina-Fishman, M., Zahavi, J.: Laser alloying and cladding for improving surface properties. Appl. Surf. Sci. **106**, 263–267 (1996)
161. Cooper, K.P., Ayers, J.D.: Laser melt-particle injection processing. Surf. Eng. **1**(4), 263–272 (1985)
162. Rehn, L.E., Picraux, S.T., Wiedersich, H: Surface Alloying by Ion, Electron and Laser Beams (1986)
163. Kopel, A., Reitz, W.: Laser surface treatment. Adv. Mater. Process. **156**(3), 39–41 (1999)
164. Cooper, K.P., Slebodnick, P.: Recent developments in laser melt/particle injection processing. J. Laser Appl. **1**(4), 21–29 (1989)
165. McCafferty, E., Moore, P.G.: Electrochemical behavior of laser-processed metal surfaces. In: Laser Surface Treatment of Metals, pp. 263–295. Springer, Dordrecht (1986)
166. Schneider, M.F.: Laser cladding. Dimensions [mm] **14**, 10 (1998)
167. Cerri, W., Martinella, R., Mor, G.P., Bianchi, P.: Laser deposition of carbide-reinforced coatings. Surf. Coat. Technol. **49**(1–3), 40–45 (1991)
168. Barner-Kowollik, C., Bastmeyer, M., Blasco, E., Delaittre, G., Müller, P., Richter, B., Wegener, M.: 3D laser micro-and nanoprinting: challenges for chemistry. Angew. Chem. Int. Ed. **56**(50), 15828–15845 (2017)
169. Chen, T.-H., Fardel, R., Arnold C.B.: Ultrafast z-scanning for high-efficiency laser micromachining. Light: Sci. Appl. **7**(4), 17181–17181 (2018)
170. Geiger, M., Vollertsen, F.: The mechanisms of laser forming. CIRP Ann. **42**(1), 301–304 (1993)
171. Magee, J., Watkins, K.G., Steen, W.M.: Advances in laser forming. J. Laser Appl. **10**(6), 235–246 (1998)

Introduction to Gas and Solid State Laser Techniques in Cutting Process

Şenol Bayraktar and Cem Alparslan

1 Introduction to Lasers

The basis of the laser is based on Albert Einstein's theory of excited radiation in 1916. According to this theory, the excited atom descends to a low energy level. As a result, the atom is expected to emit photons. These emitted photons produce a monochromatic light beam with the same force and direction. Thus, energy emerges [1]. The basis of the laser which started with Albert Einstein, continued when Rodolph W. Landenburg proved the existence of excited radiation and negative absorption in 1928. The possibility of number density inversion by Valentin Fabrikant in 1940 caused a question mark in the minds. The studies gained momentum with the first demonstration of induced radiation in the hydrogen spectrum by Williams Lamb and Retherford in 1947. Charles Townes was inspired by previous works and discovered the first instrument called MAZER (Microwave Amplification of Stimulated Emission of Radiation) based on stimulated radiation in 1951. Joseph Weber and Alexander Prokhorov Nikolai independently discovered MAZER at the same time. Gordon Gould first used the "Laser" word in the literature in 1957. The meaning of the "Laser" word is "Light Amplification by Stimulated Emission of Radiation" [2, 3]. The efficiency of the laser depends on the emission of radiation-induced by the absorption of electromagnetic energy or photons by atoms. Photons known as discrete packets of light emit spontaneously without outside interference. This is called spontaneous emission.

On the other hand, electrons emit the excess energy as light, as they fall from high energy to low energy levels. If the photon's energy is exactly matched with the excess energy released when an electron transitions to a low energy level, the emission of

Ş. Bayraktar (✉) · C. Alparslan
Faculty of Engineering and Architecture, Department of Mechanical Engineering, Recep Tayyip Erdoğan University, 53100 Rize, Turkey
e-mail: senol.bayraktar@erdogan.edu.tr

J. Radhakrishnan and S. Pathak (eds.), *Advanced Engineering of Materials Through Lasers*, Advances in Material Research and Technology,
https://doi.org/10.1007/978-3-031-03830-3_2

light can be stimulated. This is called induced or stimulated emission of radiation. Lasers can generate photons as a coherent light beam compared to different light sources. They can focus on very small areas and produce monochromatic light due to this feature [4]. The first laser in history was produced from pink ruby by Theodore Maiman using the theories of Charles Townes and Arthur L. Schawlow in 1960 [5]. The use of laser increased after 1960. Thus, it contributed to new developments in different fields. Javan and some of his colleagues focused on a laser that could work with helium–neon gas in 1961 [6]. Robert Hall discovered semiconductor lasers in 1962. Nd:YAG lasers were invented by Geusi, Markos and Uiteit at Bell laboratories in 1964. Later, a gas laser cutting process containing a mixture of carbon dioxide was discovered by Kumar Patel to use it in the industry at Bell laboratories [7]. Gas lasers began to be used in cutting and drilling processes for diamond mining in 1965. Laser cutting processes depending on the developing industry in 1967 started to be applied in very wide areas and had a critical place in the aviation industry. It was preferred to cut many materials in the early 1970s. It was used for laser marking processes in barcode readers in supermarkets in 1974 [8]. A large number of commercial laser cutting machines were manufactured in various industries in the 1980s. Thus, a significant contribution was provided to the industrial revolution [9]. Lasers were divided into many types like ion, ruby, semiconductor, fiber, gas and Nd: YAG lasers and started to be used in various applications in the following years [10]. Laser technology continues to be popular with an increasing usage area in the twenty-first century. Laser cutting has become a helpful process in many fields like electronic, automotive, medical, aerospace and defence industries. Laser technology is also used in supermarkets, surgeries, cd players, telephone networks and many different areas apart from the cutting process. Some features of the laser beam are as follows;

- Direction can be given
- Since they are light waves produced in the same phase, their intensities are higher
- It is smooth and has little deviation
- It can give high energy to a small point
- Wavelength is single or monochromatic
- It can be spread in short pulse patterns
- It has high energy level

Information about the working principle of gas and solid-state laser techniques is given in the first stage of this book chapter. Comparative analysis of gas and solid-state laser use in cutting processes and the requirements for processing materials are presented. The importance of laser machining methods with the developing technology, the areas where they are used in the industry, the reason for preference, machining parameters, machining outputs and differences according to different machining methods are discussed in the following stages. The inferences obtained by examining the current studies in the literature using gas and solid-state laser cutting techniques are presented comparatively.

2 Why is Used Laser?

Development in industrial areas is increasing rapidly depending on the beginning of the age of technology. Therefore, the importance of the three main elements like rapid manufacturing, low cost, and high quality in machining materials is increasing. It aims to manufacture a workpiece according to the desired form and tolerances at a low cost and short time. This causes the preference for different machining processes. Workpieces can be manufactured with the desired precision and dimensional accuracy using the laser machining technique among these processes. Cutting costs are lower because laser machining uses very little energy. High power density, rapid heating and melting cause partial material vaporization in the cutting zone in industrial cutting applications where laser technology is used [11]. The heat of the laser beam is sufficient to initiate combustion as a typical "oxygen fuel" for cutting low-hardness steel materials in industrial applications. This beam can easily cut metal. For example, the laser beam simply melts the material in cutting stainless steel, and high-pressure nitrogen is used as the assist gas to cut the molten metal [12]. Compared to alternative conventional cutting methods [13–16], some advantages and disadvantages of the laser cutting method have been tabulated. These are given in Table 1.

One of the most significant factors in choosing the laser cutting process is the ability to cut different materials. These materials are generally steel, titanium, aluminum, brass, stainless steel, paper, wood, polymer composite, ceramic, nylon and plastic. It can also be preferred for rough cutting before machining. For example, the rough area is cut in the laser before the precision surface of the workpiece is obtained. Then, the finishing operation is performed on the milling machine. Thus, alternative solutions can be created for precision workpiece machined surfaces. In addition, the use of high-cost cutting tools can be minimized (Fig. 1).

3 Fundamental Principles of Lasers

It is necessary to know the basic structure of light to understand the working principle of lasers. Light consists of photons or packets of energy. Since photons can act as both waves and particles, all the energy generated in the light is carried by photons [17]. The working system of the laser is also based on the excitation of photons. Some assist gases like carbon dioxide are used to obtain laser light. Thanks to these assist gases, when energy is given by electricity, light or a similar way, the atom's electrons are excited. Thus, the transition from the low energy level to the high energy level is ensured. The energy is released as photons with the effect of the difference between the energy levels during the transition. The excitation process continues by energizing the system. Then, more atoms are excited by reflecting the photons through the mirrors located at the two ends of the laser [18]. As a result, the beamed photons come out with the same phase and frequency and form the laser

Table 1 Advantages and disadvantages of laser cutting

Advantages	Disadvantages
• Precision can be better as the laser beam is not eroded during the process	• High maintenance costs
• Contactless process	• Thickness/diameter ratio is limited
• Low installation costs	• Chemical changes and deteriorations occur in the material due to thermal effects
• Low contamination and machining flexibility	• Blind hole cannot be drilled
• Good surface quality	• Laser beam reflects from shiny surfaces
• Since laser systems have a small heat-affected zone, the chance of bending the cut material is also reduced	• Programming knowledge and qualified personnel are required
• Machining time is short as cutting can be performed at high cutting speeds	
• It can focus on very small diameters	
• 3D materials can be cut	
• Less heat is transferred to the material during machining	
• Better results can be measured at corners	
• No mold costs	
• Control and automation is easy	
• Non-metallic materials, so hard, brittle and ductile materials can be machined	
• No tool wear	

beam (Fig. 2). The material cutting process using the laser beam consists of three steps. These are melting, vaporization, and chemical degradation.

The basis of laser cutting is the interaction between the workpiece and the laser beam. A laser beam, various components and auxiliary tools are used to perform the cutting process precisely (Fig. 3) [19]. Focusing optics (1) allows focusing the laser beam on the machining area with lens and mirror. The laser beam (2) heats to melt the workpiece. The Gas Jet (3) removes the molten material from the cutting zone. The gas moves away from the nozzle coaxially with the laser beam. Dragline (4) refers to the trace pattern that occurs at the cutting edge. It is usually parallel to the laser beam when the cutting speed is low. Melting or Slag (5) is formed by directing the laser beam along the contour and locally melting the material. Cutting Edge on Workpiece (6) refers to the geometry of the surface that the laser beam contacts. As a result of the relative movement of the workpiece and the laser beam, the cutting process occurs on the workpiece. The width of the kerf is formed, which reveals the cutting edge size. The difference between the kerf width and the focused laser beam width is so small. The laser beam and cutting gas pass through the inside of the nozzle (7) and ensure that the beam and gas are reached to the workpiece. Cutting

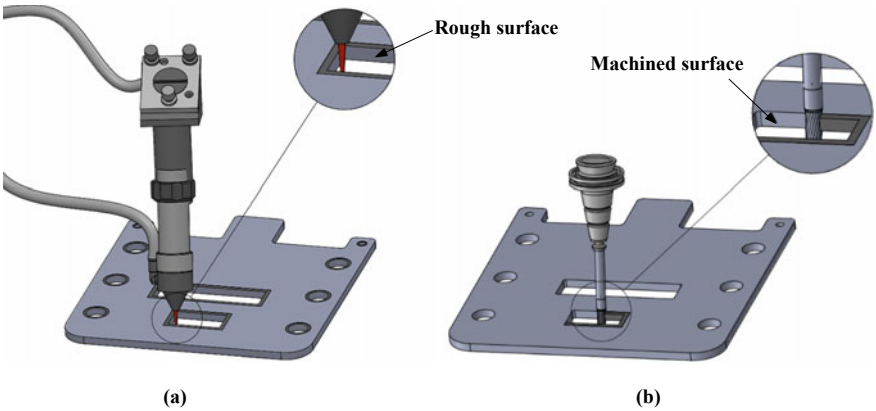

Fig. 1 Conventional and un-conventional cutting methods, **a** Laser cutting and **b** Finish operation in milling after laser cutting

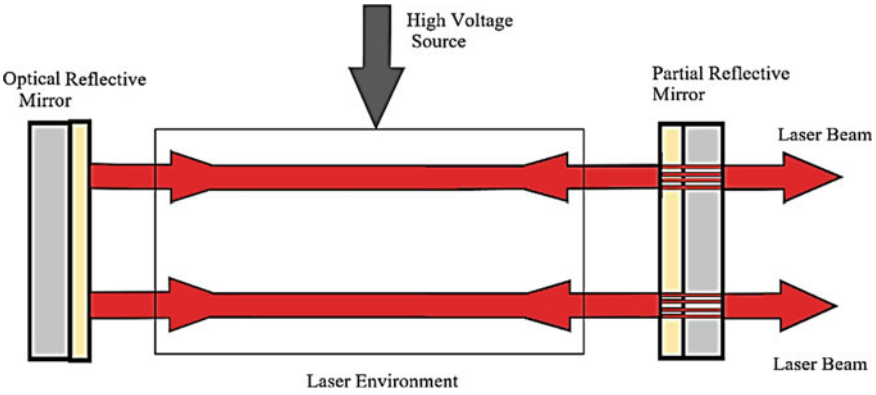

Fig. 2 Laser beam formation

Direction (8) is the movement of the workpiece in a certain direction. As a result of this movement, kerf is formed.

A laser beam is a column of light with very high intensity and a single wavelength. The laser beam diameter is usually 1/4 inch as it feeds through the laser resonator. The beam can be rotated in desired directions using various mirrors or beam benders before focusing on the plate. This process is carried out with a special lens or an angled mirror in the laser head. Mirrors or fibre optics are used to direct the coherent beam to a lens that focuses it on the work area. It is passed through a focusing lens for better beam energy density, stability and shape. The laser beam passes through a chamber with compressed gas immediately after passing through the region focused by the lenses. The laser combined with assist gases in this chamber strikes the plate and cuts the material [20]. In industrial applications, the laser head of a CNC laser

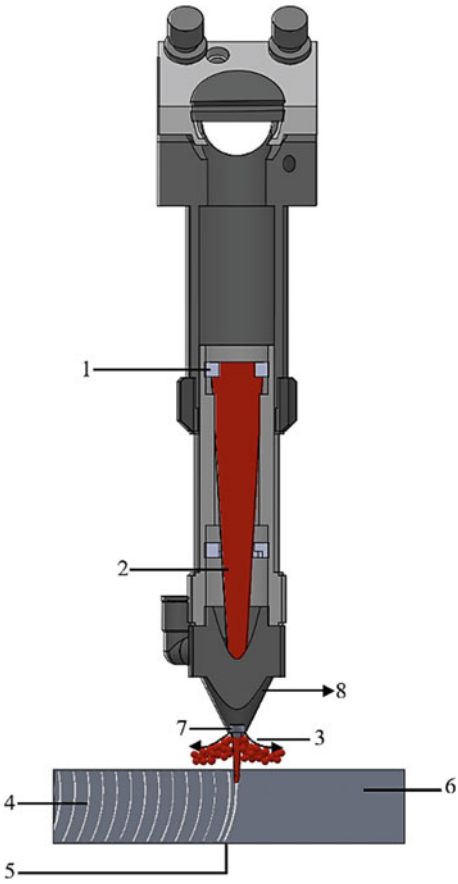

Fig. 3 The structure of the laser cutting process

machine can easily move on the metal part to be cut, and the cutting process can be carried out efficiently. A capacitive height control system keeps constant the distance between the nozzle and the cut plate. This distance is vital in terms of machining quality. Because the focus point is not adjusted well, this process may not be efficient [21].

The first process of the workpiece is usually drilling in CNC laser cutting. The initial values for the drilling process on the material are set in the CNC laser. Thus, the laser light is activated. As a result of the activation of the laser, PLC (Programmable Logic controller) sensors switch from sleep mode to operating mode of the drilling system. After the drilling process is completed, the cutting parameters are entered into the system. Optimum values such as focal length of the material to be cut, cutting speed, cutting gas, gas pressure, standoff distance is defined to the machine. In addition, the threshold values calculated during the drilling process in the first stage are also defined to the CNC machine in this step (Step 1) [22]. After the parameters are defined to the machine in the second stage, the laser head approaches the hole

point of the material. The purpose of this process is that the assist gas in the system penetrates the material better (Step 2). The laser starts to work with the initial values of the cutting operation in the third stage (Step 3). PLC takes the sensors from sleep mode and switches the monitoring system to operating mode for cutting in the fourth stage (Step 4). The system monitors the threshold values by measuring them instantly. If the instantaneously measured threshold values remain above a certain time, the system proceeds to step 7. Otherwise, it goes to step 6 (Step 5). If there is no problem in the cutting process, the CNC machine turns off the laser beam with PLC and finishes the material cutting process (Step 6) [23]. Since the measured instantaneous threshold values are below the voltage values, the problem in the cutting process is detected by the embedded processor and the system sends the signal that there is an error during the cutting process (Step 7). After the error cutting signal is sent, the CNC laser machine turns off the laser beam using PLC and stops all its moving axes.

The laser head moves away from the cutting position. The system makes changes for the first entered parameters and returns to step 2. CNC laser repeats this process three times. If there is an error in the system after this process, the laser passes the cut part and starts the cutting process of the other part. If the same problem is encountered in the new workpiece to be cut, the machine stops completely and warns the operator with an error message (Step 8) (Fig. 4) [24].

The increase in the applications of laser technology in the industry has also revealed safety problems. In particular, it was determined that laser operators should be trained in detail. The laser beam can cause serious damage to the human eye, which can cause loss of vision. In addition, if the necessary precautions are not taken, burns may occur on the skin. The first step towards the need for laser safety was taken in 1973 when the American National Standard Institute published the safe use of lasers (ANSI Z136.1). Later, The International Electrotechnical Commission brought the IEC 825 standard on laser use and safety. Today, ANSI Z131 and IEC 825

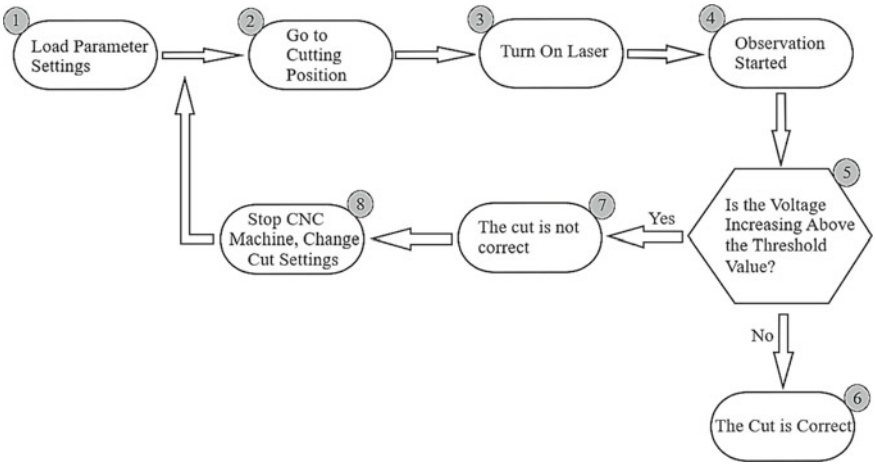

Fig. 4 Algorithm sequence in laser cutting process

standards are used in the industry and protection methods from laser operations are being developed. Lasers are divided into various hazard classes to ensure operational safety, following worldwide laser standards. Class 1 means that it is not harmful to the eyes or skin. They are lasers used in closed systems. Class 1 M means that it is not harmful to eyes and skin unless used with focusing optics. Class 2A refers to visible and harmless lasers not intended for imaging. Class 2 refers to the visible laser. The eye reflex is sufficient to protect. It is harmless in exposure up to 0.25 s. Class 2 M means harmless at exposure up to 0.25 s unless used with focusing optics. Class 3A refers to visible laser. It is stated to be similar to Class 2 unless used with focusing optics. Class 3R replaces Class 3A. It's not dangerous as long as it's not focused. Class 3B covers medium-power lasers (5–500 mW visible/invisible). It is harmful to the eyes when looked at unprotected. It does not harm by scattering or penetrating. Class 4 is high power laser (>500mW visible/invisible). Reflections and scattering of the beam damage the eyes and skin [25].

4 Commonly Lasers Used in the Cutting Process

Laser cutting is one of the most used machining methods in the industry. It is the process of removing the material from the surface or volume of the workpiece in a controlled manner by heating it with a laser beam. The basis of the cutting process is the laser beam, which can be directed, focused and shaped. Reflective optics are used in this process. Laser cutting, which has an extensive usage area, can machine many materials such as nickel, steel, chrome, titanium, aluminum, wood, rubber. Carbon dioxide (CO_2) laser as the cutting device was used as an assist gas to cut 1 mm thick steel plate in 1967 [26]. The cutting process is carried out by heating, melting or evaporating the material using susceptible parameters. The material surface is brought to the ignition temperature by the laser beam during cutting. Thus, the oxygen used in the cutting process oxidizes the cutting edges of the material and burns it. Thanks to the kinetic effect of oxygen, the melted dross is sprayed in the cutting zone. The cutting edge is formed by laser head or material movement. This method aims to provide 40% of the energy required for the cutting process with the exothermic reaction occurring in the cutting by the burning process of the material. Thus, high cutting speeds can be achieved at low laser powers. It is the most preferred method for cutting unalloyed steel and thin materials [27]. The material cutting edge is melted by the laser beam focused on the material's surface to be cut in the melt cutting process. The waste material is removed from the cutting surface thanks to the kinetic energy of the gas used. Accordingly, the material can be melted in the cutting zone with the total laser beam energy. It is generally used in the machining of stainless steel [28]. The material cutting edge to be cut evaporated with a focused high-intensity laser beam in the evaporative cutting process. The evaporated material is removed from the material surface by the high kinetic energy of the gas beam. Optimum cutting surface and less heat-affected zone (HAZ) are obtained in this method [29]. Laser parameters such as cutting power, cutting speed, beam profile, pulse energy, pulse

frequency, pulse width, assist gas, gas pressure, focusing point, nozzle setting and standoff distance must be controlled to obtain a quality result in laser cutting. The laser power must be constant during cutting for maximum machining efficiency. Constant output power can be obtained 5–10 min after the laser beam is formed. It should be checked at regular intervals to stabilize this constant power obtained [21]. The area of influence on the surface to be cut depends on the focusing distance after focusing the laser beam. It should be noted that the allowable focusing diameter is less than 0.12 mm for a 2.5 inch diameter lens and less than 0.2 mm for a 5 inch diameter lens. The beam profile should be adjusted depending on the focusing diameter for the desired quality cut. Since the laser beam profile expands during cutting, the refraction angle of the beam must be kept constant. In addition, the focus point may vary depending on the type of material used and the type of cutting. Therefore, the correct focusing point must be determined before starting the cutting process. For example, the focal point should be very close to the surface for sheets with a thickness of up to 6 mm, and a certain distance from the surface for sheets with a thickness of 8 mm and above in the cutting by the burning process of sheet materials. Finally, the nozzle should be selected according to the material and cutting type for a quality product in laser cutting. The focused laser beam should be matched with the centre of the nozzle after checking the nozzle entrance. The centre-focused beam should not be offset by more than 0.05 mm [30]. The laser cutting process can be preferred in terms of ease of manufacture, minimum deformation in the cutting area, elimination of mould costs and application in different materials. In addition, better surface quality can be achieved, and time savings can be provided due to high cutting speeds. Some parameters must be determined according to optimum values to achieve the desired surface quality, dimensional accuracy and machining efficiency in laser cutting [31]. These parameters are material, laser system and operation parameters. Material parameters include the thermal and physical properties of the material. It affects the machining ability of the laser. Laser system parameters are wavelength, beam quality, maximum power output and material thickness [32]. These parameters characterize the properties of the laser beam. Data such as cutting speed, laser power, the focal distance of the lens, the pressure of assist gas, type of gas, nozzle diameter, standoff distance, pulse energy, pulse frequency, pulse width are operation parameters. They are parameters that can be changed to improve the quality of the cutting process [33]. Optimization of these parameters is crucial for optimal machining capability. In particular, all parameters that can be optimized in the laser cutting process can be changed depending on the type and thickness of the material. The effect of the cutting parameters on the cutting quality is determined by examining the output data like the change in the hardness of the material, the surface and edge roughness, the height of the dross, the slope of the cutting path, the HAZ width (Fig. 5), and the microhardness. As a result of the cutting process, characteristic features may occur in the material. For example, differences in structural properties like microstructure and microhardness change can be observed due to overheating on the cutting surface in metals. Lines may form in the cutting area due to the effect of cutting gas. Dross may occur due to melting under the cutting surface. This dross can continue along the cutting edge. In particular, dross causes the gap between the materials to be assembled

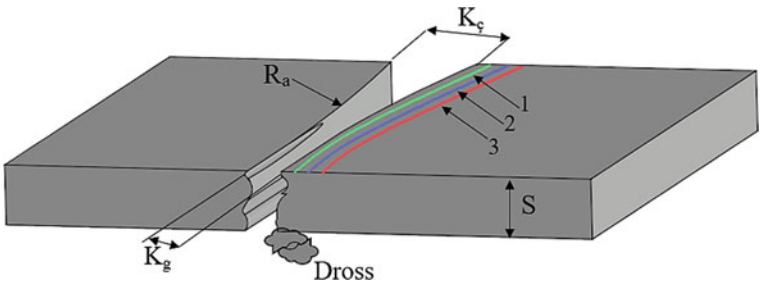

Fig. 5 The structure of the laser cutting zone, Kg: Width at the start of cutting versus Kc: Width at the end of cutting, Ra; Surface roughness, S: Sheet thickness, 1: Oxidized layer, 2: Recast layer and 3: HAZ

between each other. Thus, assembly errors occur in mechanical systems. Therefore, careful selection of machining parameters are significant for maximum workpiece quality. However, microstructural changes occur with the effect of thermal stresses that may occur on the cutting surface. This situation adversely affects the magnetic properties of silicon sheets used in electrical machines. In addition, dross formation in these materials increases iron losses by causing gap formation during the packaging of silicon sheets. Therefore, the efficiency of electrical machines decreases [34]. Accordingly, it is necessary to determine the cutting parameters by considering the material type, thickness and using the area.

Different materials exhibit different machining characteristics. While the cutting zone width is 0.1 mm in the machining of carbon and alloy steels by the laser cutting method, the HAZ width varies between 0.1 and 0.3 mm. Generally, the cutting surfaces are smooth and slightly rough. If oxygen is used in the cutting processes, oxidation occurs on the cutting edges. Nitrogen is used as cutting gas for materials up to 4 mm thick in steel materials. It can give better results in cutting high alloy and stainless steel materials. Nitrogen gas is widely used to obtain an oxide-free, fast and dross-free process. When drilling using nitrogen gas in stainless steels thicker than 5 mm, it is important to have precise focus settings. Thus, better drilling/cutting can be performed [35]. Aluminium-based materials can be cut with laser up to 6 mm thickness due to their high reflectivity and thermal conductivity properties. A continuous beam wave can form the cutting surface in higher quality and desired form.

The cutting process is slower than steel-based materials [36]. Copper and brass materials can be cut with laser up to 3 mm thick, as they have more thermal conductivity and reflectivity than aluminum. However, a cutting process up to 3 mm sheet thickness can be performed using nitrogen in brass material. Titanium materials can be cut up to 7 mm sheet thickness when nitrogen gas is used. Cutting techniques are generally similar for non-metallic materials. For example, in alternative materials, wooden materials thicker than 25 mm can be cut, while this thickness exceeds 50 mm in acrylic materials [37].

The cutting gases must be selected in accordance with the cutting method for the efficiency of the laser cutting process. Dross accumulation and burr formation can be reduced by using oxygen gas to cut by the burning process. Compressed air should be used for cutting sheet materials. Since 80% of the air is nitrogen, it should be preferred for cutting by melting. Gases with low reaction rates should be used to remove the material from the cutting zone in cutting methods by melting or evaporation. The most suitable gases for these processes are Nitrogen and Argon. Today, these gases are routinely used in cutting for different materials and thicknesses.

The most used laser types in industrial application areas are gas and solid-state lasers. Nd:YAG (Neodymium-doped yttrium aluminium garnet) solid-state and CO_2 gas lasers are the most used in material machining. The Nd:YAG laser consists of glassy solid yttrium aluminium garnet in neodymium. The active medium in this type of laser is a bar of neodymium ions and yttrium–aluminium-garnet crystals. The beam is obtained with this rod. As the length of the rod increases, the energy also obtained increases.

Two lamps on both sides stimulate the laser material. The materials in these systems are in an elliptical cavity with high reflectivity for reflecting the light intensely on the material [38]. There are three different focal points in the ellipse. The lamps are at two points on the outside, and the laser material is at the inner focal point. The light with this system is reflected, and it is provided to pass over the material again. Since heating occurs during the processes, the materials are surrounded by pipes through which cooling water is passed. The laser beam in CO_2 lasers is produced in the resonator of the laser beam generator, which is connected to cutting gas, electrical energy and cooling unit. The energy obtained by electrical, chemical or nuclear sources is converted into an electromagnetic beam at a special frequency. The resonator consists of two spherical mirrors. One of them is fully reflective, while the other is partially permeable. The resonator, one of the essential parts of laser cutting machines, is designed in different ways. Many criteria are taken into account in the design of a resonator. These are the laser gas mixture, the pump source, the cooling and the geometric structure of the resonator. These criteria play a crucial role in achieving maximum machining efficiency and beam quality. Thus, better-machined surface quality can be obtained due to less molten material formation in the cutting zone with high beam quality [39].

4.1 Gas Lasers

Electricity is discharged in the working system of gas lasers. These lasers generate a beam as a result of passing through the gaseous medium of the active substance. The active medium in gas lasers usually consists of a gas mixture. One of the components in the mixture transfers its excitation to the other by collisions. It is the first type of laser in which power is obtained by converting electrical energy into a laser beam and generating continuous laser light [40]. The most crucial laser types in gas lasers are Helium–Neon (He–Ne) and CO_2 lasers. The gases in the He–Ne gas laser are

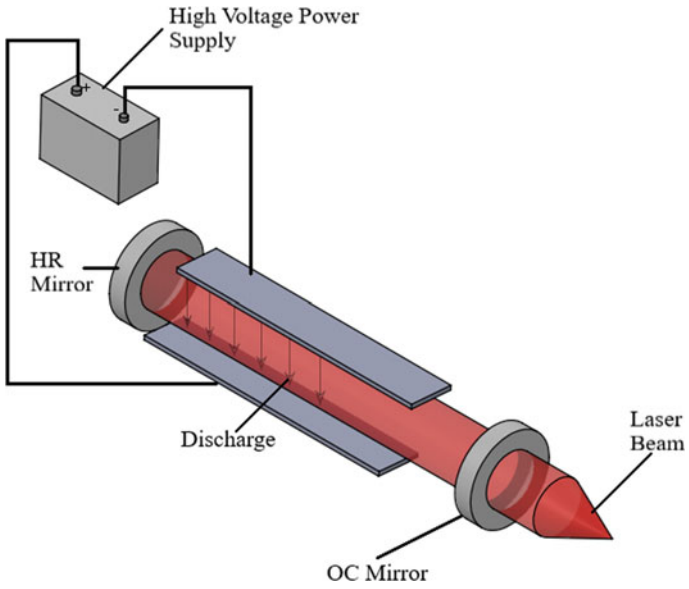

Fig. 6 Three-dimensional structure of gas laser

ionized under high voltage. The He atoms collide with the existing Ne atoms and reach the exciting level. Then, the atoms that reach the high energy level transfer the gained energy to the equivalent energy level in the Ne atoms. As a result, photon emission occurs. These photons emit light with the help of mirrors (Fig. 6).

Generally, CO_2 is used as a shielding gas in laser sources. Although CO_2 lasers are the oldest laser method, they are still used and developed. The most significant reason for this is that the desired power levels have not been reached yet. CO_2 lasers still used today are the lasers with the highest power (up to 50 kW) that can emit continuous waves. It is the system with the highest efficiency compared to different systems. Output efficiency is defined as the ratio of the output laser power to the electrical input power. The laser can be supplied by a direct current source or by radio frequencies. It emits infrared radiation with a wavelength of 9–11 μm. However, the most commonly used wavelength is 10.6 μm. While it was previously used to cut sheet materials like stainless steel [41], due to some modifications, materials such as metal, wood, acrylic, glass, paper, cardboard, textile, polymers, foils, leather have also begun to be cut.

4.2 Solid-State Lasers

Solid-state lasers are generally the type of laser in which the active medium consists of a solid substance. Ions are used as the conduction element. These ions generally

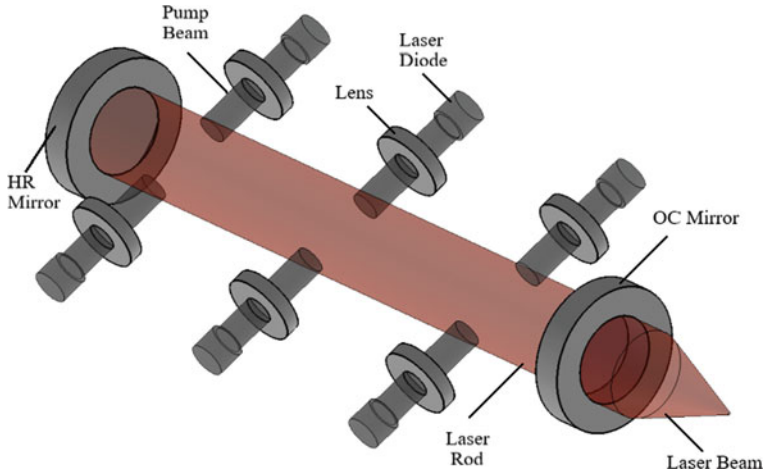

Fig. 7 Three-dimensional structure of solid-state laser

consist of transition elements like Chromium (Cr), Titanium (Ti) or materials such as Neodymium (Nd), Ytterium (Yb), Erbium (Er), which are known as rare elements. Solid-state lasers began to be developed with the pink ruby crystal discovered by T. Maiman in 1960. The research trend for different materials has increased considerably with the discovery of ruby lasers. It has been observed that there is rapid development in solids, gases and liquids. The schematic structure of the solid-state laser is given in Fig. 7.

The structure of a solid-state laser has a rod consisted of different materials. The ends of this rod are polished to be straight and parallel to each other. This rod is covered with a mirror for the reflection of laser light. The sidewall of the rod is designed as transparent so that the pumper can send the light from the lamp to the rod. A pumper lamp can be mounted near or wrapped around the rod. It can also be focused on the rod using a mirror. After Ruby lasers, uranium (U) doped calcium fluoride (CaF_2) started to be used as the first solid-state material. When they were first found, they were operated using a single-pulse logic. Then, the continuous-wave operation was also included. Thus, it was transformed into a continuous operation mode. CaF_2 was used until yttrium aluminium garnet was found as an assist material for Nd [42]. Solid-state lasers are used in the military, medicine, radiation source, distance measurement, target determination, biological measurement, medical imaging.

5 Evaluation of Machining Performance in Laser Cutting

Workpieces must be subjected to machining operations to use as final products in manufacturing. Therefore, conventional and non-conventional machining techniques are used. The laser cutting technique is also among the non-conventional machining

techniques. Laser power, cutting speed, assist gas and cutting gas type, gas pressure, operation mode (continuous/pulse), material type and thickness are generally independent variables for laser cutting performance. Dependent variables or experimental outputs are usually determined as material removal rate, surface roughness, surface microhardness, dross height, kerf width, and HAZ. Namely, maximum machining efficiency can be obtained from the dependent variables by controlling the independent variable parameters. The performance of experimental outputs has been revealed by using different variables on different materials in recent years. Accordingly, in some studies, Yılbaş et al. investigated dimensional analysis for kerf width and life cycle for less material waste in laser cutting of Ti–6Al–4 V alloy, 304 steel, Inconel 625 and alumina materials. Scanning speed (m/s): 0.05–0.1, power (W): 300–1500, frequency (Hz): 1500, nozzle gap and diameter (mm): 1.5, focus setting (mm): 127 and N_2 pressure (kPa): 550 used as cutting conditions. It has been stated that N_2 gas is used to prevent excessive oxidation reactions during cutting, and increasing the laser output power or decreasing the cutting speed increases the kerf width. It has been determined that this situation is related to the long time of the laser beam in the cutting section due to the low cutting speed. It was observed that the change in kerf size increased significantly due to the exothermic reaction at high temperatures in the cutting zone due to the high oxygen affinity of titanium alloys. Namely, the liquid metal solidifies on the cutting surface due to the cooling effect depending on the convection of the high-pressured assist gas and causes the formation of a cast layer (Fig. 8). The rate of change in kerf width is low in alternative materials. It has been stated that the damage to the environment is greatest due to laser cutting of Inconel 625 [43].

Chaki et al. modelled the surface roughness and material removal rate with ANN (Artificial neural network)–NSGAII (Non dominated sorting genetic algorithm-II) when cutting AA1200 aluminium plate of 1.2 mm thickness using Nd:YAG laser. Different cutting speeds (V:1.1; 1.5- and 1.8 m/s), pulse energy (E:4.5; 6.8 and 9 J) and pulse width (W: 0.5; 1 and 1.5 ms), constant nozzle diameter: 1.5 mm, standoff distance: 6 mm, spot diameter: 0.24 mm and N_2 assist gas pressure: 6 bar were used. It was determined that the BPNN (Backpropagation neural network) 3-6-2 network used with the Bayesian regularisation algorithm is the best ANN structure in terms of predictive ability. According to Pareto-optimal, the minimum surface roughness was calculated as V: 1.2 mm/sn, E: 4.5 J and W: 0.5 ms for Ra: 6.23 μm. Optimum conditions for maximum MRR: 57.494 mg/min were determined as V: 1.8 mm/s, E: 6.8 J and W: 0.5 ms. It was observed that the surface roughness increased with the increase of cutting speed and pulse energy in the Pareto-optimal region. It was determined that MRR increased proportionally with cutting speed and pulse energy. It was found that the cutting speed has the greatest effect on MRR and surface roughness, and the proposed model can be efficient for the prediction of operational parameters [44]. Sharifi and Akbari investigated the effect of process parameters on the edge quality and cutting zone temperature of Al-6061 T6 alloy in laser cutting. Cutting speed, laser power, sheet thickness and standoff distance were used as independent variables. It was stated that the maximum cutting speed should be used to reach the cutting temperature. It was found that the cutting zone temperature

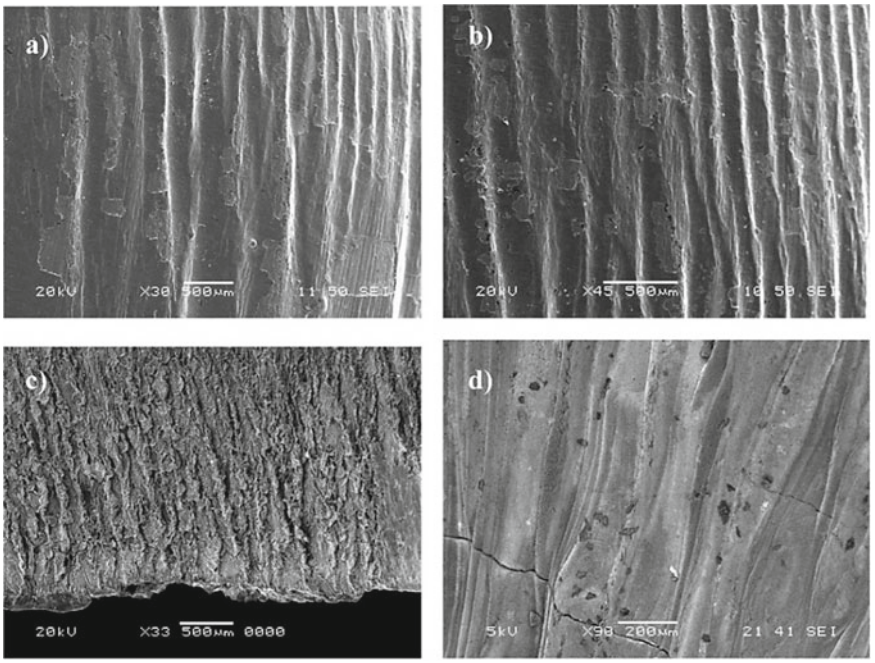

Fig. 8 SEM images of the cutting surfaces (Laser power: 1500 W and Cutting speed: 0.07 m/s), **a** stainless steel 304, **b** Inconel 625, **c** Ti-6Al-4 V alloy and **d** alumina [43], (reprinted with permission of Springer Nature, 2017)

significantly affected the surface roughness, depending on the temperature effect on the melt flow in the kerf area (Fig. 9) [45].

Haddadi et al. studied the cutting quality characteristics of polystyrene in CO_2 laser cutting. They stated that the performance of experimental outputs such as dross height, bottom and top kerf widths, the ratio of top kerf width to bottom kerf width depends on the process parameters in laser cutting of polymer materials. They used a 3 mm polystyrene plate, three different laser powers (60, 70 and 80 W), cutting speed (6, 10 and 14 mm/s), and covering and without gas parameters. It was stated that HAZ decreases with increasing laser power and cutting speed, and the use of covering plays a vital role in controlling HAZ width. It was found that the advantage

Fig. 9 Cutting edge striation pattern formation at different cutting speeds of 1 mm thickness material, **a** 2 m/min, **b** 3 m/min and **c** 4 m/min [45], (reprinted with permission of Springer Nature, 2021)

of high cutting speed is more effective than laser power, and cutting speed is the most crucial parameter affecting the cutting angle and kerf width. It was observed that the dross height decreases with the increase of cutting speed in the case of without covering gas, and the optimum cutting parameters were laser power: 60 W and cutting speed: 14 mm/s using covering gas [46]. Elsheikh et al. predicted the kerf quality index in cutting polymethylmethacrylate (PMMA) material using CO_2 laser with the random vector functional link network (RVFL) algorithm. Gas pressure, sheet thickness, laser power and cutting speed were independent variables for model prediction. In addition, the rough area ratio showing the quality index, the width of the top and bottom sections affected by the heat, the surface roughness and the kerf taper angle were defined as dependent variables. Since the top surface of the plate is exposed to more heat than the bottom surface, the width of the top kerf is larger, and it increases the width of the kerf depending on the amount of melted material. It was observed that the molten material causes swirling in the overheated top surface due to the exposure of the top surface to more shielding gas. As a result, it was found that the surface roughness of the top kerf region was higher than the bottom kerf surface. The width of the down HAZ zone was determined to be wider than the up HAZ due to the convection cooling of shielding gas on the top surface. It was found that the developed mathematical model could be used successfully according to the kerf quality coefficient indices ranging from 0.954 to 0.991 [47]. Elsheikh et al. experimentally investigated and optimized the top kerf width (TKW), bottom kerf width (BKW) and kerf taper (KT) in laser cutting of polymethylmethacrylate plate with CO_2 gas. Taguchi L_{18} orthogonal array experiment design and different gas pressure (1 and 3 bar), sheet thickness (4, 6 and 12 mm), cutting speed (100, 200 and 300 mm/min) and laser power (120, 135 and 150 W) parameters were used. It was observed that TKW, BKW and KT decreased depending on the increase in sheet thickness, a decrease in TKW and BKW and an increase in KT with increasing cutting speed. It was determined that it was a moderate effect on KT, as it causes a small decrease in TKW and BKW with laser beam power. Gas pressure had a moderate effect on TKW and BKW, while it had a negligible effect on KT. According to the regression models, they showed a strong relationship between statistical analysis results and experimental results [48]. Anghel et al. optimized the surface quality of 304 stainless steel miniature gears in CO_2 laser cutting. They used different laser power (1500, 2000 and 2500 W), cutting speed (1, 2 and 3 m/min), focal position (-1.5, -2.5 and -3.5 mm) and gas pressure (10, 13 and 16 bar) in the research. It was stated that high laser power, low cutting speed, and moderate focal position and gas pressure should be used for maximum surface quality. Optimum values were determined as laser power: 2407 W, focal position: -2.4 mm, cutting speed: 1.25 m/min and gas pressure: 12.5 bar for the lowest surface roughness value (0.43 μm). While a pattern was formed in the top section of the cut surface, a smooth surface with small dross was observed in the bottom section (Fig. 10) [49].

Khosraim et al. investigated the effect of machining factors on the kerf characteristic of PMMA material in CO_2 laser cutting. They used different gas pressure (1 and 3 bar), sheet thickness (4, 6 and 12 mm), cutting speed (100, 200 and 300 mm/min) and laser power (120, 135 and 150 W) parameters. Kerf deviation,

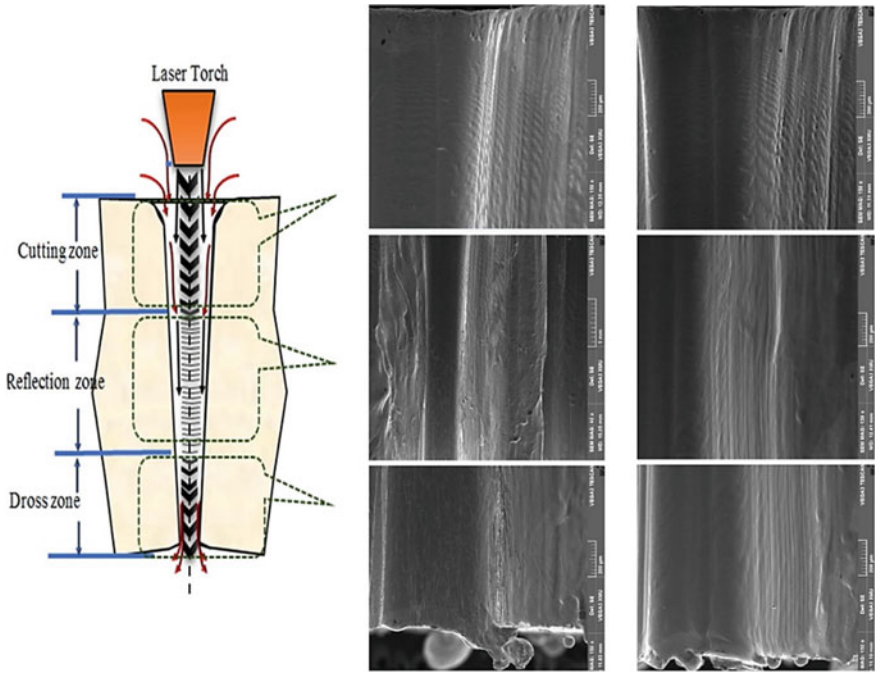

Fig. 10 Machined surface structure at optimum cutting parameters [49], (reprinted with permission of Elsevier, 2020)

top and bottom HAZs, maximum surface roughness and rough area were measured as the experimental outputs or dependent variables. It was found that the cutting surface consists of rough, moderate and smooth regions, and the surface roughness was higher in the region close to the top surface with the effect of overheating than in other regions. It was observed that the maximum surface roughness varied between 7.94 and 25.05 μm, and the cutting speed was a dominant parameter on the kerf deviation. In addition, it was found that laser power was a significant effect on bottom HAZ, while sheet thickness was a dominant effect on top HAZ, surface roughness and rough area. It was observed that all other dependent variables increased with the effect of supercooling in the top region due to the increase in gas pressure [50]. Aoud et al. optimized surface roughness with Taguchi technique using different laser power (1, 2 and 3 kW), cutting speed (480, 1440 and 2400 mm/min) and gas pressure (2, 8 and 14 bar) in CO_2 laser cutting of Ti-6Al-4 V alloy. It was determined that laser power, cutting speed and pressure were effective on surface roughness and the best surface quality was obtained with high cutting speed and high laser power. The cutting parameters for optimum surface quality were calculated as laser power: 3 kW, cutting speed: 2400 mm/min and gas pressure: 2 bar [51]. Leone and Genna investigated the HAZ in the Nd:YAG laser cutting process of 1 mm thickness CFRP (Carbon fibre reinforced plastic) material. They stated that approximately

10 mm/s cutting speed and 95 W average power would be sufficient to cut CFRP sheet using pulsed Nd:YAG. It was found that the thermal damage in CFRP was caused by matrix damage, fibre pulls out, carbonized material layer and holes. It was observed that the maximum HAZ size occurred in the centre of the laminate and varied in the range of 170–1600 μm. Constant average power, high pulse energy and low overlapping factor cause lower HAZ. Minimum HAZ value was obtained at the duration: 0.2 ms, frequency: 185 Hz, pulse energy: 0.5 J, overlapping factor: 80% and maximum cutting speed (10.8 mm/s) parameters [52]. Rajesh et al. optimized the independent variables using RSM (Response surface methodology) in austenitic stainless steel cutting process with Nd:YAG laser. They used different lamp current (19, 20, 21, 22 and 23 A), pulse frequency (0.4; 0.8; 1.2; 1.6 and 2 kHz), gas pressure (0.5: 1; 1.5; 2 and 2.5 kg/cm^2) and pulse width (2, 6, 10, 14 and 18%) as independent variable. It was seen that lamp current was more effective on outputs than other independent variables and the hole output diameter decreased with the increase of the lamp current. It was determined that the optimum output value of the hole diameter was obtained with low lamp current, high pulse frequency, moderate pulse width and low gas pressure [53]. Gautam and Mishra were optimized kerf width, kerf deviation and kerf taper using different lamp currents (160, 180 and 200 A), pulse width (2, 2.3 and 2.6 Ms), pulse frequency (20, 25 and 30 Hz), air pressure (8, 9 and 10 kg/cm^2) and cutting speed (50, 100 and 200 mm/min) independent variables in the pulsed Nd:YAG laser cutting process of 1.6 mm thick basalt fibre reinforced composite material. According to the ANOVA (Analysis of variance) results, it was observed that the most important factor for kerf width and kerf taper was lamp current while cutting speed was observed for kerf deviation. It was found that pulse frequency was the least important factor for outputs, and these outputs were significantly affected by pulse width. They calculated optimum independent variable parameters as lamp current: 190.84 A, pulse width: 2.29 ms, pulse frequency: 29.2 Hz, air pressure. 8.07 kg/cm^2 and cutting speed: 51 mm/min [54]. Çavuşoğlu investigated the surface morphology of 2024-T3 aluminium alloy in the CO_2 laser cutting process. Different laser power (1800, 2600 and 3400 W), cutting speed (3.5; 5 and 6.5 m/min) N_2 assist gas, gas pressure of 8 bar, the focal distance of 120 mm and continuous wave were used for tests. It was determined that the best surface quality was obtained at laser power: 2600 W and cutting speed: 5 m/min, and the surface roughness increased with increasing cutting speed. It was observed that HAZ increased with the increase of laser power and decreased with cutting speed. It was stated that the least dross size was seen with the increase of laser power, and there was no linear relationship between cutting speed and dross size. In addition, it was revealed that the hardness of the cutting edge was not affected by the laser power and cutting speed [55]. Apart from the laser cutting process, the ultrafast lasers are effectively implemented in micromachining process for the development of functional surfaces [56–61].

6 Concluding Remarks

Since its discovery, lasers have facilitated human life in many fields such as the automotive, aviation and aircraft industries, engineering, textiles, and medicine. Especially, cutting materials using laser beams has an important place in terms of current and future processes in the manufacturing sector. Laser cutting is a thermal material removal method and can be used as an alternative to conventional or non-conventional machining techniques in manufacturing engineering materials. The reasons for preference are material versatility, no tool wear or cutting tool necessity, manufacturing flexibility, dimensional stability and cutting-edge quality. Regardless of hardness or density, all materials can be cut quickly and with ideal surface quality using laser cutting. All materials, from very thin materials to thick materials, can be cut at high speeds. It has been determined that cutting speed, laser power, lamp current, pulse width, nozzle distance, gas pressure, pulse energy, pulse frequency and plate thickness independent variable parameters are generally used in the laser cutting process. These independent variable parameters reveal surface roughness, HAZ, kerf deviation, kerf width, kerf taper and dross height outputs as dependent variables. It has been stated that optimum cutting conditions have been investigated with statistical analysis techniques like Taguchi, ANOVA, and RSM for experimental outputs in time and cost savings. It has been revealed that the optimum cutting conditions determine according to the minimum surface roughness, kerf width, kerf deviation, kerf taper, dross height and HAZ criteria. Thus, the effectiveness of the experimental results is revealed by statistical analyzes and it is possible to obtain more data sets. It has been observed that the cutting zone is examined in three stages, and they consist of rough, moderate and soft surfaces in the literature studies. It has been observed that the surface quality decreases and there are differences in microhardness values in the rough region with overheating. It has been determined that the surface quality is relatively better in moderate and soft areas. In addition, it has been revealed that cutting speed and laser power are the most important variables on experimental output. Today, studies on laser technology continue. It is thought that higher quality and different materials can be produced using techniques with high cutting speed and laser power. It is predicted that multi-criteria decision-making techniques such as PSO (Particle swarm optimization), TOPSIS (Technique for order of preference by similarity to ideal solution), ELECTRE (Elimination Et Choix Traduisant la REaite), VIKOR (Vise Kriterijumska Optimizacija I Kompromisno Resenje), MULTIMOORA (Multi-Objective Optimization by Ratio analysis), AHP (Analytic Hierarchy Process), COPRAS (COmplex PRoportional ASsessment) will enable different alternatives to be obtained for experimental outputs in laser cutting.

References

1. Einstein, A.: The quantum theory of radiation. Physikalisch Zeitschrift **18**, 121 (1917)
2. Asyalı,M.H., Kara, S., Yılmaz, B.: What is Biomedical Engineering. Nobel Academic Publishing (2014)
3. Carpene, E., Höche, D., Schaaf, P.: Fundamentals of laser-material interactions. In: Schaaf P. (eds.) Laser Processing of Materials. Springer Series in Materials Science, Heidelberg (2010)
4. Maiman, T.H.: Optical and micro wave-optical experiments in ruby. Phys. Rev. Lett. **4**(11), 564 (1960)
5. Maiman, T.H.: Stimulated Optical Radiation in Ruby. Pergamon Press (1960)
6. Javan, A., Bennett, W.R., Herriott, D.R.: Population inversion and continuous optical maser oscillation in a gas discharge containing a he-ne mixture. Phys. Rev. Lett. **6**, 106–110 (1961)
7. Patel, C.K.N.: Continuous-wave laser action on vibrational-rotational transitions of CO_2. Phys. Rev. **136**, 1187–1193 (1964)
8. Olsen, F.O.: Laser Cutting. Laser Technologies in Industry, International Society for Optics and Photonics (1988)
9. Querry, M.: Laser Cutting. Pergamon Press, Institute for Industrial Technology Transfer (1989)
10. Sakadzic, S., Demirbas, U., Mempel, T.R., Moore, A., Ruvinskaya, S., Boas, D.A., Sennaroglu, A., Kartner, F.X., Fujimoto, J.G.: Multi-photon microscopy with a low-cost and highly efficient Cr:LiCAF laser. Opt. Express **16**(25), 20848–20863 (2008)
11. Choudhury, I., Shirley, S.: Laser cutting of polymeric materials: an experimental investigation. Optik Laser Technol. **42**(3), 503–508 (2010)
12. Eltawahni, H., Hagino, M., Benyounis, K., Inoue, T., Olabi, A.G.: Effect of CO_2 laser cutting process parameters on edge quality and operating cost of AISI316L. Opt. Laser Technol. **44**(4), 1068–1082 (2012)
13. Chagnot, C., Dinechin, G., Canneau, G.: Cutting performances with new industrial continuous wave Nd-YAG high power lasers for dismantling of former nuclear workshops. Nucl. Eng. Design. **240**, 2604–2613 (2010)
14. Dubey, A.K., Yadava, V.: Laser beam machining-a review. Int. J. Mac. Tools Manuf. **48**, 609–628 (2008)
15. Steen, W.M., Mazumder, J.: Laser Material Processing. Springer, Berlin (2010)
16. Chryssolouris, G.: Laser Machining: Theory and Practice. Springer, Berlin (1991)
17. Serway, R.A., Faughn, J.S., Vuille, C.: College Physics. Saunders College Publication (2008)
18. Covissar, R.A.: Principles and Practice of Laser Dentistry. Elsevier (2016)
19. Madić, M., Kovačević, M., Radovanović, M., Blagojević, V.: Software tool for laser cutting process control—solving real industrial case studies. Facta Uni. Series: Mech. Eng. **14**, 135–145 (2016)
20. Webb, C.E., Jones, J.D.C.: Handbook of Laser Technology and Applications. Institute of Physics Publishing (2004)
21. John, C.I.: Laser Processing of Engineering Materials Elsevier (2005)
22. Fox, M., French, P., Peters, C., Hand, D., Jones, J.: Applications of optical sensing for laser cutting and drilling. App. Opt. **41**(24), 4988–4995 (2002)
23. Chiang, L.E., Ramos, J.: CNC control of a laser cutting machine. In: Proceedings of IEEE International Symposium on Industrial Electronics, pp. 236–241 (1994)
24. Baştürk, S.: Computer aided part program generation for a laser cutting machine. J. Nav. Sci. Eng. **5**(2), 75–88 (2009)
25. American National Standard for Use of Lasers-ANSI Z136.1 (2014)
26. Hilton, P.A.: Early days of laser cutting. In: Proceedings of the Lasers in Material Processing, pp.10–16 (1997)
27. Mair, H.: Differentiation of The Thermal Cutting Processes Laser Cutting, Plasma Cutting and Oxy-Fuel Cutting According to Technical and Economic Points of View. DVS-Berichte Band (2004)
28. Powell, J.: CO_2 Laser Cutting. Springer, Berlin (1993)

29. Danzer, W.: New insights into the sequence of the laser, plasma and oxy-fuel cutting processes, presented using high speed recordings. Int. Cutting Technol. Conf. **97**, 5–8 (1997)
30. Urguplu, M., Koksal, S.: The effect of laser cutting process parameters on the quality of metalic components. In: International Symposium on Innovative Technologies in Engineering and Science (2015)
31. Gabzdyl, J.T.: Effects of gases on laser cutting of stainless steels. In: Laser Materials Processing. Proceedings of the International Congress on Applications of Lasers and ElectroOptics (1996)
32. Petring, D.: Laser Cutting. LIA handbook of laser materials processing, Laser Institute of America (2001)
33. Natarajan, R.: An experimental and theoretical study of heat transfer effects during a laser-cutting process. Iowa State University, U.M.I Dissertation Information Service, pp. 10–12 (1990)
34. Bayraktar, S., Turgut, Y.: Effects of different cutting methods for electrical steel sheets on performance of induction motors. Proc. Inst. Mech. Eng. Part B: J. Eng. Manuf. **232**(7), 1287–1294 (2018)
35. Manohar, M., Bodnar, N.R., Asfahani, R.I., Chen, N., Huang, C.: Succesful laser cutting of steel sheets. Fabricated Steel Structures Symposium, USA (2004)
36. Ketting, H.O., Olsen, F.O.: High pressure off-axis laser cutting of stainless steel and aluminum. In: Proceedings of International Conference on Laser Advanced Materials Processing (Science and Applications), pp. 607–612 (1992)
37. Davis, J.R., Semiatin, S.L.: Forming and Forging. ASM Metals Handbook (1993)
38. Buchfink, G.: The Laser as a Tool. Vogel Buchverlag (2007)
39. Meijer, J.: Laser beam machining (LBM), state of the art and new opportunities. J. Mater. Proc. Technol. **149**(1–3), 2–17 (2004)
40. Zefferer, H., Petring, D., Beyer, E.: Investigations of the Gas Flow in Laser Beam Cutting. DVS-Bericht (1991)
41. Forbes, N.: The role of the gas nozzle in metal-cutting with CO_2 lasers. In: Proceedings of the Laser 75 Opto-Electronics, pp. 93–95 (1975)
42. Quintero, F., Pou, J., Lusquiños, F., Boutinguiza, M., Soto, R., Pérez-Amor, M.: Comparative study of the influence of the gas injection system on the Nd:Yttrium-Aluminum-Garnet laser cutting of advanced oxide ceramics. Rev. Sci. Instrum. **74**, 4199–4205 (2003)
43. Yilbas, B.S., Shaukat, M.M., Ashraf, F.: Laser cutting of various materials: Kerf width size analysis and life cycle assessment of cutting process. Optik Laser Technol. **93**, 67–73 (2017)
44. Chaki, S., Bathe, R.N., Ghosal, S., Padmanabham, G.: Multi-objective optimization of pulsed Nd: YAG laser cutting process using integrated ANN–NSGAII model. J. Intell. Manuf. **29**(1), 175–190 (2018)
45. Sharifi, M., Akbari, M.: Experimental investigation of the effect of process parameters on cutting region temperature and cutting edge quality in laser cutting of AL6061T6 alloy. Optik **184**, 457–463 (2019)
46. Haddadi, E., Moradi, M., Ghavidel, A.K., Ghavidel, A.K., Meiabadi, S.: Experimental and parametric evaluation of cut quality characteristics in CO_2 laser cutting of polystyrene. Optik **184**, 103–114 (2019)
47. Elsheikh, A.H., Shehabeldeen, T.A., Zhou, J., Showaib, E., Abd Elaziz, M.: Prediction of laser cutting parameters for polymethylmethacrylate sheets using random vector functional link network integrated with equilibrium optimizer. J. Intell. Manuf. **32**(5), 1377–1388 (2021)
48. Elsheikh, A.H., Deng, W., Ezzat Showaib, A.: Improving laser cutting quality of polymethyl-methacrylate sheet: experimental investigation and optimization. J. Mater. Res. Technol. **9**(2), 1325–1339 (2020)
49. Anghel, C., Gupta, K., Jen, T.C.: Analysis and optimization of surface quality of stainless steel miniature gears manufactured by CO_2 laser cutting. Optik **203**, 164049 (2020)
50. Khoshaim, A.B., Elsheikh, A.H., Moustafa, E.B., Basha, M., Showaib, E.A.: Experimental investigation on laser cutting of PMMA sheets: Effects of process factors on kerf characteristics. J. Mater. Res. Technol. **11**, 235–246 (2021)

51. Aoud, B.E., Boujelbene, M., Boudjemline, A., Bayraktar, E., Salem, S.B., Elbadawi, I.: Investigation of cut edge microstructure and surface roughness obtained by laser cutting of titanium alloy Ti-6Al-4V. Mater. Today: Proc. **44**, 2775–2780 (2021)
52. Leone, C., Genna, S.: Heat affected zone extension in pulsed Nd: YAG laser cutting of CFRP. Comp. Part B: Eng. **140**, 174–182 (2018)
53. Rajesh, P., Nagaraju, U., Gowd, G.H., Vardhan, T.V.: Experimental and parametric studies of Nd: YAG laser drilling on austenitic stainless steel. Int. J. Adv. Manuf. Technol. **93**(1), 65–71 (2017)
54. Gautam, G.D., Mishra, D.R.: Firefly algorithm based optimization of kerf quality characteristics in pulsed Nd: YAG laser cutting of basalt fiber reinforced composite. Comp. Part B: Eng. **176**, 107340 (2019)
55. Cavusoglu, O.: The 3D surface morphological investigation of laser cutting process of 2024–T3 aluminum alloy sheet. Optik **238**, 166739 (2021)
56. Jagdheesh, R., Mudali, U.K., Nath, A.K.: Laser processed Cr–SiC coatings on AISI type 316L stainless steel. Surf. Eng. **23**(2), 93–98 (2007)
57. Jagdheesh, R., Ocaña, J.L.: Laser Machined Ultralow Water Adhesion Surface by Low Pressure Processing. Mater. Lett. **270**, 127721 (2020)
58. Jagdheesh, R., Tur, A., Ocaña, J.L.: The effects of pulse period on nanosecond laser microfabrication. Lasers Eng. **37**(4–6), 333–343 (2017)
59. Jagdheesh, R., Valarmathi, A., Sivakumar, M.: Influence of laser beam polarization on micromachining of crystalline silicon using Ultrafast laser pulses. Lasers Eng. **32**(1–2), 19–35 (2015)
60. Jagdheesh, R., Kopeček, J., Brajer, J., Mocek, T.: Superhydrophobic microspiked surface structures by ultrashort laser patterning. Surf. Eng. **37**(10), 1266
61. Jagdheesh, R., BičišŤová, R., Brajer, J., Mocek, T.: Laser-induced Superhydrophobic and Oleophobic Surface Structures on Float Glass. Lasers Eng **50**, 289–298 (2021)

Laser Cutting of Ceramic Matrix Composites

Sundar Marimuthu, Niall Burtt, Helen Elkington, and Bethan Smith

1 Introduction

Over the last decade there has been an increased interest from the aerospace sector to develop lightweight, high-efficiency aero-engines. Wider use of composites, specifically ceramic matrix composites (CMC), is paramount to developing high-performance aero-engines. High-temperature CMCs such as alumina oxide-based CMC (Ox-Ox CMC) and silicon carbide-based CMC (SiC–SiC CMC) have been identified as an excellent alternative for both high and low-temperature aero-engine parts, such as turbine blades, combustion chambers, heat shields and turbine shrouds [1]. This leads to reductions in weight, increased energy efficiency, and prolonged service life.

Ox-Ox CMCs are composite materials, consisting of an alumina oxide ceramic matrix reinforced with alumina oxide ceramic reinforcing fibres. Ox-Ox CMCs exhibit low density (one-third of the density of aerospace superalloy), high bending strength, high thermal shock resistance, and good stability in oxidising and moisture-rich atmospheres. Ox-Ox CMCs can be used at operating temperatures of ~1200 °C [2], exceeding conventional alloy-based materials which have an operating temperature of ~1000 °C.

SiC–SiC composite materials offer a working temperature of 200–300 °C greater than nickel based alloys, whilst maintaining a higher specific strength [3]. Compared to materials currently used within the aerospace industry, SiC–SiC composites have the potential to reduce the weight of components by over 30%, and improve fuel efficiency by 10% [1].

S. Marimuthu (✉) · N. Burtt · H. Elkington · B. Smith
The Manufacturing Technology Centre, Ansty Business Park, Coventry, UK
e-mail: Sundar.Marimuthu@the-mtc.org

J. Radhakrishnan and S. Pathak (eds.), *Advanced Engineering of Materials Through Lasers*, Advances in Material Research and Technology,
https://doi.org/10.1007/978-3-031-03830-3_3

Despite their clear benefits, CMCs are not widely used due to their low machinability. This is attributed to their hardness, fracture toughness, high melting temperature, and the high viscosity of the melt pool.

Tool-based machining of Ox-Ox CMC results in high thermal and mechanical loads, causing damage to the tool and the CMC substrate. CMCs typically display higher machining forces than other composites, thus suffer from brittle fracture-based material removal. This raises significant concerns for the surface integrity of CMC components, especially for aerospace applications where small imperfections can result in catastrophic failure of components [4]. Although melt infiltration process can be used to manufacture SiC–SiC CMC components to near-net-shape [5], an edge trimming process is often required to obtain the final desired shape. Mechanical machining of SiC–SiC CMC is challenging due to the abrasive nature of the material, resulting in tool failure/wear [6] and excessive burr formation. Thus significant research in manufacturing engineering is directed towards non-traditional machining [7] of CMCs, including laser-based manufacturing processes [8].

Whilst there has been limited research into the suitability of conventional machining for long fibre CMCs [4], non-conventional machining techniques have the potential to negate typical concerns that occur with the machining of composite materials. Compared to other non-traditional manufacturing processes, laser-based manufacturing process [9–15] is considered to be the most suitable technique [16] for cutting industrial components. This is due to its quality, productivity [17], and ease of automation [18].

Laser-based cutting is exploited across manufacturing industries to process a range of materials, with thicknesses of tens of millimetres [19]. However, the current understanding of the laser cutting process, and its mechanism, is predominantly based on monolithic metals [19] or alloys [16]. This leaves some concerns regarding the suitability of laser cutting CMCs, due to their high melting temperature and anisotropic thermal properties.

Laser-based cutting of composites is challenging due to changes in the thermo-physical properties within the composite material. Existing research on laser cutting of composites predominantly focuses on carbon fibre reinforced polymer (CFRP) based material [20]. A variety of laser systems have been used for processing CFRP composites, from continuous wave (CW) to femtosecond pulsed lasers. Different types of laser cutting mechanisms have been proposed and used, such as fusion, reactive fusion, and cold ablation. Fusion cutting is based on the heating, melting and melt-ejection by the action of vapour pressure and the inert gas jet. Reactive-fusion based cutting relies on the use of reactive gas to initiate an exothermic reaction which aids in increasing the cutting efficiency. The cold ablation based cutting process uses ultra-short pulse lasers, such as a femtosecond laser, to remove the material without damaging the surrounding material.

Naubrand [21] found that laser-cutting CMC, using a 5 kW continuous wave CO_2 power laser, resulted in damage to the cut surface, with a thick recast layer observed over the cut surface. This recast layer was brittle and could be removed by manual deburring, resulting in an irregular surface. Macro cracks were also observed on the laser cut surfaces—minimising these thermal defects is essential for the exploitation

of CMCs [21]. Using a pulsed laser instead of a CW laser can reduce these thermal defects. Bluemel [22] used various laser sources to investigate laser cutting CFRP composites. He concluded that, compared to CW and ultra-short pulse lasers, a high-power nanosecond pulsed laser was a worthwhile trade-off for cutting CFRP in terms of both speed and quality. Herzog [23] investigated the effect of wavelength and other key process variables in cutting CFRP, and summarised that cutting using Nd:YAG lasers reduces the heat affected zone (HAZ) compared to disc or CO_2 lasers, and that the HAZ can be controlled by using a multi-pass cutting approach.

Most recent research on laser machining of SiC–SiC CMC focuses on short and ultra-short pulse laser processing. Costil et al. [24] investigated micromachining of CMC using a Nd:YAG nanosecond pulsed laser, whilst Liu et al. [25] investigated drilling of CMC using a femtosecond laser. These studies provide a detailed insight into short/ultra-short pulse laser machining of CMC, however the productivity of these lasers doesn't come close to the manufacturing industrial requirements.

Over the last few years, water-jet guided (WJG) laser technology [26] has been explored as an technology to achieve thermal defect free cutting and drilling. The WJG laser typically uses a nanosecond pulse Q-switch laser operating at ~535 nm wavelength. Sun [27] used a WJG laser for cutting CFRP and summarised that the cut surface produced by the WJG laser cutting process is similar to the cut quality observed using electric discharge machining. Recently, Marimuthu et al. used a WJG laser to drill nickel superalloys coated with thermal barrier coating [28] and aluminium metal matrix composites [29]. He showed excellent machining quality but at the expense of machining productivity. Another key application for the WJG laser is the processing of exotic materials such as diamonds [30] and semiconductors [31], which are difficult to process using other technologies.

As discussed, the current understanding of laser cutting concentrates on the processing of metals, alloys, or CFRP composites. Despite the widespread advantages of CMCs, there is a lack of research and knowledge into laser cutting CMC. This chapter aims to overcome this gap by investigating laser-based cutting of Ox-Ox and SiC–SiC CMC. This chapter will focus on laser cutting CMCs using three types of laser source—continuous wave fibre laser, quasi-continuous wave millisecond fibre laser, and nanosecond water-jet guided laser.

2 Materials and Methods

The SiC–SiC CMC workpiece used within this research is formed bi-directionally, with a material thickness of 2 mm. Figure 1 shows the microstructure of the SiC–SiC CMC material, which reveals the layered pattern of fibres at 0 and 90 degrees. As observed in Fig. 1, the uneven fill of the matrix between fibres shows the material state before laser processing.

The Ox–Ox CMC used in this work is from Pritzkow Spezialkeramik, Germany, and is of 3 mm thickness. The material consisted of layers of fibres which are perpendicular to one another moving from layer to layer, as shown in Fig. 2. Due to this struc-

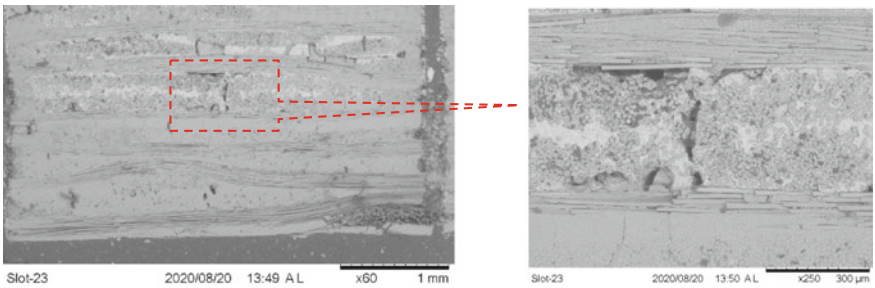

Fig. 1 Image showing the fibre layout of the SiC–SiC CMC

Fig. 2 Cross-sectional scanning electron microscopic image of the Ox-Ox CMC used in the study

ture, the fibre orientation could have a significant effect on machining performance. Therefore, where appropriate, the analysis considered each orientation separately.

Three types of laser source were used; continuous wave (CW), millisecond pulse (MSP), and a water-jet guided laser (WJG). Continuous wave and millisecond pulse laser trials were carried out using a DMG LT50 5-axis laser system equipped with a quasi-continuous wave (QCW) fibre laser source operating at 1064 nm wavelength. The QCW laser can operate at a peak laser power of 20 kW, average laser power of 2 kW, and pulse duration ranging from 0.2–10 ms. A schematic of the laser cutting optical arrangement is shown in Fig. 3. The experimental laser trials utilise a 100 µm fibre, collimator lens of 120 mm, and focusing lens of 150 mm which gives a theoretical spot diameter of 125 µm. The distance between the nozzle and workpiece was kept constant at 1 mm, based on the expected enhancement of the gas-dynamic performance, and in line with the findings by Tuersley et al. [32].

The WJG laser machining was performed using a Synova LCS305 laser system. This system has a 400 W nanosecond laser that operates at a 535 nm wavelength. Green wavelength is normally used with the WJG laser technology to maximise the

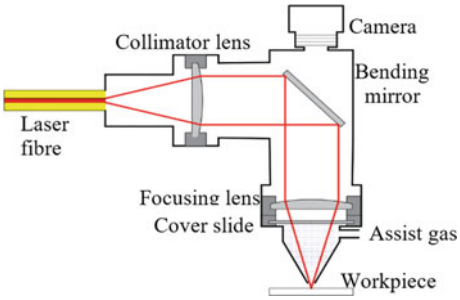

Fig. 3 Schematic of the optical arrangement used for the laser cutting process

laser transmission through the water-jet. The laser beam is focused on the laminar water-jet that has a diameter of 50–100 μm and operates at a pressure of 100–400 bar. This laser beam is guided within the water jet through total internal reflection. The length of the WJG laser can be from 10 to 60 mm. Figure 4a and Fig. 4b show a photograph and a schematic of the WJG laser.

For the analysis, optical microscopy was used to determine the kerf width at the cut entrance and exit. The cut wall taper was derived from these values. A Zeiss scanning electron microscope was used to analyse the cut cross-section and material microstructure. X-ray spectroscopy was used to determine material compositions at the cut surface and in the process affected area.

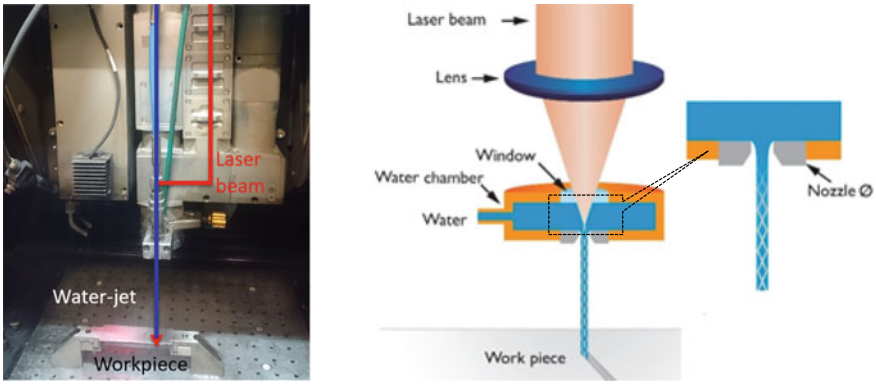

(a) Photograph view (b) Operating principle

Fig. 4 Water-jet guided laser process

3 Laser Cutting of Ox-Ox CMC

As discussed in the literature [33, 34], the thermal effects of the machining process significantly impact the cut quality. Thus, where possible, minimising this thermal input is proposed to be beneficial. The recast layer [35] is defined as the melted material that has failed to be ejected from the surface by the action of laser (or the assist gas or the water-jet). The recast layer was measured for the three laser sources to obtain an indication of the thermal effects based on the processing parameters.

The experimental design was produced to determine the parameters for each laser to achieve optimum machining performance before comparing the systems for their suitability for Ox-Ox CMC machining. Table 1 shows the experimental parameters, and ranges used for cutting the Ox-Ox CMC. Due to the water-jet laser being a multi-pass process the speed listed in the table is not the scanning speed, but instead the overall speed to cut the sample. This therefore highlights the true processing speed of the WJG in comparison to the CW and MSP laser techniques.

The laser-cut samples were analysed for geometrical imperfection and thermal damage. The heat affected zone and the recast layer have been measured as they are critical to the service life of post–machined components, as discussed by Neubrand [21].

A desirable cut geometry is one which is uniform across the length of the work-piece, at both the entry point and exit point of the laser. To ensure that the cut widths calculated are accurate, and to understand the consistency of the cut across the length, 10 different measurements were taken across the laser entry points. This is shown in Fig. 5a, and was repeated for the exit points. The importance of fibre orientation on the cut geometry was highlighted by Negarestani [33], therefore each cut was cross-sectioned, with measurements taken at 10 points—5 for each fibre orientation (Fig. 5b). This provides an understanding of the uniformity of the cut.

Figure 6 shows the influence of scanning speed and power on the recast layer thickness for the CW, and MSP lasers. For both lasers, the recast layer thickness can be seen to increase with the scanning speed to a maximum point before decreasing. A lower scanning speed results in better melt ejection and subsequently lower recast

Table 1 Experimental variables and their range

Laser type	Continuous wave	Millisecond pulsed	Water-jet guided
Variable	Range		
Average power	750–2000 W	750–2000 W	154–206 W
Overall cutting speed	500–8000 mm/min	500–2000 mm/min	50–100 mm/min
Pulse duration	–	0.2–6 ms	220–880 ns
Number of scanning passes	1	1	30–60
Gas/water pressure	5–20 bar	7–20 bar	150–250 bar
Gas composition	Argon, oxygen, air, nitrogen	Argon, oxygen	–

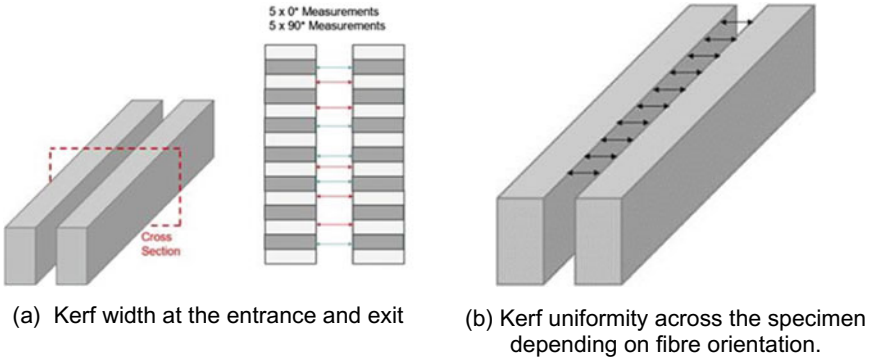

Fig. 5 Schematics representation of the cut geometry measurement methodology

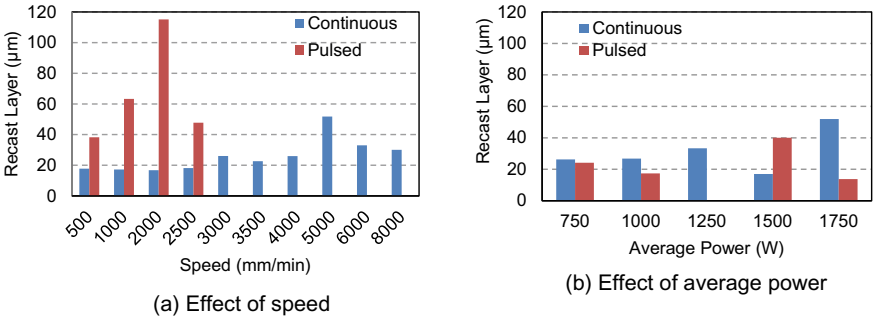

Fig. 6 Influence of laser parameters on recast layer thickness generated from continuous and pulsed wave laser cutting of Ox-Ox CMC (shroud gas composition: oxygen, gas pressure: 7 bar)

layer thickness. Figure 6a also shows that the MSP laser generates a significantly higher recast layer compared to a CW laser. Figure 6b shows that an increase in average power increases recast layer thickness. This is due to the increased thermal input, and subsequently higher molten material formation.

Unlike CW and MSP laser, the WJG produced no noticeable recast layer across the cut surface. As shown in Fig. 7, the original parent material (see Fig. 2) can be seen at the WJG cut surface. This indicates that WJG laser cutting of Ox-Ox CMC results in recast layer free cutting.

Alongside minimising the thermal effects of the laser cutting process, a uniform cut geometry is essential for the exploitation of both the CMC material and the laser technology. Cut uniformity was analysed by taking measurements from a cross-section of the cut (as shown in Fig. 5) and, as previously discussed within the literature, is greatly affected by the fibre orientation within the sample. Figure 8 demonstrates this whereby the horizontal fibres can be seen to protrude from the cut surface whilst the fibres perpendicular to these are visible as black dots along the cut surface.

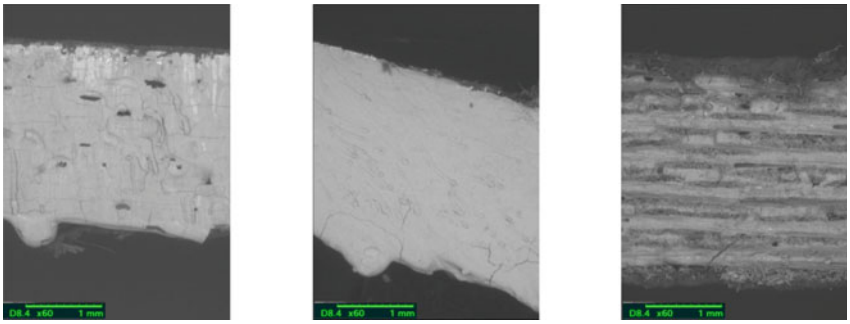

(a) Continuous wave laser (b) Millisecond pulsed laser (c) Water-jet guided nanosecond laser

Fig. 7 Scanning electron microscopic images of the cut surface area of the Ox-Ox CMC sample processed using different laser cuttings techniques

Fig. 8 Cross-sectional SEM image showing a WJG laser cut sample

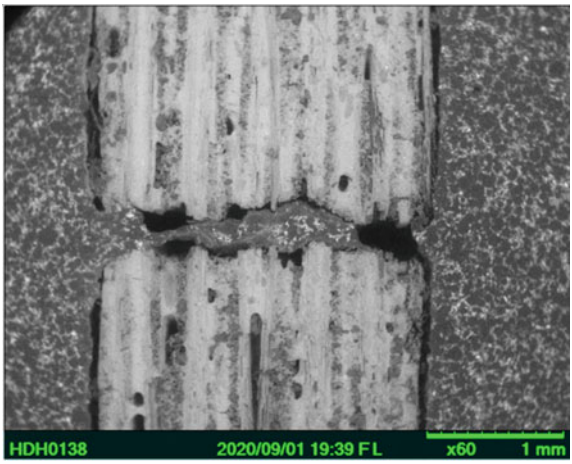

Figure 9 shows the effect of cutting speed on kerf width. As Fig. 9a shows, a kerf width of ~250 μm was observed with CW lasers laser cutting of 3 mm Ox-Ox CMC. The entrance kerf width of the MSP (Fig. 9b) decreases as speed is increased. This is due to the reduction in pulse-to-pulse overlap. A straighter cut was also achieved at slower speeds, and as the speed increased the cut became less consistent. This is possibly due to the low input energy, which changes the cut dynamics over the egress region of the cut (Fig. 9).

A different trend was observed for the WJG laser (Fig. 9c), where a straighter cut was observed at a higher scanning speed. As the scanning speed is increased, the interaction time between the sample and WJG laser is reduced, resulting in a narrower kerf width. As the overall cutting speed of the WJG is significantly lower than the other two laser sources, drawing direct comparisons between this trend and

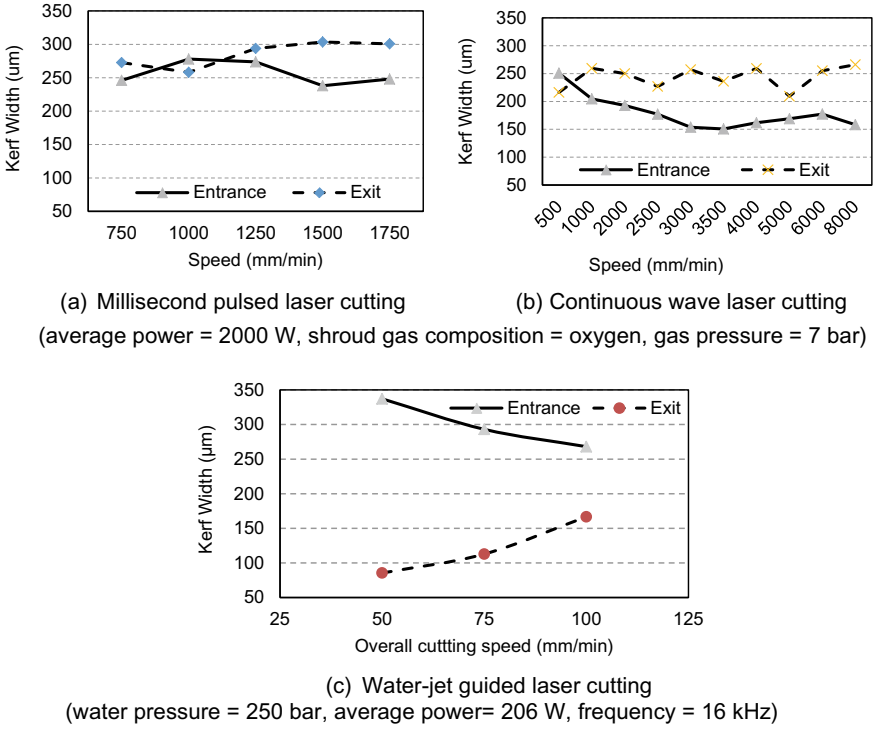

(a) Millisecond pulsed laser cutting (b) Continuous wave laser cutting
(average power = 2000 W, shroud gas composition = oxygen, gas pressure = 7 bar)

(c) Water-jet guided laser cutting
(water pressure = 250 bar, average power= 206 W, frequency = 16 kHz)

Fig. 9 Effect of scanning speed on the kerf width produced from laser cutting

the other laser techniques may be inappropriate. However, from the data available it could be suggested that at a certain speed the exit width becomes wider than the entrance width, as seen in the gas-assisted laser techniques.

Oxygen, air, argon, and nitrogen were investigated as an assist gas for the CW laser and the results are shown in Fig. 10. Oxygen gas resulted in a higher entrance kerf due to the additional exothermic reaction over the laser-material interaction zone. As a result of this, the recast layer thickness is greater for oxygen compared to the other gases.

The effect of assist gas composition on cut wall taper in CW laser cutting of Ox-Ox CMC is shown in Fig. 11. Inert gas (argon or nitrogen) results in minimal wall taper compared to a reactive gas such as oxygen or compressed air. This is possibly due to less heat generated through using an inert gas.

Figure 12a shows the effect of argon pressure on the cut kerf. Unlike laser cutting of alloys, the assist gas pressure has very little effect on CW laser cutting of Ox-Ox CMC. The slight decrease in entrance cut width with an increase in gas pressure should be attributed to the cooling effect at higher gas pressures. Figure 12b shows the effect of water-jet pressure on Ox-Ox cut kerf width. The water pressure had

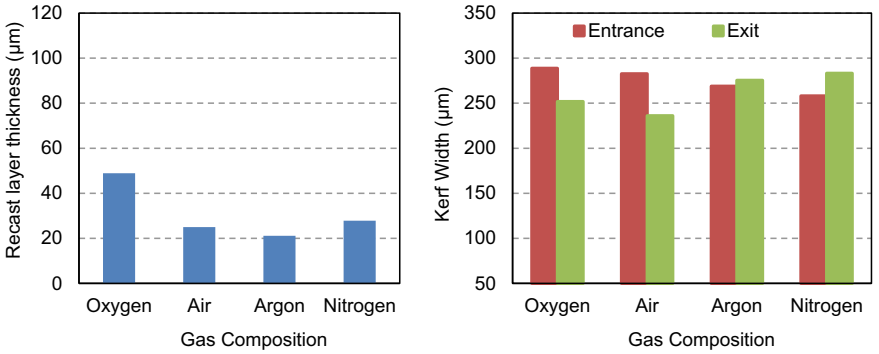

Fig. 10 Effect of assist gas on the recast layer, entrance and exit kerf widths for continuous laser cutting (power = 2000 W, speed = 1500 mm/min, pressure = 7 bar)

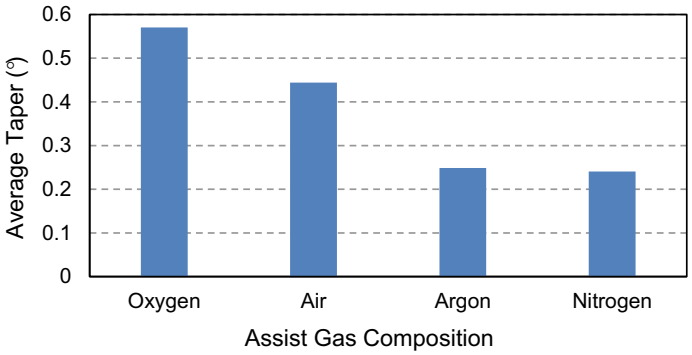

Fig. 11 Effect of assist gas composition on cut kerf taper with continuous wave laser (power = 2000 W, speed = 1500 mm/min, pressure = 7 bar)

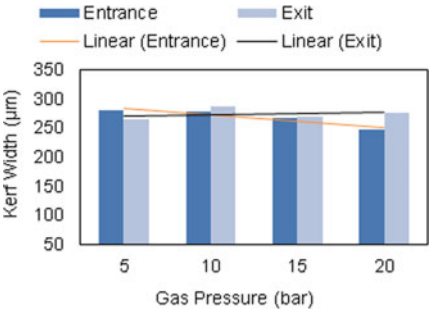

(a) Continuous wave laser

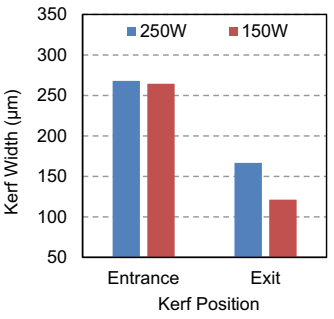

(b) Water-jet guided laser (speed = 100 mm/min, power = 200W)

Fig. 12 Effect of pressure on cut kerf width

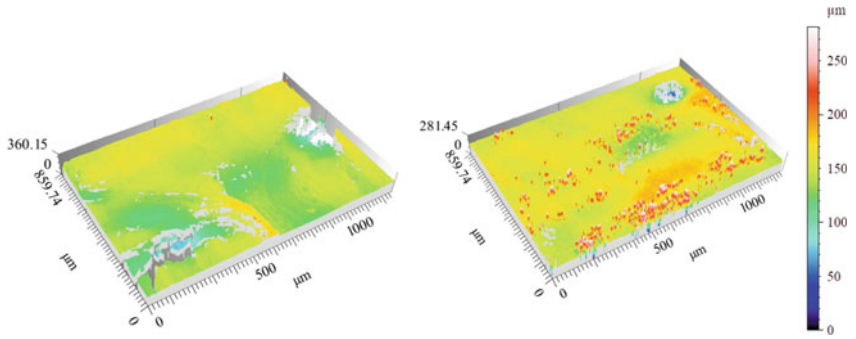

(a) Continuous wavelength (b) Millisecond pulsed wavelength

Fig. 13 Surface roughness for the cut surfaces of the laser cut CMCs

a greater effect on the exit kerf width, highlighting the need for sufficient water pressure for material expulsion within the cut.

As previously outlined, the lack of recast layer following cutting using the WJG laser left the fibres exposed (Fig. 7c), meaning that the surface roughness could not be accurately tested. For the CW and MSP however, surface roughness was comparable, with the MSP laser generating a rougher surface than the CW laser, as shown by the topography graphs in Fig. 13.

As stated within the previous literature [33], minimising the thermal effects is essential for successful machining. As shown in Fig. 7, the WJG laser can produce a cut surface with minimal thermal damage. This is attributed to both the nanosecond pulse laser and the water-jet, minimising the thermal energy input into the workpiece. The comparisons between thermal input of CW and MSP laser were less clear. Both techniques consistently produced a recast layer, but the thickness of this layer varied significantly depending on the parameters used. The hypothesis drawn from the literature was that the recast layer would be thinner for MSP laser compared to CW laser. However due to the reduced intermittent thermal input, this was not always observed.

As shown in Fig. 14, all the experiments carried out using the MSP laser resulted in a thicker recast layer compared to the CW. This is due to the intermittent nature of the MSP laser whereby material removal is inhibited. Whereas the continuous wavelength ensures continuous removal of the molten material, thus resulting in a thinner recast layer. The specific energy has minimal effect on the recast layer suggesting that the thermal input of the laser is less important compared to the material removal mechanism. Based on this, and the understanding that minimising the recast layer is highly favourable for the cutting of CMCs, the WJG shows clear potential over the conventional laser processing techniques. However, if selecting between the MSP laser and the CW laser, the latter is more favourable.

Figure 7c shows a typical surface of the WJG laser-cut Ox-Ox CMC, free from any thermal defects such as the recast layer. Whilst the WJG offers clear benefits

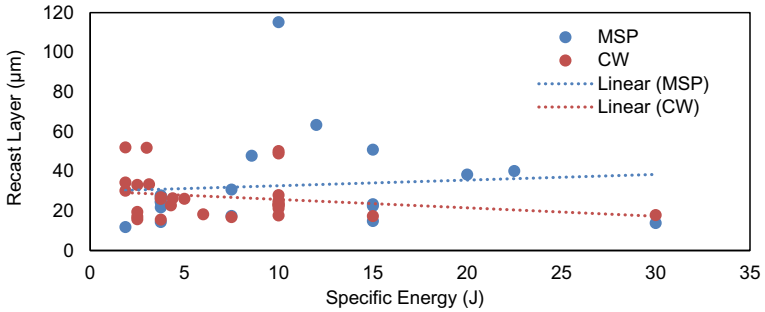

Fig. 14 Effect of laser specific energy on the recast thickness for millisecond pulse laser and continuous wave laser cutting of Ox-Ox CMC

in terms of the recast layer, accurate cut geometry is also key in achieving high-quality cuts. As shown in Figs. 9c and 12b, by increasing the speed and the water pressure WJG can produce a cut edge with minimal taper. As the speed is increased the WJG material interaction time is reduced, resulting in a smaller kerf. The exit kerf also widens, giving a more uniform cut. This effect occurs due to the higher scanning speed creating a more turbulent water-jet within the cut walls. This aids material removal, resulting in a wider cut width. The turbulent jet also explains the effect of greater water pressure, which also resulted in a wider exit kerf, reducing the cut taper by improving flow rate. This flow rate also aids the heat transfer from the workpiece surface, further demonstrating the suitability of the WJG laser [36]. A caveat to simply increasing the water pressure and speed is the water-jet pressure result in chipping of the top layer (close to the cut edge) as shown in Fig. 15.

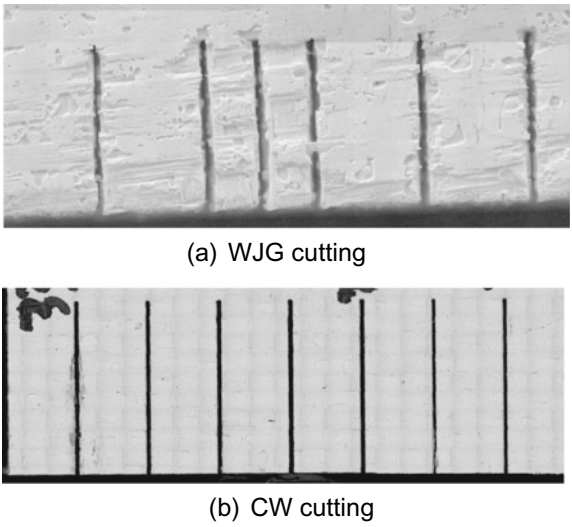

Fig. 15 Optical microscope images of sample surface after laser cutting

Table 2 Preferential parameters for CW and WJG lasers with their corresponding typical results with these parameters

		Continuous wave laser	Water-jet guided laser
Parameters	Speed (mm/min)	Low to medium	Medium to high
	Power (W)	Medium	High
	Gas/Water pressure (bar)	High	High
	Gas composition	Argon	N/A
Results	Recast layer thickness (μm)	20–50	0
	Cut taper	0.25°	1.34°
	Overall cutting speed	1500 mm/min	50 mm/min

Based on the results discussed earlier, the CW laser can be considered a better option when compared to the MSP laser. WJG laser demonstrates significantly better cutting performance in terms of thermal damage, however its overall cutting speed is significantly less than CW laser cutting. An overall comparison of these techniques can be seen in Table 2.

4 Laser Cutting of SiC–SiC CMC

Initial trials were performed to determine the laser parameters that result in through cutting. The results in this report cover MSP laser cutting trials, and include investigations into the following variables; shroud gas selection, peak power, cutting speed, pulse duration and frequency.

The first set of experiments focused on understanding the effect of assist gas composition on the single-pass cutting of SiC–SiC CMC, and the effects of assist gas composition on the kerf width. The results are shown in Fig. 16. Figure 16a and b show the SEM cross-sectional image of the cut produced with argon and oxygen gas respectively. As shown in the figure, using oxygen gas resulted in a larger entrance kerf of ~230 μm compared to 150 μm using argon assist gas. This is associated with the heat generated during the exothermic reaction between oxygen and silica carbide. As noticed from Fig. 16c, the use of argon as an assist gas results in the lowest taper angle of 0.57° compared to other gases—oxygen produced a taper angle of 1.47°. Although there is a significant variation between the entry and exit widths when using oxygen gas, a uniform cut surface is created.

The effect of laser peak power (at constant average power) on the kerf width and cut quality is shown in Fig. 17. The cross-section of the laser cut with a peak pulse power of 2.5 kW shows that there is a minimum level of internal thermal damage—as shown in Fig. 17a, the entry to exit kerf width is within 5 μm. Figure 17b shows the laser cut with a pulse power of 0.5 kW, demonstrating that there is excessive thermal damage within the cut channel. Figure 17b also shows that most of the thermal damage can be seen on the parallel cut fibres. Cut with a narrower kerf width, and nearly zero

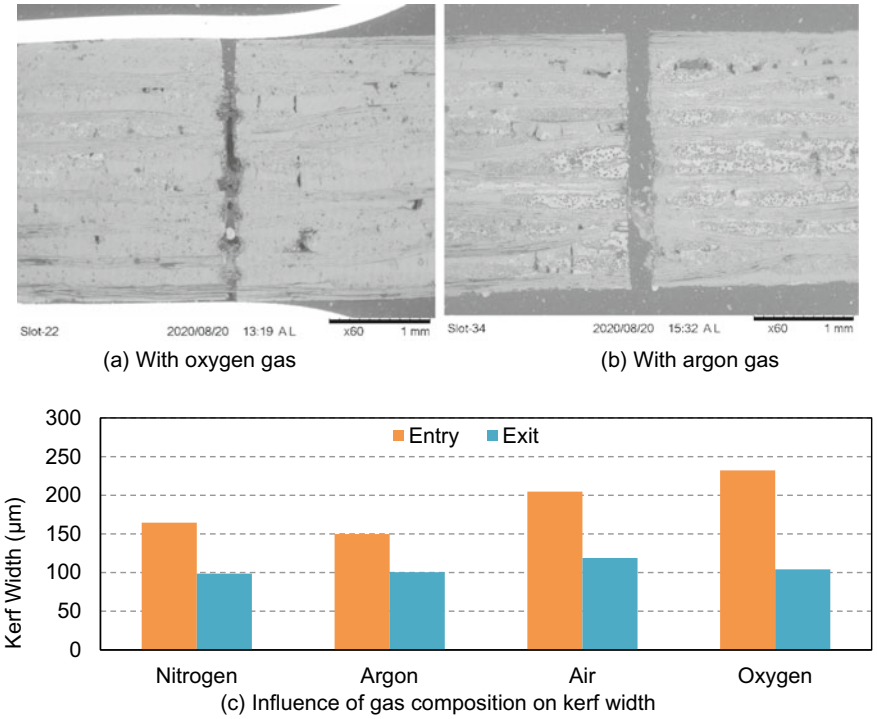

Fig. 16 Effects of gas composition on cut characteristics (frequency = 200 Hz, cutting speed = 600 mm/min, pulse duration = 0.5 ms, peak power 2.5 kW, average power = 250 W, gas pressure = 7 bar)

degree cut taper was observed at higher peak power. Cut quality decreased as peak power decreased. The excess thermal damage at lower peak power is attributed to the incomplete melting and removal of the SiC–SiC CMC.

Figure 18 shows the effect of cutting speed on the kerf width. Entrance kerf width marginally decreases (from 170 µm at 400 mm/min to 125 µm at 700 mm/min) as speed is increased. This is attributed to the reduction in laser-material interaction time as the speed increases. A scanning speed of 300 mm/min results in less taper, thus should be ideal for cutting 2 mm thick SiC–SiC CMC. Alongside the parameters highlighted within this results section, pulse duration and frequency were also varied. However, they were observed to have little effect on the resultant machined material surface quality and cut geometry.

Based on the results in this study, the optimum peak power and speed have been determined for achieving high-quality cut geometry for MSP laser cutting of SiC–SiC CMC. A cut with a low taper and minimal thermal damage was achieved with a laser peak power of 2.5 kW (Fig. 17) and a speed of 300 mm/min (Fig. 18). Using these parameters, a good quality cut can be produced.

Figure 19 shows the SEM images of the cut cross-sections produced with argon

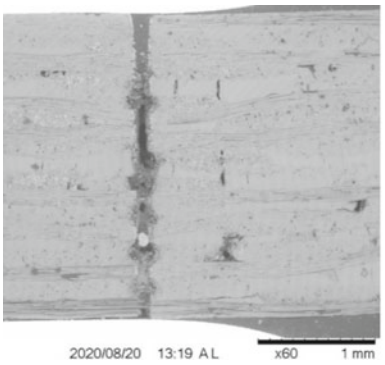

(a) Cut section at peak power of 2.5 kW

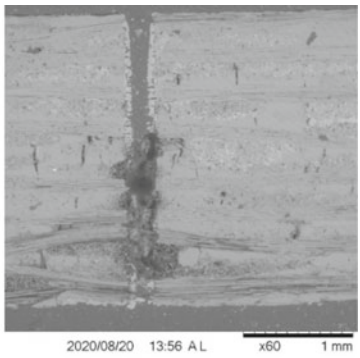

(b) Cut section at peak power of 0.5 kW

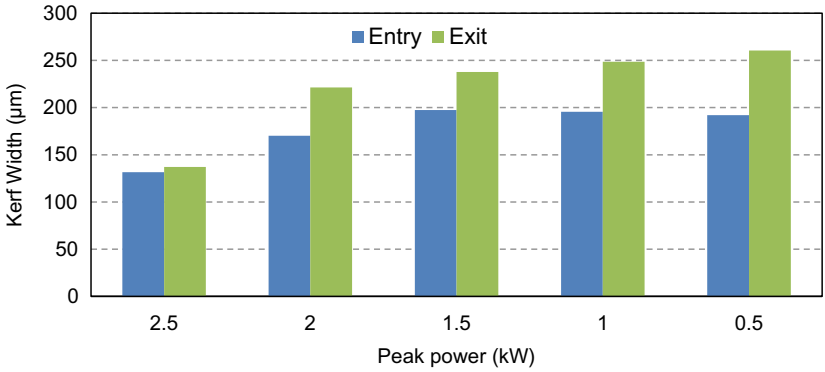

(c) Influence of peak power on kerf width

Fig. 17 Effect of peak power on cut characteristics (pulse duration = 0.5 ms, cutting speed = 300 mm/min, average power = 250 W, gas composition = argon, gas pressure = 7 bar)

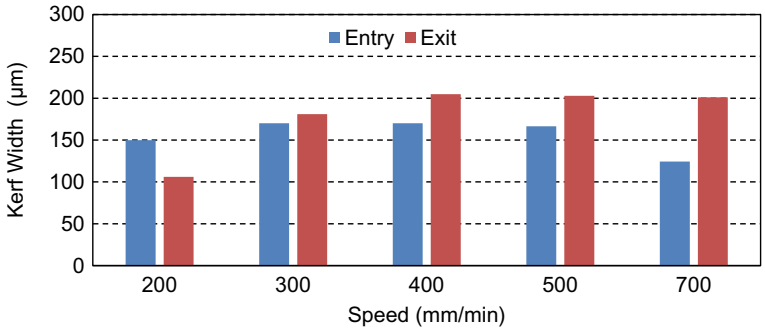

Fig. 18 Effect of cutting speed on kerf width (frequency = 100 Hz, pulse duration = 1 ms, average power = 250 W, gas composition = argon, gas pressure = 7 bar)

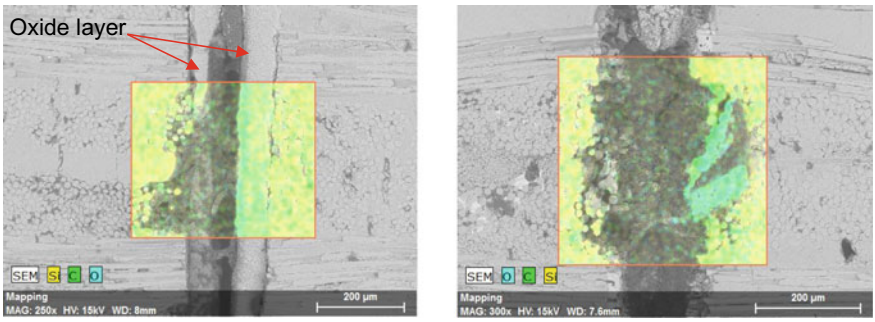

(a) Argon (b) Oxygen

Fig. 19 Optimised cut geometries used with different shroud gas compositions (Frequency = 200 Hz, pulse duration = 0.5 ms, peak power = 2.5 kW, gas pressure = 7 bar)

and oxygen assist gas. Oxygen resulted in a wider kerf width and a thick oxide layer forming. As seen within the images, the oxide layer aids in minimising the thermal damage over the bulk material. Compared to oxygen, when selecting an inert gas as the shroud gas (Fig. 19b), the thermal damage appears to be greater. The oxide layer over the cut surface is expected to act as a sealant, addressing pores or imperfections within the base material cut surface. This oxide layer may also act as a protective layer, preventing deterioration of the exposed SiC fibre during the aero-engine operation. Jarmon et al. [37] validated the benefit of the recast layer for long term performance through conducting fatigue testing on laser machined SiC–SiC CMC in a steam environment. The tests showed that the recast layer limited oxygen attack on the fibre interfaces, benefitting mechanical performance.

5 Conclusion

An experimental investigation was performed to understand the characteristics of laser cutting CMCs. The following conclusions were drawn based on the experimental results.

- The experimental results conclude that using a peak laser power of 2.5 kW, a cutting speed of 300 mm/min, and a shroud gas composition of argon (gas pressure 7 bar) produced a cut kerf width of 134 µm and a taper angle close to zero.
- A small amount of thermal damage occurred to some of the perpendicular fibres, leading to areas of poor cut width uniformity. However, the overall cut geometry was still deemed to be of good quality with little oxidation.
- Water-jet guided laser cutting offers excellent cutting quality, with no heat-affected zone or recast layer observed. However, the overall cutting speed is limited to 50 mm/min for an average laser power 206 W, and a cut wall edge taper of ~1.3° was noted.

- Continuous wave laser cutting exceeds millisecond pulse laser cutting in terms of both cutting speed, and cut quality.
- A 3 mm Ox-Ox CMC can be cut using a 2000 W average power continuous wave laser, at a cutting speed of ~1500 mm/min, and an argon shroud gas pressure of 20 bar. This results in recast layer thickness of ~25 μm and cut taper of ~0.25°.

Acknowledgements This research was supported by the UKRI Future Leaders Fellowship under grant number MR/V02180X/1 and the MTC core research funding under Grant no. 34751-03.

References

1. Ohnabe, H., et al.: Potential application of ceramic matrix composites to aero-engine components. Compos. A Appl. Sci. Manuf. **30**(4), 489–496 (1999)
2. Pritzkow, W., A. Nöth, and A. Rüdinger, *Oxide ceramic matrix composites—Manufacturing, machining, properties and industrial applications.* Ceram. Appl, 2015. **3**(2).
3. Marshall, D.B., Cox, B.N.: Integral textile ceramic structures. Annu. Rev. Mater. Res. **38**, 425–443 (2008)
4. Diaz, O.G., et al.: The new challenges of machining Ceramic Matrix Composites (CMCs): review of surface integrity. Int. J. Mach. Tools Manuf **139**, 24–36 (2019)
5. Bansal, N.P.: Handbook of Ceramic Composites, vol. 200. Springer Science & Business Media (2006)
6. An, Q., et al.: Machining of SiC ceramic matrix composites: a review. Chin. J. Aeronaut. (2020)
7. Mehta, K.M., Pandey, S.K., Shaikh, V.A.: Unconventional machining of ceramic matrix composites–a review. Mater. Today: Proc. (2021)
8. Kamba, Y., et al.: Precise laser cutting of ceramic matrix composites using short pulse hybrid ArF laser. In: Laser Applications Conference. Optical Society of America (2020)
9. Gautam, G.D., Pandey, A.K.: Pulsed Nd: YAG laser beam drilling: a review. Opt. Laser Technol. **100**, 183–215 (2018)
10. Jagdheesh, R., et al.: Superhydrophobic microspiked surface structures by ultrashort laser patterning. Surf. Eng. 1–11 (2021)
11. Jagdheesh, R., et al.: Laser-induced superhydrophobic and oleophobic surface structures on float glass. Lasers Eng. (Old City Publishing) **50**, 2021
12. Jagdheesh, R., Ocaña, J.: Laser machined ultralow water adhesion surface by low pressure processing. Mater. Lett. **270**, 127721 (2020)
13. Jagdheesh, R., Tur, A., Ocaña, J.: The effects of pulse period on nanosecond laser microfabrication. Lasers Eng. (Old City Publishing) **37** (2017)
14. Jagdheesh, R., Valarmathi, A., Sivakumar, M.: Influence of laser beam polarization on micromachining of crystalline silicon using ultrafast laser pulses. Lasers Eng. **32**(1–2), 19–35 (2015)
15. Jagdheesh, R., Mudali, U.K., Nath, A.: Laser processed Cr–SiC coatings on AISI type 316L stainless steel. Surf. Eng. **23**(2), 93–98 (2007)
16. Sharma, A., Yadava, V.: Experimental analysis of Nd-YAG laser cutting of sheet materials – a review. Opt. Laser Technol. **98**, 264–280 (2018)
17. Marimuthu, S., et al.: An experimental study on quasi-CW fibre laser drilling of nickel superalloy. Opt. Laser Technol. **94**, 119–127 (2017)
18. Morar, N.I., et al.: Investigation of recast and crack formation in laser trepanning drilling of CMSX-4 angled holes. Int. J. Adv. Manuf. Technol. **95**(9–12), 4059–4070 (2018)
19. Marimuthu, S., et al.: Effect of process parameters on the cutting quality in lasox cutting of mild steel. Int. J. Adv. Manuf. Technol. **40**(9–10), 865–874 (2008)

20. El-Hofy, M.H., El-Hofy, H.: Laser beam machining of carbon fiber reinforced composites: a review. Int. J. Adv. Manuf. Technol. (2018)
21. Neubrand, A., et al.: Investigation of cutting-induced damage in CMC bend bars. In: MATEC Web of Conferences. EDP Sciences (2015)
22. Bluemel, S., et al.: Comparative study of achievable quality cutting carbon fibre reinforced thermoplastics using continuous wave and pulsed laser sources. Phys. Procedia **56**, 1143–1152 (2014)
23. Herzog, D., et al.: Investigations on the thermal effect caused by laser cutting with respect to static strength of CFRP. Int. J. Mach. Tools Manuf **48**(12–13), 1464–1473 (2008)
24. Costil, S., et al.: Surface modification of ceramic matrix composites induced by laser treatment. Appl. Surf. Sci. **255**(5), 2425–2432 (2008)
25. Chai, Y., Zhou, X., Zhang, H.: Effect of oxidation treatment on KD–II SiC fiber–reinforced SiC composites. Ceram. Int. **43**(13), 9934–9940 (2017)
26. Richerzhagen, B., Richerzhagen, B.: Development of a System for Transmission of Laser Energy. EPFL, Switzerland (1994)
27. Sun, D., Han, F., Ying, W.: The experimental investigation of water jet–guided laser cutting of CFRP. Int. J. Adv. Manuf. Technol **102**(1), 719–729 (2019)
28. Marimuthu, S., Smith, B.: Water-jet guided laser drilling of thermal barrier coated aerospace alloy. Int. J. Adv. Manuf. Technol **113**(1), 177–191 (2021)
29. Marimuthu, S., et al.: Water-jet guided laser drilling of SiC reinforced aluminium metal matrix composites. J. Compos. Mater. **53**(26–27), 3787–3796 (2019)
30. Shi, G., et al: Analysis and evaluation of natural diamond cut by water jet-guided laser. In: 4th Annual International Conference on Material Engineering and Application (ICMEA 2017). Atlantis Press (2018)
31. Sibailly, O., Richerzhagen, B.: Laser dicing of silicon and composite semiconductor materials. In: Photon Processing in Microelectronics and Photonics III. International Society for Optics and Photonics (2004)
32. Tuersley, I., Hoult, T., Pashby, I.: The processing of SiC/SiC ceramic matrix composites using a pulsed Nd–YAG laser: part I: optimisation of pulse parameters. J. Mater. Sci. **33**(4), 955–961 (1998)
33. Negarestani, R., et al.: Nano-second pulsed DPSS Nd: YAG laser cutting of CFRP composites with mixed reactive and inert gases. Int. J. Adv. Manuf. Technol. **49**(5–8), 553–566 (2010)
34. Marimuthu, S., et al.: Laser cutting of aluminium-alumina metal matrix composite. Opt. Laser Technol. **117**, 251–259 (2019)
35. Marimuthu, S., et al.: Characteristics of hole formation during laser drilling of SiC reinforced aluminium metal matrix composites. J. Mater. Process. Technol. **271**, 554–567 (2019)
36. Kalyanasundaram, D., et al.: Design and validation of a hybrid laser/water-jet machining system for brittle materials. J. Laser Appl. **20**(2), 127–134 (2008)
37. Jarmon, D., Ojard, G., Brewer, D.: Laser machining of melt infiltrated ceramic matrix composite. In: Advanced Processing and Manufacturing Technologies for Structural and Multifunctional Materials, vol. VI, pp. 113–121

Laser Shock Peening: A Walkthrough

R. Sundar

1 Introduction

Demonstration of oscillations in optical frequency using ruby crystal by Theodre Maiman in 1960 [1], not only opened up the field of lasers but also marked the beginning of applications of lasers in various fields that includes material science and metallurgy. Unlike conventional light sources, lasers are coherent source of light with well defined directionality, polarization and confined to single wavelength with some spread as dictated by laser physics [2, 3]. Lasers can be focused to tighter spot diameter when compared with conventional light and on special conditions it is even possible to achieve the diffraction limited spot diameter that corresponds to a diameter equivalent to the incident laser wavelength. Active mediums that can emit laser light exists in all the three forms of matter solid, liquid and gas emitting at different wavelengths ranging from Ultra Violet (UV) to far Infra Red (IR) of electromagnetic spectrum. As far as time domain is concerned, lasers are available in continuous wave, milli, micro, nano (ns), pico (ps) and femtoseconds (fs) time durations. For interested readers very good books on the fundamentals of lasers are given in references [2, 3]. In this chapter we will confine only to lasers of high energy and of nano second pulse durations as it is more relevant to the topic intended to be addressed here.

Pulsed lasers in the order nano second pulse width and high laser energy ranging from few 100 mJ to few tens of joules when focussed, results in highly intense electromagnetic field at the focal plane of the lens, that is capable of breaking the air and creating plasma and associated shock waves. In late 1960's it was explored to apply the laser generated shock waves to manipulate metallurgical properties of

R. Sundar (✉)
Physical Metallurgy Division, IGCAR, Kalpakkam, India
e-mail: sundarpmd@igcar.gov.in

J. Radhakrishnan and S. Pathak (eds.), *Advanced Engineering of Materials Through Lasers*, Advances in Material Research and Technology,
https://doi.org/10.1007/978-3-031-03830-3_4

metals [4, 5] and hence improve the application based performances of the metals and alloys. Thus the process of laser shock peening came to existence.

As a preamble, LSP is a non contact surface/subsurface modification technique which is purely a mechanical process facilitated by light pulses that can introduce high strain rate of uni axial compression of the order of 10^6 s^{-1}–10^7 s^{-1} [6]. LSP is unique in not altering the surface roughness yet introducing a significant compressive stress on the surface and subsurface of the samples. Thus, paving way for enhanced metallurgical properties, like increasing hardness, fatigue life, and resistance to corrosion [7–12]. The LSP has been tried successfully on numerous metals and alloys to improve various properties, listing all of them would be beyond the scope of this chapter and countless literature is available in this regards.

This chapter is designed to give a walkthrough on LSP process covering the topics such as; LSP process, processing parameters associated with LSP like laser wavelength, pulse width, role of absorptive coating and transparent overlays etc. From the metallurgical perspective it is planned to address the strengthening mechanism due to LSP in terms of microstructural change and its effect in modifying the mechanical properties of the metals and alloys. Before adapting any process it is imperative to have an unbiased comparison of the process under consideration with existing competitive process in terms of technical supremacy and economic viability. Therefore a conscious effort would be made to compare the LSP with at least one of the prevalent competitive process. Discussion on variants of LSP such as peening without coating, warm laser peening and oblique angle peening are also included as they may provide potential solutions for some interesting application needs.

2 Laser Shock Peening Process

Whenever, a high energy, short pulse width laser (few 100's of mJ to J and few ns to few 10's of nano seconds), say for example 500 mJ, 10 ns laser is focussed, on the target material, a thin layer of target material undergoes instantaneous vaporization. The plume thus generated, absorbs energy form the incoming laser beam leading to ionizing of electrons from atoms, thereby creating high temperature high pressure (~10,000 K and in GPa) [13] plasma and subsequent shock wave. The shock wave imparts a mechanical impulse on the target. As the intense shock wave propagates through the substrate, the material is plastically deformed resulting in creation of Residual Compressive Stress (RCS) up to some depth from the surface [14]. Plastic deformation occurs only when the magnitude of the shock wave is greater than the dynamic yield stress of the material (Huguniot Elastic limit, HEL). As the shock wave propagates into the material, it deforms the subsequent layers and in the process shock wave attenuates resulting in the decrease in its magnitude. When the shock wave magnitude falls below HEL of the material, plastic deformation does not occur. Therefore shock wave creates a RCS on the surface and RCS decreases with depth from the surface. This kind of direct ablation is not an efficient process as the plasma expansion occurs in all direction as shown in Fig. 1 marked as A.

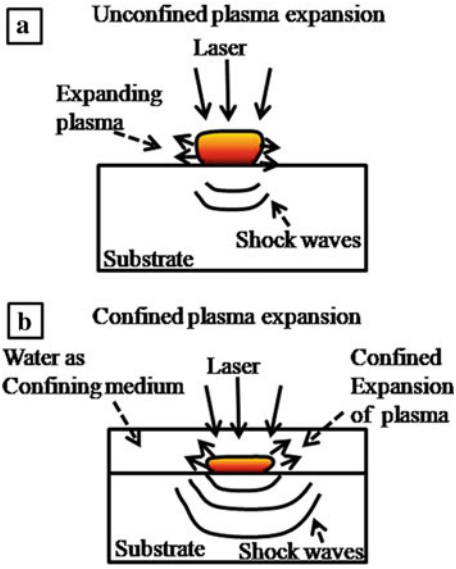

Fig. 1 **a** Shows unconfined expansion of plasma. **b**) Shows confined expansion of plasma under water as confining medium

In early 1970's Fairhand and Clauer [16] showed that by confining the expansion of plasma, it is possible to enhance the magnitude of shock wave by more than an order of magnitude and the plasma pressure duration by 2–3 times [17]. Confinement of plasma expansion can be achieved by applying a transparent overlay such as water or glass over the substrate [14]. Transparent overlay limits the plasma from expanding in all directions there by giving more impulsive momentum to the material, Fig. 1 marked as B. Further, direct interaction of laser with substrate can lead to localized melting of thin layer of material resulting in induced tensile stress. In order to avoid the thermal effects, a sacrificial coating such as black paint or tape is applied over the substrate [18]. Besides protecting the surface from melting, sacrificial layer is also shown to augment the shock wave duration. By applying a sacrificial coating and transparent over lay, the process can be made more efficient in terms of increasing the shock pressure by 30–50% [17]. Figure 2 shows the actual laser peening process under confined plasma expansion configuration with sacrificial coating layer as well as transparent overlays.

2.1 Plastic Deformation

Fabbro et al. [19] had proposed an analytical model for shock pulse generation under confined expansion mode also called as water confined mode. The process can be understood as three step process, first step; when laser is "on", a thin layer of the order of few tens of microns of material undergoes instantaneous vaporisation called as ablation. The ablated material absorbs energy from the incoming laser beam and

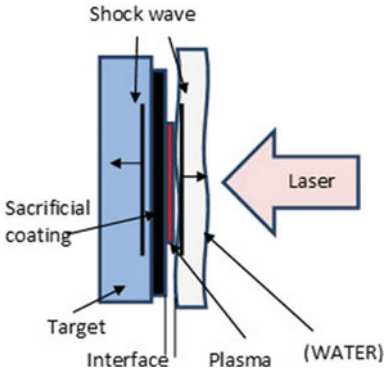

Fig. 2 Laser shock peening process [15] (reprinted with Permission from Taylor and Francis 2019)

plasma is created, followed by generation of shock wave whose pressure would be 2–3 times [17] higher than the direct ablation mode. The second step; deals when laser is "off", here the plasma maintains pressure which falls over time as a result of adiabatic cooling, resulting in target acquiring impulse momentum during these two steps. In the third and final step; recombination of plasma occurs and expanding gas in the interface of transparent medium and substrate generates canon ball like effect imparting more momentum. Under this model, scaling law for pressure can be given as [13, 20].

$$P_{max}\left(10^8 Pa\right) = 0.10\sqrt{\frac{\alpha}{2\alpha+3}}\sqrt{Z}\sqrt{I_0} \tag{1}$$

$$\frac{2}{Z} = \frac{1}{Z_1} + \frac{1}{Z_2} \tag{2}$$

Where Z is in (g cm^{-2} s^{-1}) is reduced shock impedance between the target and the confining medium, P is pressure, α is interaction efficiency, I_0 is laser intensity in GW/cm^2, Z_1 & Z_2 are acoustic impedance of the target and confining medium respectively, I_0 is given by.

$$I_0 = \frac{E}{\pi r^2 t_p} \tag{3}$$

Where E is laser energy per pulse, t_p is the laser pulse width and r the laser spot radius. Under water confinement mode Eq. 1 can be approximated to.

$$P(GPa) = 1.02\sqrt{I_0(GWcm^{-2})} \tag{4}$$

Various theoretical models [21–28] have been tried by different researchers to understand the LSP process such as role of coating, ionisation of plasma, water evaporation and energy loss on the physical process of water confined expansion

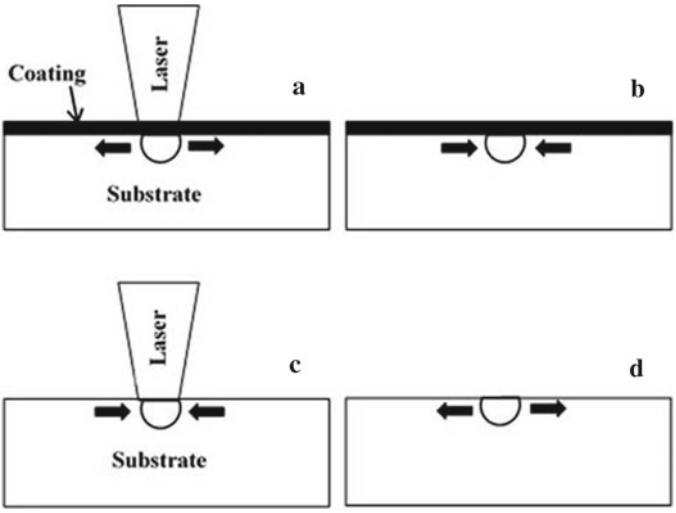

Fig. 3 **a** Coated substrate interacting with laser **b** Coated surface after laser pulse **c** Substrate without coating interacting with laser **d** Uncoated surface after laser pulse [15]. (Reprinted with Permission from Taylor and Francis, 2019)

(WCE) of plasma [21]. Besides investigating theoretically on WCE, studies were also done on material response to LSP, prediction of magnitude and direction of induced stress. Artificial neural network modelling and molecular dynamic simulations [26–28] are some of other theoretical models explored to study the shock wave and material interactions.

The mechanism by which residual compressive stress (RCS) is created by LSP can be understood as follows [29–31]; Shock wave created by the laser striking the target coated with sacrificial layer induces a uni-axial depression at the interaction zone and dilatation in the surface layers Fig. 3 marked as a & b [15]. When the laser beam is off, the surrounding layer around the affected area reacts by generating compressive stress. In the case of substrate without coating the surface dilation expanding sideways is created due to thermal effects causing plastic deformation. Once the laser is off, thermal dilation ceases to exist; the surrounding area reacts to create tension to minimize the deformation Fig. 3 marked as c & d.

2.2 Role of Coatings and Transparent Overlays

Application of coatings as well as transparent overlay makes LSP efficient. However, it must be noted that adequate selection process is to be adapted in selection of material to serve as transparent over lay as well as coating. As far as coating is concerned black paint, adhesive tapes and metallic coatings/tapes have served as protective coatings. Metallic coatings with low acoustic impedance compared to

base metals can help to achieve higher stresses, hence facilitating use of low laser energies for required induced stress. Coatings, be it black paint or adhesive tape, must have good adhesion to the substrate and survive at least few shots of laser pulses before thinning down and subsequent tearing due to ablation by laser. Tearing of adhesive tapes can lead to exposing the base metal to thermal effects. In the case of paints, author has observed in several instances that due to shock wave, black paint comes out as flakes not only at the region of interaction but also from adjacent areas. Therefore it is essential to select suitable sacrificial coating. In case of adhesive tapes, thickness of tape, its adhesiveness and its ability to withstand more number of pulses should be considered while exercising the choice for selection.

With respect to the transparent overlay, it must be noted that the layer should not contribute to attenuating the laser energy due to absorption. Material must have less absorption for the incoming laser beam; otherwise, laser energy would be attenuated due to absorption in the transparent overlay depending on the thickness of overlay through which it traverses. Appropriate acoustic impedance is not only important for sacrificial coating but also for transparent overlay too. It is essential to choose the material with proper acoustic impedance so that there is efficient coupling of shock wave energy to the substrate. Glass is known to have better acoustic impedance match when compared to water to produce more peak pressure (of 5 GPa) as against water (3 GPa) [13, 32]. Glass is susceptible for breaking due to shock wave; therefore water is generally used as transparent overlay. However, in the case of water the disadvantage is, it can saturate the plasma pressure due to parasitic plasma creation beyond certain laser intensity [33]. Laser wavelength and pulse width has significant role in saturating plasma pressure and will be discussed in subsequent sections. Further, constant replacement/ filtering of the water is essential since debris due to ablation can pollute the water resulting in lower break down thresholds and hence saturation of shock pressure. In summary the confined expansion mode can increase the magnitude by more than an order and pressure duration by 2 to 3 times when compared with direct ablation or unconfined expansion of plasma [19, 31].

2.3 Lasers and Work Station for Peening

Shock waves are generated due to adiabatic expansion of the plasma, created by laser having high intensity in the order of few GW/cm^2. Achieving high intensity directly, demands laser beam of very high energy in the order few hundred joules per pulse. Laser with few hundred joules of energy per pulse could be huge, comprising of multi stage laser amplifiers, beam shaping systems and other associated systems like cooling, electronics etc. Such laser systems are intense in terms of technology, infrastructure and cost thus it can forbid a potential user to explore the LSP as potential alternative. However, alternately, high intensities can also be created by focusing the lasers to smaller spot diameters in the range of few 100's of microns. In focused geometry lasers of pulse energies in the range of few hundred mJ to few

joules and nano second pulse duration would be sufficient and they are commercially available too.

Generally nano second laser pulses and energy in range of couple of joules when focussed can generate adequate intensity required for LSP. As far as laser wavelength is concerned, IR is a preferred choice, though lasers in visible and near UV too can bring peening effect. Choice of wavelength on the LSP would be discussed in later sections. Among the other reasons in selecting the laser, the prime consideration is given for easy commercial availability of laser systems. Availability of such laser systems not only serves the research purpose of LSP but also provides bright prospect in adapting the technique by the industry, if found to be technically superior process for the intended application. Nd:YAG laser best suits this need, brighter side of the Nd:YAG laser is; it is commercially available up to few Joules of energy and 10–20 ns pulse width. It is also possible to custom design the laser for user needs. Nd:YAG lasers are rugged and relatively maintenance free and importantly it supports other wavelengths by means of higher harmonic generations leading to availability of 0.532 nm (Second harmonic: green laser visible region of spectrum), 0.355 and 0.266 nm (third and fourth harmonic: UV region of spectrum).

For the given laser energy, laser spot sizes to achieve high intensities of the order of GW/cm^2 would be in the range of few hundred microns. Hence in order to achieve large area of peening, the substrate has to be scanned by the laser beam either by moving the laser beam or the substrate. Therefore a computer controlled workstation supporting linear movements in x & y directions are required. Workstation is moved at a specified speed in x and y directions and this is synchronised with laser pulse repetition rate in order achieve required pulse per mm^2 on the substrate. Workstation also includes a closed loop water flow system with suitable filters for contamination free running water on the surface of the substrate to act as transparent overlay. When the laser beam hits the target covered by water, water splashes and it can smear water droplets on focusing lens and this can alter the effective focal length of the lens. Water splashing problem can be circumvented by introducing a series of suitable diameter apertures along the path of the laser beam. Further, introducing continuous flow of compressed air at high pressure around the apertures would ensure no water drops from splashing reaches the lens surface. Schematic of peening setup is shown in Fig. 4 and actual system while peening is shown in photograph Fig. 5.

2.4 Peening Parameters and Its Limitations

Primarily two important limitations in WCE of plasma arise due to wavelength and pulse width of the laser used for LSP. Incidentally both are related to plasma creation mechanism in WCE and can be understood by categorising the mechanism under three types namely; (a) plasma creation, (b) saturation of plasma and (c) interaction efficiency (α). All the three mechanisms are influenced by laser wavelength and pulse duration. Plasma creation is due to two types of process namely Avalanche Ionisation (AI) and Multi Photon Ionisation (MPI). A very brief introduction to AI and MPI

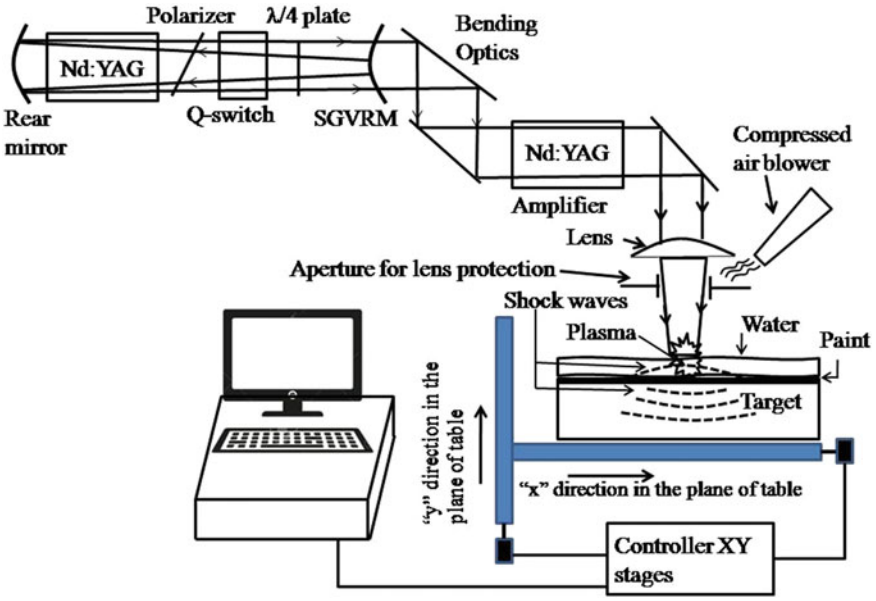

Fig. 4 Schematic of experimental setup for LSP

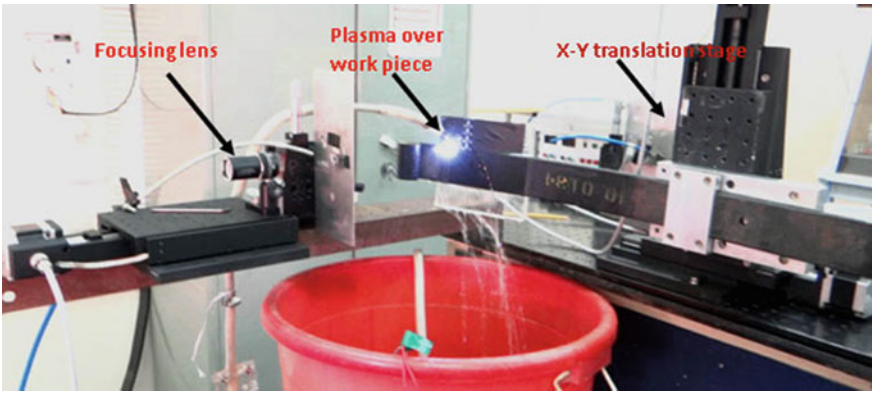

Fig. 5 Photograph of the actual system while peening [15]. (Reprinted with Permission from Taylor and Francis, 2019)

process, are as follows; a free electron or a conduction electron can absorb energy from incoming laser beam by joule heating also called as inverse Bremsstrahlung and get accelerated. Once it acquires adequate kinetic energy exceeding the ionisation potential of bound electron it can knock the bound electron, process is also called as impact ionisation and the process repeats resulting in avalanche ionisation [34, 35]. In MPI, at higher field strength due to ultra short laser pulses, bound electron

can be lifted to conduction band by absorbing more than one photon of energy hν. Where, h is plank's constant and ν is the incident frequency of laser light. When nhν is greater than the ionization potential (n is the number of photons) or bandgap, ionisation occurs. MPI is predominant in UV while AI in IR lasers, thus wavelength plays a significant role in plasma creation.

Discussing on saturation of plasma in WCE, irrespective of wavelength beyond certain laser power density plasma pressure saturation is observed because of parasitic plasma creation on water surface due to the water breakdown. Water breakdown threshold decreases with decreasing wavelength which in turn limits the achievable peak pressure. Threshold intensity for breakdown decreases from 10 to 4 GW/cm^2 as we move from 1064 to 355 nm wavelength [36], corresponding to peak pressure of 5GPa at 1064 nm and 3.5 GPa at 355 nm. This is second limitation that arises due to wavelength. Another effect that can be associated is reduction in effective laser pulse duration due to parasitic plasma creation. Due to parasitic breakdown at the water surface which is dependent on interacting laser wavelength, the plasma at the interface of overlay and substrate experiences a screening effect leading to effect similar to shortening of laser pulse over the target and hence contributing to saturation of plasma pressure.

Interaction parameter α is defined as a fraction of plasma internal energy contributing to pressure rise in laser plasma. Under the assumption that same laser energy being absorbed at IR & UV, local plasma density is higher for UV and this must lead to decreased plasma temperature for UV. If the plasma were to be considered under thermodynamic equilibrium then the part of internal energy devoted for ionisation turns out to be lower or otherwise energy contributing for pressure raise is higher for UV. Hence parameter α contribution is higher for shorter wavelengths. It is around 0.25 for IR and 0.4 for green and UV [35–37]. LSP is possible with lasers in either end of the visible spectrum, provided the limitations are considered on case to case basis.

In the selection of pulse width it is to be noted that again AI and MPI process are dependent on pulse width too. Since cross-section for MPI process is extremely small [34], it requires very high field strength such as one due to ultra short pulses, hence MPI is more associated with ultra short (fs) pulses while AI is predominant with ns second pulses. Threshold value for plasma creation shows scattered values in the case of AI process as this process is known to be statistical in nature [34, 35]. Further, depth of peened layer is proportional to pulse width (t_{pw}) times pulse pressure (P), so, for fs pulses peening effect depth is shallow. Long pulse durations in the order of milliseconds do not produce plasma as the intensities are too low even after focussing, further it also inflicts unwanted thermal effects like melting. Hence, LSP is generally confined to ns pulse width regime. It is also to be noted that there are variants in peening process and one such process is peening without sacrificial coating (LPWC). In LPWC it is shown [38] that pulse width > 40 ns induces melting and < 13 ns results in insufficient peening. Generally pulse widths in the order of 20–30 ns are preferred. In summary, a clear objective on type of peening and the requirement of peening magnitude and depth influences the pulse width selection for peening.

Other parameters of laser that can affect the peening outcome are discussed below; Laser spot diameter makes its impact on influencing the peening throughput and peening depth. Smaller spot diameter takes more time to cover a given area of peening hence low throughput. Further, for shorter spot size the beam attenuates at $1/r^2$ while for bigger spot size (in this chapter, spot size or spot diameter refers to laser beam diameter and are measured at $1/e^2$ points of the spatial profile of the laser beam) this dependence is 1/r [38]. Therefore the bigger spot size can give good peening depth, however, at the cost of plasma pressure due to reduced intensity of the laser beam. Since a focusing lens produces continuously changing spot size as a function of propagating distance from the lens, a large degree of freedom to select the spot diameter is available under focussing geometry. It is possible to place the specimen at a suitable location along the laser path to realize choice of spot size and hence the intensity. Variation of laser intensity as a function of laser spot size for a given laser energy is shown in the Fig. 6. As the laser beam propagates after the lens, beam diameter becomes minimum at focal plane and increases on the either side of it. Since the intensity is inversely dependent on square of spot radius, it would be maximum, for minimum spot radius resulting in air breakdown around the focal plane. Therefore it is always preferred to place the target before the focal plane of the focussing lens.

Pulse to pulse overlap in the peening process is optimized to produce uniform peening effect. This overlap is arrived at by considering the spot size laser repetition rate and the translation speed of the work station, overlap of the spots (η) is given by (CI / D)*100 [39, 40]. Where, CI is coincidence length and D is the spot diameter, CI can be modified by changing the laser repetition rate. Other than pulse to pulse

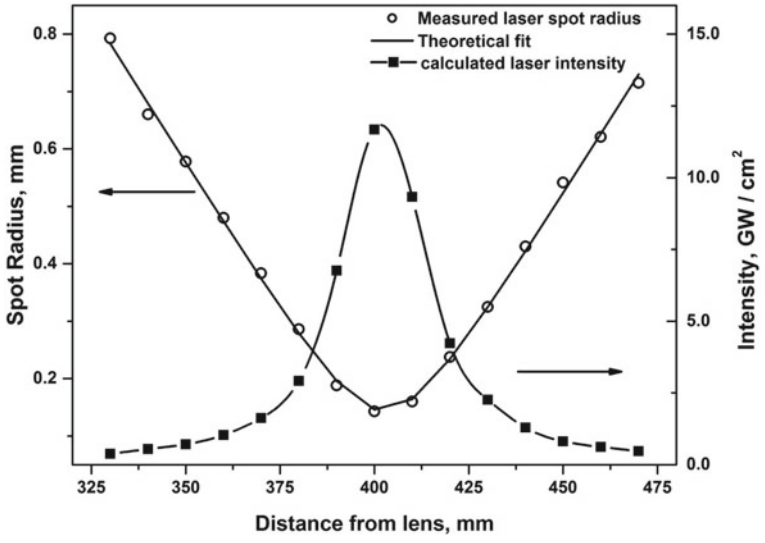

Fig. 6 Variation of laser intensity as a function of laser spot size for a given energy

overlap, number of pulses incident on a given area defined as pulse density is also responsible for uniformity, magnitude and depth of peening. It must also be noted that sacrificial coating must also withstand the increased pulse density before it succumbs to tearing. It is seen in the literature that residual compressive stress of −170 Mpa due single impact and −340 for triple impact besides broadening of X-ray diffraction peaks for 7075 alloys [6]. In case of 55% carbon steel increase in depth was observed from 0.9 mm to 1.8 mm in multiple impacts [38].

3 Competing Processes

Other competing processes that can introduce compressive stress are shot peening, ultrasonic peeing, water jet peening, low plasticity burnishing, deep rolling and cavitation peening [41–46]. As it would be beyond the scope of this chapter to dwell upon all competing processes, a brief part here is devoted for shot peening. Among the above said, shot peening (SP) is generally adapted for industrial applications due to its economic viability. In shot peening steel /ceramic balls of around 4 to 5 mm diameter are fired at high kinetic energy towards the target material. This creates a dimple on the surface resulting in highly shocked and compressively stressed surfaces. Though an RCS is created on the surface it may not be as deep as the one observed due to LSP. Further, dimpling of the surface due to impact alters the materials roughness, sometimes this change in surface roughness, can act as stress raisers and eventually defeating the purpose of the shot peening exercise. SP is also known to create more surface hardness probably due to the fact that SP involves the peak pressure durations that are 10–20 times longer resulting in higher dislocation generation and motion, further SP is of multi-axial loading hence can activate more slip planes [6]. In the case of LSP negligible or no surface roughness change is observed as this is a non contact process. LSP also induces higher surface RCS vis a vis better depth of RCS when compared with shot peening. However, LSP may be a bit costlier and technically demanding process for the industries to adapt. Table 1 compares the effects due to SLP and SP.

Table 1 Comparison of SP and LSP [15] (Reprinted with Permission from Taylor and Francis, 2019)

	Strain rate (s^{-1}) [6, 38]	Cold work (%) [47]	Peening depth (mm) [47]	Roughness Ra (μm)[9]
Shot peening	10^3–10^4	15–50	~0.2	4.52 (X20 steel)
Laser peening	10^6–10^7	5–7	~1–2	0.98

4 Characterization

The next and the important step are to quantitatively evaluate the effects of LSP on the substrate to ensure that adequate surface modification is achieved for the targeted application. Quantitative characterization involves measuring the RCS magnitude and depth, hardness, phase transformations, microstructure changes, physical, mechanical and thermal property changes associated with LSP. Widely used techniques are hardness measurements, stress measurements, and profile changes by X-ray diffraction, mechanical properties by tensile and fatigue testing's. Though thermal property also gets affected by LSP there is a scarcity in research publications on role of LSP over thermal properties of the material.Author has published in one of his research article a comparison of thermal diffusivity changes of peened and unpeened specimens of alloy D9[48]. Besides revealing RCS profile of peened samples, X-ray diffraction can also give clues on phase transformations and microstructure changes such as nano grain formations. Optical Microscopy (OM), Scanning Electron Microscopy (SEM), Transmissions Electron Microscopy (TEM) and Electron Back Scattered Diffraction (EBSD) technique associated with SEM can give us complete information on microstructure modifications.

To start with LSP effect is assessed by X-ray diffraction based stress measurement for magnitude of the induced RCS. X-ray diffraction method adapts standard d Vs $\sin^2 \Psi$ technique to evaluate the stress [49–52]. Similarly stress affected depth is determined by repeated sequential etching of the sample for a known thickness of 40-50 μm and measuring stress by XRD until RCS value reduces to zero. Figure 7 shows the RCS on the surface (marked as A) and the depth (marked as B) of the peened SAE9260 steel [7]. Induced RCS increases the hardness of the material; therefore it is also a general practice to measure the hardness of the peened samples to directly have qualitative estimate of peening effect.

Since peening affects greatly at surface (up to a depth of 30–40 μm) when compared with rest of the peening affected depth, increase in hardness on the surface would be distinct and high. Profiling the hardness as a function of peening affected depth would show a gradient decrease in hardness with highest value at the surface and settling to that of the hardness of the substrate beyond peening affected depth.

Microscopy can give information on microstructural changes which can be correlated to change in other properties of the material due to LSP. Though OM can give qualitative evidence on the peening effect, SEM, EBSD can give a clearer picture on slips, slip bands, deformation bands, grain orientation etc. Though an estimate on dislocation density created due to peening can be figured out using XRD peak broadening, dislocation densities in terms of dislocation walls and tangle can be clearly observed in TEM. The said techniques can be used to establish the effect of LSP on the material without ambiguity, however the effect of LSP on material properties such as corrosion, fatigue and wear properties are to be investigated separately to quantitatively evaluate the role of peening. Fine tuning of the peening parameters would help in achieving the targeted objective of the experiment. Flow hart shown in Fig. 8, gives the process flow of LSP to achieve the objective.

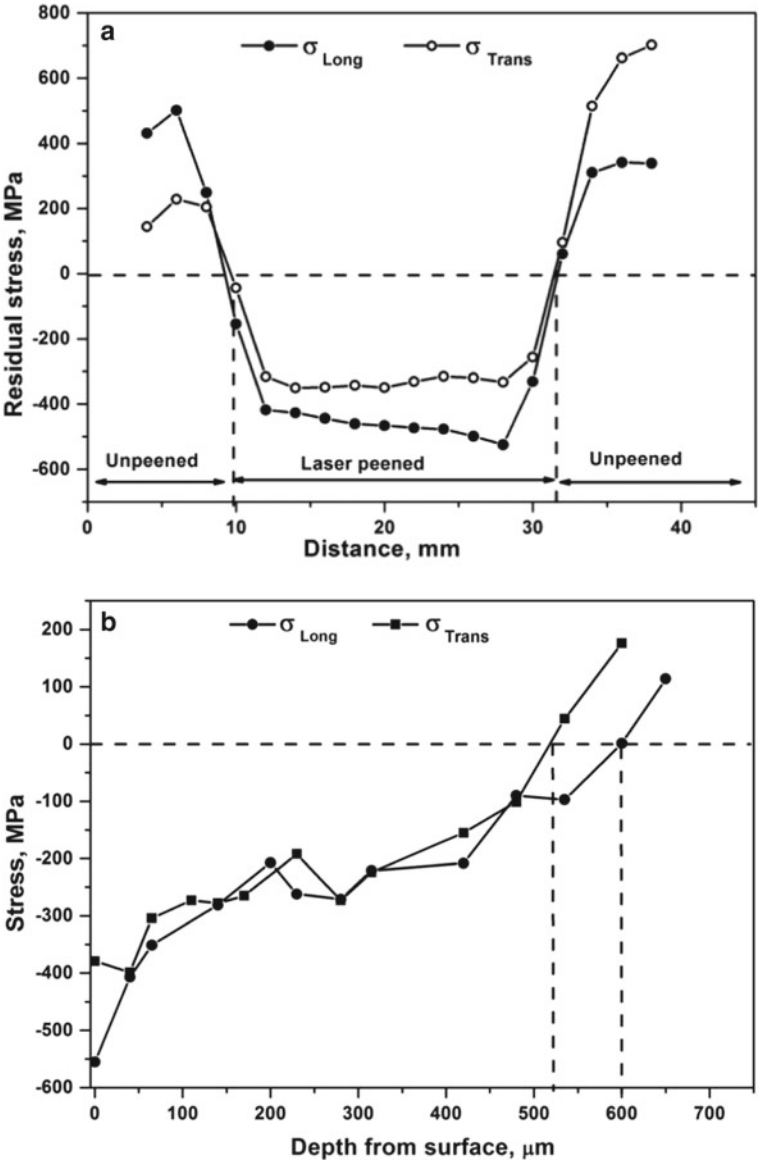

Fig. 7 **a** surface residual stress measured on peened and unpeened region, **b** Depth profile of the RCS due to LSP

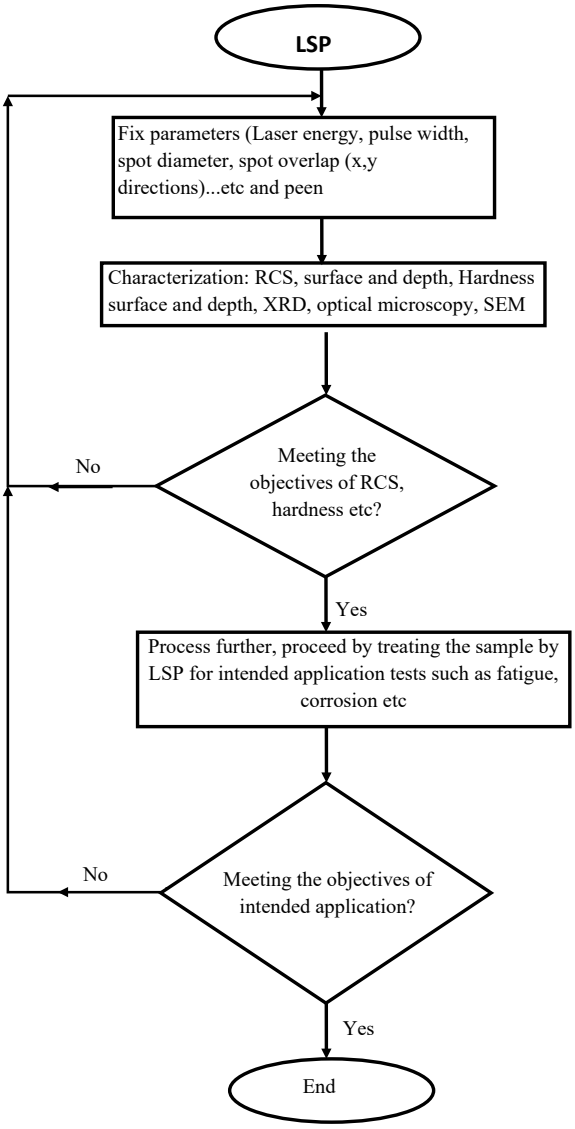

Fig. 8 Process flow chart for LSP

4.1 Microstructural Change Due to LSP

Besides inducing RCS, LSP is also known to strengthen the material by microstructure modifications. Plastic deformation due to LSP is extremely fast and involves huge pressure pulse in times scale of nanoseconds, therefore, strain to order of 10^6–10^7/s is not uncommon [53–55]. High strain and rate at which it is achieved in LSP process has a direct impact on grain refinement resulting in grains of the order of

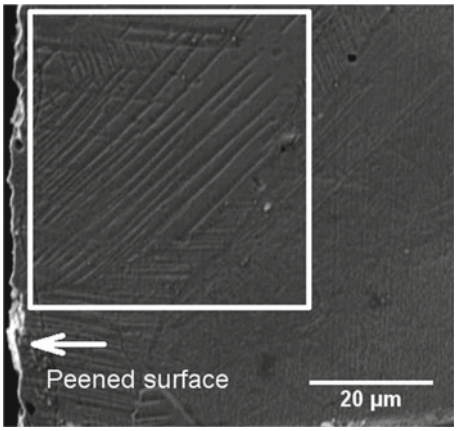

Fig. 9 Secondary electron image, showing signatures of plastic deformation on the surface due, to LSP [48]

few tens of nm. The grain refinement mechanism is deeply influenced by factors like crystal structure, stacking fault energies and deformation process [56] of the concerned material. Significant signature of LSP in modifying the microstructure is, it is confined to surface/suburface. As explained earlier, as the shock wave propagates through the material it induces plastic deformation only as long as it's magnitude is greater than HEL, therefore plastic deformation is not uniform and it is maximum on the surface and reduces as a function of depth.

Deformation bands can be seen clearly In Fig. 9 on the peened surface indicated within white coloured square. LSP generates rich dislocation densities, stacking faults and Mechanical Twins (MT). For example ODS 304 steel dislocation density of 9.04 $\times$ 10^{12} m $^{-2}$ and twin density of 6.12 $\times$ 10^{12} m^{-2} were recorded [53]. It is generally understood that the sequence of grain refinement begins with generation of high dislocation densities from different slip systems [57, 58]. When the stress caused by the pileup of such large dislocation densities crosses a threshold, mechanical twins are created. This may be in single direction or parallel and they divide original coarse grain Fig. 10. Purpose of Fig. 10 is to represent a gross idea on the process behind grain refinement. It must be noted that due to short interaction time of order of ns, the dislocations created by LSP cannot move far, [59] resulting in tangled dislocation structures [60]. Aggregation of dislocations can lead to formation of dislocation walls and a less probability in annihilation of dislocations of opposite configuration to reduce the strain energy. Dislocation walls can change crystal orientation [57], contributing towards sub grain formation.

Interaction of MT can lead to phase transformation such as Deformation Induced Martensites (DIM) in the case of low SFE material. Interaction of MT and DIM can lead to formation of nanocrystalline size of the order of few tens of nanometre [61]. Microstructure response and grain refinement because of shock waves were categorized in to sub micron and nano meter category [62]. Lu et al. have elaborated the refinement mechanism of commercially pure titanium due to shock wave by multi directional mechanical twin-mechanical twin (MT-MT) intersection in case of sub

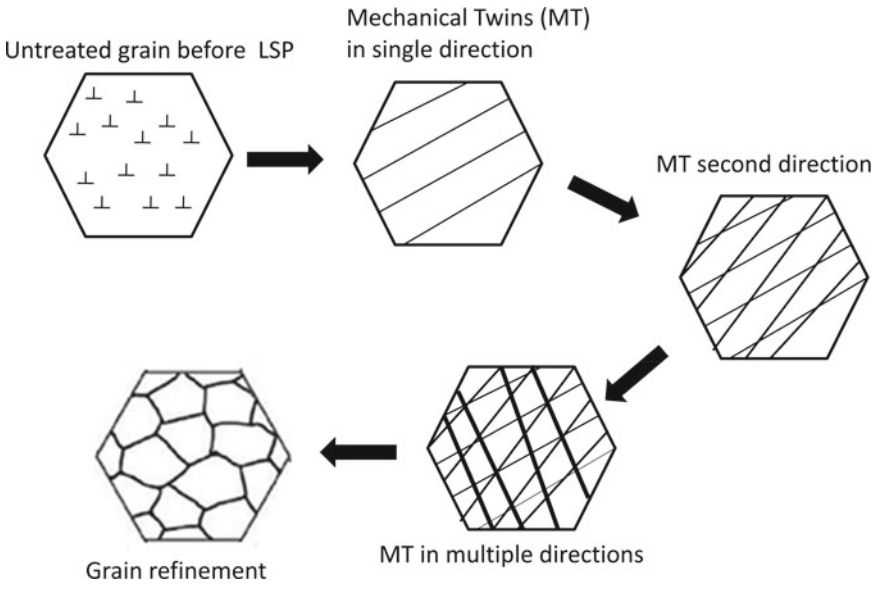

Fig. 10 Schematic of grain refinement mechanism

micron level grains and MT and dislocation wall (DW) intersections for nanometer scale [63, 64]. In materials like SS316 DIM is not always formed by LSP while it is seen for SS304. Here again SFE of the material plays a significant role in the formation of DIM. Lower the SFE, formation of martensite phase from austenite phase can be seen [64]. Particularly in low SFE austenitic steel deformation twins plays significantly in DIM formation [56]. Evidence for microstructure transformation can be obtained from SEM, TEM and Phase analysis using XRD profiles. Qualitative information on microstructure changes can also be inferred from optical microscopy.

4.2 X-ray Diffraction Analysis

Besides lattice parameter, X-ray diffraction analysis can reveal rich information on the phase changes and microstructure modifications that has occurred on the materials which has undergone plastic deformation. For example presence of DIM in austenitic steels can be seen as occurrence of BCC peaks along with austenitic FCC peaks on the xrd profile analysis. A reasonable estimate on the volume fraction of martensite can be arrived at using xrd profile analysis. Figure 11 shows the xrd profile of peened alloy D9 compared with annealed specimen. It can be seen that no DIM peaks are seen in the specimen while Karthik & Swaroop [65] have reported presence of martensitic phase in AISI 321 steel by laser peening without coating. Both presence and absence of DIM due to LSP can be seen in literature [61, 66, 67]. XRD not only reflects

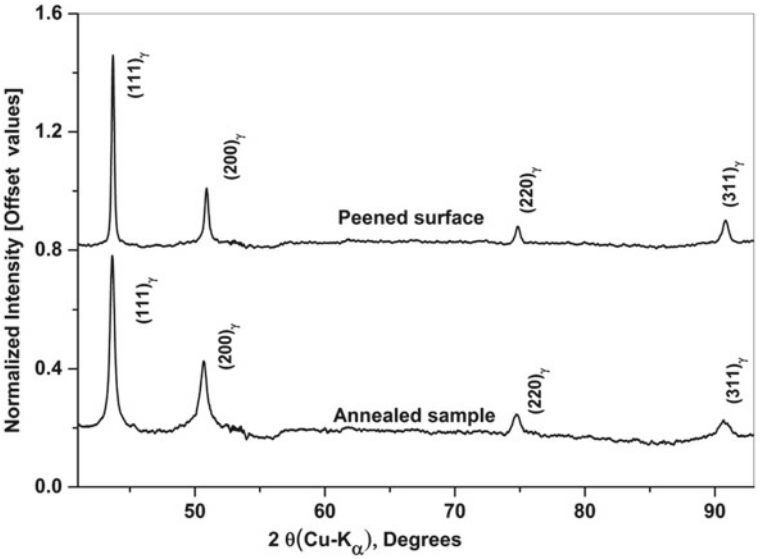

Fig. 11 XRD profile of peened and annealed alloys D9 [48]

the phase changes but also the peak shifts, change in Full Width Half Maximum (FWHM represented as β) of the peaks are an indication of presence of compressive or tensile stress and microstructure modifications that has resulted due to plastic deformation. Deformation induces changes in lattice spacing's and hence resulting in peak shifts [65], while nano size sub-grains formation results in peak broadening. With FWHM of xrd peaks it is also possible to estimate crystallite size and micro strain by Scherer's formula [68]. A plot of sinθ Versus β cosθ yields a straight line where the slope represents the strain and with y intercept it is possible to arrive at crystallite size. It must be pointed out that appropriate correction for instrument broadening must be taken in to account before calculations. It is also possible to estimate the dislocation densities by modified Williamson Hall method [69] using lattice micro strain obtained using scherer's formula.

4.3 Hardness

Change in hardness gives a direct indication of the plastic deformation and for LSP, this hardness would exhibit a decreasing trend as a function of peening affected depth. Hardness is generally measured by hardness tester with suitable load to make an indentation on the surface. Hardness as function of depth is profiled by repeatedly measuring hardness at constant distance on the cross section of the peened sample from surface. Generally distance interval of hardness measurement is maintained to be greater than 2.5 times the average diagonal length of the indent impression of the

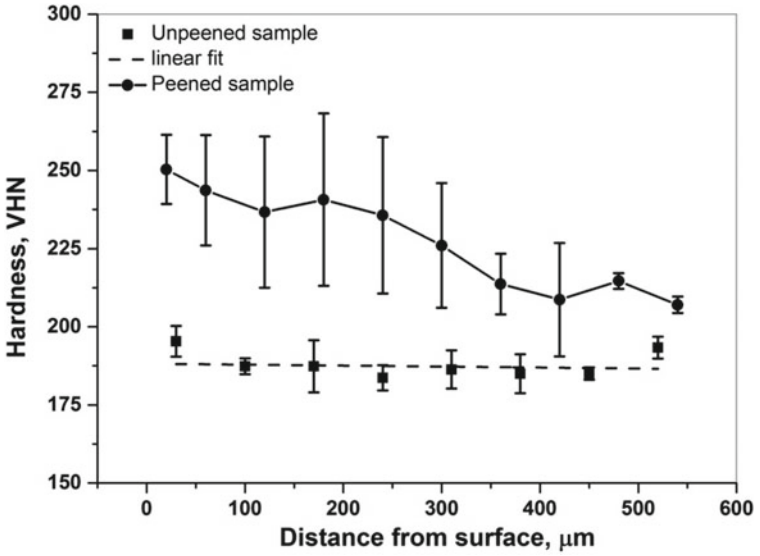

Fig. 12 Hardness profile of the cross section of the peened and unpeened sample with linear fit shown for unpeened sample [48]

hardness indenter [70]. Constant spatial interval in measurement is to ensure that every new measurement is not within the sphere of influence of previous measurements. One such plot of hardness as the function of depth for laser shock peened sample is shown in the Fig. 12. Under the investigated peening parameter [48] it can clearly be seen that the hardness has increased considerably when compared to unpeened sample. For the sample considered, shown in Fig. 12 the increase in surface hardness amounted to ~32%.

Characterizations such as hardness testing, RCS measurement and structural profile by XRD and microstructure evaluation are general techniques adapted to identify and freeze the peening parameters to achieve the targeted material property enhancement. Targeted objective could be anything such as to improve corrosion or fatigue resistance, wear properties etc., but the exercise begins with identification of the experimental parameters to achieve the goals. As briefed in earlier sections, parameter optimization involves, choosing laser energy, wavelength, pulse width, repetition rate, interacting laser spot diameter, laser spot overlap, and pulse density. Besides above said parameters it is even studied the role of scanning direction, scanning patterns, coaxial water flow and water flow from sides on the peening [71–73]. Therefore it is imperative to optimise the parameters to achieve efficient peening effects.

5 LSP Effect on Mechanical Properties of Metals and Alloys

5.1 Fatigue Life Enhancement

It is clearly seen that, LSP introduces RCS, modifies surface and subsurface microstructure, induces work hardening, and increases the hardness, yield stress and ultimate tensile stress. Mechanical properties such as fatigue and fretting fatigue, tensile properties can be enhanced by such modifications. In one of our study [7] we have showed that LSP increases the fatigue life of SAE9260 (C: 0.56–0.64, Si: 1.5–1.8, Mn: 0.7–1.0, S: $\leq$ 0.035, Bal: Fe) spring steel for automobile applications. We have also compared the performance of the shock peened spring steel with shot peened (SP) spring steel and showed that LSP treated specimen exhibited better performance than the shot peened. It has been observed that change in surface roughness of the samples due to both the process deferred, with shot peened specimen showing larger surface roughness. Higher roughness by itself can be detrimental under actual operating conditions that can lead to failure of the specimen and it has also been observed in one of our experimental sample. Surface roughness of the LSP and shot peened samples are shown in Fig. 13. In the figure BM stands for base metal and SP for shot peening.

After subjecting the steel to LSP & SP, fatigue life was determined by 150 kN servo- hydraulic UTM in three-point bend loading configuration as shown in Fig. 14. The results are tabulated in Table 2 . It is not just that LSP improved the fatigue life

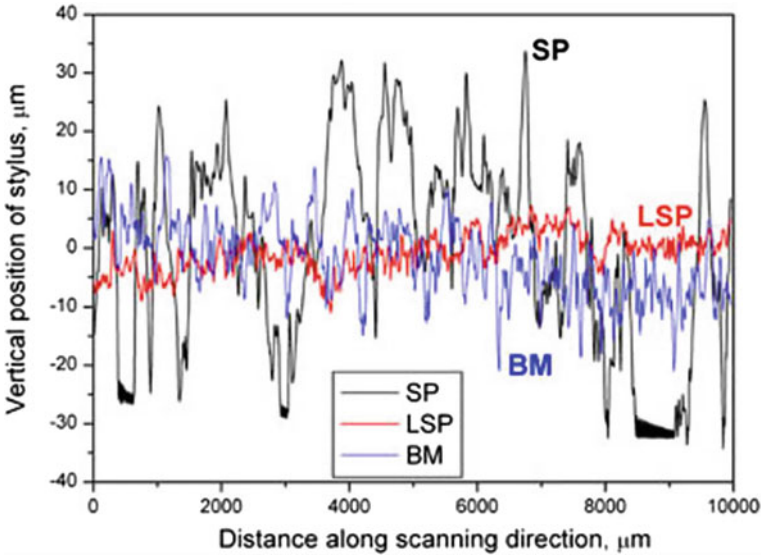

Fig. 13 Surface roughness comparison of shot peened (SP), LSP and base metal [15]

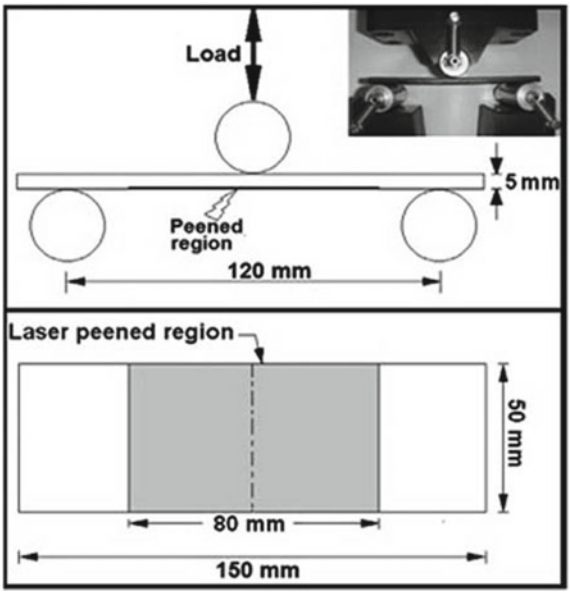

Fig. 14 Schematic of three point bend testing with actual photo as insert [7] (Reprinted with Permission from Elsevier, 2012)

Table 2 Comparison of fatigue life of unpeened, shot peened and LSP treated samples.

Unpeened (x 10^5cycles)	Shot Peened (x 10^5cycles)	Laser Shock Peened (x 10^5cycles)
0.85	19.15	109
0.82	15.3	104
1.25	9.21	112
All the specimens failed	All the specimens failed	None of the specimen failed

of the spring steels, in an another study we even demonstrated that life extension of the spring steel which has undergone 50% of its life cycle can be rejuvenated by LSP and its service life can be effectively extended [8].

Fretting fatigue of the turbine blades of low pressure steam turbines of thermal power plants were improved by LSP. Blades made of martensitic steel DINXR30Cr13(C:0.18–0.22, Cr;12–13, Ni:0.62, Mn: $\leq$ 0.7, Si: $\leq$ 0.5 and Fe: Bal) and Ti6Al4V (Al:5.8–6.1, V:3.9–4.1, Ti: Bal) experiences high rotation speeds (~3000 rpm) and the fir tree shape blade roots are subjected to centrifugal loading and oscillatory behaviour due to rotation of turbine and steam pressure respectively, leading to fretting fatigue at the contact zones of root and hence causing crack initiation and propagation and finally the failure of the component. As an industrial practice the roots of the blades are shot peened but not without disadvantages due to surface roughness as stated earlier. LSP of the blades were tried at root and it was realised that resistance to fretting fatigue has increased [9].

5.2 LSP on Stress Corrosion (SC) and Inter Granular Corrosion (IGC)

Stress corrosion and resulting cracking (SCC) occurs when a susceptible material with tensile stress is exposed to any corrosive environment as shown in Fig. 15. SCC is prevalent in steam generator tubes, heat exchangers and fuel clad tubes of nuclear power generators. Chemical and petrochemical industries too face SCC related problems leading to costly replacements of affected components. LSP seems to be a viable solution for enhancing the resistance to stress corrosion and inter granular corrosion cracking's (IGC). Machining activities done on the component during fabrication stages, leaves behind tensile stress, besides making the surface sensitive to electro chemical activity, as a result the surface becomes more susceptible to SCC. Primary effect of LSP is to introduce RCS, as this alleviates the tensile stress on the surface which is one of the three contributing factor for SCC, hence material acquires enhanced resistance to SCC. One such study on SS304L [10, 11] (C:0.02, Cr:18: Ni:10.55, Mn:1.2, Si:0.28, Mo:0.277, S: 0.001, P: 0.015, and Fe: Bal) is shown here as an example. In this study the SS304L was subjected to LSP at different peening parameters and evaluated for resistance to SCC by exposing the peened surface to boiling solution of $MgCl_2.6H_2O$ (155 $\pm$ 1 °C) for about 8 h (in accordance with ASTM G36 [74]) at the highest peening laser energy the SCC tested specimen displayed crack free surface as shown in Fig. 16.

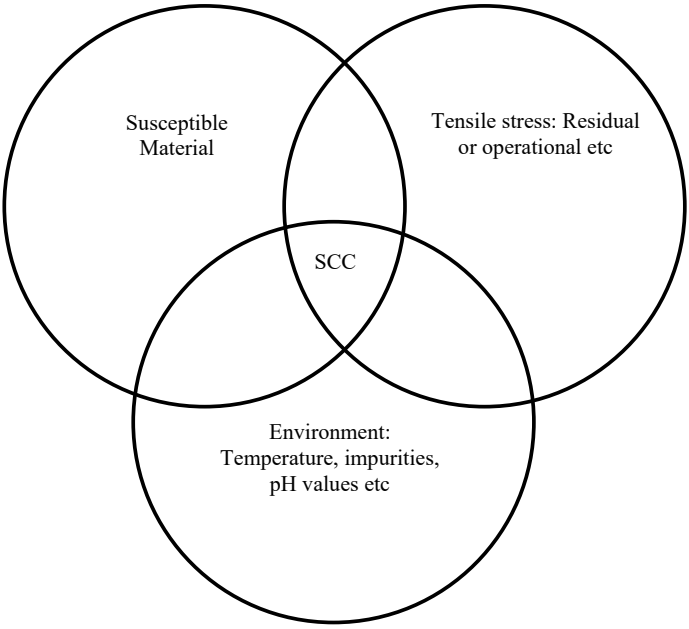

Fig. 15 Schematic representation of three contributing factors for stress corrosion

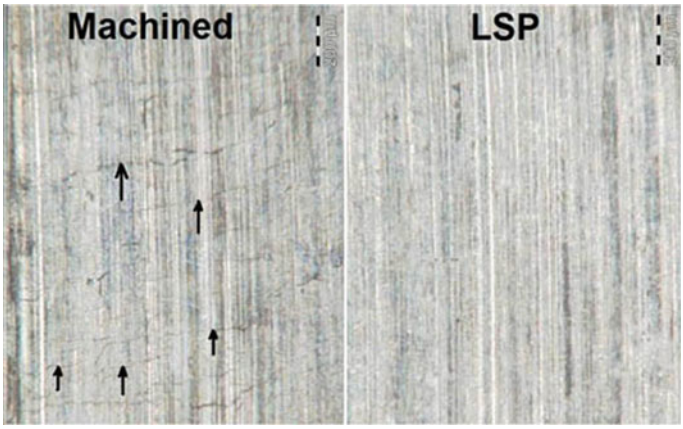

Fig. 16 SCC tested sample, unpeened/machined portion shows cracks while it is absent in LSP treated portion [10]. (Reprinted with Permission from Springer Nature, 2016)

Just as RCS due to LSP is applied to improve SCC resistance, microstructure modification due to LSP is explored in improving the resistance to IGC. LSP is known to introduce mechanical twins, high dislocation densities and other defects which finally results in nano grain formations. This feature is exploited to circumvent IGC. IGC is caused by inter granular formation of chromium rich carbides resulting in depletion of chromium in the regions adjacent to grain boundaries, and this process is called sensitization. LSP is known to produce nano grain formations which effectively does the fragmentation of inter granular network of chromium rich carbides and hence can enhance the resistance to IGC. In one such study on SS304L [12] it was shown that enhancement in resistance to IGC on triple peened SS304L. Triple peening is nothing but achieving higher laser pulse density per square mm. Sacrificial coating applied on the substrate before peening, gets torn off after specific number of pulses, this imposes a limitation on pulse density (pulses per mm^2). In triple peening, a given area is peened three times. After peening the given area with specific overlap and scan rate, the damaged sacrificial coating is removed and fresh coating is applied. Second round of peening is done on the same surface under the same parameters and the process is repeated so forth. It was proved beyond doubt that micorstructure modification due to LSP can be effectively used in suppressing the IGC.

5.3 Thermal Transport Due to LSP

Heat is transported inside the metals/alloys by means of electrons and phonons. Phonons are the quantum of energy associated with lattice vibrations just as photons for light energy. Transport of thermal energy in the material can be evaluated by its thermal conductivity k (W/m-K) or thermal diffusivity α (m^2/s) and these parameters

are connected by the relation Eq. 5.

$$\alpha = \frac{k}{\rho c_p} \tag{5}$$

Where c_p is isobaric specific heat capacity (J/kg-K), ρ is the density (kg/m^3). C_p & ρ can be estimated/measured at different temperatures as per ASTM E1269 – 11 standards & ASTM E228-17 standard respectively [75, 76]. Thermal Diffusivity (TD) can be measured directly using commercially available laser flash analyser (LFA) [77, 78]. LFA instrument, fires a laser pulse of appropriate energy and pulse width on the rear side of the sample of appropriate thickness. Temperature raise on the other side of the sample as a function of time is monitored by an IR detector maintained at cryogenic temperature by liquid nitrogen. A plot between temperature raise in terms of detector signal voltage Vs time is recorded and a plot is shown in Fig. 17 The plot is fitted with standard models on heat conduction in bulk material to evaluate the thermal diffusivity of the sample under test. In Fig. 17 continuous line shows signal recorded by the detector of LFA instrument and dashed line shows the theoretical model fit. From the following equation TD α can be evaluated.

$$\alpha = \frac{0.1388L^2}{t_{0.5}} \tag{6}$$

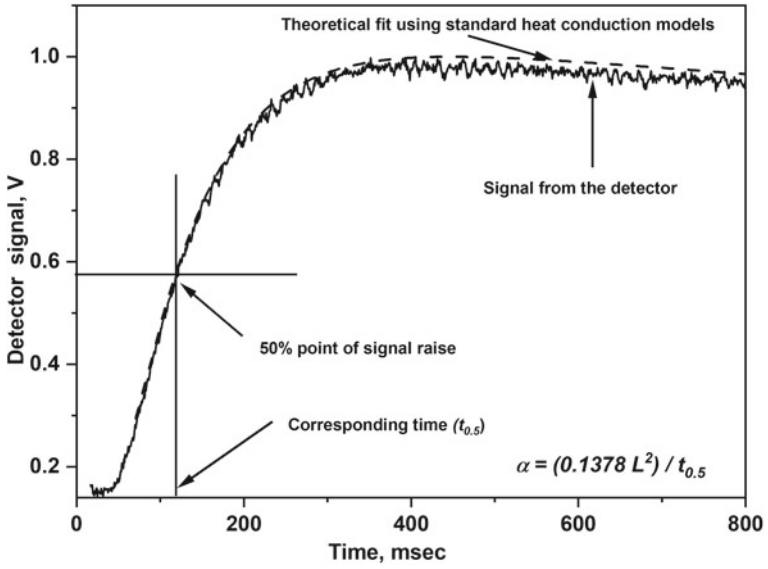

Fig. 17 IR detector signal and theoretical fit from the LFA instrument in measuring the TD of the sample

where $t_{0.5}$ is the time taken by the signal to reach half its maximum height and L is the sample thickness. The physical meaning behind thermal diffusivity can be understood as the propagation speed of heat when temperature changes over time [79]. When the material is not plastically deformed or when it is stress free it exhibits a TD which would be different when compared with that of its plastically deformed state. LSP process introduces RCS and microstructure modification resulting in variations in lattice parameters. Changes in lattice parameter and more grain boundaries due to nano grain formation due to plastic deformation can effectively scatter the thermal carriers resulting in reduced mean free path, which in turn can decrease the thermal diffusivity of the treated material. A drop in thermal diffusivity was observed for laser shock peened alloy D9 and the Fig. 18 shows the TD variation of shock peened and annealed alloy D9. A maximum of 4.6% decrease at 300 ^{0}C and an average decrease of 3.4% $\pm$ 0.77% in thermal diffusivity over the range of 25 to 700 ^{0}C was observed for peened sample when compared with unpeened sample. The variation is subjected to the magnitude of deformation that has taken place due to chosen peening parameters. In general it is evident that TD can be altered by plastic deformation. Role of plastic deformation towards thermal property modifications is an interesting area in which there is scarcity in research publications.

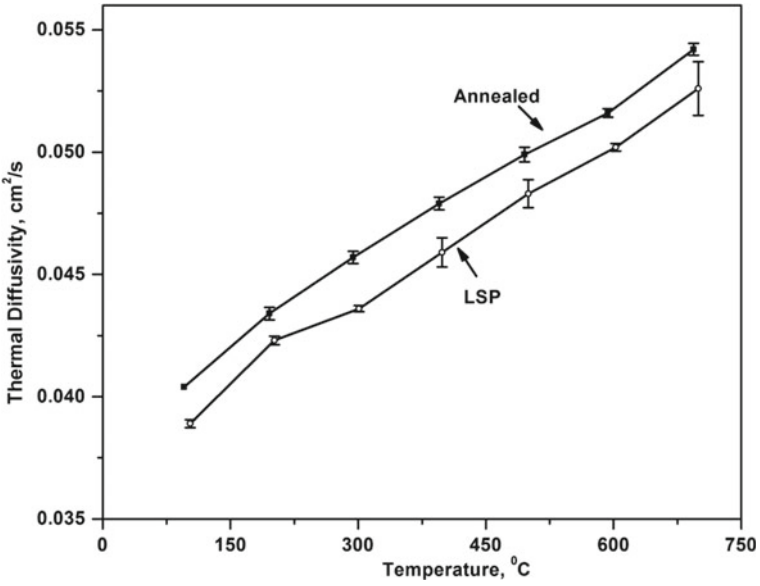

Fig. 18 Comparison of TD variation of annealed and peened alloy D9 [48] (Reprinted with Permission from Taylor and Francis, 2020)

6 Variants of LSP Process

Paint less peening also called as laser peening without coating (LPWC) is a variant of peening process in which no sacrificial coating is employed, thereby eliminating issues associated with application of sacrificial coatings such as poor adhesion, tearing and matching acoustic impedance with substrate. In peening without coating, laser with high repetition rate is employed [80]. It needs proper peening parameter optimisation in order to eliminate surface melting. Generally peening without coating is done under water, where substrate is in immersed condition. Since absorption of Nd:YAG laser wavelength (1064 nm) is high in water, Second harmonic of ND:YAG laser (532 nm- Green colour) is preferred for underwater peening or LPWC[40]. Yuji sano et al. [40] has reported a RCS to a depth exceeding 1 mm in type 304 and 316L austenitic steel by LPWC. Extended fatigue life and resistance to SCC for sensitized austenitic steel and nickel based alloys by peening without coating has also been reported by Yuji sano et al. [81].

Warm laser peening (WLSP) is another peening process, in which samples are maintained at higher temperature while undergoing LSP. Liao et al. [82, 83] has shown that with WLSP it is possible to bring highly dense nanoscale precipitates and dislocations in AA6061 alloy. They have concluded that WLSP influences the nucleation rate by decreasing chemical driving force.

Coupling laser light to the fibre optics is a generally adapted technique to transport the laser beam to target where direct line of sight access may not be possible. Coupling high energy short pulse width laser such as the one used for LSP to an optical fibre is a difficult task due to the very large intensities of laser light. To couple the laser beams to fibre it has to be focussed to a small diameter such that it fall within the acceptance angle and well within the core diameter of the optical fibre. Due to high energy, short pulse width and tighter spot diameter due to focussing intensity at the focal plane could be of order of few GW/cm^2 Fig. 6 and that can create air break down, making it difficult to couple LSP lasers to fibres. Further, fibre core diameter is of order of few hundred microns, and lasers with such intensity can invariably damage the fibres. However, with innovative idea of using [84, 85] a beam homogenizer to make multiple focal spots was adapted to distribute the laser intensity and then couple it to 1.5 mm core fibre. One such system of 20 MW peak power at the output end of the fibre was used for LSP on nuclear plant components [81]. It is envisaged after research study that fibre coupled lasers as mentioned above are potential candidate for strategic application to in-service preventive maintenance and rejuvenation of aged nuclear reactors for effectively preventing SCC [81, 82, 84–86]. LSP to reactor core shrouds of actual nuclear plants are being applied since 1999 in Japan [85].

Austenitic steel pipes used in corrosive environments experiences SCC in its inner surfaces. Employing LSP to the inner walls of the pipes can alleviate the SCC problem, however, LSP of interior of pipes is a challenging task, it is even more challenging, when the diameter of the pipes are small. Manoeuvring the laser for LSP by bending optics and focusing it to the inner walls of pipes needs lot of space for mechanical mounts; this limits the LSP application to the cylindrical geometry

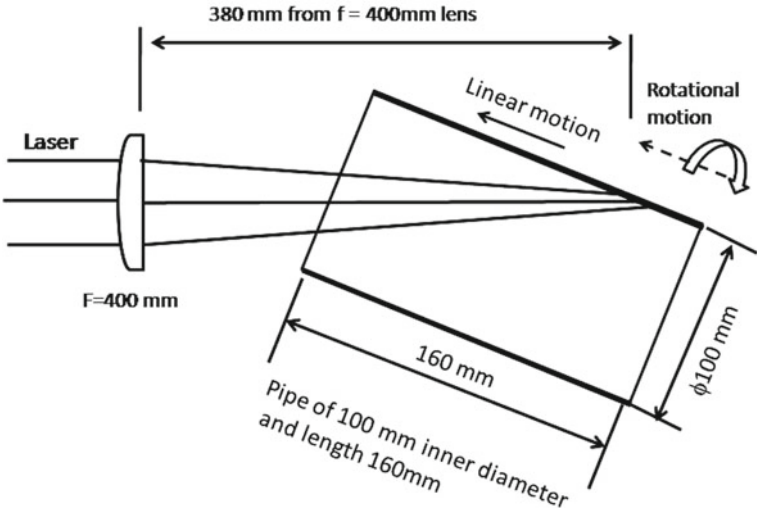

Fig. 19 Configuration to peen interior of 100 mm diameter tube using 400 mm focal length lens at angle of incidence of 62°

work pieces. This issue can be resolved partially by employing oblique angle of incidence peening as shown in Fig. 19. Peening length of the pipes is limited by its diameter. By peening SS304L pipe of 100 mm diameter at 62° angle of incidence, using 400 mm focal length lens, a peening length of 160 mm from the entrance of the pipe was achieved. Peening was done by alternately rotating the pipe by 360° at specific angular speed of few degrees/second and one linear motion (mm/s) till the required length is peened. Rotational and linear motions are indicated in Fig. 19. The peening produced RCS of 280 MPa in along longitudinal and 160 MPa in transverse directions. Peening affected depth was 0.480 mm on either direction. It was also shown that such oblique peening increased the resistance for SCC for the pipe. Around 25% of area was SCC affected for unpeened specimen and it was only 1–2% for oblique angle peening [10]. Some corollary studies such as effect on LSP due to scanning direction while peening and water flow (transparent overlay) configuration were also pursued to enrich the peening process. It was shown that material response is sensitive to peening direction [71, 72]. Coaxial water flow for transparent layer was studied in order to circumvent unstable and lack of flatness in layer thickness and in water flowing sideways configuration [73].

Besides the above said improvements to the LSP, innovative upgrades such as WLSP, LPWC, oblique incidence peeing, hybrid peening is evolving with a promise of attractive benefits. In hybrid peening LSP is coupled with some other laser based material processes. In one such process continuous wave Nd:YAG laser is used to fill the cracks caused due stress corrosion on SS304L by selectively and precisely melting the crack up to its depth and subsequently subjecting the so treated to sample to LSP. Besides refurbishing the cracks, tensile stress is also induced by melting thereby

bring in tensile stress which is a contributing factor for SCC. By shock peening the treated surface tensile stress is eliminated and compressive stress is induced. With this technique it was demonstrated that SC affected component can be rejuvenated [11]. Another hybrid process is peening is coupled to laser Additive Manufacturing (AM) where layer by layer AM is followed by LSP. After building each layer in AM the layer is subjected to LSP, in order to offset the stress distribution due to thermal process of AM and to improve the mechanical strength of the AM printed objects [87, 88].

As per author's view, though the LSP is known since 1960's its adaption in shop floor of the industries is not that encouraging except for few giant industries like aerospace. Primary reason being the cost involved in capital investment on laser system and associated characterisation equipments may not be attractive for industries. Further, evolving a process procedure and subsequent quality assurance certification can be tedious and time consuming process to ensure the quality of the LSP processed end product. LSP application to suit the industry specific need also involves multi disciplinary team of skilled workforce competent in understanding different branches of science & engineering such as laser physics, plasma physics, electronics, mechanical engineering, instrumentation and metallurgy. Though it may cost relatively less once the technique is established for specific application, but establishing it may be a problem which may need meticulous effort.

7 Summary

An effort to present bird's eye view of the LSP technology is attempted in this chapter. Since realization of laser in 1960's, application of laser to generate shock wave and to use it to modify the material properties has been explored in length and breadth. LSP technique has spread its tentacles in improving the material property of many metals and alloys for different applications. An effort has been made to explain the LSP process, identify and optimize the process parameters for best output results. Significance of LSP parameters such as wavelength, pulse width, laser spot size and workstation parameters were elaborated. Importance of sacrificial coating and transparent overlay to augment the pressure pulse magnitude and duration is dwelled upon. LSP effect on material property such as, fatigue, corrosion and thermal transport were demonstrated with example. Finally variants of LSP such as peening without coating, oblique peening and warm laser peening were highlighted. Conscious effort has been made to supplement the chapter with adequate literature to enrich the text and to encourage further reading for the interested readers.

Acknowledgements Author would like to express his sincere thanks to the editors Dr. Jagdheesh and Dr. Pathak for inviting me to contribute a chapter for the book. Author also would like to deeply appreciate and acknowledge his colleagues at RRCAT, Indore, India for their support given to him in not only to design and develop pulsed Q-switched Nd:YAG laser exclusively for peening purpose but also for setting up peening facility and subsequent LSP related activities for more than a decade.

References

1. Maiman, T.H.: Stimulated optical radiation in ruby. Nature **187**, 493–494 (1960)
2. Silfvast, W.T.: Laser Fundamentals, 2nd edn. Cambridge University Press (2004)
3. Davis, C.C.: Lasers and Electro-Optics, 2nd edn. Cambridge University Press (2014)
4. Skeen, C.H., York, C.M.: Laser induced "blow off" phenomena. Appl. Phys. Lett. **12**, 369 (1968)
5. Gregg, D.W., Thomas, S.J.: Momentum transfer produced by focused laser giant pulses. J. Appl. Phys. **37**, 2787–2789 (1966)
6. Peyre, P., Fabbro, R., Merrien, P. et al: Laser shock processing of Aluminium alloys. Application to high cycle fatigue behaviour. Mater. Sci. Eng. A **A210**, 102–113 (1996)
7. Ganesh, P., Sundar, R., Kumar, H., et al.: Studies of laser peening on spring steel for automotive applications. Opt. Laser Eng. **50**, 678–686 (2012)
8. Ganesh, P., Sundar, R., Kumar, H., et al.: Studies on fatigue life enhancement of pre-fatigued spring steel specimens using laser shock peening. Mater. Des. **54**, 734–741 (2014)
9. Pant, B.K., Sundar, R., Kumar, H. et al: Studies towards development of laser peening technology for martensitic stainless steel and titanium alloys for steam turbine applications. Mater. Sci. Eng. A **587**, 352–358 (2013)
10. Sundar, R., Ganesh, P., Sunil Kumar, B., et al.: Mitigation of stress corrosion cracking susceptibility of machined 304L stainless steel through laser peening. J. Mater. Eng. Perform **25**, 3710–3724 (2016)
11. Gupta, R.K., Sundar, R., Sunil Kumar, B., et al.: A hybrid laser surface treatment for refurbishment of stress corrosion cracking damaged 304L stainless steel. J. Mater. Eng. Perform. **24**, 2569–2576 (2015)
12. Gupta, R.K., Sunil Kumar, B., Sundar, R., et al.: Enhancement of intergranular corrosion resistance of type 304 stainless steel through laser shock peening. Corros Eng. Sci. Technol. **52**, 220–225 (2017)
13. Hong, X., Wang, S., Guo, D., et al.: Confining medium and absorptive overlay: their effects on a laser-induced shock wave. Opt. Laser Eng. **29**, 447–455 (1998)
14. Peyre, P., Berthe, L., Vignal, V., et al.: Analysis of laser shock waves and resulting surface deformations in an Al–cu–li aluminum alloy. J. Phys. D Appl. Phys. **45**, 335304 (2012)
15. Sundar, R., Ganesh, P., Gupta, R.K. et al.: Laser shock peening and its applications: a review. Lasers Manuf. Mater. Process. **5**, 270–282 (2019)
16. Fairhand, B.P., Clauer, A.H., Jung, R.G.: Quantitative assessment of laser-induced stress waves generated at confined surfaces. Appl. Phys. Lett. **25**, 431–433 (1974)
17. Peyre, P., Berthe, L., Scherpereel, X., et al.: Experimental study of laser-driven shock waves in stainless steels. J. Appl. Phys. **84**, 5985–5992 (1998)
18. Sundar, R., Kumar, H., Kaul, R., et al.: Studies on laser peening using different sacrificial coatings. Surf. Eng. **28**, 564–568 (2012)
19. Fabbro, R., Fournier, J., Ballard, P., et al.: Physical study of laser-produced plasma in confined geometry. J. Appl. Phys. **68**, 75–784 (1990)
20. Ding, K., Ye, L.: Laser shock peening performance and process simulation. WoodHead publishing in materials, Woodhead Publishing Limited and CRC Press LLC (2006)
21. Wu, B., Shin, Y.C.: A self-closed thermal model for laser shock peening under the water confinement regime configuration and comparisons to experiments. J. Appl. Phys. **97**, 113517 (2005)
22. Wu, B., Shin, Y.C.: A one-dimensional hydrodynamic model for pressures induced near the coating waterinterface during laser shock peening. J. Appl. Phys. **101**, 023510 (2007)
23. Wu, B., Shin, Y.C.: Two dimensional hydrodynamic simulation of high pressures induced by high power nanosecond laser matter interactions under water. J. Appl. Phys. **101**, 103514 (2007)
24. Cao, Y., Shin, Y.C.: Shock wave propagation and spallation study in laser shock peening. J. Eng. Mater. Technol. **132**, 041005–1–041005–8 (2010)
25. Wei, X.L., Ling, X.: Numerical modeling of residual stress induced by laser shock processing. Appl. Surf. Sci. **301**, 557–563 (2014)

26. Ayed, M., Frija, M., Fathallah, R.: Prediction of residual stress profile and optimization of surface conditions induced by laser shock peening process using artificial neural networks. Int. J. Adv. Manuf. Technol. **100**, 2455–2471 (2019)
27. Gace, S.S.: Molecular dynamics simulation of shock waves in laser-material interaction. Ph.D thesis, Iowa State University (2009). https://lib.dr.iastate.edu/cgi/viewcontent.cgi?article=1712&context=etd. Accessed 13 Aug 2021
28. Ren, Z., Ye, C., Dong, Y.: Molecular dynamic simulation of surface amorphization of NiTi under dynamic shock peening. In: Proceedings of the ASME 2015 international manufacturing science and engineering conference. MSEC2015. June 8–12 2015, Charlotte, North Carolina, USA (2015). https://doi.org/10.1115/MSEC2015-9320
29. Peyre, P., Fabbro, R., Berthe, L., et al.: Laser shock processing of materials, physical processes involved and examples of applications. J. Laser Appl. **8**, 135–141 (1996)
30. Fournier, J., Ballard, P., Merrien, P., et al.: Mechanical effects induced by shock waves generated by high energy laser pulses. J. Phys. III Fr. **1**, 1467–1480 (1991)
31. Peyre, P.: Fabbro, R, "Laser shock processing: a review of the physics and applications." Opt. Quant. Electron. **27**, 1213–1229 (1995)
32. Massse, J.-E., Barreau, G.: Laser generation of stress waves in metal. Surf. Coat. Techno. **70**, 231–234 (1995)
33. Berthe, L., Fabbro, R., Peyre, P., et al.: Shock waves from a water-confined laser generated plasma. J. Appl. Phys. **82**, 2826–2832 (1997)
34. Liu, X., Du, D., Mourou, G.: Laser ablation and micromachining with ultrashort laser pulses. IEEE J. Quantum Electron. **33**, 1706–1716 (1997)
35. Noack, J., Vogel, A.: Laser-induced plasma formation in water at nanosecond to femtosecond time scales: calculation of thresholds, absorption coefficients and energy density. IEEE J. Quantum Electron. **35**, 1156–1167 (1999)
36. Fabbro, R., Peyre, P., Berthe, L., et al.: Physics and applications of laser shock processing of materials. SPIE 3888 (2000)
37. Berthe, L., Fabbro, R., Peyre, P., et al.: Wavelength dependent of laser shock-wave generation in the water-confinement regime. J. Appl. Phys. **85**, 7552 (1999)
38. Montross, C.S., Wei, T., Ye, L. et al.: Laser shock processing and its effects on microstructure and properties of metal alloys: a review. Int. J. Fatigue **24**, 1021–1036 (2002)
39. Hu, Y., Yao, Z.: Overlapping rate effect on laser shock processing of 1045 steel by small spots with Nd:YAG pulsed laser. Surf. Coat Techol. **202**, 1517–1525 (2008)
40. Sano, Y., Obata, M., Kubo, T., et al.: Retardation of crack initiation and growth in austenitic stainless steels by laser peening without protective coating. Mater. Sci. Eng. A **417**, 334–340 (2006)
41. Jiang, X.P., Man, C.-S., Shepard, M.J., et al.: Effects of shot-peening and re-shot-peening on four point bend fatigue behaviour of Ti–6Al–4V. Mat. Sci. Eng. A **468–470**, 137–143 (2007)
42. Statnikov, E.S., Korolkov, O.V., Vityazev, V.N.: Physics and mechanism of ultrasonic impact. Ultrasonics **44**, 533–538 (2006)
43. Srivastava, M., Tripathi, R., Hloch, S., et al.: Potential of using water jet peening as a surface treatment process for welded joints. Procedia Eng. **149**, 472–480 (2016)
44. Paul, S.P., Cammett, J.T.: The influence of surface enhancement by low plasticity burnishing on the corrosion fatigue performance of AA7075-T6. Int. J. Fatigue **26**, 975–982 (2004)
45. Delgado, P., Cuesta, I.I., Alegre, J.M., Díaz, A.: State of the art of deep rolling. Precis Eng. **46**, 1–10 (2016)
46. Soyama, H., Saito, K., Saka, M.: Improvement of fatigue strength of aluminium alloy by cavitation shotless peening. J. Eng. Mater. Technol. **124**, 135–139 (2002)
47. Prevey, P.S.: The effect of cold work on the thermal stability of residual compression in surface enhanced IN718. In: 20th ASM heat Treating Society Conference Proceedings, 9–12, Oct 2000, St.Louis, MO
48. Sundar, R., Sudha, C., Rai, A.K., et al.: Effect of laser shock peening on the microstructure, tensile and heat transport properties of Alloy D9. Lasers Manuf. Mater. Process. **7**, 259–277 (2020)

49. Cullity, B.D: Elements of X-ray diffraction, copyright 1956. Addison-Wesley publishing company, USA
50. Pineault, J.A, Belassel, M., Brauss, M.E.: X-ray diffraction residual stress measurement in failure analysis. In: Becker, W.T., Shipley, R.J. (Eds.), Failure Analysis and Prevention, ASM International, vol. 11, pp. 484–497. https://doi.org/10.31399/asm.hb.v11.a0003528
51. Noyan, I.C., Cohen, J.B., Iischner, B.: Residual Stress-measurement by diffraction and interpretation. Springer Series on Materials Research and Engineering. New York (1987)
52. Rossini, N.S., Dassisti, M., Benyounis, K.Y., et al.: Methods of measuring residual stresses in components. Mater Des. **35**, 572–588 (2012)
53. Yan, X., Wang, F., Deng, L. et al.: Effect of laser shock peening on the microstructures and properties of oxide-dispersion-strengthened austenitic steels. Adv. Eng. Mater. **20**, 1700641(1–8) (2018)
54. Fabbro, R., Peyre, P., Berthe, L., et al.: Physics and applications of laser-shock processing. J. Laser Appl. **10**, 265–279 (1998)
55. Hatamleh, O.: A comprehensive investigation on the effects of laser and shot peening on fatigue crack growth in friction stir welded AA 2195 joints. Int. J. Fatigue **31**, 974–988 (2009)
56. Nakada, N., Ito, H., Matsuoka, Y., et al.: Deformation-induced martensitic transformation behaviour in cold-rolled and cold-drawn type 316 stainless steels. Acta Mater. **58**, 895–903 (2010)
57. Li, X., Zhang, Y., Zhang, Q., et al.: Mechanism of grain refinement induced by laser shock processing in az31 magnesium alloy. J. Wuhan Univ. Technol.-Mater. Sci. **33**, 611–615 (2016)
58. Cao, J., Cao, X, Jiang, B., et al.: Microstructural evolution in the cross section of Ni-based superalloy induced by high power laser shock processing. Opt Laser Technol. **141**, 107127 (2021)
59. Gill, A., Telang, A., Mannava, S.R. et al.: Comparison of mechanisms of advanced mechanical surface treatments in nickel-based superalloy. Mater. Sci. Eng. A **576**, 346–355 (2013)
60. Kattoura, M., Mannava, S.R., Qian, D. et al.: Effect of laser shock peening on residual stress, microstructure and fatigue behaviour of ATI 718Plus alloy. Int. J. Fatigue **102**, 121–134 (2017)
61. Zhou, L., He, W., Luo, S., et al.: Laser shock peening induced surface nanocrystallization and martensite transformation in austenitic stainless steel. J. Alloys Compd. **655**, 66–70 (2016)
62. Lu, J.Z., Wu, L.J., Sun, G.F., et al.: Microstructural response and grain refinement mechanism of commercially pure titanium subjected to multiple laser shock peening impacts. Acta Mater. **127**, 252–266 (2017)
63. Hu, J., Lou, J., Sheng, H., et al.: The effects of laser shock peening on microstructure and properties of metals and alloys: a review. Adv. Mater. Res. Online: 2011-10-07. ISSN: 1662–8985, vols. 347–353, pp. 1596–1604
64. Lu. J., Hultman, L., Holmstrom, E., et al.: Stacking fault energies in austenitic stainless steels. Acta Mater. **111**, 39–46 (2016)
65. Karthik, D., Swaroop, S.: Influence of laser peening on phase transformation and corrosion resistance of AISI 321 steel. J. Mater. Eng. Perform **25**, 2642–2650 (2016)
66. Lim, H., Lee, M., Kim, P., et al.: Laser shock peening of AISI 304 stainless steel for the application to seawater desalination pump components. Desalin. Water Treat. **33**, 255–260 (2011)
67. Mordyuk, B.N., Milman, Y.V., Iefimov, M.O., et al.: Characterization of ultrasonically peened and laser-shock peened surface layers of AISI 321stainless steel. Surf. Coat. Technol. **202**, 4875–4883 (2008)
68. Suryanarayana, C., Norton, M.G.: X-ray diffraction—a practical approach, pp. 63–98. Plenum Press, New York (1998).
69. Williamson, G., Smallman, R., III.: Dislocation densities in some annealed and cold worked metals from measurements on the X-ray debye-scherrer spectrum. Philos. Mag. **1**, 34–46 (1956)
70. Howard, C.B.: Development of novel small scale mechanical tests to assess the mechanical properties of ex-service Inconel X-750 CANDU reactor components. Ph.D dissertation University of California, Berkeley (2018)

71. Kallien, Z., Keller, S., Ventzke, V., et al.: Effect of laser peening process parameters and sequences on residual stress profiles. Metals **9**, 655 (2019)
72. Xu, G., Luo, K.Y., Dai, F.Z., et al.: Effects of scanning path and overlapping rate on residual stress of 316L stainless steel blade subjected to massive laser shock peening treatment with square spots. Appl. Surf. Sci. **481**, 1053–1063 (2019)
73. Wang, H., Huang, Y., Zhang, W.: The study of laser shock peening with side-water spraying and coaxial-water feeding technology. Int. J. Lightweight Mater. Manuf. **1**, 102–107 (2018)
74. ASTM: G36 94(2018), Standard practice for evaluating stress-corrosion-cracking resistance of metals and alloys in a boiling magnesium chloride solution. In: ASTM International, West Conshohocken, PA (2018)
75. ASTM E1269 – 11: Standard test method for determining specific heat capacity by differential scanning calorimetry
76. ASTM E228 – 17: Standard test method for linear thermal expansion of solid materials with a push- rod dilatometer
77. ASTM E1461 – 13: Standard test method for thermal diffusivity by the flash method
78. Parker, W.J., Jenkins, R.J., Butler, C.P., et al.: Flash method for determining thermal diffusivity, heat capacity and thermal conductivity. J. Appl. Phys. **32**, 1679–1684 (1961)
79. Salazar, A.: On thermal diffusivity. Eur. J. Phys. **24**, 351–358 (2003)
80. Sano, Y., Akita, K., Sano, T.: A mechanism for inducing compressive residual stresses on a surface by laser peening without coating. Metals **10**, 816 (2020)
81. Sano, Y.: Quarter century development of laser peening without coating. Metals **10**, 152 (2020)
82. Liao, Y., Ye, C., Kim, B.-J., et al.: Nucleation of highly dense nanoscale precipitates based on warm laser shock peening. J. Appl. Phys. **108**, 063518 (2010)
83. Liao, Y., Ye, C., Cheng, G.J.: A review: Warm laser shock peening and related laser processing technique. Opt. Laser Technol. **78**, 15–24 (2016)
84. Schmidt-Uhlig, T., Karlitschek, P., Yoda, M., et al.: Laser shock processing with 20 MW laser pulses delivered by optical fibers. Eur. Phys. J. AP **9**, 235–238 (2000)
85. Yoda, M., Mukai, N., Sano, Y., et al.: Fiber-delivered laser peening system to improve mechanical properties of metal surface. WIT Trans. Eng. Sci. **33** (2001); WIT Press, www.witpress.com. ISSN 1743-3533
86. Zhu, J., Jiao, X., Zhou, C., et al.: Applications of underwater laser peening in nuclear power plant maintenance. Energy Procedia **16**, 153–158 (2012)
87. Kalentics, N., Boillat, E., Peyre, P., et al.: 3D laser shock peening – a new method for the 3D control of residual stresses in selective laser melting. Mater. Des. **130**, 350–356 (2017)
88. Madireddy, G., Li, C., Liu, J., et al.: Modeling thermal and mechanical cancellation of residual stress from hybrid additive manufacturing by laser peening. Nanotechnol. Precis. Eng. **2**, 49–60 (2019)

Laser Re-Melting of Atmospheric Plasma Sprayed High Entropy Alloy

Himanshu Kumar, Chandra Kumar, S. G. K. Manikandan, M. Kamaraj, and S. Shiva

1 Introduction

High entropy alloys (HEAs) is a novel class of material, composed of at least five primary elements in equiatomic or near equiatomic ratio between 5 at. % to 35 at. % of the chemical composition [1, 2]. In comparison to traditional alloys, high-element alloys have improved wear resistance and microhardness properties. However, wear application requires improvements to the qualities of the surface, such as reduced surface roughness, increased surface hardness, resistance to wear, corrosion resistance and free surface imperfections to improve component life. There have been numerous laser-based surface modification techniques developed in the last decade to improve these properties. These techniques include laser annealing [3], laser surface alloying [4], laser shock peening (LSP) [5], selective laser melting (SLM), laser remelting (LR) [6], laser metal deposition (LMD) [7] and laser micromachining [8–13]. In particular among the laser surface treatment techniques like LR is a promising technology to improve the properties of components by engineering the microstructure and releasing residual stress in contrast to traditional methods of surface treatment. While LR techniques have been extensively reported to enhance the surface properties, wear and corrosion properties of various alloy such as titanium alloy [14], aluminium alloy [15], 314L stainless steels [16] and nickel-based superalloy [4]

H. Kumar · C. Kumar · S. Shiva (✉)
Laboratory for Advanced Manufacturing and Processing, Indian Institute of Technology Jammu, Jagti, Jammu & Kashmir 181221, India
e-mail: shiva.sekar@iitjammu.ac.in

S. G. K. Manikandan
Indian Space Research Organization Propulsion Complex, Mahendragiri, India

M. Kamaraj
Department of Metallurgical and Materials Engineering, Indian Institute of Technology Madras, Chennai, India

J. Radhakrishnan and S. Pathak (eds.), *Advanced Engineering of Materials Through Lasers*, Advances in Material Research and Technology,
https://doi.org/10.1007/978-3-031-03830-3_5

applicable in various applications, only a few studies have reported the LR treatment of high entropy alloy [17–20].

LR approaches are more commonly used for engineering applications in several industries commercially. LR techniques utilize different source of laser such as Nd:YAG laser, CO_2 laser, diode laser and excimer laser. Laser source selection depends upon the efficiency, maintenance costs and laser system availability. LR of air plasma sprayed $FeCoCrNiAl_{0.5}$ HEA was reported by Jin et al. [17], The phase was found to be changed from FCC to BCC by using LR technique, which further results in an increasing hardness and reduced wear volume friction coefficient and wear depth. In addition, abrasive wear mechanism was exposed using ball on disc wear test [17]. A. Erdogan et al. has used the LR process at the electric current assistive sintered $CoCrFeNiAl_{0.5}Ti_{0.5}$ HEA and investigated the wear behaviour. X-ray diffraction revealed that the laser re-melted HEA had changed in phase results in improved hardness and superior wear resistance [19]. Doleker et al. explained the effect of laser remelting on the CoCrFeNiAlxTiy HEA oxidation behaviour, LR technique improves the oxidation resistance of Electric Current Assistant Sintered (ECAS) HEA by providing a more uniform, reduced oxide formation microstructure [20]. Zhang et al. investigated the corrosion behaviour of cast, annealed, and laser-remelted AlFeNiCoCuCr high entropy alloys in 3.5 percent NaCl solution, they revealed that the LR process provided the best pitting corrosion resistance among all three methods [21].

High entropy alloys are a class of alloys with a high entropy of mixing ($\Delta Smix \geq 1.5$) that are designed for use in extremely high-temperature applications. This means that the microhardness, wear resistance, oxidation resistance, and corrosion resistance of these alloys are maintained even when exposed to extremely high temperatures. This chapter discusses the LR processing of high entropy alloys, including a commonly used high entropy alloy in LR, as well as the effects of LR processing on microstructure, microhardness, and wear behaviour of high entropy alloys.

2 Evolution of Laser-Based Surface Modification

Surface modification using a laser in real time is an attempt to alter the surface of the specimen in order to increase the density, hardness, wear-resistance, and surface roughness of the sample in the application. Surface modification techniques were used to prevent failures from occurring on a component's surface as a result of wear, corrosion, and friction, thereby postponing premature failure and extending the service lifetimes of components. Because of the diverse nature of laser-based surface modification techniques, they may be applied to a wide range of materials, making them particularly well suited for use in the field of surface engineering. The use of laser-based surface modification techniques improves the resilience of components to common surface flaws such as wear, corrosion, and high temperature [2, 3]. Additionally, the same surface modification technology can be applied to the reclamation of components, the correction of processing errors, and the restoration

of dimensional loss in parts caused by wear. The potential of laser-based surface modification techniques to modify surfaces is what industries are attracted to. The laser surface modification technique was initially developed by researchers in order to disperse metal powders with low melting temperatures (below 400 °C) onto a substrate by heating the powder with a laser. As a result, laser surface alloying (LSA) was developed as a method of altering the chemical composition of materials in order to adjust their microstructure and surface qualities [22, 23]. This procedure consists of heating the material's surface with a high-power energy beam in order to disseminate the extra alloying elements on the surface of the substrate, followed by quick solidification in order to improve surface attributes such as wear and corrosion resistance. When it comes to generating a high-quality alloy layer on a substrate, laser process factors such as laser power, scanning speed, and spot diameter are critical. Excessive melting of the substrate material and evaporation of low melting point alloying materials as a result of increasing laser power density result in undesirable surface qualities and inadequate metallurgical connection between the substrate and the alloyed layer [24]. When utilising laser surface alloying, the most significant drawback is that pores and cracks appear on the sample, which can be reduced even more by using post-processing techniques such as annealing [25].

Similarly, in the laser-based surface modification technology, laser cladding (LC) was brought to the attention for its crack-free surface, low dilution ratio, and refined microstructure. There are several advantages of laser cladding: reduced porosity, increased durability, lower thermal distortion, resistance to wear, corrosion and strong metallurgical bonding between cladded layer and substrate [26, 27]. Laser cladding includes the modification of the surface by changing the size, phase transition and chemical composition of the substrate. It uses a high energy laser beam to melt the thin powder layer deposited on the substrate surface and solidify it quickly. Rapid cooling inhibits low-melted metal powder evaporation, further reduces recrystallization and improves hardness. Laser process factors including laser power, scanning speed and laser spot diameter play a critical role in producing the high quality cladding layer, similar to laser surface alloying. Various laser based surface modification techniques were depicted in Fig. 1. The introduction of laser surface texturing (LST) entails removing materials from the surface of component in order to increase the friction, roughness and self-lubricating properties of the components used in the various application. LST is also utilised to improve the adherence between the coating and the substrate as a pre-processing approach before different coating processes [28]. LST technology has widely applied in the various area of application like zirconia implants used for improving wettability in biomedical application and laser textured silicone surface would improve the heat transmission during the nucleate pool boiling of water [29, 30].

In many applications, improvement of the desired surface characteristics without altering the specimen dimensions is preferred. Laser surface hardening (LSH) was developed in this agreement. Laser surface hardening is a sort of laser heat treatment used to improve surface hardness without altering its dimensions and chemical composition of the component. This technique uses ductile materials such as iron and steel components for the change of phases from bainite to martensitic, resulting in

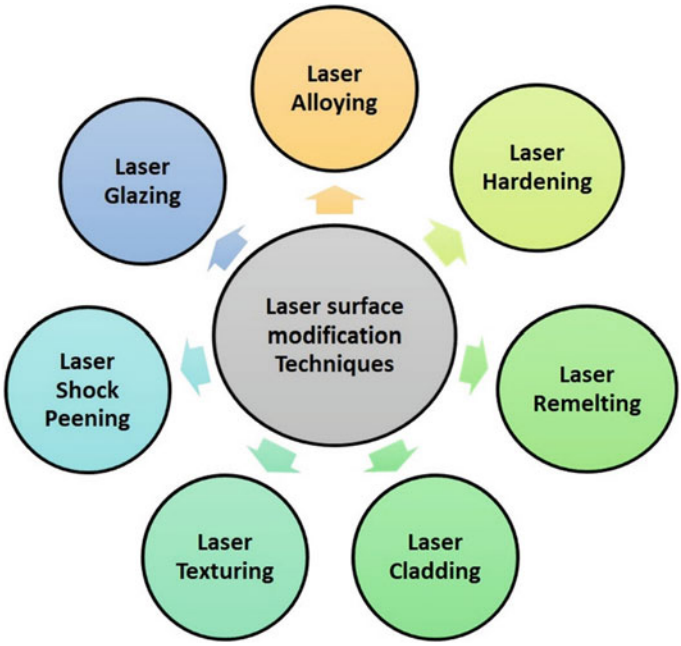

Fig. 1 Evolution of laser based surface modification techniques

enhanced hardness [31]. It uses a high-power laser beam to heat the surface and then self-quenching leads to changes in the microstructure and increased hardness. Laser surface hardening is prominent technique due to several benefits such as contactless heat treatment, unnecessary extra quenching media and automated processes, as compared to conventional heat treatment. This method is a fantastic alternative for heat treatment for automotive engine components such as camshaft [32].

In addition, laser shock peening (LSP) has been introduced in order to improve the surface properties of components such as ductility, improve fatigue life, enhance fatigue strength and prevent crack initiation and growth. LSP produces compressive residual stress without affecting the chemical composition and component dimensions to improve components' fatigue properties [33]. In this process, a high energy laser wave hit the sample and generates the shock waves. These shock waves can lead to persistent plastic deformation of the workpiece, which results in residual stress that is compressive in nature. Research into LSP is attracting attention because of its unique characteristics, which include contactless procedures, lower contamination, and the capacity to create more profound compressive residual stress. There are numerous automotive and aerospace components surface were laser processed in order to improve their service life and fatigue strength. Laser Glazing (LG) is another type of laser based surface modification method that uses a high energy laser beam to melt and quickly solidifies the surface of the component without changing the chemical composition. The sample surface is capable of producing a glassy finish like

bulk metallic glass with an amorphous and non-crystalline structure. LG enhances wear and corrosion resistance of both metals and ceramic materials [34–36]. LG technology can therefore be applied in places where the primary objective is a glassy surface with improved hardness and a high lubrication surface. A more controlled (amorphous or crystalline) homogeneous microstructure with less contamination can be achieved through the LG process. Recent studies show that optimising the laser process parameters such as slow scan speed and high laser power leads to a higher depth of fusion and prevents stress corrosion cracking [37]. Laser melting is the following and widely used laser-based surface modification technique (LR). In this process, a high energy laser beam melts the surface of the component and solidifies rapidly results in a change in the microstructure of material without changing the chemical composition. Laser remelting widely used to improve the wear resistance, hardness and corrosion resistance of the components and decrease the micro-cracks and pores present at the sample surface [38]. Among the various laser-based techniques discussed there are several advantages to laser remelting methods given as follow.

1. The LR approach improves the surface qualities without affecting the chemical components and dimension of the treated component [39].
2. LR technique widely employed to micro-polish medical implants to prevent bacterial adhesion and to produce a smoother surface on the implant surface [40].
3. The LR processing improves the thermomechanical characteristics of ceramics and metals by altering the microstructure of the material during rapid solidification [41].
4. By enhancing the diffusion rate of the coating, the LR process increases the adhesion between the coating and the substrate as well as the hardness of composite coatings [42].

Whenever it comes to improving the desired properties, the laser process parameters are extremely important. It is essential to optimise the laser power, spot diameter, scanning speed, and hatch spacing for remelting in order to prevent laser ablation. Laser ablation is useful in many situations, such as laser machining, laser cutting, and laser drilling operations, however it is not desirable in remelting operations.

3 Laser Material Interaction

The interaction of laser with materials is a key aspect of laser surface modifications. Various methods such as electron beam and laser beam can be applied in material processing. In contrast to laser beam irradiation, the electron beam possesses roughly the same absorption capacity, albeit the electron beam required expensive instrumentation and a vacuum to operate. Due to its efficient and unsophisticated instrumentation the laser attracts attention, with the same unit operating continuous wave (CW) and pulsed mode. The pulsed and CW laser have a varied influence

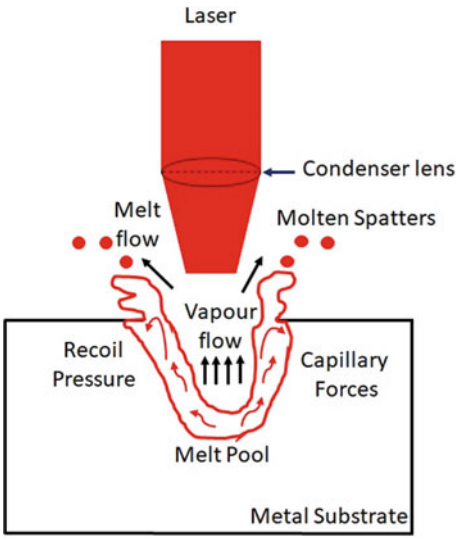

Fig. 2 Schematic representation of laser material interaction

on the material processing and can be intelligently selected for the intended process according to a suitable laser type based on the absorption coefficient of the materials. The laser source, optical resonator, beam reflectors, lens and specimen holding unit is part of a simple laser system. The industrial laser system, however, has an accurate laser guide system such as optical fibre suitable for complicated workwise. Safety measures are required to protect operators against laser beam exposure. A schematic illustration of the interaction between laser materials as seen in Fig. 2.

In laser-based surface modification techniques, laser materials interaction plays a vital role. The absorption of laser energy is crucial for any laser-based surface processing operations and the laser irradiance on the sample surface should be continuous. Two types of laser-material interaction are resonant and non-resonant. The generation of photons and localised heat are subject to resonant interactions. Interaction between laser material involves many processes, such as laser absorption, energy transfer to the lattice photon, and heat transfer in bulk. Heat transfer occurs from the surface to the bulk of the material establishing the thermal gradient and melting.

Furthermore, the Marangoni flow begins inside the molten pool and melt convection takes place due to capillary action. Then molten pool deformation arises by recoiling pressure generated due to declining vapour at melt surface followed by material expulsion, melt convection and solidification. A major parameter is the laser intensity and the wavelength of the laser beam. High intensity causes the material to evaporate, whereas the low intensity causes the material to melt. The laser intensity should be optimised for laser surface treatment to prevent laser ablation. Pulse duration and pulse repeat rate affect the depth of laser penetration beneath the material surface. The laser-material interaction processes were presented in Fig. 3. The laser material interaction is influenced by various parameters, e.g. laser power, scanning speed, overlapping, scanning pattern and laser spot diameter.

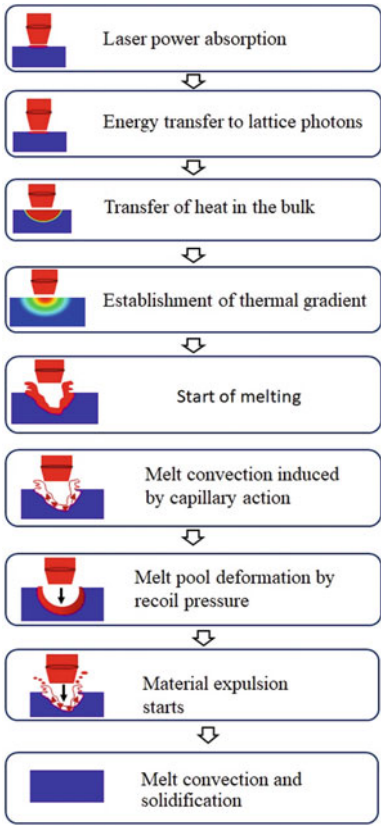

Fig. 3 Process involved during the laser material interaction

3.1 Absorption of Laser Power

Laser light induces a structural effect on the materials after its absorption. Different investigations have been carried out in the last decade to understand the process of laser absorption [43]. When the material is subjected to monochromatic coherent laser incidence, there are several phenomena, such as reflection, absorption and laser light transmission will occur as shown in Fig. 4a. Furthermore, absorbed laser energy leads to material heating and melting. Laser energy in the form of an electromagnetic wave interacts with a specific amount of kinetic energy on the material surface. These electrons also collide with other elements in the alloy and become ionised to generate plasma. After attaining the melting point, it transfers its energy to the lattice photons, significant in the heating and melting of the material.

Laser absorption depends on several aspects, such as laser light wavelength, light polarisation (e.g. linear or circular), incidence angle and laser light intensity. It also depends on the material types for metal, whether pure metal or alloys. Besides, laser absorption relies on the surface roughness of the sample. If a micro-hole or a pit is

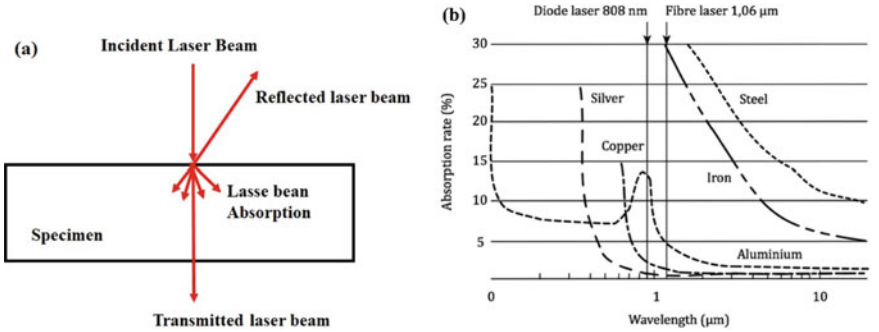

Fig. 4 **a** Phenomenon occur during laser-material interaction and **b** Absorption rate as a function of wavelength for common metals [43]. (Open Access from the URL_ http://www.diva-portal.org/smash/get/diva2:999341/FULLTEXT01.pdf)

present on the material surface, the light reflected in it is contained and the absorption rate is increased. A laser absorbed by an oxide layer, reflected on the bulk metal surface, which is again reflected by the oxide layer, increases the absorption power, resulting in the production of thick oxide layer [43]. The absorption rate of different materials depends upon the wavelength of the heating source. Laser absorption was illustrated in Fig. 4b as a function of the wavelength for typical metals.

3.2 Laser Beam Heating

The energy absorbed by the material as a consequence of laser light absorption is not heat, but rather the kinetic energy of free electrons. Although this energy cannot be converted directly into heat, the many mechanisms involved in converting the absorbed laser energy into heat [44]. There are three steps involved in converting the laser power in to heat, the first step is spatial and temporal randomization motion of excited particles through collision. The second step is energy transmission to lattice using numerous mechanism, and the last step is heat flow from high to the low heat region. Different processes of heat transfer entail an equation depending on the thermal characteristics of the base material [45]. The residual heat stress on the sample surface is caused by a gradient in the heat flow. The elasticity of material absorbed small thermal stress but if it reaches a limit, material cracks and yields. The amount of heat required for melting the surface can be determined by the material's wavelength, laser power, and thermal and optical properties of the material. A laser with a short pulse duration and a wavelength suitable for the high absorption coefficient and utilised to avoid bulk heating of specimen [45].

3.3 Laser Beam Melting

When the heating of the laser beam approaches the melting threshold, the material is melted. Material melting is caused by latent heat and melting enthalpy. The energy required for the melting (ΔH_{er}) and melt enthalpy (ΔH_{me}) relationship is vital for understanding the behaviour of the material during melting [46]. For metals, the ($\Delta H_{me}/\Delta H_{er}$) ratio shall be less than 1, while for semiconductors it shall be greater than 1. In contrast to the metal lattice, a high melt enthalpy value causes the semiconductor lattice to melt more slowly than the metal lattice. The convection and quick solidification of the melt are responsible for the melting of the material surface, the formation of crystalline and noncrystalline characteristics, and the distribution of metal in the melt.

3.4 Convection and Solidification

The solidification process after laser melting begins with the creation of atomic nuclei in the material (crystalline or amorphous) that vary according to the rate of heat flow of the laser. There will be a number of nucleation mechanisms involves until the material is fully solidified. By using the convection process the material is re-solidified till it reaches the ambient temperature without any structural modifications. The re-solidification procedure is more time-consuming compared to the solidification process [46]. Crystal nucleation and growth take happen in the range of temperatures between melting and glass transition temperatures. Bulk metallic glasses are produced by quick cooling without nucleation or growth.

4 Effect of Laser Remelting on Surface Properties

The laser remelting technique greatly improves the surface qualities of several mechanical components such as density, surface roughness, microhardness, wear and corrosion resistance. Generally, it performed on the various components and thermally coated components made in addition to increase the surface qualities. Research is still under way to detect the chemical influence of this technique.

4.1 Surface Density

Compared to conventional coatings, thermally sprayed coatings and additively manufactured components have increased porosity, which is advantageous in high-temperature applications. Nonetheless, in the context of wear resistance applications,

Table 1 Effect of laser remelting on surface roughness

Materials	Mode of operation	Surface roughness (μm)		References
		Before LR	After LR	
Ti6Al4V	Continuous	12.0	1.5	[32]
Stainless Steel	Pulsed	85.3	42.0	[34]
AlSi10Mg	Continuous	13.34	9.94	[42]
Ti6Al4V	Continuous	3.4	2.2	[43]

this is not recommended. LR is a highly effective approach for improving density and surface qualities. It has been reported that, with laser remelting enhance the relative density of component by 100 percent and surface quality by 90 percent [38]. LR grabs the attention of researchers because it transforms the microstructure from a granular to a lamellar structure, which results in an increase in density. The density of selective laser melted parts is improved by 2.37 percent as a result of the LR process [47]. Porosity and density are inversely proportional; laser remelting reduces porosity while simultaneously increasing density [48]. It is possible for pores to form during the coating process because to insufficient fusion and air entrapment. These pores operate as stress concentration locations, making them prone to fracture initiation.

4.2 Surface Roughness

Despite the fact that surface roughness is advantageous in a variety of applications such as grinding wheels and emery paper, it is strongly undesirable in wear resistance applications. When sliding contacts are used, a higher surface asperity contact results in abrasive wear. In recent years, laser remelting has become increasingly popular as a post-processing technique for reducing the surface roughness of various additively manufactured components and thermally sprayed coatings for wear resistance applications, as illustrated in the Table 1.

4.3 Microhardness

The average micro hardness of the additively produced components and the thermally sprayed coating is lower because of the porosity on the sample surface. Laser remelting improves the surface density considerably, as mentioned in the previous section, and leads to increased surface hardness. Laser remelting disrupts the surface oxide layers, eliminates the manufacturing surface defects like pore and voids and improves the component surface morphology. Laser trajectory affects the microhardness and mechanical properties; parallel and circular trajectories lead to

Table 2 Microhardness values of various materials post LR

Materials	Mode of operation	Microhardness (VHN)		References
		Before LR	After LR	
AlSi10Mg	Continuous	117.7	121.6	[42]
Ti6Al4V	Continuous	223.8	270.6	[32]
Ni–Cr-Co-Ti-V	–	700	900	[45]
$CoCrFeNiAl_{0.5}Ti_{0.5}$	Pulse	610	859	[14]
$FeCoCrNiAl_2Si_2$	Pulse	500	1085	[12]

increased sample microhardness in contrast to other techniques of trajectory [49]. Microhardness of different laser-remelted material is given in Table 2.

4.4 Wear Resistance

There is literature evidence that laser remelting increases wear resistance by increasing the density of the surface, reducing surface roughness, and increasing the microhardness value of additively built and thermally sprayed coated components. [19, 49]. LR technique considerably decreases surface roughness and other imperfections, as well as increases the wear resistance qualities of the material useful for the sliding wear application [50]. In comparison to the laser cladded sample, the laser remelted alloy demonstrates superior wear resistance of the NiCrCoTiV high entropy alloy [51]. The formation of numerous complex phases during the LR process in the instance of the high entropy alloy $FeCoCrNiAl_{0.5}Si_{1.5}$ results in increased wear resistance of the coating [17].

4.5 Corrosion Resistance

All mechanical and automotive components are subjected to a variety of corrosive conditions and high temperatures, which causes the material to degrade as a result of chemical and electrochemical processes. Various surface modification techniques have been developed in order to preserve the components life against corrosion, laser re-melting is one of a kind. If any surface flaws such as micro-cracking, pit and void on the component area are present, environmental exposure leads to oxidation corrosion. If water is caught in pores or microcracks as a stagnant fluid, then it causes pitting corrosion. Literature reports that laser remelting improved the pitting corrosion resistance of plasma-sprayed Cr3C2-NiCr coating [48]. The $CoCrFeNiAl_{0.5}$ high entropy alloy was recently subjected to the LR process, which resulted in improved oxidation resistance [20].

5 High Entropy Alloy (HEA)

Yeh et al. [1] and Cantor et al. [2] developed novel materials known as high entropy alloys or multi-component alloys, which are also known as cantor alloys. In contrast to the traditional alloy, it is composed of a mixture of a minimum of five elements in an equiatomic or nearly equiatomic ratio with a concentration ranging from 5 to 35 percent. The entropy of mixing is a significant factor in distinguishing it from the conventional alloy. The mixing entropy of the alloy is represented by the Eq. 1.

$$\Delta S_{mixing} = -R \sum_{i=1}^{N} m_i \, ln \, N \tag{1}$$

where, R is the novel gas constant, m_i is the atomic percentage of ith principal element, and N is the number of principle element present in the alloy. The mixing entropy alloy is classified into three types: low entropy, medium and high entropy alloy, as shown in Fig. 5.

Recently, high-temperature alloys (HEA) have demonstrated excellent wear and corrosion resistance qualities in high-temperature applications [4, 5]. A high mixing entropy employed in a variety of application areas can result in the formation of microstructures such as BCC, FCC and HCP, as well as a mixture of all solid solutions. Adding Cr to a steel improves its corrosion resistant qualities, as well as promoting the formation of the BCC phase, which increases its hardness. Ni and Co increase the probability of the FCC phase forming and, as a result, increase the ductility of the material by transitioning it from the BCC phase to the FCC phase.

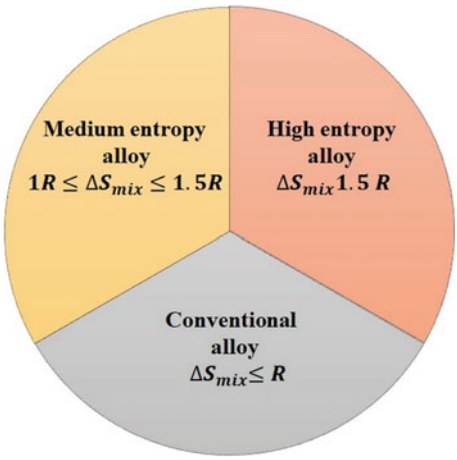

Fig. 5 Schematic of the evolution of high entropy alloy

6 Atmospheric Plasma Spray Coating (APS)

Atmospheric plasma spray is a sort of electrical-based thermal spray technique. This process is a surface modification technique by adding a layer on the components in order to prevent premature component failure. Thermal spray techniques are categorized into three types based upon combustion (e.g., detonation gun, High-velocity oxy-fuel and flame spray), electrical-based (e.g., atmospheric plasma spray, Vacuum plasma spray, and arc spray) and cold spray. These spray techniques are deployed in various applications based upon the material and temperature sensitivity which protect the surface from wear and corrosion and enhance the life of the component. Combustion-based spray techniques are suited for low temperature melting metals and not for high melting and ceramics. Electric spraying techniques are developed to alleviate this problem. As high temperature spraying technologies for temperature sensitive materials like nanocrystalline and copper (Cu) and Al are inappropriate for these two approaches, cold spraying techniques have been developed [39]. Electrical based plasma spray techniques are divided into two types, Atmospheric plasma spray (APS) and Vacuum plasma spray (VPS). To achieve vacuum and high maintenance costs, VPS needed a more advanced instrumentation facility. Due to inexpensive capital costs and lower maintenance requirements, APS are commonly used. APS is an electrically charged plasma-based thermal spraying process; when DC current is applied to the anode and cathode of the plasma gun, spark will be generated and ionized the plasma gas formation of the plasma jet at high temperature. Argon and hydrogen supplied respectively as primary and secondary plasma gas. The argon gas utilised to pour the powder particle to the plasma jet as a carrier gas. The kinetic energy is transmitted from the plasma jet to the powder particle and it begins to melt. Melted powder finally flowed through the converging diverging section of the nozzle with supersonic speed, which impacted and solidified at the substrate. APS is commonly utilised for the application of high temperature and wear resistance on high entropy alloys [48]. In contrast to other thermal spraying techniques, APS techniques have unique advantages.

1. APS is suited for materials such as high-temperature ceramics, high-entropy and refractory alloys consisting of high-melting point metallic elements [52, 53].
2. APS is a versatile technique for depositing the particle size range from 10–100 μm at any shape and size of the substrate material [54].
3. The axial plasma torch used in APS process is able to produce nano coating, which enhances heat conductivity and hardness and reduces surface defects [55].
4. For higher temperature, wear and corrosion resistance applications, APS is advantageous [56].
5. In order to limit heat flow within reactors and thermal applications, the APS is utilised widely for thermal barrier coating [57].

7 Experimental Procedure

At first, a mild steel plate of dimension 100 × 100 × 5 mm was cut and cleaned on the surface with an ethanol bath prior to deposition. The adhesion between the coating and the substrate mostly depends on the cleaning of the substrate and its surface roughness and the morphology of powder. Before deposition, the powder particle of all elements was blended correctly. Powder particle size and shape play an essential role in improving the deposition efficiency of the atmospheric plasma spray process. Accordingly, a particle size range of 10–40 μm was chosen for the deposition. As a result of the high impact speed, powder particles smaller than 10 microns fly away, while particles larger than 40 microns do not have adequate diffusion and homogeneity in the deposited sample. The use of circular shape powder was chosen to improve deposition efficiency because irregular or flacked shape powders splat and deform in a non-uniform manner during deposition, increasing the level of porosity in the final product. Prior to deposition, the powders were preheated to prevent surface oxidation Also it was ensured that the powders used are of spherical shape. The surface morphology of Ti and Ni powders are as shown in Fig. 6. The schematic diagram of the APS set up used in the current study for depositing the HEA sample is as shown in Fig. 7. A high entropy alloy powder with an equiatomic fraction of FeAlCoCrNiTi has been premixed and placed in the hopper, where it is forced into the plasma jet through the carrier gas argon. In order to generate a spark, a power supply is applied to both the anode and the cathode. The flow of argon (Ar) and hydrogen (H_2) gas as a plasma gas to the nozzle and ionisation results in the development of a plasma jet. A convergent thermal resistance nozzle has been employed for the high speed flow of plasma gas. The powder observes heat from the plasma jet, partially or completely melted, and impacts and solidify at the substrate with a sonic speed.

FeAlCoCrNiTi's high entropy alloy coating was successfully coated with atmospheric plasma spray; the deposited sample can be seen in Fig. 8. Visual inspec-

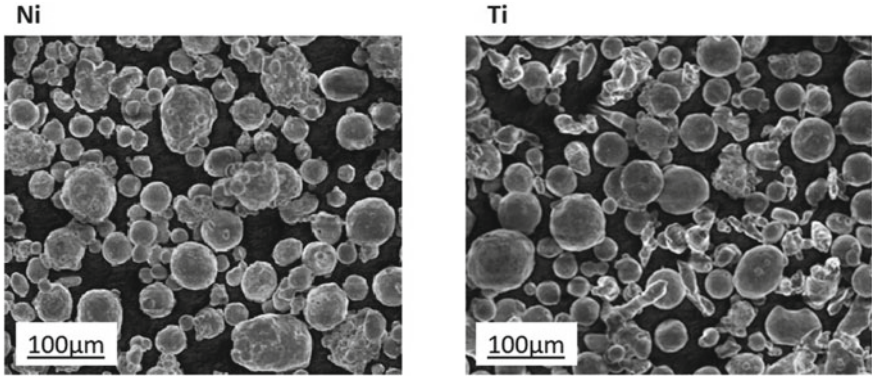

Fig. 6 Surface morphology of Ni and Ti powder particle

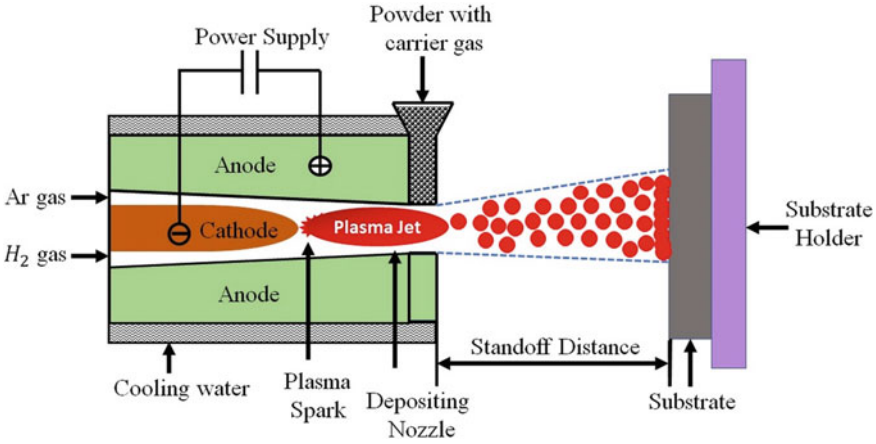

Fig. 7 Schematic representation of atmospheric plasma spray process

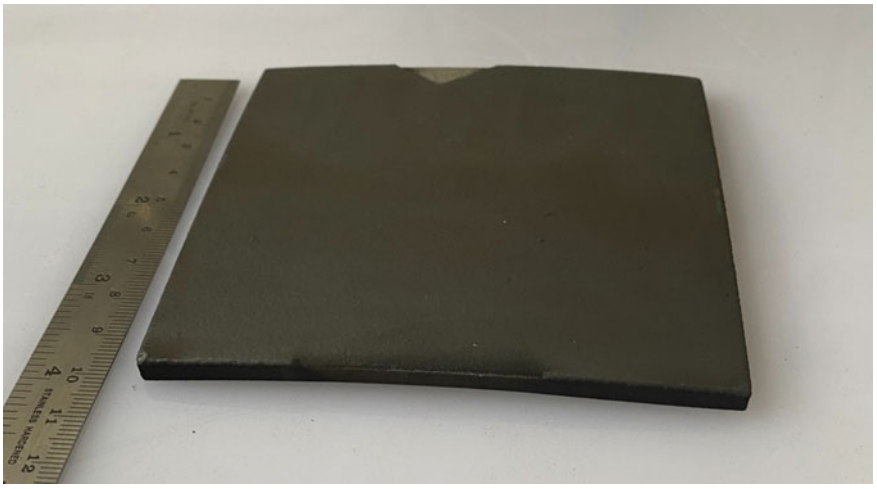

Fig. 8 FeAlCoCrNiTi high entropy alloy deposited using atmospheric plasma spray

tion showed robust metallurgical connection between the substrate and the alloy, no visible crack and the pore in the sample surface.

Laser remelting on the high entropy alloy sample deposited by the APS was undertaken to improve surface morphology and mechanical properties. It is obvious from a literature that the pulsed lased sample has higher mechanical properties as opposed to the continuous laser [40]; in this agreement the pulsed laser has been applied surface processing of materials. Prior to laser processing, the sample of APS coated high entropy alloy with ethanol was cleaned. Figure 9 shows a schematic diagram of the process of laser remelting and scanning pattern. It comprise of a

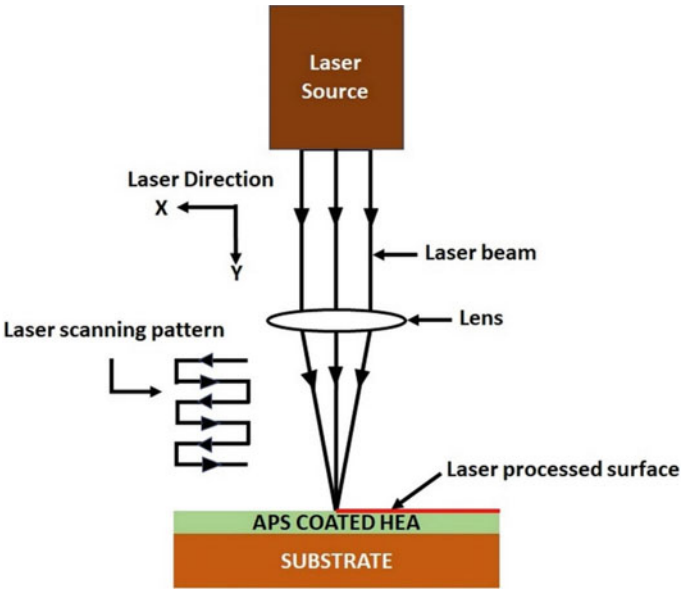

Fig. 9 Schematic of laser remelting process

high power laser source that has been used with Nd:YAG laser in pulsed mode. The laser diode excites the neodymium-doped yttrium aluminium garnet crystal known as stimulated emission. When the crystal absorbs the energy, its electron reaches its higher level of energy (unstable state). Excited electrons return to a lower energy status by emitting the photon with the in form of light energy. Continuous photon emissions and laser beam generation require population inversion (no of electrons in the excited state should be higher than the lower state). The population inversion generated using the optical pumping method called stimulated emission. The laser is transmitted through an optical resonator and focused on the material sample with the help of a condenser lens. The sample is subjected to beam energy absorption, surface melting and solidification.

In order to attain the specified qualities, the laser process parameter plays an essential role. Laser remelting process parameters such as laser power, hatch spacing, and scanning speed are tuned in order to prevent laser ablation during the laser-material contact interaction. The table below contains the optimum process parameter that was used for this work. 3. A Hatch line scanning pattern was utilised to remelt the FeAlCoCrNiTi HEA sample that had been treated with APS. To analyse the change in surface morphology after laser remelting, a scanning electron microscope (Model: Supra55, and Manufacturer: Zeiss) was used post-processing to examine the surface morphology of the sample after laser remelting. The roughness of the surface before and after laser remelting was examined with a surface profilometer (Model: NT9080 and Make Veeco). The mechanical characteristics have been evaluated before and after laser remelting to assess the process effectiveness of the mechanical qualities

Table 3 Process parameter used for laser remelting process

Parameter	Unit	Value
Laser power	W	210
Scanning speed	mm/min	2.8
Spot diameter	mm	2
Pulse frequency	Hz	10
Pulse duration	ns	10
Overlap	%	90
Wavelength	nm	532

and deploy them on a wear resistance application. The hardness tester (Vicker Model: VMH 002, and Make: UHL) is used to assess the pre- and post-laser re-melting micro hardness of the samples. In the next section, the surface characteristics of the sample deposited was discussed (Table 3).

8 Results and Discussions

The pre-mixed powder has been deposited with atmospheric plasma spray and the scanning electron spectroscopy has been applied to the as-sprayed sample in order to confirm surface morphology and surface defect free deposition. Figure 10a showed a smooth deposition of FeAlCoCrNiTi high-entropy alloy coating with few unmelted particles on the surface of the sample. The laser melting was performed using a pulsed laser on the as-sprayed material. The laser remelting effect and improvement in the microstructure was investigated using scanning electron microscopy. As displayed in Fig. 10b, the sample is revealed a dense surface with no pore and unmelted powder particles were completely melted after the laser remelting process. The particles found on the sample surface are not ablated since the laser

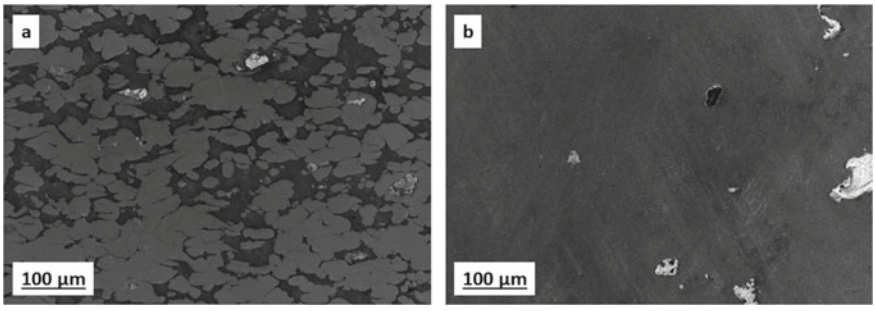

Fig. 10 SEM of APS coated FeAlCoCrNiTi sample **a** as coated state, **b** post laser processing

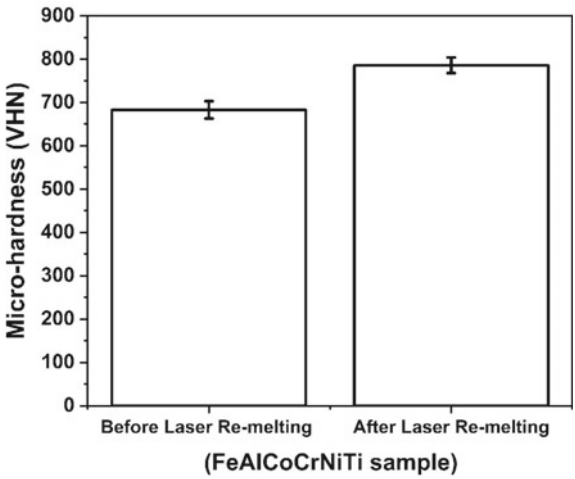

Fig. 11 Micro-hardness result of alloy sample before and after laser remelting process

power is optimised and the scanning speed is adequate to melt the surface of the high entropy alloy coating [58, 59].

Figure 11a showed that the particle partially melted during the APS coating process could be attributed due to less dwell time during the powder particle injection at the deposited sample. Porosity is also observed at the surface of the sample due to powder particle impact and splat behaviour. In contrast, laser remelted specimen s display the appropriate melting of the deposited coating and homogenous surface melting, as demonstrated in Fig. 11b. Laser remelted high entropy alloy reveals that the surface is free of contamination and porosity. After laser remelting, the surface density is enhancing. The surface roughness has been reduced significantly from 17.22 μm to 4.53 μm.

The mechanical characteristics of laser-remelted specimens should also be improved. A microhardness test was carried out before and after the laser melting process to study the improving mechanical properties. The sample was mirror polished and prepared according to standard methods of metallography. The polished sample was placed in Vicker's hardness testing machine for the proper impression of the indenter on the sample surface and test was performed under 200 g of load for 30 s of dwell time. The indenter impingement was performed at several places without any overlap to achieve the average hardness value of the sample. A micro-hardness test showed that laser-remelted specimens exhibit a higher hardness value of 778 VHN compared to APS-coated specimens as displayed in Fig. 11. Samples of laser remelted alloy show brittle nature, while the APS-coated sample has a low micro hardness due to a higher level of porosity and a lower density of surfaces in processing.

9 Future Scope of Work

The described methodology clearly shows efficient changes are brought into practise in HEAs by the effect of laser surface processing. The studies about the behaviour of the HEAs when treated with conventional furnace based heat treatment can be compared with laser based treatments to figure out the efficiency of non-conventional laser based technique with the conventional process. The mentioned study will clearly give an idea about the behaviour of HEAs under both conventional and non-conventional techniques.

10 Conclusions

- Laser remelting is a widely adaptable technique for laser-based surface modification without altering the chemical composition of the sample. This technique is used to improve the surface morphology, microstructure, surface roughness and microhardness of the material. In this chapter, exposure to APS coated high entropy alloy surface melting with pulsed laser is critical in order to obtain the desired surface properties, such as reduced microhardeness to increase surface rughness applicable to the use of wear resistance and fatigue resistance application. The following conclusion can therefore be drawn from this study.
- Laser remelting of the FeAlCoCrNiTi APS coated shows improved finished surface and surface roughness has been reduced.
- Laser re-melted FeAlCoCrNiTi show improved surface hardness value in contrast to the non-melted specimen.
- This laser remelted high entropy alloy coating can be deployed in various wear resistance applications due to improved hardness and surface finish.

Acknowledgements The authors thank the financial support provided by the Indian Space Research Organization (ISRO) for providing the financial support to carry out the experiments through the Respond Scheme (Project Sanction no. ISRO/RES/3/844/19-20)

References

1. Yeh, J.W., Chen, S.K., Lin, S.J., Gan, J.Y., Chin, T.S., Shun, T.T., Tsau, C.H., Chang, S.Y.: Nanostructured high-entropy alloys with multiple principal elements: novel alloy design concepts and outcomes. Adv. Eng. Mater. **6**, 299–303 (2004)
2. Cantor, B., Chang, I.T.H., Knight, P., Vincent, A.J.B.: Microstructural development in equiatomic multi-component alloys. Mater. Sci. Eng. A. **375**, 213–218 (2004)
3. Shiva, S., Palani, I.A., Paul, C.P., Kamaraj, M.: Advanced laser based surface treatment techniques to improve the quality of the products. In: Gupta, K. (eds.) Materials Forming, Machining

and Post Processing. Materials Forming, Machining and Tribology. Springer, Cham (2020). https://doi.org/10.1007/978-3-030-18854-2_9
4. Jiang, P.F., Zhang, C.H., Zhang, S., Zhang, J.B., Chen, J., Liu, Y.: Fabrication and wear behavior of TiC reinforced FeCoCrAlCu-based high entropy alloy coatings by laser surface alloying. Mater. Chem. Phys. **255**, 123571 (2020). https://doi.org/10.1016/j.matchemphys.2020.123571
5. Tong, Z., Liu, H., Jiao, Zhou, W., Yang, Y., Ren, X.: Improving the strength and ductility of laser directed energy deposited CrMnFeCoNi high-entropy alloy by laser shock peening, Addit. Manuf. **35**, 101417 (2020). https://doi.org/10.1016/j.addma.2020.101417
6. Wang, Y., Li, R., Niu, P., Zhang, Z., Yuan, T., Yuan, J., Li, K.: Microstructures and properties of equimolar AlCoCrCuFeNi high-entropy alloy additively manufactured by selective laser melting. Intermetallics **120**, 106746 (2020). https://doi.org/10.1016/j.intermet.2020.106746
7. Cai, Y., Zhu, L., Cui, Y., Han, J.: Manufacturing of FeCoCrNi + FeCoCrNiAl laminated high-entropy alloy by laser melting deposition (LMD). Mater. Lett. **289**, 129445 (2021). https://doi.org/10.1016/j.matlet.2021.129445
8. Amaya-Vazquez, M.R., Sánchez-Amaya, J.M., Boukha, Z., Botana, F.J.: Microstructure, microhardness and corrosion resistance of remelted TiG2 and Ti6Al4V by a high power diode laser. Corros. Sci. **56**, 36–48 (2012). https://doi.org/10.1016/j.corsci.2011.11.006
9. Osório, W.R., Cheung, N., Spinelli, J.E., Cruz, K.S., Garcia, A.: Microstructural modification by laser surface remelting and its effect on the corrosion resistance of an Al–9wt%Si casting alloy. Appl. Surf. Sci. **9**, 2763–2770 (2008). https://doi.org/10.1016/j.apsusc.2007.10.013
10. Ghorbani, J., Li, J., Srivastava, A.K.: Application of optimized laser surface remelting process on selective laser melted 316L stainless steel inclined parts. J. Manuf. Process. A **56**, 726–734 (2020). https://doi.org/10.1016/j.jmapro.2020.05.025
11. Liu, G., Du, D., Wang, K., Pu, Z., Chang, B.: Hot cracking behavior and mechanism of the IC10 directionally solidified superalloy during laser remelting. Vacuum **181**, 109563 (2020). https://doi.org/10.1016/j.vacuum.2020.109563
12. Jin, B., Zhang, N., Guan, S., Zhang, Y., Li, D.: Microstructure and properties of laser remelting FeCoCrNiAl0.5Six high-entropy alloy coatings. Surf. Coat. Technol. **349**, 867–873 (2018). https://doi.org/10.1016/j.surfcoat.2018.06.032
13. Wang, C., Yu, J., Zhang, Y., Yu, Y.: Phase evolution and solidification cracking sensibility in laser remelting treatment of the plasma-sprayed CrMnFeCoNi high entropy alloy coating. Mater. Des. **182**, 108040 (2019). https://doi.org/10.1016/j.matdes.2019.108040
14. Erdogan, A., Döleker, K.M., Zeytin, S.: Effect of laser remelting on electric current assistive sintered CoCrFeNiAlxTiy high entropy alloys: formation, micro-hardness and wear behaviors. Surf. Coat. Technol. **399**, 126179 (2020). https://doi.org/10.1016/j.surfcoat.2020.126179
15. Mert Doleker, K., Erdogan, A., Zeytin, S.: Laser remelting influence on isothermal oxidation behavior of electric current assisted sintered CoCrFeNi, CoCrFeNiAl0.5 and CoCrFeNiTi0.5Al0.5 high entropy alloys. Surf. Coat. Technol. **407**, 126775 (2021). https://doi.org/10.1016/j.surfcoat.2020.126775
16. Zhang, X., Guo, J., Zhang, X., Song, Y., Li, Z., Xing, X., Kong, D.: Influence of remelting and annealing treatment on corrosion resistance of AlFeNiCoCuCr high entropy alloy in 3.5% NaCl solution. J. Alloys Compd. **775**, 565–570 (2019). https://doi.org/10.1016/j.jallcom.2018.10.081
17. Jagdheesh, R., Mudali, U.K., Nath, A.K.: Laser processed Cr–SiC coatings on AISI type 316L stainless steel. Surf. Eng **23**(2), 93–98 (2007). https://doi.org/10.1179/174329407X169421
18. Jagdheesh, R., Ocaña, J.L.: Laser machined ultralow water adhesion surface by low pressure processing. Mater. Lett **270**, 127721 (2020). https://doi.org/10.1016/j.matlet.2020.127721
19. Jagdheesh, R., Tur, A., Ocaña, J.L.: The effects of pulse period on nanosecond laser microfabrication. Lasers Eng. **37**(4–6), 333–343 (2017)
20. Jagdheesh, R., Valarmathi, A., Sivakumar, M.: Influence of laser beam polarization on micromachining of crystalline silicon using ultrafast laser pulses. Lasers Eng. **32**(1–2), 19–35 (2015)
21. Jagdheesh, R., Kopeček, J., Brajer, J., Mocek, T.: Superhydrophobic microspiked surface structures by ultrashort laser patterning. Surf. Eng. **37**(10), 1266 (2021). https://doi.org/10.1080/02670844.2021.1874651

22. Jagdheesh, R., BičišŤová, R., Brajer, J., Mocek, T.: Laser-induced superhydrophobic and oleophobic surface structures on float glass. Lasers Eng. **50**, 289–298 (2021)
23. Kwok, C.T., Wong, P.K., Man, H.C.: Enhancement in corrosion and electrical wear resistance of copper via laser surface alloying with NiTi. Surf. Coat. Technol. **408**, 126804 (2021). https://doi.org/10.1016/j.surfcoat.2020.126804
24. Laketić, S., Rakin, M., Momčilović, M., Ciganović, J., Veljović, Đ, Cvijović-Alagić, I.: Influence of laser irradiation parameters on the ultrafine-grained Ti45Nb alloy surface characteristics. Surf. Coat. Technol. **418**, 127255 (2021). https://doi.org/10.1016/j.surfcoat.2021.127255
25. Chi, Y., Gu, G., Yu, H., Chen, C.: Laser surface alloying on aluminum and its alloys: a review. Opt. Lasers Eng. **100**, 23–37 (2018). https://doi.org/10.1016/j.optlaseng.2017.07.006
26. Li, Y., Shi, Y.: Microhardness, wear resistance, and corrosion resistance of AlxCrFeCoNiCu high-entropy alloy coatings on aluminum by laser cladding. Opt. Laser Technol. **134**, 106632 (2021). https://doi.org/10.1016/j.optlastec.2020.106632
27. Zhang, S., Han, B., Li, M., Zhang, Q., Hu, C., Jia, C., Li, Y., Wang, Y.: Microstructure and high temperature erosion behavior of laser cladded CoCrFeNiSi high entropy alloy coating. Surf. Coat. Technol. **417**, 127218 (2021). https://doi.org/10.1016/j.surfcoat.2021.127218
28. Kromer, R., Costil, S., Verdy, C., Gojon, S., Liao, H.: Laser surface texturing to enhance adhesion bond strength of spray coatings—Cold spraying, wire-arc spraying, and atmospheric plasma spraying. Surf. Coat. Technol. **352**, 642–653 (2018). https://doi.org/10.1016/j.surfcoat.2017.05.007
29. Han, J., Zhang, F., Van Meerbeek, B., Vleugels, J., Braem, A., Castagne, S.: Laser surface texturing of zirconia-based ceramics for dental applications: a review. Mater. Sci. Eng. C **123**, 112034 (2021). https://doi.org/10.1016/j.msec.2021.112034
30. Serdyukov, V., Starinskiy, S., Malakhov, I., Safonov, A., Surtaev, A.: Laser texturing of silicon surface to enhance nucleate pool boiling heat transfer. Appl. Therm. Eng. **194**, 117102 (2021). https://doi.org/10.1016/j.applthermaleng.2021.117102
31. Han, X., Zhang, Z., Pan, Y., Barber, G.C., Yang, H., Qiu, F.: Sliding wear behavior of laser surface hardened austempered ductile iron. J. Mater. Res. Technol. **9**, 14609–14618 (2021). https://doi.org/10.1016/j.jmrt.2020.10.050
32. Lasota, I., Protsenko, V., Matyushkin, A., Kuznetsov, M., Gook, S.: Laser surface hardening of engine camshaft cams. Mater. Today: Proceed. **30**, 478–482 (2020). https://doi.org/10.1016/j.matpr.2019.12.400
33. Shiva, S., Palani, I.A., Paul, C.P., et al.: Laser shock peening of Ni-Ti bulk structures developed by laser additive manufacturing. J. Mater. Eng. Perform. (2021). https://doi.org/10.1007/s11665-021-05799-w
34. Pavan, M.: PhD Thesis, Laser shock peening for fatigue life enhancement of aerospace components (2008)
35. Yan, Z., Guo, L., Li, Z., Yu, Y., He, Q.: Effects of laser glazing on CMAS corrosion behavior of Y2O3 stabilized ZrO2 thermal barrier coatings. Corros. Sci. **157**, 450–461 (2019). https://doi.org/10.1016/j.corsci.2019.06.025.
36. Lawrence, J., Li, L.: High power diode laser surface glazing of concrete. J. Laser Appl. **12**(3), 116–125 (2000). https://doi.org/10.2351/1.521920
37. Stutzman, A.M., Rai, A.K., Alexandreanu, B., Albert, P.E., Sun, E.J., Schwartz, M.L., Reutzel, E.W., Tressler, J.F., Medill, T.P., Wolfe, D.E.: Laser glazing of cold sprayed coatings for the mitigation of stress corrosion cracking in light water reactor (LWR) applications. Surf. Coat. Technol. **386**, 125429 (2020). https://doi.org/10.1016/j.surfcoat.2020.125429
38. Yasa, E., Deckers, J., Kruth, J.: The investigation of the influence of laser remelting on density, surface quality and microstructure of selective laser melting parts. Rapid Prototyp. J. **17**, 312–327 (2011). https://doi.org/10.1108/13552541111156450
39. Shiva, S. et al.: Development of CuAlNi shape memory alloy structures using cold spray deposition technique with laser remelting. In: Pathak, S., Saha, G. (eds.) Cold Spray in the Realm of Additive Manufacturing. Materials Forming, Machining and Tribology. Springer, Cham (2020). https://doi.org/10.1007/978-3-030-42756-6_7

40. De Giorgi, C., Furlan, V., Demir, A.G., Tallarita, E., Candiani, G., Previtali, B.: Laser micro-polishing of stainless steel for antibacterial surface applications. Procedia CIRP **49**, 88–93 (2016). https://doi.org/10.1016/j.procir.2015.07.055
41. Antou, G., Montavon, G., Hlawka, F., Cornet, A., Coddet, C., Machi, F.: Modification of ceramic thermal spray deposit microstructures implementing in situ laser remelting. Surf. Coat. Technol. **172**, 279–290 (2003). https://doi.org/10.1016/S0257-8972(03)00431-6
42. Li, Y., Wu, Y., Wang, W., Lei, M., Li, X.: (2021) Microstructure and mechanical properties of the Ni-B-Ti composite coating on TA2 prepared by pre-plating and laser remelting, Surf. Coat. Technol. **405**, 126567, https://doi.org/10.1016/j.surfcoat.2020.126567
43. Bergstrom, D.: The Absorption of Laser Light by Rough Metal Surfaces - PhD Thesis, Lulea University of Technology (2008)
44. Phipps, C., Zhigilei, L., Polynkin, P., Gruzdev, V., Bohn, W., Scharring, S.: Laser interaction with materials: introduction. J. Opt. Soc. Am. B **35**, LIM1-LIM2 (2018). https://doi.org/10.1364/JOSAB.35.00LIM1
45. Von Allmen,, M., Blatter A.: Heating by laser light. In: Laser-Beam Interactions with Materials. Springer Series in Materials Science, vol 2. Springer, Berlin, Heidelberg (1995). https://doi.org/10.1007/978-3-642-57813-7_3
46. Von Allmen, M., Blatter, A.: Melting and Solidification. In: Laser-Beam Interactions with Materials. Springer Series in Materials Science, vol 2. Springer, Berlin, Heidelberg (1995). https://doi.org/10.1007/978-3-642-57813-7_4
47. Liu, B., Li, B.-Q., Li, Z.: Selective laser remelting of an additive layer manufacturing process on AlSi10Mg. Results Phys. **12**, 982–988 (2019). https://doi.org/10.1016/j.rinp.2018.12.018
48. Shi, P., Yu, Y., Xiong, N., Liu, M., Qiao, Z., Yi, G., Yao, Q., Zhao, G., Xie, E., Wang, Q.: Microstructure and tribological behavior of a novel atmospheric plasma sprayed AlCoCrFeNi high entropy alloy matrix self-lubricating composite coatings. Tribol. Int. **151**, 106470 (2020). https://doi.org/10.1016/j.triboint.2020.106470
49. Zhao, Y., Wu, X., Du, H., Shangguan, X., He, W.: Influence of different laser remelting paths on the microstructure of a spray coating: Defect prevention and tribological properties. Surf. Coat. Technol. **367**, 11–18 (2019). https://doi.org/10.1016/j.surfcoat.2019.01.118.
50. Xi, W., Song, B., Wang, Z., Yu, T., Wang, J., Dai, Y.: Effect of laser remelting on geometry and mechanical properties of YCF102 cladding layer. Surf. Coat. Technol. **408**,126789 (2021). https://doi.org/10.1016/j.surfcoat.2020.126789
51. Cai, Z., Cui, X., Liu, Z., Li, Y., Dong, M., Jin, G.: Microstructure and wear resistance of laser cladded Ni-Cr-Co-Ti-V high-entropy alloy coating after laser remelting processing. Opt. Laser Technol. **99**, 276–281 (2018). https://doi.org/10.1016/j.optlastec.2017.09.012
52. Qing, Y., Yao, H., Li, Y., Luo, F.: Plasma-sprayed ZrB2/Al2O3 ceramics with excellent high temperature electromagnetic interference shielding properties. J. Eur. Ceram. Soc. **41**, 1071–1075 (2021). https://doi.org/10.1016/j.jeurceramsoc.2020.10.031.
53. Meghwal, A., Anupam, A., Luzin, V., Schulz, C., Colin Hall, B.S., Murty, R.S., Kottada, C.C., Berndt, A.S., Ang, M.: Multiscale mechanical performance and corrosion behaviour of plasma sprayed AlCoCrFeNi high-entropy alloy coatings. J. Alloys Compd. **854**, 157140 (2021). https://doi.org/10.1016/j.jallcom.2020.157140
54. Lee, DoSung, Yun, S., Han, J.-W., Song, MinYoung, Kim, YoungGeun, Lee, JongKweon, Choi, J., Chang, S., Hong, S., Kim, JaeHwang: Microstructural evolution and mechanical properties of atmospheric plasma sprayed Y2O3 coating with state of in-flight particle. Ceram. Int. **47**, 3853–3866 (2021). https://doi.org/10.1016/j.ceramint.2020.09.246
55. Fauchais, P., Etchart-Salas, R., Rat, V., Coudert, J. F., Caron, N., Wittmann-Ténèze, K.: Parameters controlling liquid plasma spraying: solutions, sols, or suspensions. J. Therm. Spray Technol. **17**(1), 31–59 (2008). https://doi.org/10.1007/s11666-007-9152-2
56. Xiao, J.-K., Wu, Y.-Q., Zhang, W., Chen, J., Wei, X.-L., Zhang, C.: Microstructure, wear and corrosion behaviors of plasma sprayed NiCrBSi-Zr coating. Surf. Coat. Technol. **360**, 172–180 (2019). https://doi.org/10.1016/j.surfcoat.2018.12.114
57. Cao, Y., Ning, X., Wang, Q.: Thermal shock behavior of Ba(Mg1/3Ta2/3)O3-YSZ double-ceramic-layer thermal barrier coatings prepared by atmospheric plasma spraying. Surf. Coat. Technol. **409**, 126842 (2021). https://doi.org/10.1016/j.surfcoat.2021.126842

58. Vaithilingam, J., Goodridge, R.D., Hague, R.J.M., Christie, S.D.R., Edmondson, S.: The effect of laser remelting on the surface chemistry of Ti6al4V components fabricated by selective laser melting. J. Mater. Process. Technol. **232**, 1–8 (2016). https://doi.org/10.1016/j.jmatprotec.2016.01.022
59. Chong, K., Zou, Y., Wu, D., Tang, Y., Zhang, Y.: Pulsed laser remelting supersonic plasma sprayed Cr3C2-NiCr coatings for regulating microstructure, hardness and corrosion properties. Surf. Coat. Technol. **418**, 127258 (2021). https://doi.org/10.1016/j.surfcoat.2021.127258.

Surface Morphology of Nimonic Alloy 263™ in Nanosecond Pulsed Laser Ablation

Zhehao Jiang, Sunil Pathak, S. Subramani, J. Radhakrishnan, and Sundar Marimuthu

Abbreviations

CPA	Chirped Pulse Amplification
DLW	Direct laser writing
EDM	Electrical Discharge Machining
FWHM	Full width Half Maximum
HAZ	Heat Affected Zone
LBM	Laser Beam Machining
LIP	Laser Induced Plasma
MOPA	Master Oscillator Power Amplifier
MRR	Material Removal Rate
Nd:YAG	Neodymium-doped Yttrium Aluminium Garnet

Z. Jiang
Loughborough University, Loughborough, UK

S. Pathak
Hilase Centre, Institute of Physics, Academy of Sciences of the Czech Republic, Za Radnici 828, 25241 Dolni Brezany, Czech Republic

S. Subramani
Department of Inorganic Chemistry, University of Chemistry and Technology Prague, Technick´a 5, 166 28 Prague 6, Czech Republic

J. Radhakrishnan (✉)
UPM Laser Centre, Universidad Politécnica de Madrid, 28031 Madrid, Spain
e-mail: r.jagdheesh@upm.es

S. Marimuthu
The Manufacturing Technology Centre, Ansty Business Park, Coventry, UK

Z. Jiang
Zhehao Jiang presently working at BSH Electrical Appliances Co., Ltd Nanjing, Nanjing, Jiangsu, People's Republic of China

J. Radhakrishnan and S. Pathak (eds.), *Advanced Engineering of Materials Through Lasers*, Advances in Material Research and Technology,
https://doi.org/10.1007/978-3-031-03830-3_6

PLA	Pulse Laser Ablation
SEM	Scanning Electron Microscope
Yb:YAG	Ytterbium-doped Yttrium Aluminium Garnet

1 Introduction

Precision machining of ultra-hard materials and superalloys are the prime limitations of conventional tool machining [1, 2]. Moreover, direct tool contact could ascend the mechanical stress load and probably change the alloy microstructure [2]. Nimonic Alloy 263™ is a class of nickel-based superalloys with extraordinary characteristics in excellent thermal conductivity, superb mechanical strength, and remarkable rust resistance, used in the rigorous operating conditions in gas turbine engines [3, 4]. Hence, it was recognized that advanced machining processes are expected to be developed under this age background. Nowadays, various non-contact based fabrication techniques have been more and more mature, including electrochemical machining (ECM), abrasive jet machining (AJM), and electrical discharge machining (EDM), ion beam micromachining (IBMM), and laser beam machining and micromachining (LBM, LMM) and so forth [4].

Laser beam machining (LBM) is a widely used advanced machining process, especially popular in welding, cutting, drilling, and hardening metallic sheets [4, 5]. Laser Beam Machining (LBM) is a machining method that uses a laser beam to engrave metallic and non-metallic materials. In this technique, a high-intensity laser beam is directed towards the workpiece, and the laser's thermal energy is transmitted to the workpiece's surface (workpiece). The heat generated at the surface warms, melts, and vaporizes the w/p components [5]. LBM, in general, is concerned with machining and material processing such as heat treatment, alloying, cladding, sheet metal bending, and so on. This type of processing uses the energy of coherent photons or laser beams, which are mostly transformed into thermal energy when they contact most materials. Moreover, the lasers are now used in regenerative machining and fast prototyping and procedures like stereolithography and selective laser melting [6].

Usually, continuous waved lasers are suitable for metallic sheet welding and hardening, which should attribute to its constant average power output. In contrast, rather than continuous waved lasers, pulsed lasers are used in deep penetration applications due to their intense power density. Pulsed lasers used for applications can be divided into millisecond (ms), microsecond (μs), nanosecond (ns), picoseconds (ps), and femtoseconds (fs) those five categories up to their pulse durations [6–8]. In order to recycle costly advanced engineering materials like Nimonic Alloy 263™, pulsed laser ranges from short pulse (ms-ns) to ultrashort pulse (ps-fs) are used in ablating material surface coating or cracked surface substrate layer. For pulsed laser ablation, the photon substrate interaction mechanism goes through heating, melting, boiling, and vaporization these four periods with an increase of power density [9]. It has been very well researched [10–12] that a higher material removal rate can be achieved in

the high power density that laser beam can penetrate deeper in the targeted irradiated area. Jeong et al. [13] and Palanco et al. [14] observed that a large amount of ionized ejected material could transfer into plasma plume, absorbing the consecutive laser energy and restricting the following: ablation. The higher power density applied i.e., over a saturation point 4–5 $\times$ 10^8 W/cm^2 may lead to a more obvious plasma shielding effect; it would be found when the power density is over a saturation point. In recent years, ultrashort UV laser ablation has become acclaimed because of its high power density that can alter material ejection mechanism from explosive melt dominated to vaporization dominated while descending plasma shield effect [15]. Once the pulse duration is no longer than the picosecond regime, the ablation process does not induce a melting process because there is less interaction time available for thermal diffusion via heat conduction. Compared to short-pulse laser ablation, undesirable heat effects on the valuable substrate in the form of micro-cracks, recast layer, and HAZ can be greatly minimized via material vaporization [16, 17]. Nevertheless, high operating costs and complex setup are the significant issues restricting its application scope.

Recently, a new fibre-based amplifier technology (MOPA) in a few ns pulse duration instead of chirped Pulse Amplification (CPA) ultrashort pulse in several ps or fs regimes was developed in balancing cost and ablation performance [18]. Compared to the traditional Q-switched fibre laser, MOPA fibre laser uses controllable pulse durations separately in each pass, meaning quality and efficiency can be achieved simultaneously through rough-based high material removal at premiere scanning and precisely based low material removal at post scanning [19]. Unlike peak power significantly reduced with increased laser frequency in Q-switched laser, limited peak power reduction by using higher frequency MOPA fibre laser [20].

In this chapter, a univariate experiment in changing a single parameter while keeping others constant is used to explore process parameters including pulse duration, frequency, power density, and scanning speed effects on MOPA ns fibre laser ablation Nimonic Alloy 263™. The optimum value of each parameter could be filtered out after parametric analysis according to the performance on ablation depth or surface roughness.

2 Materials and Methods

In the present work, an SPI MOPA pulsed fibre laser with wavelength 1.06 μm, FWHM pulse duration from 19 to 46 ns with frequency ranges from 1 to 1000 kHz was used as the power source. A moving direct laser writing (DLW) galvo scanner worked on Nimonic Alloy 263™ samples of dimension 75(L) $\times$ 15(W) $\times$ 2(T) mm in scanning speed up to 100 mm/s was used in the present experimentation. The details of the levels of parameters used in the experiment are shown in Table 1.

The scanner head is fitted with an F-Theta lens with a focal position to the top of the workstation, 178 mm (176 mm + 2 mm mild steel base). Due to the high thermal conductivity of Nimonic Alloy 263™, high laser power density could lead to substrate sheet deformation, shown in Fig. 1a. The 2 mm mild steel base was

Table 1 Parameters and levels use for experimentation

S.no	Optimum frequency (kHz)	Pulse duration (ns)	Peak power (kW)	Speed (mm/s)
1	70	46	13	1
2	70	46	13	5
3	70	46	13	10
4	70	46	13	20
5	70	46	13	50
6	70	46	13	80
7	158	37	11	1
8	158	37	11	5
9	158	37	11	10
10	158	37	11	20
11	158	37	11	50
12	158	37	11	80
13	350	23	10	1
14	350	23	10	5
15	350	23	10	10
16	350	23	10	20
17	350	23	10	50
18	350	23	10	80

clamped below the targeted substrate to minimize the residual heat effect. For the fair thermal conductivity of mild steel, partial heat can be shared by the mild steel base; thus, the severity of deformation can greatly descend, shown in Fig. 1b. The laser beam scanned 15 mm in lines varying with speed change in the longitudinal width direction, and the intermediate section was chosen to avoid the acceleration effect. Spot diameter was estimated to the spot size of the ablation removal threshold by the method provided by Liu (1982) and theoretically calculated refer to Eq. (1) [18].

$$d = 2.44\frac{f\lambda}{D} \tag{1}$$

where d is the spot diameter, f is the focal length, λ is the wavelength, and D is the beam diameter. The spot diameter was calculated to be 32 μm.

Precise control of lens-to-substrate distance at constant 178 mm was ensured to provide a stable spot diameter of 32 μm on the laser-substrate interaction zone. A 2 bar extractor was used to inhale ejected hazard in mid-air, and all experiment progress was performed without any assisted gas auxiliary. Eventually, optical and scanning electronic microscopes (SEM) was used to analyze ablated samples.

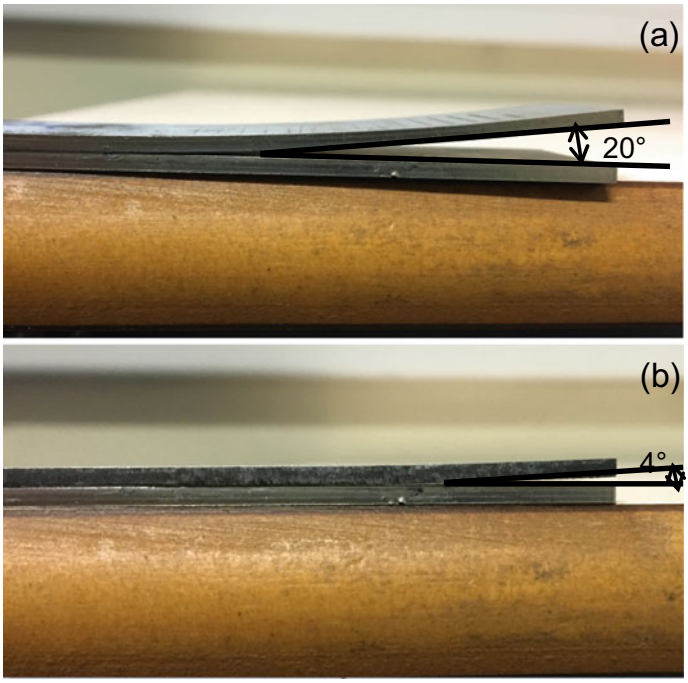

Fig. 1 Deformation comparison between **a** clamped without mild steel base, **b** clamped with mild steel base (Pulse duration = 46 ns, frequency = 70 kHz, power density = 16.2×10^5 kW/cm^2)

3 Results and Discussion

Referring to Eqs. (2) and (3), power output is determined by frequency and pulse duration.

$$P_{avg} = E \times f \tag{2}$$

And,

$$P_{peak} = \frac{E}{\Delta T} \tag{3}$$

Where P_{avg} is the average power, P_{peak} is the peak power, E is the pulse energy, and ΔT is the pulse duration.

According to synchronized consideration of the connection between each process parameter, so before exploring the effects of power density on laser ablation, the significance of researching the relationship among pulse duration, frequency, and ablation performance is noticeable.

3.1 Frequency Effects on Power Output

MOPA in the machine enables altering an extensive range of pulse duration, and a wide selection of corresponding optimum laser frequency ranges from 0 to 1000 kHz for different usage. Laser frequency represents the cycle time of one pulse shot, starting from one pulse to the beginning of the following pulse. Pulse duration delegates the duration of pulse-substrate interaction. Pulse duration is a phase of laser frequency without takt time. The optimum frequency at constant pulse duration can achieve the maximum output peak power, as shown in Fig. 2. In this diagram, the optimum frequency for laser FWHM pulse duration at 46 ns is 70 kHz, giving 100% peak power output. With the increase of laser frequency, the peak power output decreases, varying with it. Peak power output can be regulated via changing laser frequency for a particular laser pulse duration. Pulse duration will not be altered with the change of laser frequency, and there is no direct relationship between laser frequency and pulse duration.

3.2 Pulse Duration Effects on Ablation Depth

When the pulse durations changed during the progress, the optimum frequency automatically varied with it. To identify the effects of pulse duration on ablation depth, three dispersed FWHM pulse duration parameters in scope range were selected (46 ns pulse duration with optimum frequency 70 kHz, 37 ns pulse duration with optimum frequency 158 kHz, and 23 ns pulse duration with optimum frequency 350 kHz).

The ablation appearances of PLA on the flat nickel superalloy at one pass for selected pulse durations are shown in Fig. 3a 46 ns, (b) 37 ns, and (c) 23 ns at

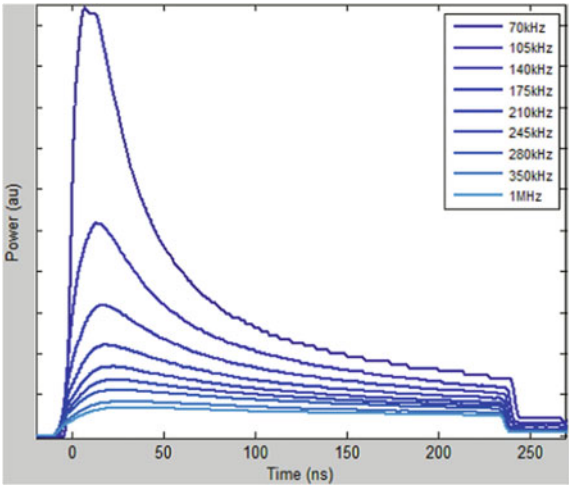

Fig. 2 Diagram showing frequencies effect on peak power at FWHM pulse duration 46 ns

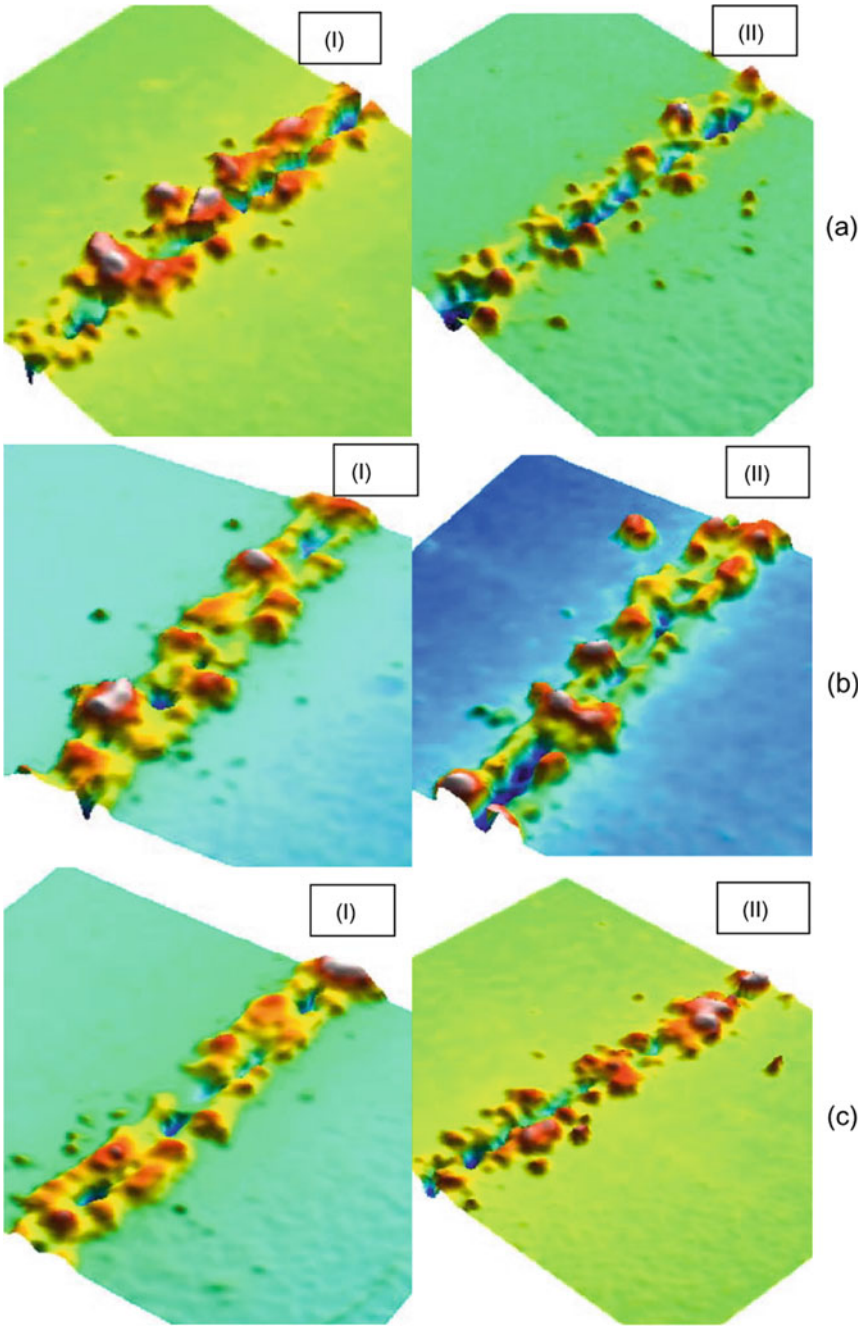

Fig. 3 Ablation appearance of different pulse durations **a** 46 ns, **b** 37 ns, and **c** 23 ns at different speed (I) 1 mm/s and (II) 50 mm/s

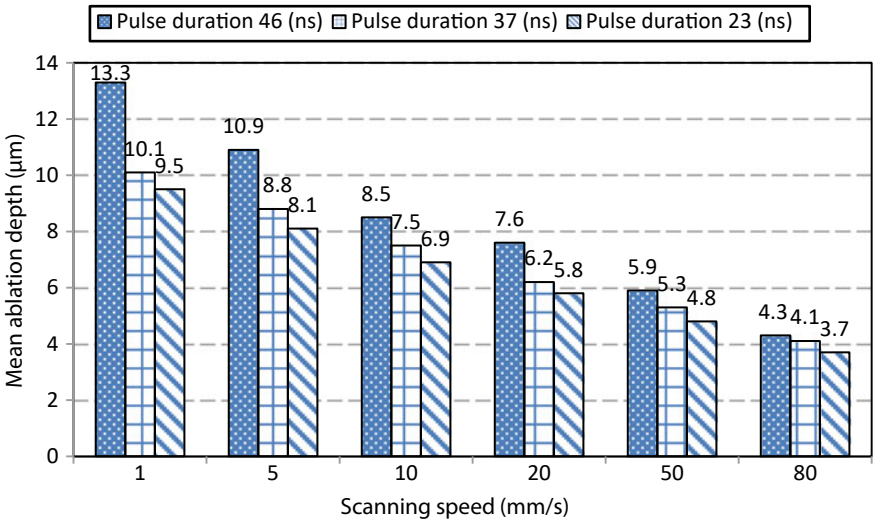

Fig. 4 Effect of pulse durations on mean ablation depth at maximum power output

two different speeds (I) 1 mm/s and (II) 50 mm/s. The optimum frequency gave the maximum peak power output, and respective were 13 kW, 11 kW, and 10 kW. As can be seen from the Figure, maximum peak power output led to a large amount of redeposited debris scattered alongside the ablation line, and higher scanning speed performed more obvious debris deposited phenomenon than lower speed. Mean ablation depth for the 18 sets of ablation lines is calculated and shown in Fig. 4.

From Fig. 4, it is evident that a higher pulse duration laser results in higher ablation depth due to longer effective laser-substrate interaction reaction and higher pulse peak power. Laser with pulse duration of 46 ns gave out a 13.3 μm mean ablation depth while other twos only had 10.1 μm and 9.5 μm at laser scanning speed 1 mm/s, respectively. Moreover, the mean ablation depth gradually decreases with increasing laser scanning speed in a decreasing exponential function trend. Laser pulse duration 46 ns with peak power 13 kW exhibited good ablation depth performance.

3.3 Power Density Effects on Ablation Performance

It is known that the plasma shield could be formed in a nanosecond laser regime when the laser power density is over 4–5 $\times$ 10^5 kW/ cm^2 [9, 13–15]. The calculation for power density can refer to Eq. (4).

$$F = \frac{P}{A} \tag{4}$$

Table 2 Calculations for the power density (kW/ cm^2)

S.No	Power percentage (%)	Peak power (kW)	Power density (kW/cm^2)
1	10	1.3	1.6×10^5
2	20	2.6	3.2×10^5
3	30	3.9	4.8×10^5
4	40	5.2	6.5×10^5
5	50	6.5	8.1×10^5
6	60	7.8	9.6×10^5
7	70	9.1	11.3×10^5
8	80	10.4	12.9×10^5
9	90	11.7	14.5×10^5
10	100	13.0	16.2×10^5

where F is power density (W/cm^2), P is laser power, and A is beam cross-sectional area.

The machine's effective beam cross-section spot diameter was 32 μm, so the effective beam cross-sectional area here was 8.04×10^{-6} cm^2. The calculation results for different power percentages are shown in Table 2.

All the ablation lines were applied to unify the speed parameter for a scanning speed of 4 mm/s. Top view of ablation lines under optical microscope at power density (a) 3.2×10^5 kW/cm^2, (b) 8.1×10^5 kW/cm^2 and (c) 14.5×10^5 kW/cm^2 are shown in Fig. 6 at the same magnification 10×. As shown in Fig. 5, with increasing power density, the melting zone became larger, and a more evident heat-affected edge along the longitudinal line direction can be seen. For power density 14.5×10^5 kW/cm^2, the melting pool diameter could reach 131.65 μm, whereas only 62.82 μm for power density 3.2×10^5 kW/cm^2. The appearances of ablation lines under using power density (a) 1.6×10^5 kW/cm^2, (b) 4.8×10^5 kW/cm^2, (c) 8.1×10^5 kW/cm^2 and (d) 14.5×10^5 kW/cm^2 are shown in Fig. 6.

As shown in Fig. 6, nearly no material removal happened when using power density 1.6×105 kW/cm^2, and with an enhancement of power density, material removal became manifest in the presence of debris deposited and ablation depth. The appearance of ablation lines under power density (c) 8.1×10^5 kW/cm^2 and (d) 14.5×10^5 kW/cm^2 look similar to others.

Figure 7a shows the captured laser-induced plasma flume working at scanning speed 4 mm/s with power density 12.9×10^5 kW/cm^2; it justifies that the plasma effect occurs when the laser power density reaches a specific value in MOPA ns fibre laser ablation. The mean ablation depth for all 10 set lines is analyzed in Fig. 7b. As illustrated in Fig. 7b, the ablation depth increases with laser power density in a positive linear correlation. The power density for the nickel superalloy ablation threshold is close to 1.6×10^5 kW/cm^2. The variation was amplified from 1.6×10^5 to 8.1×10^5 kW/cm^2 till it reached saturation point at power density 8.1×10^5 kW/cm^2. The power density over the saturation point was likely affected by the plasma shielding

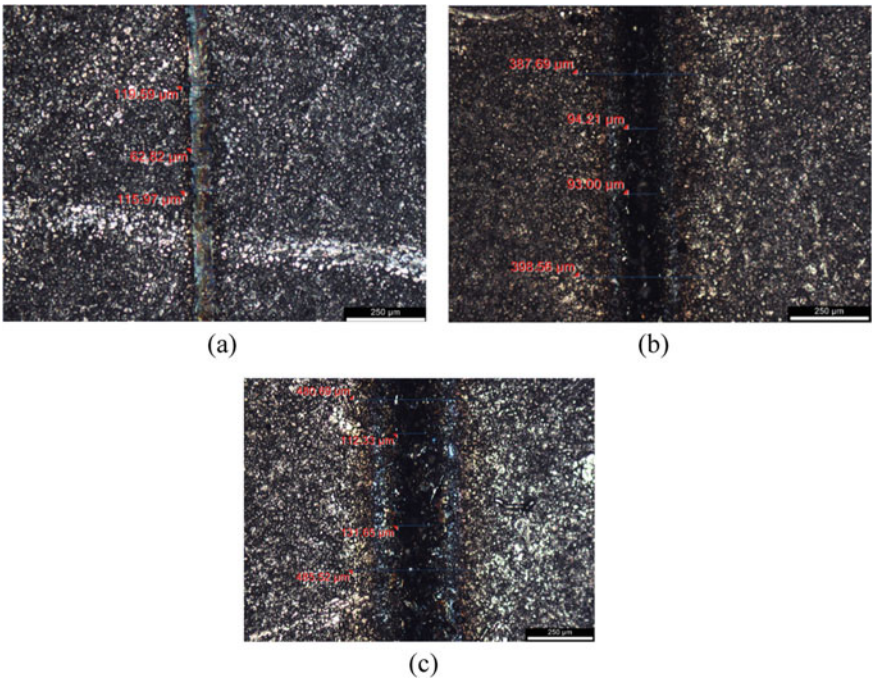

Fig. 5 Top view of ablation lines under optical microscope at power density at **a** 3.2×10^5 kW/cm^2, **b** 8.1×10^5 kW/cm^2 and **c** 14.5×10^5 kW/cm^2 (Scanning speed = 4 mm/s, pulse duration = 46 ns)

effect. The plasma cloud in the air absorbed the partial laser energy, and only specific energy could penetrate through the plasma cloud and strike on the substrate. The efficiency for laser irradiance was significantly discounted after penetrating the plasma shield, and with an increase of power density, the side effect of plasma became more apparent. The phenomenon is defined as Inverse Bremsstrahlung Absorption, a process of photons absorbed, scattered, and reflected by ionized gas electrons that lead to energy losses [12]. So power density at 8.1×10^5 kW/cm^2 with laser pulse duration is chosen due to its best cost performance on power usage and ablation efficiency. Power density at 8.1×10^5 kW/cm^2 corresponds to laser frequency 105 kHz at pulse duration 46 ns.

3.4 Scanning Speed Effects on Ablation Performance

Laser scanning speed is another pivotal process parameter that influences ablation performance. Veiko et al. [21] researched Q-switched ns fibre laser ablation of monocrystalline silicon and found that the laser ablation depth with increased scanning speed reflected a linear decline. Laser scanning speed effects on mean ablation

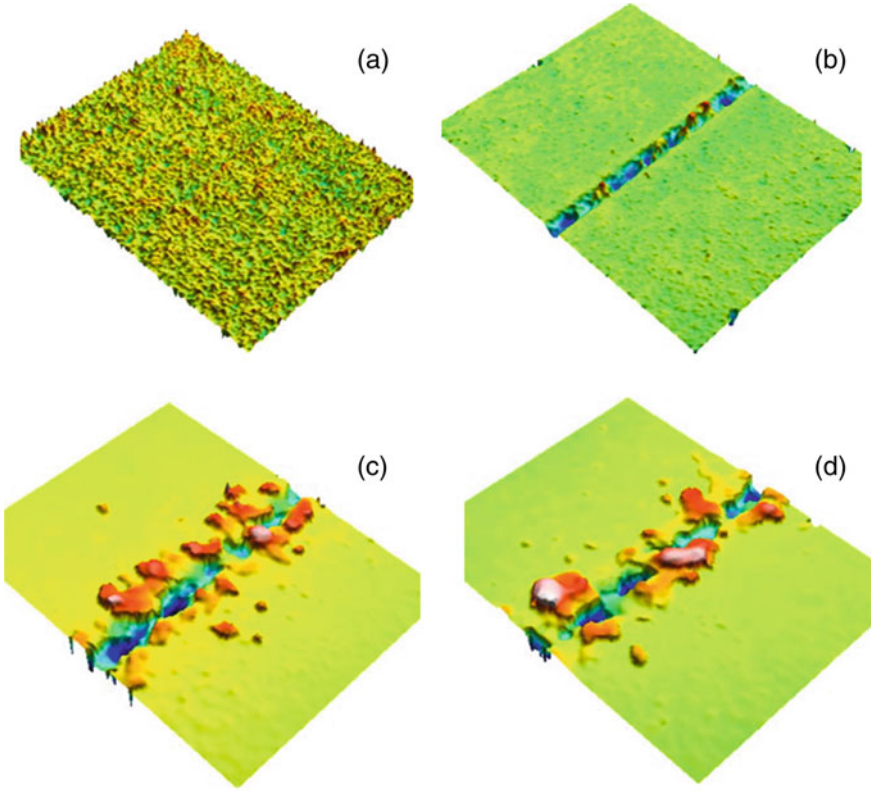

Fig. 6 Appearance of ablation lines at different power density **a** 1.6×10^5 kW/cm^2, **b** 4.8×10^5 kW/cm^2, **c** 8.1×10^5 kW/cm^2 and **d** 14.5×10^5 kW/cm^2 (Scanning speed = 4 mm/s, pulse duration = 46 ns)

depth and surface roughness are shown in Fig. 8a. Square markers in line represent scanning speed effects on surface roughness and values corresponding to the right side y-axis, while triangular markers in line represent scanning speed effects on mean ablation depth and values corresponding to the left side y-axis. The maximum value of mean ablation depth was 22.2 μm at speed 0.2 mm/s, and the minimum value was 2.8 μm at a speed of 100 mm/s.

Meanwhile, the maximum surface roughness value was 6.6 Ra at speed 0.2 mm/s, and the minimum value was 0.5 R_a at a speed of 100 mm/s. Unlike the linear relationship between scanning speed and mean ablation depth found in Q-switched ns fibre laser ablation, both curves show a decreasing exponential function trend with increasing scanning speed in the case of MOPA ns fibre laser ablation Nimonic Alloy 263™. It was found that an increase in scanning speed resulted in higher ablation depth whereas sacrifices surface finish to some extent.

Figure 8b reveals contour distribution of laser scanning speed on X–Y plane at laser pulse duration 46 ns with laser frequency 105 kHz applied in power density 8.1

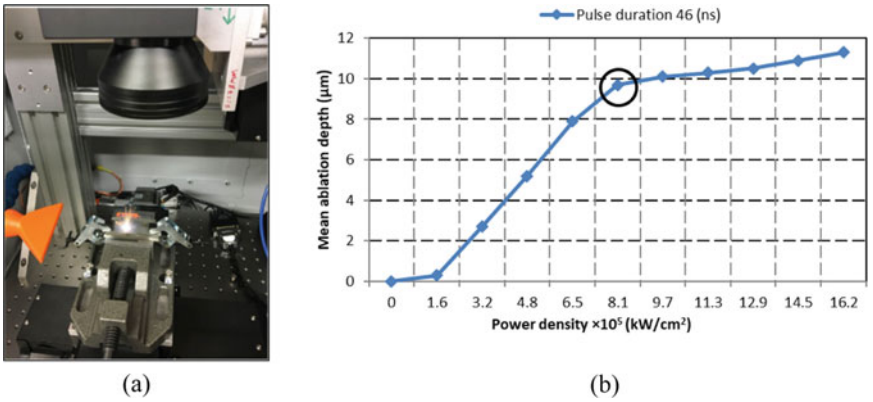

Fig. 7 **a** Laser induced plasma plume (Scanning speed = 4 mm/s, power density = 12.9 × 10^5 kW/cm^2); and **b** effects of power density on ablation depth of nickel super alloy (Pulse duration = 46 ns, scanning speed = 4 mm/s)

× 10^5 kW/cm^2 under PLA technique, which distinctly displays laser scanning speed effects on mean ablation depth and surface finish in the presence of contour density. The contour density gradually becomes sparse in the direction of arrow flow from higher speed to lower speed, which means one specific unit decrease in lower rate gives more sensitive effects on ablation efficiency.

Figure 9a,b reveal the SEM ablated line cross-section profile at scanning speeds 1 mm/s and 60 mm/s, respectively. The cross-section profiles reveal a 'V' shape in ablated grooves, and a large amount of the recast layer is re-solidified alongside the morphology, especially accumulated at the valley bottom in the light grey deep cone-shaped boundary before they were ejected by explosive melt ejection mechanism. Because low scanning speed led to higher pulses overlap, intensive laser pulse continuous shot on the melting pool, and the flux melting pool absorbed more laser energy in a unit area than high scanning speed did, which made ablation topology wider and deeper. With increasing of scanning speed from 1mms/s to 60 mm/s, the length of the recast layer decreased from 618 μm to 371 μm, and kerf width decreased from 105 μm to 67 μm. Meanwhile, a better surface finish at speed 60 mm/s than 1 mm/s in the presence of less spattered debris distributed around the rim. The hierarchy phenomenon of the recast layer shown in Fig. 9a can justify the unevenness of the ablation path. Barely any burnt HAZ was found after MOPA nanosecond fiber laser processing which should be attributed to the high thermal conductivity of Nimonic Alloy 263™.

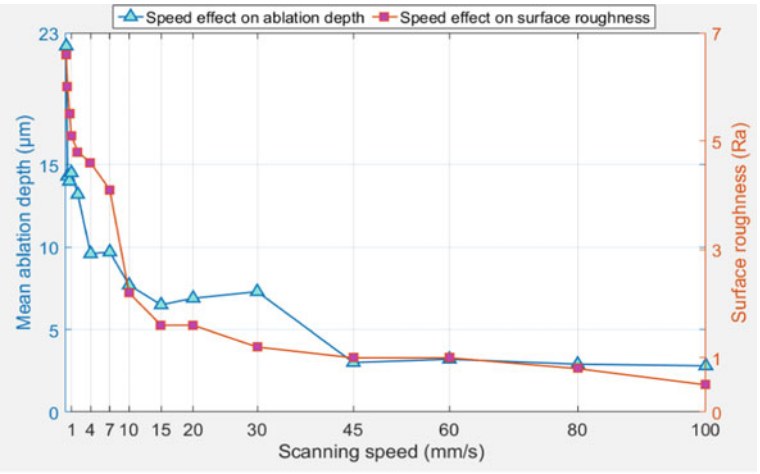

(a)

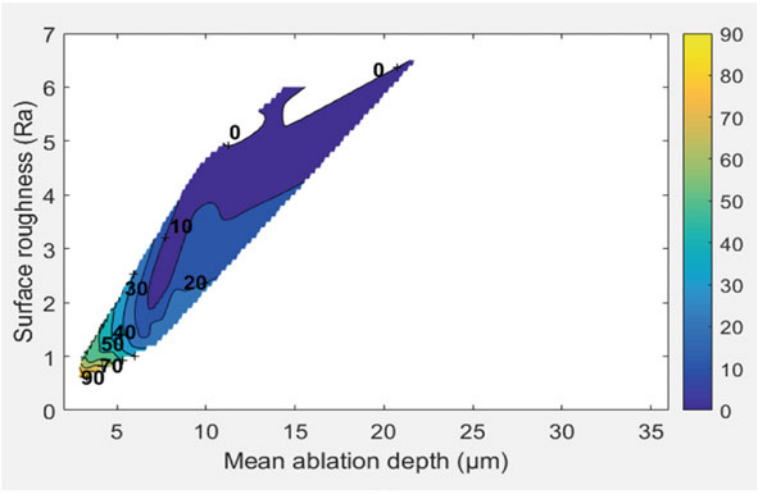

(b)

Fig. 8 Analysis of **a** laser scanning speed effects on ablation depth and surface roughness (Pulse duration = 46 ns, frequency = 105 kHz) and; **b** contour of laser scanning speed corresponds to X-axis mean ablation depth and Y-axis surface roughness (Pulse duration = 46 ns, frequency = 105 kHz, power density = 8.1 × 105 kW/cm^2)

4 Conclusion

The pilot experimental investigations were carried out to explore the effects of process parameters including pulse duration, frequency, power density, and laser scanning

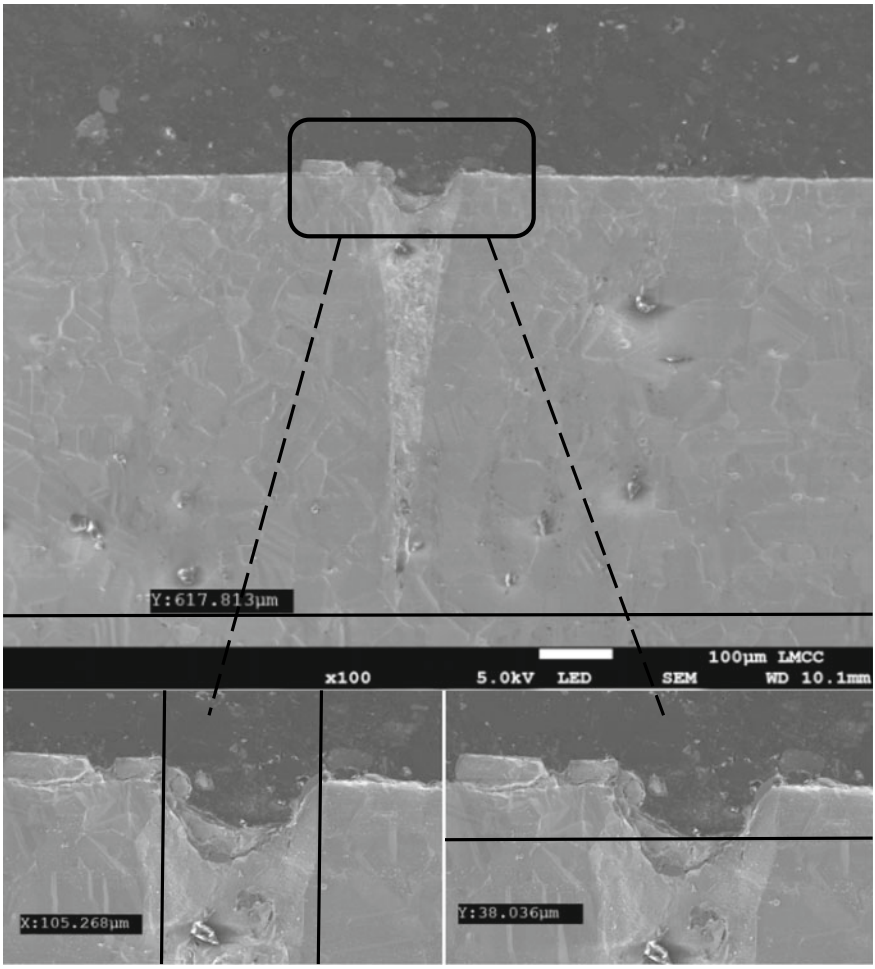

(a)

Fig. 9 Scanning electron microscopy images of **a** morphology of ablation line laser (Scanning speed = 1 mm/s, magnification 100×) and; **b** morphology of ablation line laser (Scanning speed = 60 mm/s, magnification 170×).

speed on high-frequency nanosecond pulsed laser ablation of Nimonic Alloy 263™. The following conclusions are drawn from the essence of the study.

- Nanosecond laser micromachining of Nimonic Alloy 263™ is recognized as an explosive melt ejection-dominated photo-thermal ablation.
- The optimum laser frequency corresponds to a specific laser pulse duration, giving out the maximum peak power in the MOPA laser generation system.

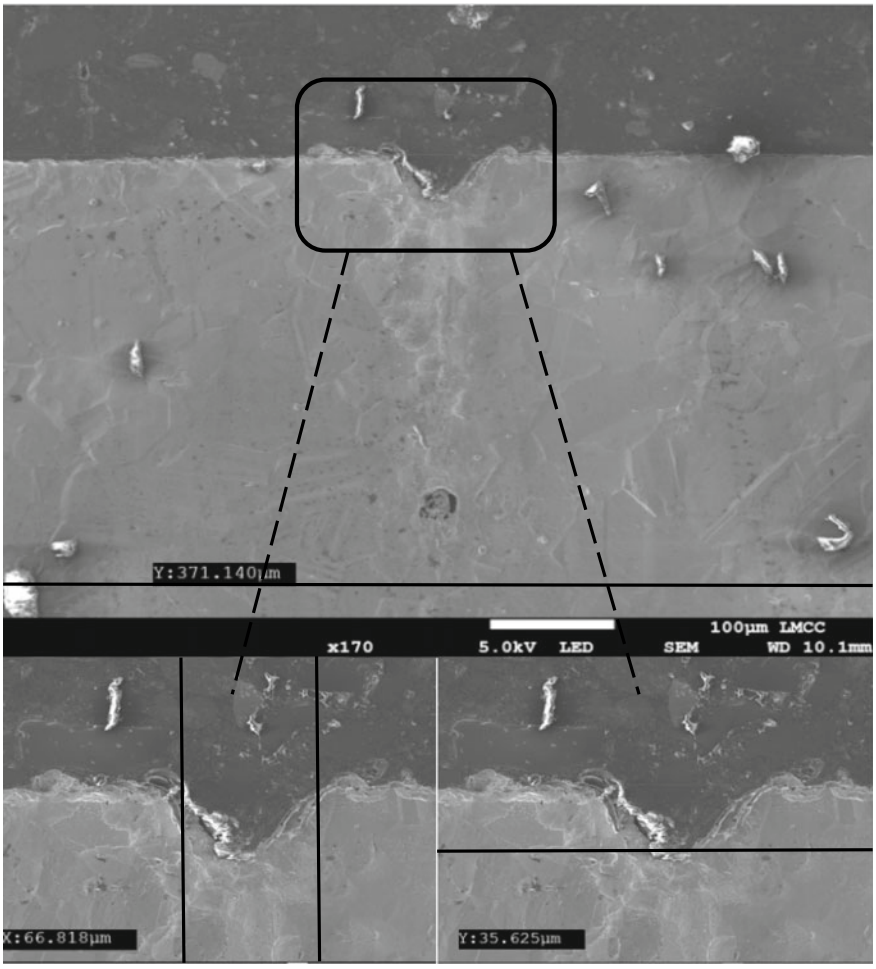

(b)

Fig. 9 (continued)

- An estimated 1.6×10^5 kW/cm^2 is the ablation threshold of the minimal material removal for the ejection mechanisms. With the increase of power density, ablation depth shared a linear ascend till the saturation point at power density 8.1×10^5 kW/cm^2.
- Laser-induced plasma cloud formed after power density reached 8.1×10^5 kW/cm^2. Plasma shield impeded the efficiency of natural laser energy ablating the Nimonic Alloy 263™ substrate.
- The 46 ns of pulse duration with laser frequency 105 kHz at power density 8.1×10^5 kW/cm^2 performed the optimum ablation in substrate penetrating.

- Increasing laser scanning speed leads to higher ablation depth whereas sacrifices surface finish to some extent.
- Few HAZ occurred after MOPA nanosecond fibre laser processing with optimum process parameters.

References

1. Pathak, S.: *Intelligent Manufacturing*. Springer Nature Switzerland AG (2021)
2. Zolpakar, N.A., Yasak, M.F., Pathak, S.: A review: use of evolutionary algorithm for optimisation of machining parameters. Int. J. Adv. Manuf. Technol. **115**, 31–47 (2021)
3. Kong, M.C., Wang, J.: Surface quality analysis of titanium and nickel-based alloys using Picosecond laser. Procedia CIRP **13**, 417–422 (2014)
4. Dubey, A.K., Yadava, V.: Laser beam machining—A review. Int. J. Mach. Tools Manuf **48**(6), 609–628 (2008)
5. Jagdheesh, R., BičišŤová, R., Brajer, J., Mocek, T.: Laser-induced superhydrophobic and oleophobic surface structures on float glass. Lasers Eng. **50**, 289–298 (2021)
6. Jagdheesh, R., Valarmathi, A., Sivakumar, M.: Influence of laser beam polarization on micromachining of crystalline silicon using ultrafast laser pulses. Lasers Eng. **32**, 19–35 (2021)
7. Jagdheesh, R., Kopecek, J., Brajer, J., Mocek, T.: Superhydrophobic microspiked surface structures by ultrashort laser patterning. Surf. Eng. **37**(10), 1266–1276 (2021). https://doi.org/10.1080/02670844.2021.1874651
8. Jagdheesh, R., Ocaña, J.L.: Laser machined ultralow water adhesion surface by low pressure processing. Mater. Lett. **270**, 127721 (2020). https://doi.org/10.1016/j.matlet.2020.127721
9. Jagdheesh, R., Tur, A., Ocaña, J.L.: The effects of pulse period on nanosecond laser microfabrication. Lasers Eng. **37**, 333–343 (2017)
10. Jagdheesh, R., Mudali, U.K., Nath, A.K.: Laser processed Cr–SiC coatings on AISI type 316L stainless steel. Surf. Eng. **23**, 93–98 (2007). https://doi.org/10.1179/174329407X169421
11. You, K., Yan, G., Luo, X., Gilchrist, M.D., Fang, F.: Advances in laser assisted machining of hard and brittle materials. J. Manuf. Process. **58**, 677–692 (2020)
12. Kaul, R., Ganesh, P., Sing, N., Jagdheesh, R., Bhagat, M.S., Kumar, H., Tiwari, P., Vora, H.S., Nath, A.K.: Effect of active flux addition on laser welding of austenitic stainless steel. Sci. Technol. Weld. Join. **12**, 127–137 (2007)
13. Petkov, P.V., Dimov, S.S., Minev, R.M., Pham, D.T.: Laser milling: Pulse duration effects on surface integrity. Proc. Inst Mech. Eng., Part B: J. Eng. Manuf. **222**(1), 35–45 (2008)
14. Shannon, M.A., Mao, X.L., Fernandez, A., Chan, W.-T., Russo, R.E.: Laser ablation mass removal versus incident power density during solid sampling for Inductively coupled plasma atomic emission spectroscopy. Anal. Chem. **67**(24), 4522–4529 (1995)
15. Horn, I., Guillong, M., Günther, D.: Wavelength dependant ablation rates for metals and silicate glasses using homogenized laser beam profiles—Implications for LA-ICP-MS. Appl. Surf. Sci. **182**(1–2), 91–102 (2001)
16. Vladiou, I., Stafe, M., Negutu, C., Popescu, I.M.: The dependence of the ablation rate of metals on nanosecond laser fluence and wavelength. J. Optoelectron. Adv. Mater. **10**(12), 3177–3181 (2008)
17. Jeong, S.H., Borisov, O.V., Yoo, J.H., Mao, X.L., Russo, R.E.: Effects of particle size distribution on Inductively coupled plasma mass Spectrometry signal density during laser ablation of glass samples. Anal. Chem. **71**(22), 5123–5130 (1999)
18. Palanco, S., Conesa, S., Laserna, J.J.: Analytical control of liquid steel in an induction melting furnace using a remote laser induced plasma spectrometer. J. Anal. At. Spectrom. **19**(4), 462 (2004)

19. Bogaerts, A., Chen, Z.: Effect of laser parameters on laser ablation and laser-induced plasma formation: a numerical modeling investigation. Spectrochim. Acta, Part B **60**(9–10), 1280–1307 (2005)
20. Penttilä, R., Pantsar, H., Laakso, P.: Picosecond Laser Processing—Material Removal Rates of Metals (2007). http://www.vtt.fi/files/research/ism/manufacturingsystems/nolamp_2007_picosencond_laser_processing.pdf. Accessed 8 May 2016
21. Lauer, B., Jäggi, B., Neuenschwander, B.: Influence of the pulse duration onto the material removal rate and machining quality for different types of steel. Phys. Procedia **56**, 963–972 (2014)

Laser-Based Post-processing of Metal Additive Manufactured Components

A. N. Jinoop, S. Shiva, and C. P. Paul

1 Introduction

Additive Manufacturing (AM), one of the nine pillars fuelling Industry 4.0, is an advanced manufacturing process used to build complex shaped components directly from 3D model data in a layer-by-layer fashion. There is a rising demand for the broad adoption of AM in various sectors, like—aerospace, medical, automobile, defence, etc. [1]. The increasing demand for AM is primarily due to the various freedoms offered by the technology in terms of shape design, material design, post-processing, and logistics. AM, initially seen as a process for concept modelling and prototyping using polymers, extended to the fabrication of metallic components with the development of high energy sources, like—laser, electron beam and arc. Thus, the term Metal Additive Manufacturing (MAM) is coined. As metals and their alloys are most commonly used in the industrial sector, MAM is widely adopted for building complex shaped and high-performance metallic components. Some of the common issues MAM built components face are loss of alloying elements, high surface roughness, porosity, distortions, cracking, delamination, etc. [2, 3]. The above issues associated with MAM attracts the deployment of post-processing techniques.

A. N. Jinoop (✉) · C. P. Paul
Laser Technology Division, Raja Ramanna Centre for Advanced Technology, Indore, Madhya Pradesh 452013, India
e-mail: anjinoop@gmail.com

C. P. Paul
e-mail: paulcp@rrcat.gov.in

Homi Bhabha National Institute, Mumbai, Maharashtra 400094, India

S. Shiva
Department of Mechanical Engineering, Indian Institute of Technology Jammu, Jammu & Kashmir 181221, India
e-mail: shiva.sekar@iitjammu.ac.in

J. Radhakrishnan and S. Pathak (eds.), *Advanced Engineering of Materials Through Lasers*, Advances in Material Research and Technology,
https://doi.org/10.1007/978-3-031-03830-3_7

Post-processing is an umbrella term that comprises the stages that an AM part experiences after coming of the AM system before the final deployment, which includes mechanical, thermal, and chemical processes. Almost all AM parts need post-processing to realize the essential properties, like—surface finish, geometrical accuracies, microstructure, and mechanical properties. The most commonly used post-processing techniques for MAM built components are heat-treatment, hot-isostatic pressing, and conventional machining [1]. With the innovations in technology, novel post-processing practices are being tried by researchers on MAM built components to modify the microstructure, mechanical properties, and surface quality as per the end-user needs. Laser is one of the potential energy sources for post-processing of MAM built components.

This chapter introduces the MAM processes and the various process-induced issues. Further, it reviews the various advancements in the laser-based post-processing techniques for MAM built components. The chapter compiles the various laser-based post-processing techniques by explaining the process, and its application to MAM built components, including the recent research works. Further, the potential laser-based post-processing techniques that can be used for tailoring the properties of MAM components will also be discussed.

2 Metal Additive Manufacturing (MAM) Techniques

MAM processes can be classified based on three different aspects, i.e. based on the energy source, feedstock material, and the nature of material feeding. The energy sources generally used in MAM are laser, electron beam, and arc and the processes are classified as Laser Additive Manufacturing (LAM), Electron Beam Additive Manufacturing (EBAM), and Arc based Additive Manufacturing, respectively. Based on the type of feedstock material, MAM processes are classified as powder-based MAM and wire-based MAM. In terms of material feeding and deposition methodology, MAM is classified into Powder Bed Fusion (PBF) and Directed Energy Deposition (DED) [1, 2].

PBF is the most commonly used MAM process globally due to its ability to build highly complex near-net-shaped metallic components using a single-step process with minimal machining requirements. Generally, PBF uses laser and electron beams as the energy sources, and they are known as Laser Powder Bed Fusion (LPBF) and Electron beam-based Powder Bed Fusion (EPBF), respectively. LPBF is commercially known by several names such as Selective Laser Melting (SLM), Laser Cusing, Direct Metal Laser Sintering (DMLS), etc. EPBF is commercially known as Electron Beam Melting (EBM). Figure 1a, b present the LPBF and EPBF systems schematic, respectively. LPBF system essentially consists of a feed container, a laser system, Galvano scanner, powder spreading system/roller/scrapper, an overflow container, etc. [4]. A powder spreader is used to spread a thin layer of powder of thickness in the range of 20–100 μm on the surface of the substrate or build plate. Subsequently, the laser is used to selectively melt regions of the powder bed as per the 2D drawing of

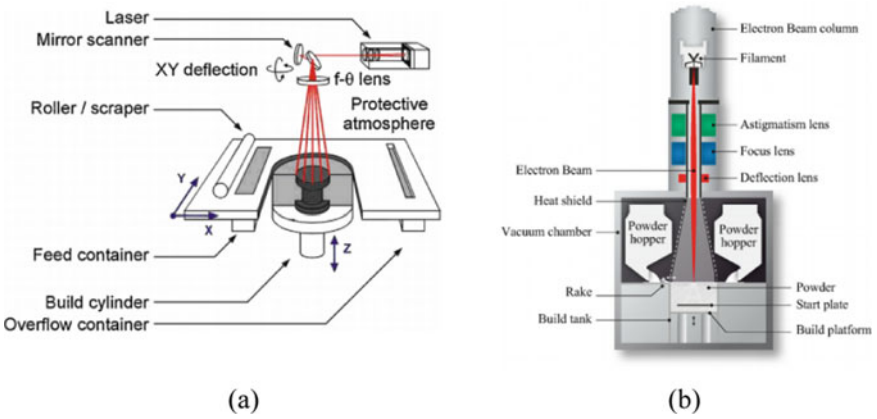

Fig. 1 Schematic of **a** LPBF [4]. **b** EPBF [6]. Fig. 1a Reprinted with permission from Elsevier 2014, and Fig. 1b Reprinted with permission from Elsevier 2018

the first layer. The laser movement is guided by using galvano scanner mirrors. Once the laser melts and consolidates the material in the first layer, the process continues with the powder spreader laying another layer of powder. This process continues till the complete part is built [1, 5]. EPBF system uses a powder hopper, powder spreader/rake, electron beam source, vacuum chamber, and electromagnetic lens. The process is similar to LPBF, while the primary difference lies in three aspects:

a. The electron beam movement is controlled by using the electromagnetic lens system in EPBF, while galvano scanner mirrors in LPBF control the laser movement.
b. EPBF takes place in vacuum conditions, while LPBF requires only a control atmosphere for the operation. The controlled atmosphere is generally achieved by using Argon or Nitrogen gas.
c. Preheating is not mandatory in LPBF, while a preheating cycle is used before the deposition of each layer in EPBF. Preheating is carried out by scanning the electron beam over the pre-placed powder bed at a high scan speed [6].

The major process parameters controlling PBF processes are the beam power (P), scan speed (V), hatch spacing (H), and layer thickness (T). Beam power is the rate of energy provided by the laser/electron beam source for melting of the material; scan speed is the speed at which the energy source is scanned over the pre-placed powder bed; hatch spacing is the distance between the centre of two successive tracks (basic building block in MAM) in a layer; layer thickness is the thickness of powder layer spread on the surface of the substrate/previously deposited layer. The effect of all the above parameters is analyzed using a combined process parameter known as Volumetric Energy Density (VED), as shown in Eq. 1.

$$\text{VED} = \frac{P}{VHT} \tag{1}$$

DED is attractive for building near-net-shaped components with intricate shapes, multi-material composition, high build rate, and large size. DED process uses an energy source to create a melt pool on the surface of a substrate onto which the raw material is added. The movement of the energy source or substrate is governed by design, which allows the deposition of the feed material as per the required geometry. Once a single track is deposited, overlapped tracks are deposited to build a layer. Subsequent to the deposition of a single layer, the energy source creates a melt pool on the previously built layer onto which feedstock is added, which deposits the material as per the required geometry to form the second layer [1]. The process continues till the final part is built. The most commonly used energy sources in DED are laser, electron beam and arc and are known as Laser Directed Energy Deposition (LDED), Electron beam Directed Energy Deposition (EDED), and Wire Arc Additive Manufacturing (WAAM), respectively [2]. Figure 2a–c present the schematic of LDED, EDED, and WAAM, respectively. As discussed earlier, EDED requires a vacuum for its operation, while LDED and WAAM generally require shielding gas for protecting the melt pool from oxidation. The most common process parameters in DED are beam power, scan speed, and material feed rate at a constant laser spot

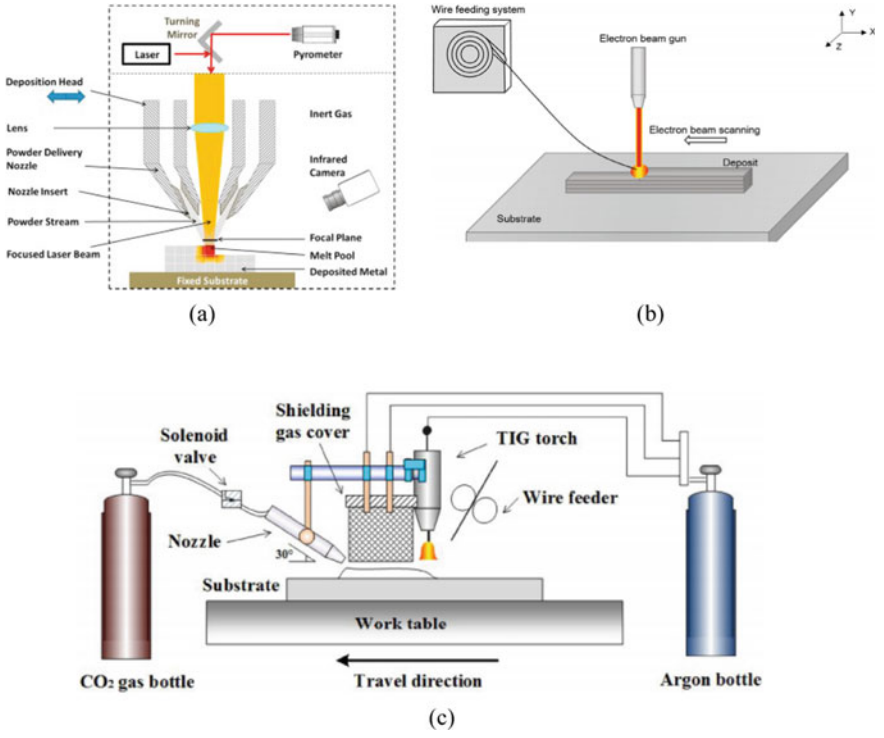

Fig. 2 Schematic of **a** LDED [7]. **b** EDED [8]. **c** WAAM [9]. Fig. 2a Reprinted with permission from Elsevier 2015, Fig. 2b Reprinted with permission from Elsevier 2018, Fig. 2c Reprinted with permission from Elsevier 2018

diameter, and three combined process parameters used in DED for developing process window for a given material are:

a. **Energy per unit length (EL)**: The ratio between the beam power and scan speed controls the amount of energy available per unit length for the deposition [1]. A low value of EL results in incomplete fusion of material, leading to discontinuous deposition, while a very high value of EL leads to cracking and excessive oxidation.
b. **Material feed per unit length (MFL)**: The ratio between the material feed rate and scan speed determines the amount of feedstock material available per unit length of the deposition. A low value of MFL results in discontinuous deposition due to the unavailability of sufficient material, while a very high value of MFL will yield a higher deposition rate [1, 10].
c. **Energy per unit material feed (EMF)**: The ratio between the beam energy and material feed rate determines the amount of energy available for deposition of the unit mass of feedstock [11, 12]. A low value of EMF results in discontinuous deposition due to the unavailability of sufficient energy for melting and depositing a given mass of feedstock, while a very high value of EMF will result in cracking [11].

3 Defects and Common Post-processing Techniques

As MAM is a process that involves high energy density, fast cooling rates, and a layer-by-layer build approach, the components are observed to have defects. The presence of these defects attracts the deployment of post-processing treatments. Some of the common defects and post-processing treatments are:

a. **Loss of alloying elements**: As MAM uses high energy density sources to melt feedstock material, localized material loss is possible during the deposition. One of the examples is in the report by Gaytan et al., where the reduction in the Al content by 10–15% is observed during EPBF of Ti–6Al–4V. The loss corresponds to a reduction of 0.6–1.0 wt% from the nominal composition [13]. The primary reason for the above loss is the vaporization of the material from the melt pool due to excess temperature in the melt pool. Generally, the loss of alloying elements is controlled by optimizing the process by controlling the melt pool temperature values and not post-processing techniques.
b. **Porosity**: The three major types of porosity observed in MAM built components are:

    - Gas porosity: These are generated either due to porosity present inside the powder particles formed during powder production or entrapped gases/vapours inside the melt pool. The most commonly used technique for powder production is atomization. The widely used atomization techniques for generating powders for MAM are gas atomization and plasma atomization due to their ability for producing spherical powders. There are chances

of gas entrapment inside the powder during gas atomization, which can get transferred to the final component. Further, during MAM, the shielding gases such as Argon and Nitrogen are generally used to control melt pool oxidation. Argon is the most commonly used gas for processing oxidation prone materials. Argon gas is insoluble in the liquid metal inside the melt pool; they remain inside it unless they flow out of the melt pool. Nitrogen is soluble in liquid metal, but it cannot process all materials [2].

- Lack of fusion porosity: Lack of fusion porosity is formed due to insufficient penetration of the melt pool of one layer into the previous layer/substrate (inter-layer porosity) or inadequate consolidation between consecutive tracks in a layer (intra-layer porosity). This is primarily due to the lower energy used for material deposition. They are generally irregular in shape.
- Keyhole porosity: When the MAM process is carried out at a very high power density, melting occurs in keyhole mode. If this mode of operation is not controlled carefully, the keyhole becomes unstable and repetitively forms and breakdown, which leaves voids inside the deposit consisting of entrapped vapour.

Porosity is generally controlled during the processing stage and post-processing stage. The commonly used post-processing technique to control porosity is the Host Isostatic Pressing (HIPing), where the part is taken to high temperature, and Argon gas is used to apply pressure from all the directions equally, which closes the sub-surface cracks/pores [14]. The HIP is commonly applied to PBF built components.

c. **Surface roughness**: Surface roughness is observed to be higher in MAM built components than in conventional manufacturing techniques. The major factors governing the surface roughness are process parameters, build orientation, support type selection, powder particle size distribution/wire diameter, scan strategy, etc. The surface roughness in MAM built components is typically more than 10 μm [15]. Machining is the most commonly used post-processing technique for reducing surface roughness [16].

d. **Cracking and Delamination**: Cracks are formed during the solidification process, and the two types of cracks generally seen in MAM components are solidification cracks and grain boundary cracks. Solidification cracks are formed when too much energy is used for deposition and occurs due to the stresses generated between solidified regions and areas that are yet to solidify. Grain boundary cracking nucleates/takes place along the grain boundaries of the material and are material dependent. They are a function of the precipitate phases formed and the grain boundary morphology. Delamination is a macroscopic defect that leads to the separation of nearby layers due to incomplete fusion between layers and large values of residual stresses [2, 3]. Cracking and delamination can be controlled during the process by tweaking the process parameters and process conditions. A post-processing technique commonly used to heal cracks is HIPing, while post-processing treatments cannot eliminate delamination.

e. **Residual stress and distortion**: Residual stress is stress that lies within a material after the removal of applied stress. It is common in MAM components

due to the large thermal gradients generated during the process. It negatively impacts the mechanical properties and acts as a driving force for changes in grain structure [2]. MAM built components primarily have tensile residual stress on the surface of the component, which allows the crack propagation to take place swiftly, resulting in lower fatigue life [17]. During MAM, when the high energy source interacts with the material, the top surface tries to expand due to the higher temperature at the surface. However, the bottom layer prevents expansion during this stage. This induces compressive stress at the top surface. During melting, the stress reduces to zero. Once the energy source moves away, solidification and cooling occur, inducing tensile stress on the top surface and compressive stress beneath it. This mechanism is known as Temperature Gradient Mechanism (TGM) [18]. This can result in distortions and variations from the intended dimensions. Residual stresses and distortions can be controlled by processing and post-processing methods. The post-processing method used to replace tensile stresses on the surface with compressive stresses is shot peening [19]. Shot peening uses hardened balls bombarded to the part surface using high pressure, leading to plastic deformation and generating beneficial residual compressive stress on the surface [20]. Distortions are reduced by using machining or polishing operations to bring the part dimensions close to the intended dimensions.

4 Laser-Based Post-processing Techniques

4.1 Laser Remelting

Laser remelting (LR) is one of the techniques applied to conventionally built components to tailor the surface texture, mechanical properties, stress pattern, etc. During LR, a laser source is used to melt the surface and subsurface region of the built components (depth: 10–1000 μm), and the laser is moved as per the required geometry. Subsequent to the melting of each track, the melt pool rapidly solidifies to generate a surface with tailored material properties [21].

During MAM, the LR process can be carried out either on the top surface of the part or in a layer-by-layer fashion. In the former case, LR modifies the surface properties by refining grain structure and improving the surface hardness, wear resistance, corrosion resistance, surface finish, relative density, etc. The process is also known as Laser Surface Melting (LSM) [21]. This can be completed using the same laser source used for deposition or a separate laser source. In the case of layer-by-layer LR or sequential layer-by-layer remelting (SLLR), remelting is applied after depositing each layer, where the same layer is re-melted using the laser as per the requisite geometry before deposition of the next layer [21]. By using LR after each layer, ~100% density can be achieved through MAM. However, on the other side, it can increase the manufacturing time, which increases the related costs. Layer-by-layer LR is generally carried out using the same laser used for material deposition.

Researchers have attempted LSM on different MAM built materials, like—SS 316L built using LPBF and LDED [21–24], Fe-Co based alloys built using LDED [25], Co-Cr alloy built using LPBF [26], etc. The studies indicate significant improvement in surface quality, surface hardness, and wear resistance. Figure 3 presents the effect of laser remelting on the surface profile of LDED built SS 316L samples [23]. Laser remelting also improves the surface hardness, wear-resistance and refines the grain structure. Figure 4 presents the effect of LSM on the microstructure, which indicates grain refinement after deploying LSM [25]. For Fe-Co alloys, remelted samples show lower coercivity and higher saturation magnetization.

Recently LSM studies are carried out on the inclined surfaces built using LPBF, which shows that surface roughness less than 1 μm is achievable by combining LSM

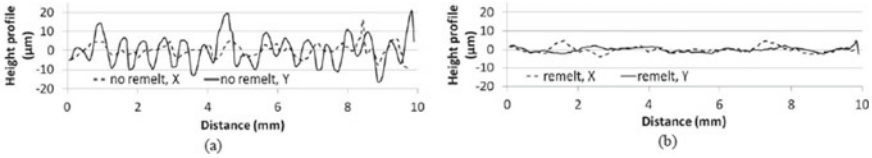

Fig. 3 Surface profile data of LDED built SS 316L **a** without remelting [23], **b** with remelting [23]. Fig. 3a and 3b, Reprinted with permission from Elsevier 2013

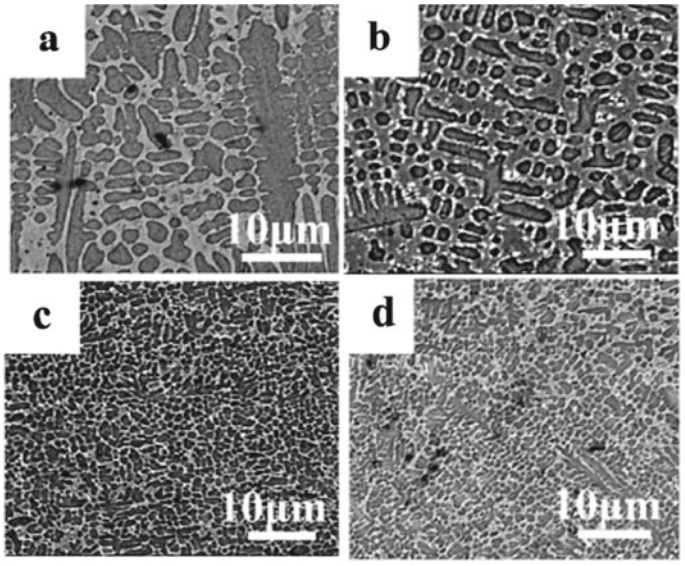

Fig. 4 Scanning electron microscope micrographs of un-remelted and remelted Fe–Co alloys: **a** un-remelted and deposited using laser power of 1400 W, **b** un-remelted and deposited using laser power of 1600 W, **c** re-melted at 2000 W and deposited using laser power of 1400 W and **d** re-melted at 2000 W and deposited using laser power of 1600 W [25]. Fig. 4a–d, Reprinted with permission from Elsevier 2019

with LPBF. During LSM of inclined surfaces, exposure time plays a significant role in controlling the surface quality. It is worth noting that LSM parameters should be optimized separately and the parameters optimized for LPBF might not be suitable for LSM. In addition, the LSM process parameters should be optimized separately for horizontal, vertical, and inclined surfaces [24].

Layer-by-layer LR/SLLR strategy is primarily used in LPBF on various materials such as NiTi [27], Cu-Al-Ni-Mn shape-memory alloy [28], AlSi10Mg [29], Ti–5Al–2.5Sn alloy [30], etc. The studies indicate that layer-by-Layer LR can significantly improve the relative density and reduce the surface roughness. In one of the studies by Wei et al. [30], it is observed that the improvement in the density has improved the material's ductility, while the strength values remain unaltered. In LDED, Koike et al. investigated laser remelting of LDED built Inconel 625 wall structures after 10-layer deposition intervals. A reduction of 61% in porosity and an improvement of 26% in hardness is observed [31]. Xin et al. [32] investigated the microstructure and mechanical properties of SS 316L thin-wall structure by combining LDED and laser remelting. Laser remelting of single track laser clad layer show reduction in the porosity, improvement in hardness, and increase in dendrite length. SLLR of the thin wall revealed regular and uniform microstructure.

The combination of laser remelting and LDED significantly improved the built structure's ultimate tensile and yield strength. Yu et al. [33] investigated the effect of SLLR on the microstructure, and mechanical properties of LDED built 17–4 PH stainless steel. The deployment of SLLR reduced the porosity level, and mechanical anisotropy in the LDED built sample. SLLR at 15 J/mm^2 revealed the least porosity and near isotropous UTS. However, it was concluded that the effect of layer-by-layer LR on the anisotropy in ductility is less because of the unavoidable interlayer defects.

One of the recent advances in this domain is the combination of laser-generated shock waves and LR to reduce the surface roughness of inclined surfaces. This novel approach uses a double-laser arrangement with a continuous wave and a pulsed laser. At first, a nanosecond pulsed laser generates shock waves, which selectively remove the powder from the inclined surfaces. The newly exposed surfaces can be consequently re-melted using a continuous wave laser or treated with a pulsed laser. The study reveals that the surface texture can be considerably enhanced for surface inclinations up to 45°, if an adequate powder removal efficiency is reached. The powder removal boundaries depend primarily on the depth, inclination angle, volume of powder to be removed, and part shape. If the powder is not eradicated, it can get attached to the part surface during melting, deteriorating product quality. Powder removal efficiency can be changed by varying the scanning strategies and using dynamic focussing systems [34].

4.2 Laser Polishing

The surface roughness of MAM built components is typically more than 10 μm owing to surface waviness due to the presence of scan tracks, layered structure, and

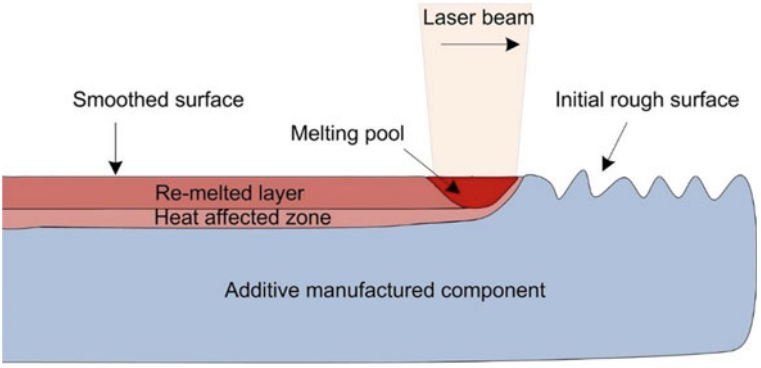

Fig. 5 Schematic of LP process [35]. Reprinted with permission from Elsevier 2018

the presence of partially melted particles [15]. Laser polishing (LP), an extension of the laser remelting process, is considered a prospective technique to minimize the surface roughness of MAM parts. LP works mainly based on the melting initiated by the thermal energy of the laser irradiation.

Figure 5 presents the schematic of the LP process. During LP, morphological peaks touch the melting temperature and melt rapidly when a laser beam of adequate energy density impacts the built surface. Subsequently, a molten pool is created on the build surface, and the liquid material redistributes to a similar level due to surface tension and gravity. Once the laser leaves, a sudden drop in the temperature of the laser-irradiated area is seen, which leads to molten pool solidification and reduction in the surface roughness [15]. The significant advantages of LP over conventional mechanical polishing methods are the following:

- Surface morphology is changed without altering the bulk properties
- High automation
- Environmental friendly
- Polishing of difficult to machine materials
- Polishing of complex geometries.

Literature shows that laser polishing is carried out on several MAM alloys such as LAM built Titanium alloys (Ti–6Al–4V and Ti–6.5Al–3.5Mo–1.5Zr–0.3Si) [15], LPBF built Co–Cr–Mo alloy [36], LPBF built Ti–6Al–4V [37], LDED built SS 316L [38], EPBF built Ti–6Al–4V [35], LPBF built CoCr alloys [39, 40], LPBF built IN718 [41], LPBF built Maraging steel [42], etc.

The effect of LP on the surface topography and surface roughness of MAM built components is presented in Fig. 6. The surface roughness of the as-built LPBF sample is ~5 μm, while the surface roughness of CoCr laser polished using optimal process parameter setting is ~0.45 μm [40]. Similarly, LP on LPBF IN718 showed a reduction of Ra from 7.5 to 0.1 μm [41]. The above studies used continuous-wave laser for LP experiments. Another approach combines continuous-wave laser polishing (macro polishing) followed by pulsed laser polishing (micro polishing), where the initial

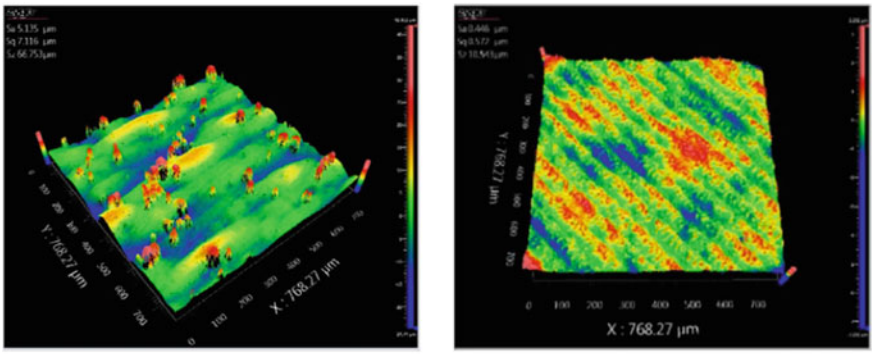

Fig. 6 Optical profiler images of LPBF built CoCr alloys **a** as-built, **b** laser polished [40]. Fig. 6a, b, Reprinted with permission from Elsevier 2018

roughness is brought down by ~70–90% by macro laser polishing. Through this stage, homogenization of the remelted surface is also achieved by redistribution of the alloying elements. Subsequently, a pulsed laser is used for micro-polishing, leading to an additional reduction in the micro and meso roughness by 50%, including spatial wavelengths up to 40 μm. Thus, for minimizing the micro-roughness and increasing the gloss level to the maximum, a common treatment of continuous and pulsed laser radiation must be carried out [43].

In addition to reducing the surface roughness, LP improves the surface properties such as corrosion resistance, hardness, and wear resistance. In terms of microstructure, studies on Ti–6Al–4V shows that LAM built sample show the presence of needle-shaped α phase and β phase, while acicular martensite α′ is seen in the LP samples as shown in Fig. 7. The zone subjected to LP also shows uniform distribution of elements, which is attributed to the formation of the martensitic α′ phase after rapid melting and cooling during laser processing. The effect is also reflected on the X-ray diffraction data presented in Fig. 7d, while the laser-polished surface mainly consists of the α'martensitic phase without β phase [15].

Studies also show that microhardness increased by 32% and 27% for Ti–6Al–4V and IN718 alloys, respectively, after laser polishing. In the case of Ti–6Al–4V, the increase in hardness is attributed to the formation of α'martensitic phase [15], while in IN718, the effect is attributed to the grain refinement during LP [41]. Supporting the increase in the hardness of the material, wear resistance also increases significantly with LP. Studies by Wang et al. on LPBF built Co Cr alloy shows that LP samples have 30% better corrosion resistance than CoCr alloys built using other thermo-mechanical treatments such as casting, annealing, ultrasonic, and hot forging [40].

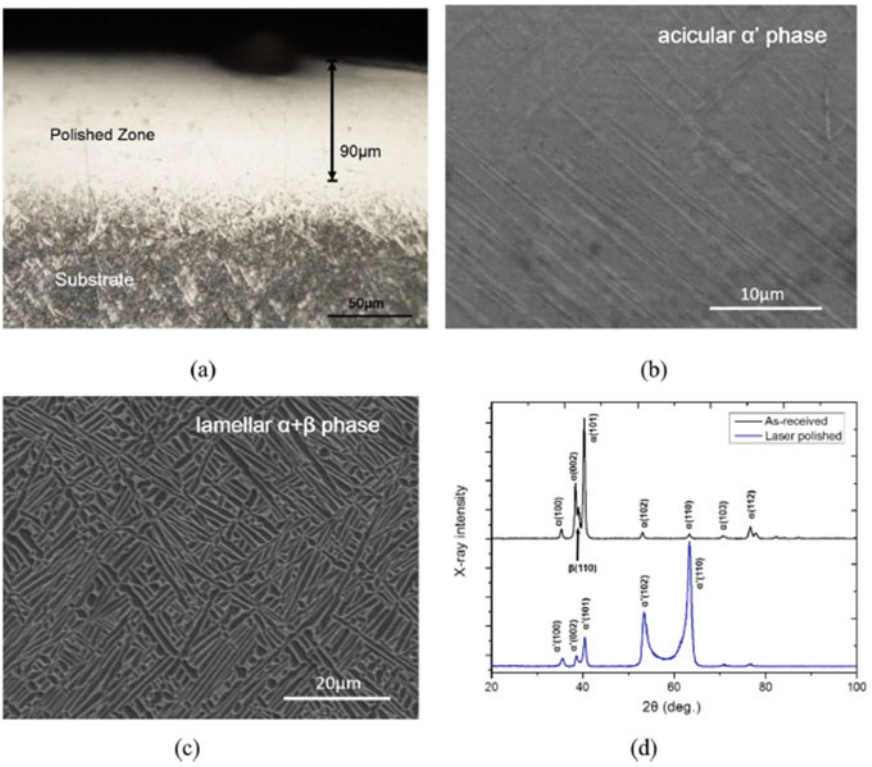

Fig. 7 Laser polished LPBF built Ti–6Al–4V, **a** cross-section, **b** microstructure of polished region, **c** microstructure of as-built region. **d** X-ray diffraction data [15]. Fig. 7a–d, Reprinted with permission from Elsevier 2017

4.3 Laser Shock Peening

Laser shock peening (LSP) is one of the non-thermal surface treatment techniques used to improve the fatigue life of engineering components, especially jet engine fan, compressor blades, etc., subjected to variable loading conditions. LSP induces residual compressive stresses, required strains and tailored microstructures in the metallic components. Thus, LSP hinders the crack propagation and thereby improving the fatigue life of components. In addition, it improves the corrosion resistance, hardness, and wear resistance of components. LSP is an attractive post-processing technique for MAM built components as the surface of the MAM components are generally dominated by tensile residual stresses due to Temperature Gradient Mechanism (TGM). The tensile residual stresses on the surface of these components can reduce the fatigue life as it allows for easy crack propagation [17].

LSP system mainly consists of a transparent layer, sacrificial/opaque layer, pulsed laser, focusing optics, and sample, as shown in Fig. 8. The opaque layer prevents the direct interaction between the focused laser beam and the sample, preventing the

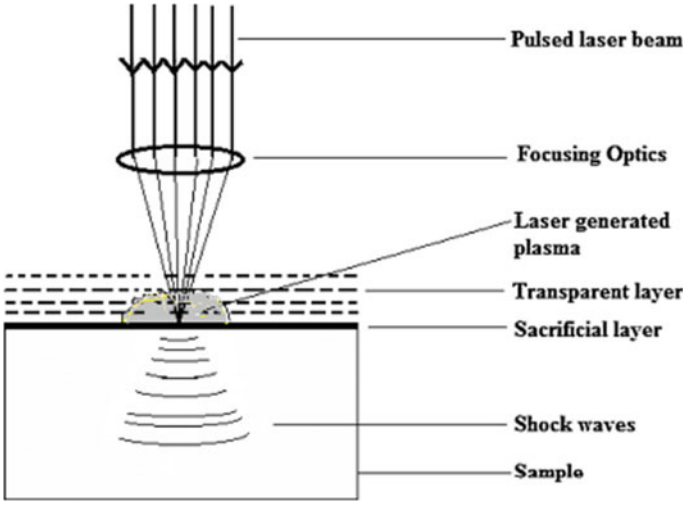

Fig. 8 Schematic of LSP process [46]. Reprinted with permission from Elsevier 2018

thermal effect on the sample surface. The transparent layer allows the laser to pass through it, and the laser beam strikes on the opaque layer. Subsequently, the opaque layer vaporizes and generates plasma by constantly absorbing the laser energy. The transparent layer prevents the expansion of the generated plasma and generates a high-pressure shock wave on the metal surface. If the magnitude of the peak pressure surpasses the materials dynamic yield strength, plastic deformation occurs [17, 44, 45].

Researchers have attempted to perform LSP on LPBF, LDED, and WAAM built components. Table 1 presents some of the works carried out in this domain. Recently, in addition to metallic alloys, LSP is also applied to composites built using LPBF as reported by Chen et al. [54]. The surface porosity significantly reduces with an increase in the number of LSP impacts as LSP induces severe plastic deformation on the sample surface, which closes the surface pores. In addition, the oxidation resistance and micro-hardness of the as-built part increase after LSP and with an increase in the number of LSP shots. Figure 9 presents the micro-hardness and residual stress and depth variation, where LSP 1, LSP 2 and LSP 3 indicate 1, 2 and 3 shots, respectively. An increase in the number of LSP shots from one to two leads to an increase in the subsurface hardness by 2.3%, while it increases by 4.3% from two to three shots. It may be noted that the saturation effect is not seen in the hardness values, which can be due to a reduction in the porosity values with an increase in the LSP shots [54].

One of the interesting advances in this domain is the application of the "3D LSP process" by a research group from Ecole Polytechnique Fédérale de Lausanne (EPFL), Switzerland, in which LSP is performed during the layer-by-layer fabrication process [59]. THE 3D LSP process is reported on SS 316L in which LSP is done after building a few layers during LPBF to attain a larger depth of residual compressive

Table 1 LSP on some of the common MAM built materials

S. No	MAM process	Material	References
1	LDED	Ti6Al4V	Guo et al. [47, 48]
2	LPBF	AlSi10Mg	Du Plessis et al. [49]
3	LPBF	Martensitic 15-5 precipitation hardenable steel	Kalentics et al. [50]
4	LPBF	Austenitic stainless steel 316L	Kalentics et al. [50], Morgano et al. [51]
5	LPBF	Inconel 718	Jinoop et al. [17]
6	WAAM	2319 Aluminum alloy	Sun et al. [52]
7	LPBF	Ti6Al4V alloy	Lu et al. [53]
8	LPBF	TiC/Inconel 625 nanocomposites	Chen et al. [54]
9	LDED	CoCrFeMnNi high-entropy alloy	Tong et al. [55]
10	WAAM	Ti17 titanium alloy	Chi et al. [56]
11	LDED	TA15 titanium alloy	Chi et al. [57]
12	LDED	Ni25/Fe104 coating	Lu et al. [58]

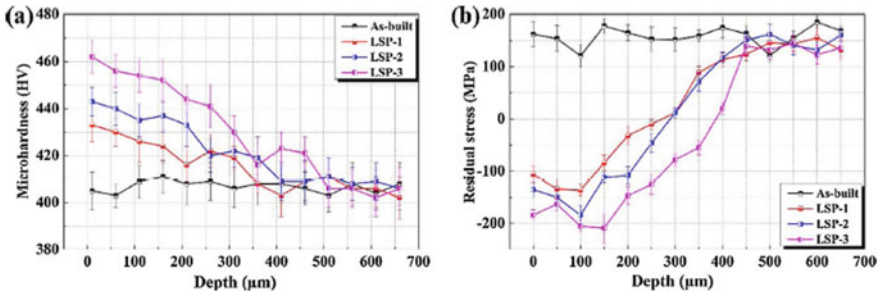

Fig. 9 Variation of **a** micro-hardness. **b** Residual stress along with the depth [54]. Fig. 9a, b, Reprinted with permission from Elsevier 2020

stresses. Figure 10a presents the variation in the residual stress distribution in as-built, conventional shot-peened, surface LSP processed and 3D LSP processed samples. 3D LSP shows a higher depth of compressive stresses, which will help to increase the fatigue life of LPBF built components. Figure 10b presents the variation in the residual compressive stresses with depth, where 1 l, 10 l, and 30 l represent the number of layers after LP is applied. 3D LSP can generate deeper compressive residual stresses than those generated by a normal LSP process. Lately, Lu et al. approached 3D LSP differently on Ti–6Al–4V by applying LSP without coating (LSP-wc) and coating (LSP-c) for intermediate layers and top layer, respectively. The key reasons for using LSP-wc during the fabrication are to generate compressive residual stress below the surface of a layer and to increase surface quality by eliminating some

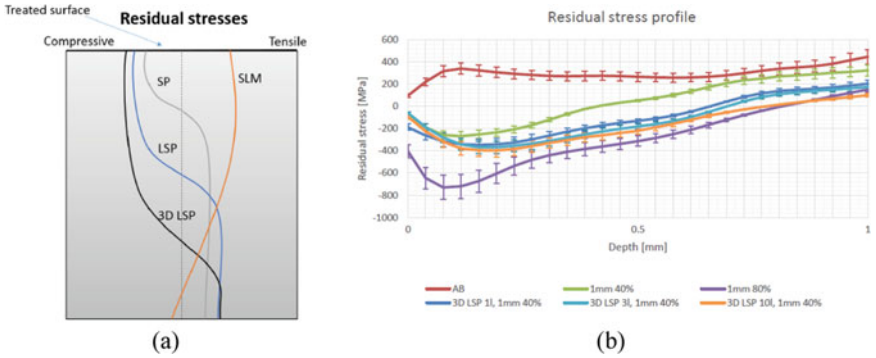

Fig. 10 3D LSP, **a** typical residual stress distribution, **b** residual stress profile at different conditions [59]. Fig. 10a, b, Reprinted with permission from Elsevier 2017

amount of material. Finishing LSP-c imparts compressive residual stress on the top layers. The above technique improves the tensile behaviour and surface hardness of the built structures with higher compressive stress values on the top surface for the peened sample compared to that of as-built samples without peening [53].

4.4 Laser Micromachining

MAM built components have a layer of partially melted powders adhered to their surface, which are generally removed using conventional techniques such as deburring (manual and tumble), CNC machining, media blasting, wet chemical processes. ultrashort laser-based laser micro-machining [60–66] is one of the techniques researched to improve the surface quality of MAM built structures. The primary advantages of using laser micro-machining as a technique for improving surface quality are:

a. Lack of physical contact, which avoids tool wear of the machining system
b. Minimal heat affected zone
c. Precise and clean features can be built [60].

During laser micromachining, plasma mediated ablation takes place, which results in the transformation of material directly from solid-state to vapour state, with no intermediate phases. When a pulsed laser, with pulse duration in femtosecond range, interacts with a material, absorption of multiple photons take place, resulting in ionization and material breakdown. Generally, the thermal diffusion time of metals is in the order of 10 ps. The major difference between the laser used in MAM and laser machining is that the laser used in MAM is generally continuous wave, while laser micromachining uses pulsed lasers. During MAM, the interaction timescale is more than the thermal diffusion time resulting in the melting and fusing of particles, while the interaction timescale is too small compared to thermal diffusion time during

laser micromachining. Figure 11 presents the variation in the surface quality of the MAM built component after laser micromachining [60].

With the help of laser micromachining, it is possible to generate nano-gratings and micro-cones on the surface of MAM components, as shown in Figs. 12a, b, respectively. Nanogratings can be generated with a single laser pass using a femtosecond laser with a pulse energy of 5 μJ and a processing speed of 20 mm/s. The nanogratings can encrypt information onto a component, such as serial numbers or verification measures. They are added at specific locations such that the functionality of the part will not be affected. In the case of micro-cone structures, the material is selectively ablated from the component surface, which aids to generate hydrophobic effects for applications, where the surface is required to remain free of liquid [60].

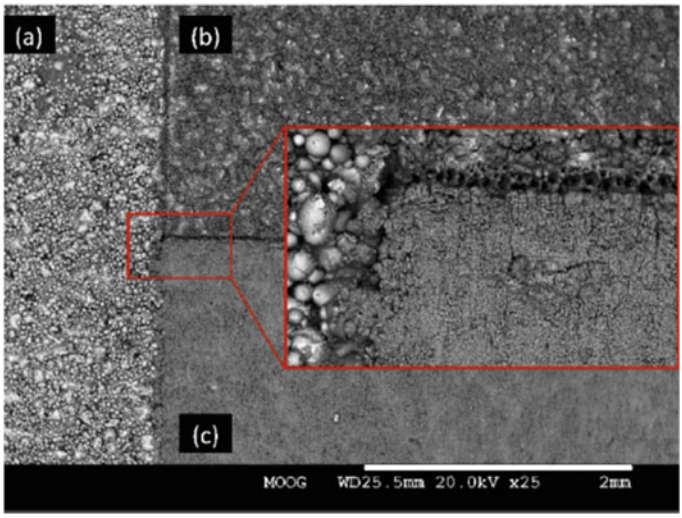

Fig. 11 Surface topography **a** as-built surface, **b** laser micromachining with laser perpendicular to AM layering direction, **c** laser micromachining with laser parallel to AM layering direction [60]. Fig. 11a–c, Reprinted with permission from Elsevier 2019

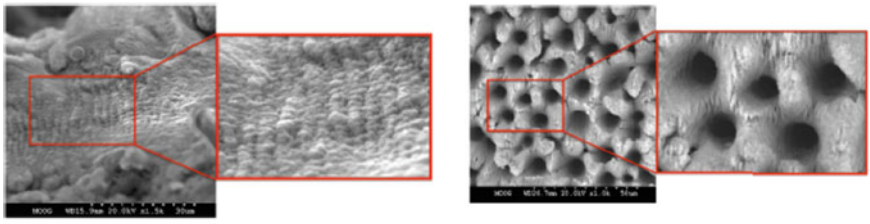

Fig. 12 Laser micromachined, **a** nano-gratings, **b** micro-cones [60]. Fig. 12a, b, Reprinted with permission from Elsevier 2019

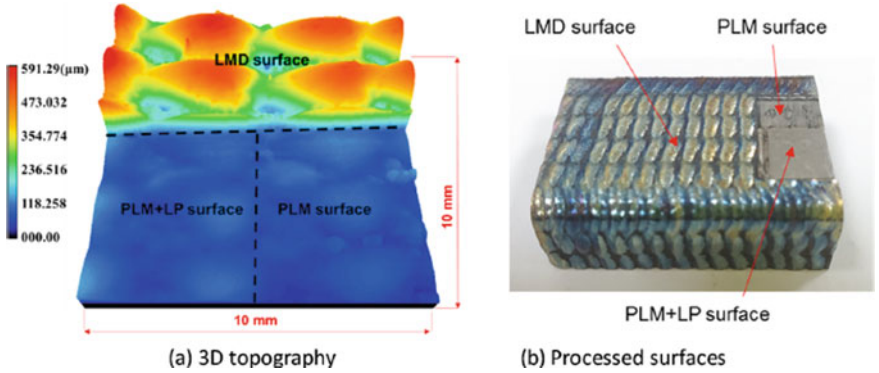

Fig. 13 Effect of different laser processing on LDED built component [67]. Fig. 13a, b, Reprinted with permission from Elsevier 2021

Another recent application is combining pico-second laser machining (PLM) with laser polishing to improve the surface quality of LDED built components, as shown in Fig. 13. LDED built component had an initial roughness of 6.62 μm, brought down to 4.89 μm by PLM. This is subsequently reduced to 0.55 μm by LP, which shows that the maximum improvement in the surface roughness is ~91.7% [61].

4.5 Laser Welding

The joining of MAM built components is one of the research interests primarily due to the following reasons:

a. During MAM, it is impossible in many situations to have all the features incorporated in a single part as the maximum part size is restricted by the machine build volume.
b. Different features require different part orientations
c. Cost aspects [68].

Laser welding is one of the joining techniques being researched for the joining of MAM built components. The primary difference between laser welding and MAM lies in that MAM uses an energy source to join shapeless materials, while in laser welding, the fusing of a seam between typically two solid parts takes place. Generally, laser welding needs a surface roughness of 1.6 μm or better, which is not seen in MAM built components. The typical surface roughness of MAM built components is in the range of 10 μm. Thus, post-machining is necessary before laser welding of MAM components [68]. However, a study by Zapf et al. shows that the maximum welding speed of MAM built parts is 67% higher than conventional parts, attributed to the higher surface roughness of MAM built components. As higher roughness of MAM components leads to multiple laser beam reflections, higher energy coupling is

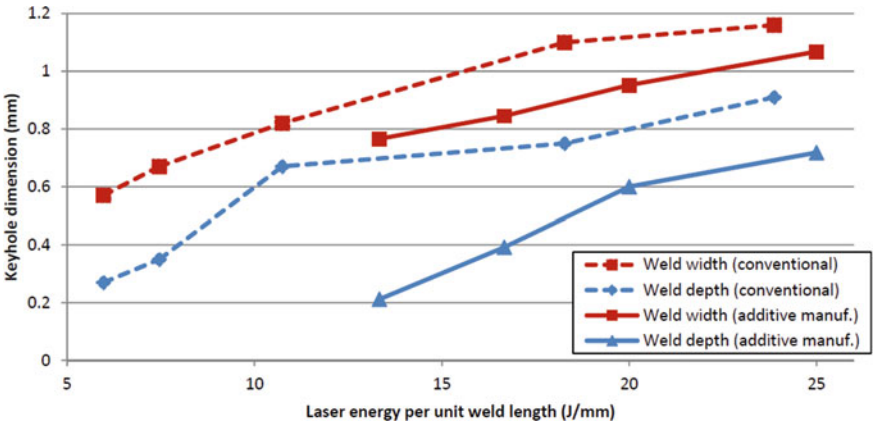

Fig. 14 Difference in keyhole dimensions between conventional and MAM components [62]. Reprinted with permission from Elsevier 2015

obtained. Further, the presence of small pores in MAM built components necessities less energy for full penetration, which is possible with higher welding speed [69].

Researchers are also interested in understanding the difference in the welding behaviour of a conventional alloy and MAM built alloy. One of the studies by Wits et al. compared the weld pool behaviour of a conventional and LPBF built Titanium. Figure 14 compares the keyhole width and depth during laser welding of conventionally built and MAM built titanium. It is seen that both conventional and MAM material shows an increase in the width and depth with an increase in the laser energy available per unit length (LEL). However, an exciting observation is that for the same LEL, the keyhole dimensions are smaller for the MAM part as compared to that of the conventional part, which is primarily attributed to the material inconsistency such as non-homogeneous microstructure, and imperfections on the MAM part such as porosity [68].

Figure 15 presents the comparison between different combinations of steel materials, where LAM-S and MS correspond to LAM built samples and conventional metallic sheets, respectively. In the MS–MS joint, the heat-affected zone (HAZ) and the weld have a hardness higher than the base plate by 200 HV, with a maximum hardness of 462 HV. A similar trend is seen in the other combinations also. However, the hardness of the LAM-S base material is considerably more than the conventional material. All hardness profiles show a comparable variation indicating a definite material similarity [69].

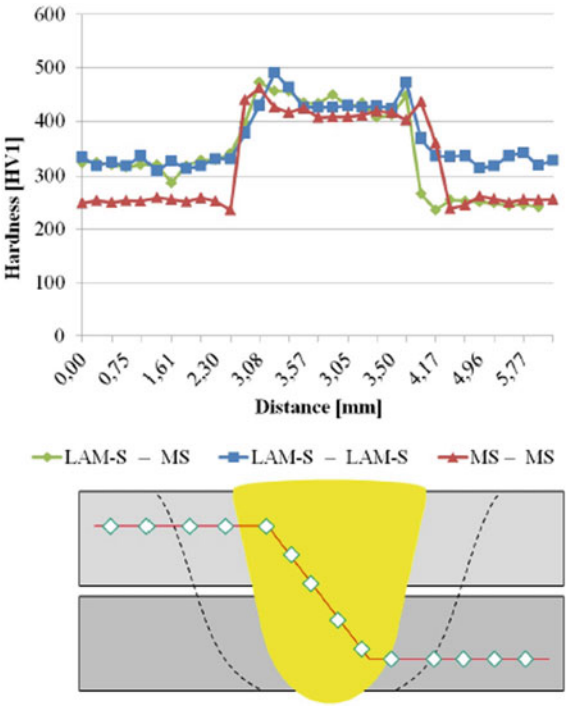

Fig. 15 Variation in micro-hardness along the deposit cross-section [69]. Reprinted with permission from Elsevier 2020

5 Potential Laser-Based Post-processing Techniques

The various laser-based post-processing techniques that can be used for MAM built components are:

a. **Laser nitriding/boriding**: Several techniques are attempted in the literature to improve the surface properties of MAM built components. Surface nitriding/boriding is one of the techniques that can be used for increased surface hardness and wear resistance. It is a thermo-chemical surface treatment in which nitrogen/boron is introduced onto the surface of the components at high temperatures. Literature shows the deployment of the plasma nitriding process for improving the surface properties of LPBF built components [70]. Laser nitriding/boriding can be potential techniques for improving surface properties. During laser nitriding, the part to be treated is kept in a chamber filled with nitrogen gas (or nitrogen gas will be fed) and a high-intensity laser beam is focused onto the sample creating nitrogen plasma near the sample surface and melting a small amount of the material from the surface. The nitrogen diffuses into the melted zone, and nitrides are formed, which increases the surface hardness. Laser boriding is generally carried out using a two-step process, where the first step involves applying a paste having amorphous boron (in powder form)

blended with diluted polyvinyl alcohol solution on the sample surface. This is followed by re-melting using a laser beam [71].

b. **Laser texturing**: The generation of textures on a metallic surface is a method to improve the surface properties, mainly tribological properties. Laser texturing is a well-known surface treatment technique that can modify the surface properties of materials by generating textures on the surface using the pulsed laser (generally pico or nanosecond lasers). During laser texturing, micro-patterns are created on the surface through laser ablation, which removes layers of materials in microscale with precision and repeatability [72]. Laser texturing can be used as a potential post-processing technique for improving/modifying the surface properties of MAM built components.

c. **Laser Engraving**: Laser engraving is a material removal process in which a laser beam is used to remove material selectivity from the surface of a component. During laser engraving, the laser creates heat energy that can vaporize the material, which aids to create images on the surface that can be seen with the visible eye. The method is fast, and the depth of material removal can be controlled by controlling the number of laser pulses used. Unlike conventional techniques, the process does not use tool bits, which gets worn out after coming in contact with the metal surface [73].

6 Conclusions

This chapter reviewed the different laser-based post-processing techniques used to modify the properties of MAM built components, like laser remelting, laser polishing, laser peening, laser micromachining, and laser welding. During MAM, laser remelting can be carried either on the top surface of the part or in a layer-by-layer fashion. Laser remelting on the top surface can tailor the surface properties such as microstructure, hardness, surface quality, wear resistance, etc. Layer-by-layer laser remelting can improve the bulk properties in addition to the surface properties. Laser polishing (LP), an extension of the laser remelting process, is considered a prospective technique to minimize the surface roughness of MAM parts. Laser shock peening (LSP) is one of the non-thermal surface treatment techniques that induce residual compressive stresses on the component surface that hinder the crack propagation and improve the fatigue life of MAM components. Laser micro-machining is used to improve the surface quality and generate microscopic features on the MAM built samples. Laser welding is used as a post-processing technique to join MAM built parts for building a component that could not be directly fabricated due to MAM system and process limitations.

It is seen that the studies on the effect of different laser-based post-processing techniques are limited to only a few alloy systems, and there is a lack of information on different engineering and medical-grade alloys. Hybrid post-processing schemes should be developed by combining different laser post-processing techniques to improve MAM components' properties.

Acknowledgements A N Jinoop acknowledges the financial support from Raja Ramanna Centre for Advanced Technology, Department of Atomic Energy, Govt. of India and Homi Bhabha National Institute, Mumbai, India.

References

1. Paul, C.P., Jinoop, A.N., Bindra, K.S.: Metal additive manufacturing using lasers. In: Singh, R., Davium, J.P., (eds) Additive Manufacturing: applications and Innovations. First CRC Press, Boca Raton, pp. 37–94 (2018)
2. Debroy, T., Wei, H.L., Zuback, J.S., Mukherjee, T., Elmer, J.W., Milewski, J.O., Beese, A.M., Wilson-heid, A., De, A., Zhang, W.: Additive manufacturing of metallic components—Process. Struct. Propert. **92**:112–224 (2018)
3. Sames, W.J., List, F.A., Pannala, S., Dehoff, R.R., Babu, S.S.: The metallurgy and processing science of metal additive manufacturing. Int. Mater. Rev. **61**, 315–360 (2016)
4. Shahzad, K., Deckers, J., Zhang, Z., Kruth, J.-P., Vleugels, J.: Additive manufacturing of zirconia parts by indirect selective laser sintering. J. Eur. Ceram Soc. **34**, 81–89 (2014)
5. Nayak, S.K., Mishra, S.K., Paul, C.P., Jinoop, A.N., Bindra, K.S.: Effect of energy density on laser powder bed fusion built single tracks and thin-wall structures with 100 μm preplaced powder layer thickness. Opt. Laser Technol. (2020). https://doi.org/10.1016/j.optlastec.2019.106016
6. Galati, M., Iuliano, L.: A literature review of powder-based electron beam melting focusing on numerical simulations. Addit. Manuf. **19**, 1–20 (2018)
7. Thompson, S.M., Bian, L., Shamsaei, N., Yadollahi, A.: An overview of direct laser deposition for additive manufacturing; part I: transport phenomena, modelling and diagnostics. Addit. Manuf. **8**, 36–62 (2015)
8. Hu, R., Chen, X., Yang, G., Gong, S., Pang, S.: Metal transfer in wire feeding-based electron beam 3D printing: modes, dynamics, and transition criterion. Int. J. Heat Mass Transf. **126**, 877–887 (2018)
9. Wu, B., Pan, Z., Ding, D., Cuiuri, D., Li, H., Xu, J., Norrish, J.: A review of the wire arc additive manufacturing of metals: properties, defects and quality improvement. J. Manuf. Process. **35**, 127–139 (2018)
10. Paul, C.P., Bhargava, P., Kumar, A., Pathak, A.K., Kukreja, L.M.: Laser rapid manufacturing: technology, applications, modeling and future prospects. Lasers Manuf. 1–67 (2013)
11. Jinoop, A.N., Paul, C.P., Bindra, K.S.: Laser assisted direct energy deposition of Hastelloy-X. Opt. Laser Technol. (2019). https://doi.org/10.1016/j.optlastec.2018.07.037
12. Yadav, S., Paul, C.P., Jinoop, A.N., Rai, A.K., Bindra, K.S.: Laser directed energy deposition based additive manufacturing of copper: process development and material characterizations. J. Manuf. Process. **58**, 984–997 (2020)
13. Gaytan, S.M., Murr, L.E., Medina, F., Martinez, E., Lopez, M.I., Wicker, R.B.: Advanced metal powder based manufacturing of complex components by electron beam melting. Mater. Technol. **24**, 180–190 (2009)
14. du Plessis, A., Macdonald, E.: Hot isostatic pressing in metal additive manufacturing: X-ray tomography reveals details of pore closure. Addit. Manuf. **34**, 101191 (2020)
15. Ma, C.P., Guan, Y.C., Zhou, W.: Laser polishing of additive manufactured Ti alloys. Opt. Lasers Eng. **93**, 171–177 (2017)
16. Dilberoglu, U.M., Gharehpapagh, B., Yaman, U., Dolen, M.: Current trends and research opportunities in hybrid additive manufacturing. Int. J. Adv. Manuf. Technol. **113**, 623–648 (2021)
17. Jinoop, A.N., Subbu, S.K., Paul, C.P., Palani, I.A.: Post-processing of laser additive manufactured Inconel 718 using laser shock peening. Int. J. Precis. Eng. Manuf. **20**, 1621–1628 (2019)

18. Jinoop, A.N., Paul, C.P., Mishra, S.K., Bindra, K.S.: Laser Additive Manufacturing using directed energy deposition of Inconel-718 wall structures with tailored characteristics. Vacuum **166**, 270–278 (2019)
19. Maamoun, A.H., Elbestawi, M.A., Veldhuis, S.C.: Influence of shot peening on AlSi10Mg parts fabricated by additive manufacturing **2**, 40 (2018)
20. Maamoun, A.H., Elbestawi, M.A., Veldhuis, S.C.: Influence of shot peening on AlSi10Mg parts fabricated by additive manufacturing. J. Manuf. Mater. Process. (2018). https://doi.org/10.3390/jmmp2030040
21. Alrbaey, K., Wimpenny, D., Tosi, R., Manning, W., Moroz, A.: On optimization of surface roughness of selective laser melted stainless steel parts: a statistical study. J. Mater. Eng. Perform. **23**, 2139–2148 (2014)
22. Kruth, J.-P., Badrossamay, M., Yasa, E., Deckers, J., Thijs, L., Van Humbeeck, J.: Part and material properties in selective laser melting of metals. In: Proceedings of the 16th International Symposium Electromachining (ISEM XVI), pp. 3–14 (2010)
23. Rombouts, M., Maes, G., Hendrix, W., Delarbre, E., Motmans, F.: Surface finish after laser metal deposition. Phys. Procedia **41**, 810–814 (2013)
24. Ghorbani, J., Li, J., Srivastava, A.K.: Application of optimized laser surface re-melting process on selective laser melted 316L stainless steel inclined parts. J. Manuf. Process. **56**, 726–734 (2020)
25. Yang, X., Liu, J., Cui, X., Jin, G., Liu, Z., Chen, Y., Feng, X.: Effect of remelting on microstructure and magnetic properties of Fe–Co-based alloys produced by laser additive manufacturing. J. Phys. Chem. Solids **130**, 210–216 (2019)
26. Richter, B., Blanke, N., Werner, C., Parab, N.D., Sun, T., Vollertsen, F., Pfefferkorn, F.E.: High-speed X-ray investigation of melt dynamics during continuous-wave laser remelting of selective laser melted Co–Cr alloy. CIRP Ann. **68**, 229–232 (2019)
27. Bayati, P., Safaei, K., Nematollahi, M., Jahadakbar, A., Yadollahi, A., Mahtabi, M., Elahinia, M.: Toward understanding the effect of remelting on the additively manufactured NiTi. Int. J. Adv. Manuf. Technol. **112**, 347–360 (2021)
28. Gustmann, T., Schwab, H., Kühn, U., Pauly, S.: Selective laser remelting of an additively manufactured Cu–Al–Ni–Mn shape-memory alloy. Mater. Des. **153**, 129–138 (2018)
29. Liu, B., Li, B.Q., Li, Z.: Selective laser remelting of an additive layer manufacturing process on AlSi10Mg. Results Phys. **12**, 982–988 (2019)
30. Wei, K., Lv, M., Zeng, X., Xiao, Z., Huang, G., Liu, M., Deng, J.: Effect of laser remelting on deposition quality, residual stress, microstructure, and mechanical property of selective laser melting processed Ti–5Al–2.5Sn alloy. Mater. Charact. **150**, 67–77 (2019)
31. Koike, R., Misawa, T., Aoyama, T., Kondo, M.: Controlling metal structure with remelting process in direct energy deposition of Inconel 625. CIRP Ann. **67**, 237–240 (2018)
32. Xin, B., Zhou, X., Cheng, G., Yao, J., Gong, Y.: Microstructure and mechanical properties of thin-wall structure by hybrid laser metal deposition and laser remelting process. Opt. Laser Technol. **127**, 106087 (2020)
33. Yu, Z., Zheng, Y., Chen, J., Wu, C., Xu, J., Lu, H., Yu, C.: Effect of laser remelting processing on microstructure and mechanical properties of 17-4 PH stainless steel during laser direct metal deposition. J. Mater. Process. Technol. **284**, 116738 (2020)
34. Metelkova, J., Ordnung, D., Kinds, Y., Van Hooreweder, B.: Novel strategy for quality improvement of up-facing inclined surfaces of LPBF parts by combining laser-induced shock waves and in situ laser remelting. J. Mater. Process. Technol. **290**, 116981 (2021)
35. Tian, Y., Gora, W.S., Cabo, A.P., Parimi, L.L., Hand, D.P., Tammas-Williams, S., Prangnell, P.B.: Material interactions in laser polishing powder bed additive manufactured Ti6Al4V components. Addit. Manuf. **20**, 11–22 (2018)
36. Richter, B., Blanke, N., Werner, C., Vollertsen, F., Pfefferkorn, F.E.: Effect of initial surface features on laser polishing of Co–Cr–Mo alloy made by powder-bed fusion. Jom **71**, 912–919 (2019)
37. Marimuthu, S., Triantaphyllou, A., Antar, M., Wimpenny, D., Morton, H., Beard, M.: Laser polishing of selective laser melted components. Int. J. Mach. Tools Manuf. **95**, 97–104 (2015)

38. Rosa, B., Mognol, P., Hascoët, J.: Laser polishing of additive laser manufacturing surfaces. J. Laser Appl. **27**, S29102 (2015)
39. Yung, K.C., Wang, W.J., Xiao, T.Y., Choy, H.S., Mo, X.Y., Zhang, S.S., Cai, Z.X.: Laser polishing of additive manufactured CoCr components for controlling their wettability characteristics. Surf. Coat. Technol. **351**, 89–98 (2018)
40. Wang, W.J., Yung, K.C., Choy, H.S., Xiao, T.Y., Cai, Z.X.: Effects of laser polishing on surface microstructure and corrosion resistance of additive manufactured CoCr alloys. Appl. Surf. Sci. **443**, 167–175 (2018)
41. Zhihao, F., Libin, L., Longfei, C., Yingchun, G.: Laser polishing of additive manufactured superalloy. Procedia CIRP **71**, 150–154 (2018)
42. Dos Santos, S.J., Seifert, H.J., Pfleging, W.: Laser surface modification and polishing of additive manufactured metallic parts. Procedia CIRP **74**, 280–284 (2018)
43. Temmler, A., Willenborg, E., Wissenbachb, K.: Laser polishing. In: Proceedings of the SPIE—International Society for Optical Engineering (2012). https://doi.org/10.1117/12.906001
44. Yadav, M.J., Jinoop, A.N., Danduk, C., Subbu, S.K.: Laser shock processing: process physics, parameters, and applications. Mater. Today Proc. (2017). https://doi.org/10.1016/j.matpr.2017.07.128
45. Danduk, C., Jinoop, A.N., Yadav, M.J., Kanmani Subbu, S.: Modeling and strategies for laser shock processing. Mater. Today Proc. (2016). https://doi.org/10.1016/j.matpr.2016.11.063
46. Dhakal, B., Swaroop, S.: Review: laser shock peening as post welding treatment technique. J. Manuf. Process. **32**, 721–733 (2018)
47. Guo, W., Sun, R., Song, B., Zhu, Y., Li, F., Che, Z., Li, B., Guo, C.: Laser shock peening of laser additive manufactured Ti6Al4V titanium alloy. Surf. Coat. Technol. **349**, 503–510 (2018)
48. Guo, W., Wang, H., Peng, P., et al.: Effect of laser shock processing on oxidation resistance of laser additive manufactured Ti6Al4V titanium alloy. Corros. Sci. **170**, 108655 (2020)
49. Du Plessis, A., Glaser, D., Moller, H., Mathe, N., Tshabalala, L., Mfusi, B., Mostert, R.: Pore closure effect of laser shock peening of additively manufactured AlSi10Mg. 3D Print. Addit. Manuf. **6**, 245–252 (2019)
50. Kalentics, N., Boillat, E., Peyre, P., Ćirić-Kostić, S., Bogojević, N., Logé, R.E.: Tailoring residual stress profile of selective laser melted parts by laser shock peening. Addit. Manuf. **16**, 90–97 (2017)
51. Morgano, M., Kalentics, N., Carminati, C., Capek, J., Makowska, M., Woracek, R., Maimaitiyili, T., Shinohara, T., Loge, R., Strobl, M.: Investigation of the effect of laser shock peening in additively manufactured samples through Bragg Edge Neutron imaging. Addit. Manuf. **34**, 101201 (2020)
52. Sun, R., Li, L., Zhu, Y., et al.: Microstructure, residual stress and tensile properties control of wire-arc additive manufactured 2319 aluminum alloy with laser shock peening. J. Alloys Compd. **747**, 255–265 (2018)
53. Lu, J., Lu, H., Xu, X., Yao, J., Cai, J., Luo, K.: High-performance integrated additive manufacturing with laser shock peening—Induced microstructural evolution and improvement in mechanical properties of Ti6Al4V alloy components. Int. J. Mach. Tools Manuf. **148**, 103475 (2020)
54. Chen, L., Sun, Y., Li, L., Ren, X.: Improvement of high temperature oxidation resistance of additively manufactured TiC/Inconel 625 nanocomposites by laser shock peening treatment. Addit. Manuf. **34**, 101276 (2020)
55. Tong, Z., Liu, H., Jiao, J., Zhou, W., Yang, Y., Ren, X.: Microstructure, microhardness and residual stress of laser additive manufactured CoCrFeMnNi high-entropy alloy subjected to laser shock peening. J. Mater. Process. Technol. **285**, 116806 (2020)
56. Chi, J., Cai, Z., Wan, Z., Zhang, H., Chen, Z., Li, L., Li, Y., Peng, P., Guo, W.: Effects of heat treatment combined with laser shock peening on wire and arc additive manufactured Ti17 titanium alloy: microstructures, residual stress and mechanical properties. Surf. Coat. Technol. **396**, 125908 (2020)
57. Chi, J., Cai, Z., Zhang, H., Zhang, H., Guo, W., Wan, Z., Han, G., Peng, P., Zeng, Z.: Combining manufacturing of titanium alloy through direct energy deposition and laser shock peening processes. Mater. Des. **203**, 109626 (2021)

58. Lu, H.F., Xue, K.N., Xu, X., Luo, K.Y., Xing, F., Yao, J.H., Lu, J.Z.: Effects of laser shock peening on microstructural evolution and wear property of laser hybrid remanufactured Ni25/Fe104 coating on H13 tool steel. J. Mater. Process. Technol. (2021). https://doi.org/10.1016/j.jmatprotec.2020.117016
59. Kalentics, N., Boillat, E., Peyre, P., Gorny, C., Kenel, C., Leinenbach, C., Jhabvala, J., Logé, R.E.: 3D laser shock peening—A new method for the 3D control of residual stresses in selective laser melting. Mater. Des. **130**, 350–356 (2017)
60. Worts, N., Jones, J., Squier, J.: Surface structure modification of additively manufactured titanium components via femtosecond laser micromachining. Opt. Commun. **430**, 352–357 (2019)
61. Jagdheesh, R., Mudali, U.K., Nath, A.K.: Laser processed Cr–SiC coatings on AISI type 316L stainless steel. Surf. Eng. **23**(2), 93–98 (2007)
62. Jagdheesh, R., Ocaña, J.L.: Laser machined ultralow water adhesion surface by low pressure processing. Mater. Lett. **270**, 127721 (2020)
63. Jagdheesh, R., Tur, A., Ocaña, J.L.: The effects of pulse period on nanosecond laser microfabrication. Lasers Eng. **37**(4–6), 333–343 (2017)
64. Jagdheesh, R., Valarmathi, A., Sivakumar, M.: Influence of laser beam polarization on micromachining of crystalline silicon using Ultrafast laser pulses. Lasers Eng. **32**(1–2), 19–35 (2015)
65. Jagdheesh, R., Kopeček, J., Brajer, J., Mocek, T.: Superhydrophobic microspiked surface structures by ultrashort laser patterning. Surf. Eng. **37**(10), 1266
66. Jagdheesh, R., BičišŤová, R., Brajer, J., Mocek, T.: Laser-induced superhydrophobic and oleophobic surface structures on float glass. Lasers Eng. **50**, 289–298 (2021)
67. Shen, H., Liao, C., Zhou, J., Zhao, K.: Two-step laser based surface treatments of laser metal deposition manufactured Ti6Al4V components. J. Manuf. Process. **64**, 239–252 (2021)
68. Wits, W.W., Jauregui Becker, J.M.: Laser beam welding of titanium additive manufactured parts. Procedia CIRP **28**, 70–75 (2015)
69. Zapf, H., Höfemann, M., Emmelmann, C.: Laser welding of additively manufactured medium manganese steel alloy with conventionally manufactured dual-phase steel. Procedia CIRP **94**, 655–660 (2020)
70. Godec, M., Podgornik, B., Kocijan, A., Donik, B.D.A.S.: Use of plasma nitriding to improve the wear and corrosion resistance of 18Ni-300 maraging steel manufactured by selective laser melting. Sci. Rep. **11**, 1–12 (2021)
71. Kulka, M., Dziarski, P., Makuch, N., Piasecki, A., Miklaszewski, A.: Microstructure and properties of laser-borided Inconel 600-alloy. Appl. Surf. Sci. **284**, 757–771 (2013)
72. Ukar, E., Lamikiz, A., Martínez, S., Arrizubieta, I.: Laser texturing with conventional fiber laser. Procedia Eng. **132**, 663–670 (2015)
73. Sculpteo Laser Engraving: a Subtractive Manufacturing Process. https://www.sculpteo.com/en/glossary/laser-engraving-definition/. Accessed 22 Apr. 2021

Advances in Superhydrophobic Surfaces: Biology to Biomimetic

S. Subramani and J. Radhakrishnan

1 Introduction

In recent years, there has been an enormous interest in studying plant leaf morphology and its evolution. It explains the possible biomimetic applications, combination of surface chemistry and architecture with their surface functionalities. The biological species have been evolved in billions of years with extremely complex multifunctional surfaces. They interact with environments, where more than 10 million existing prototypes, known as plants and animals, prevail in nature. Around 450 million years ago, in insects and plants, their functionality on biological organisms and difficulty of the hierarchical structures surpassed in all abiotic natural surfaces. Due to global environmental changes, there will be a dramatic loss of living organisms and biological models. With inbuilt particular intriguing features and sessile organisms with a variety of multifunctional surfaces, the plants dominate the group of living organisms on the earth. The primary difference between aquatic nonvascular plants and land-living vascular plants is the fascinating surface chemistry and structure. The essential feature in plants for superhydrophobicity is the shape of a single cell up to complex multicellular surface structures and polymer cuticle superimposed by epicuticular wax. The functional properties of the plant surface can be categorized into six groups:

1. Mechanical properties.
2. Impact on reflections and absorptions of spectral radiation in plant leaves,
3. Reduced water loss or Moisture harvesting.

S. Subramani
Department of Inorganic Chemistry, University of Chemistry and Technology Prague, Technická 5, 166 28, Prague, Czech Republic

J. Radhakrishnan (✉)
Centro Láser, Universidad Politécnica de Madrid, Ctra. de ValenciaKm, 7.3, 28031 Madrid, Spain
e-mail: r.jagdheesh@upm.es

J. Radhakrishnan and S. Pathak (eds.), *Advanced Engineering of Materials Through Lasers*, Advances in Material Research and Technology,
https://doi.org/10.1007/978-3-031-03830-3_8

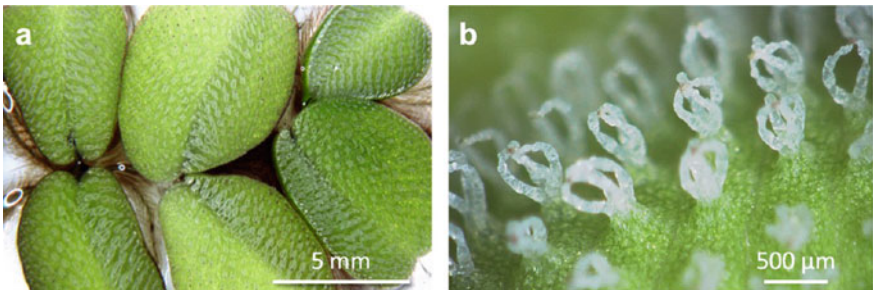

Fig. 1 Natural superwettable surfaces. **a** Salvinia molesta, **b** crown-like hairs. Reprinted (adopted) with ©permission [43]. Copyright (2015) American chemical society

4. Drag reduction,
5. Adhesion (rose petal effect) or deadhesion (Lotus effect).
6. Underwater air retention for drag reduction.

The legendary lotus leaf looks clean even in muddy environments owing to its micro and nanoscale surface structures and wax coating, which repels the water and undergo self-cleaning [1–5]. To understand the physical mechanism between the micro and nanoscale hierarchical architectures of these natural species and the related surface functionalities, intensive efforts have been devoted [6–18]. A comprehensive study is required to understand the mechanism between the micro and nanoscale architectures and its impact on the self-cleaning property of the lotus leaf [19], the fog collection of the beetle's back [20–23], the insect-capturing capability provided by the slippery surface of the pitcher plants [24–26] and the water-walking ability of water striders [7, 27–31]. All those discoveries of introducing the structure and function relationships mainly encourage the development of theoretical understanding of superwettable surfaces. Naturally, many plants and animals have surfaces exhibiting many smart properties [6, 8, 32–42], such as *Salvinia molesta* leaf covered with hydrophobic hairs (Fig. 1a). The morphology of crown-like hairs [43] is shown in Fig. 1b. Nowadays, the legendary lotus leaf structure is likely the most elaborately studied specimen for the superhydrophobic surface with interesting self-cleaning properties (Fig. 2).

For the case of surface tilt, the rolling off can be prevented by the surfaces structures, when they exhibit a large apparent water contact angle (CA) with high hysteresis [45–47]. The pinned water droplets adhere to the flowers and plants until complete evaporation, supporting the plants to survive in humid environments [48, 49]. The apparent liquid contact angle on the wet surfaces cannot be described by the Wenzel model [50]. From observing the surface of many plants and animals, liquids do not easily wet the cavities of the microtextured surfaces. Instead of wetting rough structures, the liquid drops are suspended between the air pockets which are trapped between the liquid and solid phases. This will lead to a reduction in the solid–liquid contact area. Such drops are known as Cassie [51] state droplets, and it is found to be great interest to attain a Cassie state of wetting, that denotes the low liquid adhesion

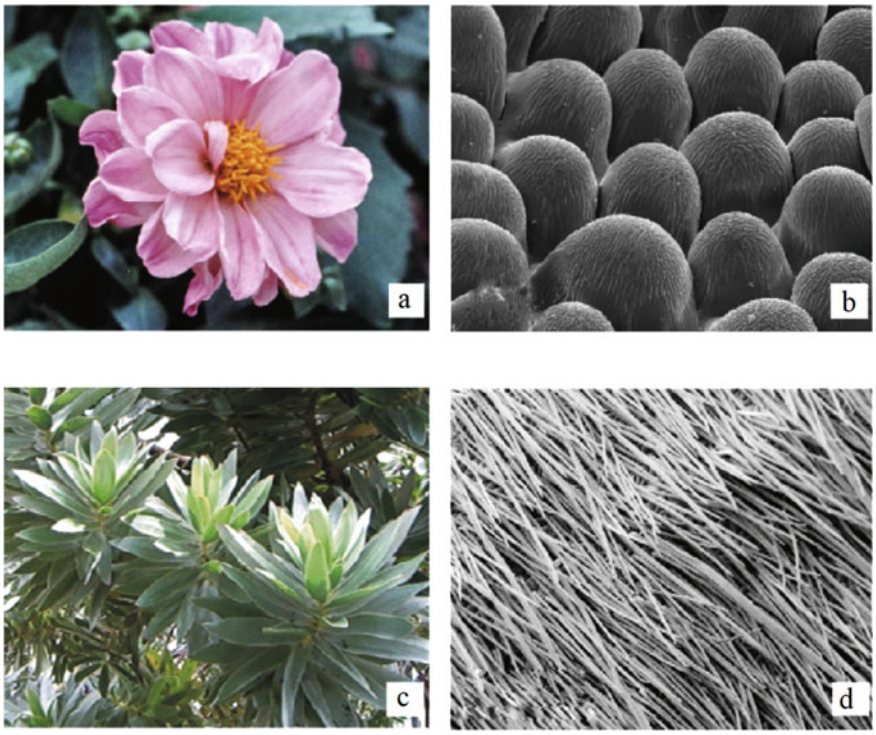

Fig. 2 **a** The velvety flower petals of Dahlia and **b** its convex microstructure of the epidermis cells, **c** Leucadendron argenteum leaves and **d** its light-reflecting hairs [44]. Reprinted (adopted) (2017) Springer Nature (https://link.springer.com/article/10.1007/s40820-016-0125-1)

[4, 51, 52]. The reasons for the water drops have high mobility on lotus leaves are, a liquid drop suspends by the leaf's nano-sized hairs on the top of microscale bumps, also the contact angle hysteresis $\Delta\Theta < 10°$. The effect of the air trap is explained in Fig. 3 with a schematic diagram. In the case of micropillar-textured solid substrates, by evaluating the surface energy cost, the criterion for forming air pockets can be deduced quantitatively.

Naturally, there are varieties of functional surfaces to undergo the terrible environments in day-to-day life. In the recent past, natural functional surfaces have achieved

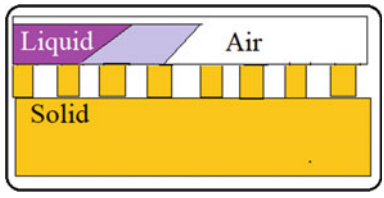

Fig. 3 Graphical illustration for the wetting of microgroove surface structures

notable attention owing to their important applications in home appliances and industrial products. The sessile organisms such as green plants contain naturally huge functional surfaces. These plants shield the terrestrial biomes of the earth and show a magnificent variety of hierarchical surface structures. These superhydrophobic structures have been analyzed with the help of scanning electron microscopy imaging techniques (SEM). In the massive plant kingdom, the Saguaro cactus (Fig. 4a) and the Titan Arum (Fig. 4b), it is possible to examine the hierarchical surface structures at the macroscopic scale. Due to the low hydro-dynamic friction and anti corrosion [53], the super-hydrophobic property with a high degree of water deadhesion of the lotus leaf has gained significant consideration among the scientists [31, 54].

The surface of solid is the first line of defense with the environment, and the surface structure plays a crucial role in defining the environmental interactions. In the case of green plants, it has diverse hierarchal structures with different functionalities. The detailed examination of the surface structures can be made possible by SEM analysis or some plants exhibit macroscopic structures as shown in Figs. 4a, b. However, the structures of the overlay wax crystals can be visualized by SEM.

The various plant surface structures are due to the difference in cell shapes and hierarchically superimposed micro/nanostructures on the surface, primarily on the

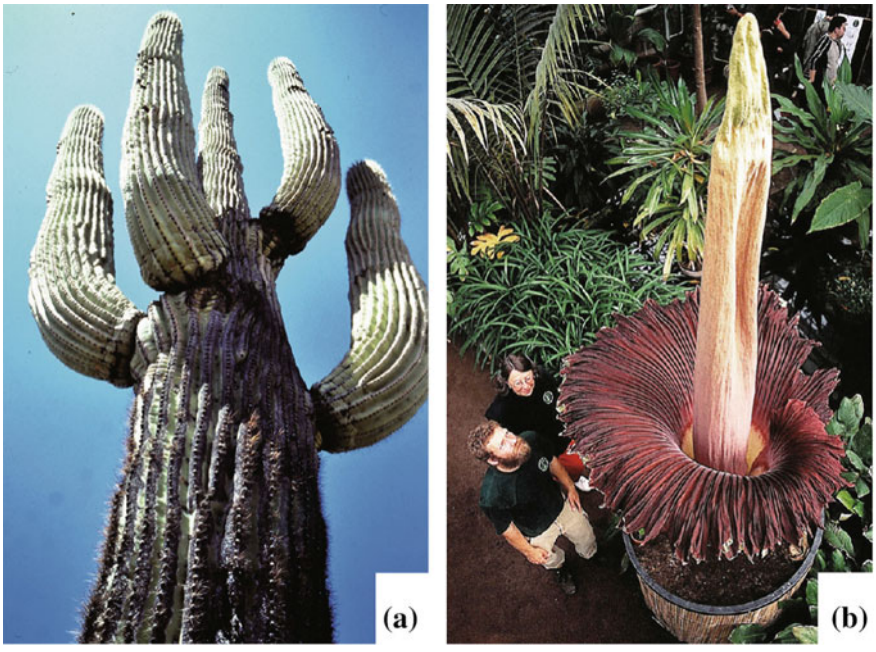

Fig. 4 The macroscopic scale view of hierarchical surface sculpturing of plants. **a** The Saguaro (Carnegiea gigantea) is one of the biggest cactus. **b** The Giant Arum (Amorphophallus titanum) [44]. Reprinted (adopted) (2017) Springer Nature (https://link.springer.com/article/10.1007/s40820-016-0125-1)

wax crystals. The diverse combination of micro and nanoscale hierarchical structures leads to a variety of surface functionalities among the plant leafs [44, 55]. Superhydrophobic property is one of the significant character exhibited by the entire or part of plant leaves. In general, most of the grasses are superhydrophobic with little exception. The superhydrophobic properties are highly unstable; for, e.g., the younger leaves are superhydrophobic, whereas the older leaves are hydrophilic. Some species like Elumus arenaruis (grass) show a static contact angle of about 161°, which is comparable with the properties of lotus leafs [44].

1.1 Surface Chemistry of Plant Leaves

The surface of vascular plants are entirely different from the aquatic plants. The aquatic plants have no cuticle and it exhibits highly hydrophilic properties. It is important to consider the vascular plant's surface for the development of biomimetic applications. In vascular plants, the outer surface of the leaves is concealed with monomolecular layers of wax, and in some cases, it is a thick crust or 3D crystals. These layers are visible in different coloration (e.g., wheat, gapes, etc.) due to the reflection of the visible wavelengths by 3D wax structures. The plant surface waxes are composed of long-chain hydrocarbons and it's derivatives. However, the chemical compositions are largely variable among the plant family and perhaps within organs of one species, for e.g., the lower and upper side of a leaf. The plant waxes have primary and secondary ketones, fatty acids, alcohols and aldehydes. Alkanes are also found in plant waxes, however, in low concentrations. The commonly available wax compounds and chain lengths are listed in Table 1. Recent research findings reported the new wax with components of methyl-branched aliphatics. Moreover,

Table 1 Chemical constituents of plant wax and spectrum of chain length

1 Aliphatic compounds		Chain length
1.1 In waxes frequently existing, however as minor compounds Alkanes	CH_3–(CH_2)n–CH_3 Odd C19–C37	Odd C19–C37
Primary alcohol[a]	CH_3–(CH_2)n–CH_2–OH	Even C12–C36
Esters	CH_3–(CH_2)n–C0–0–(CH_2)m–CH_3	Even C30–C60
Fatty acids	CH_3–(CH_2)n–COOH	Even C12–C36
Aldehydes	CH_3–(CH_2)n–CHO	Even C14–C34
1.2 In waxes rarely existing, (but if, than as major wax compounds) Ketones e.g., palmitones	CH_3–(CH_2)n–CO–(CH_2)m–CH_3	Odd C25–C33
B-diketones	CO–CH_2–CO–(CH_2)m–CH_3	Odd C27–C35
2 cyclic compounds Flavonoids	e.g., Quercetin	
Triterpene	e.g., β-Amyrin	

the temperature or intensity of light would also influence the chemical composition and the quantity of wax found on the plant surface [56, 57].

1.2 Wetting Phenomena

The interaction of liquid at the solid-gaseous phase is termed as a wetting process. The wetting process is governed by the chemistry of different phases as well as the surface structures. The wetting of a surface is governed by surface chemistry and surface structures. The wettability of the surface can be measured in terms of contact angle (CA). When the water droplets from the spherical shape on the surface and the contact area between the solid phase and liquid phase are low, it is termed as high contact angle. Wetting and non-wetting surfaces are evaluated based on the contact angle measurement and it can be hydrophobic or hydrophilic. The wetting behavior can be classified based on CA and CA-hysteresis. The CA between 0° and <10° makes the water spreads over the solid surface. The contact angle between 10° and 90° is termed as hydrophilic, whereas the CA between 90° to 150° is known as hydrophobic surfaces. In this scenario, water would not spread over the surface, however, the tilt angle is <10° [58, 59]. A perfect superhydrophobic surface can be defined as a surface with CA > 150° and low tilt angle (<10°) or low hysteresis (<5°) [60]. The superhydrophobic surfaces do not exhibit any wetting signature as well as it has the self-cleaning property [61]. The principle for evaluating the wettability of a plain surface is based on Young's equation [62]. The contact angle of a solid surface is determined by the following equation as per Young's equation.

$$\cos\theta = \frac{\gamma_{SV} - \gamma_{SL}}{\gamma_{LV}} \tag{1}$$

γSV, γSL, γLV refers to interfacial tension at the boundary between solid (S), liquid (L), and air (A).

$$\cos\theta' = \frac{r(\gamma_{SV} - \gamma_{SL})}{\gamma_{LV}} = r\cos\theta \tag{2}$$

where, 'r': the roughness factor, for rough surface $r > 1$. The contact angle linearly increases with the roughness factor, until the "r" value exceeds 1.7, above that value, the hysteresis value begins to decline in contrary to the Wenzel estimation. This declining trend of hysteresis is ascribed to the transformation from Wenzel state of wetting to Cassie -Baxter state of wetting. This change has been observed due to the air pockets trapped in the micro-scale structures.

Leading to the suspension of water drops on the rough/structured surface. As per the Cassie –Baxter model, the apparent CA is calculated based on the following equation.

$$\mathrm{Cos}\,\theta^{c} = f_1 \cos\theta_1 + f_2 \cos\theta_2 \tag{3}$$

where θ^{c} is the apparent contact angle f_1 and f_2 fractional surface of phase 1 and 2 respectively, for the case of rough surface which has one kind of asperities, and the f refers to the solid surface, the air fraction is specified as $(1 - f)$, where $\theta = 180°$ for air, the contact angle can be computed by the following equation.

$$\cos\theta^{c} = f\,(1 + \cos\theta) - 1 \tag{4}$$

As per Eq. 4, it is apparent that, for superhydrophobic surfaces, there should be a control over the fractional area of contact between the solid and liquid phases. Biomimetic explains the adoption of biological structures in engineering applications. The biological structures are carefully engineered by various techniques onto the surface of the solid materials. Considering the self-cleaning property and water repellency of the lotus leaf, successful trials have been attempted to modify the surface's wettability of solid surfaces in three ways; (a) by fabrication and micromanipulation of the surface [61], (b) fabrication of dual scale surface roughness (micro and nanoscale) [63], (c) altering the surface chemistry with chemical treatment (e.g., fluoroalkyl silane) to reduce the surface free energy [60].

2 Different Techniques to Create Superhydrophobic Structures

Extensive efforts have been devoted to the development of novel techniques to engineer the superhydrophobic surface with functional properties. A plethora of fabrication techniques has been successfully demonstrated for engineering exquisite hydrophobic and hydrophilic structures with extraordinary functions, which are comparable to or even outsmart those of natural examples in few cases.

2.1 Spin-Coating and Spray-Coating

There are two techniques, which are commonly applied to create a thin film coating on flat substrates. One method is by polymer solutions, and the other is from nanoparticle suspensions. By spray coating method, the solutions are sprayed onto the substrate and solidify as thin films. In this method, the drop of solution is cast on a substrate and then turned to form a thin film with uniform thickness. For example, to fabricate a superhydrophobic surface, the solutions of perfluorosilane titanium dioxide nanoparticles can be sprayed onto both hard and soft substrates [64]. In order to improve the adhesion between the substrate and sprayed silanized nanoparticles, glue

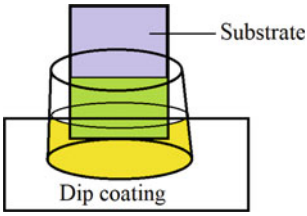

Fig. 5 Graphical representation of dip coatings

is sprayed onto the upper surface of the substrate before spraying particle suspensions [65]. The resulted microscale structures and wax coating transform the wetting property to superhydrophobicity. Composite spray suspensions containing reduced graphene oxide nanosheets, diatomaceous earth (DE) microparticles, titanium di oxide nanoparticles are also applied to develop anti-corrosion surfaces, whereas the graphene oxide improves film integrity [66].

2.2 Dip Coating Technique

The dip-coating technique or solution immersion method involves submerging a substrate in a solution to generate roughness on the surfaces (Fig. 5) [67]. For example, the flower-like clusters can be formed by submerging a copper substrate into a fatty acid solution, and forms $Cu(CH_3(CH_2)_{12}COO)_2$ which has a small sliding angle and a large water contact angle [68]. Moreover, a omniphobic surfaces can be created by immersing/dipping a copper substrate in ammonia solution or $AgNO_3$ solution at 5 °C for 36 h and further treated with the fluorinating agents to create silver dendritic needle structures or copper hydroxide nano arrays [69]. Alternatively, to obtain superwettability, the aqueous suspension comprising low surface energy fluorocarbon surfactants and nanoparticles, such as titanium dioxide, alumina and silicon dioxide can also be used. From nanoparticle formation or by repeating the dip-coating approach via pH-controlled polymer accumulation, the highly micro and nanoscale lotus-like hierarchical architectures can be obtained.

2.3 Casting

Casting is one of the wet chemical methods applied on highly porous substrates. The suspension of nanoparticles, prepolymers, crosslinkers, or bubbles can be used with the solidification process as depicted in Fig. 6. The casting technique is more often used for producing lubricant-infused slippery surfaces by infusing lubricants into the substrates. This technique is economical, facile and can be adopted for a variety of material combinations. The solidification can be made either physically or chemically, e.g., by freezing the casting [70]. For most metals and carbon-based

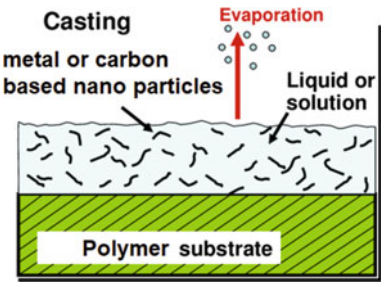

Fig. 6 Illustration of casting technique

nanoparticles, post-treatment like sintering is important. For the case of micro-droplet manipulation, hydrogels and graphene aerogels have been produced and fluorinated to enable slippery surfaces [71].

2.4 Layer-by-Layer Deposition Technique

The layer-by-layer deposition is one of the important techniques applied for the thin coating of the substrates with nanoscale thickness with many layers of polyelectrolyte films. In common, the process comprises, the adsorption of alternating polyelectrolyte layers of opposite charges occurs until a multilayer film of the essential thickness is achieved [72]. For example, as shown in Fig. 7, by alternating the deposition in cationic and anionic solutions of composite polymers, an antifogging film with a hierarchical surface texture can be created [73]. An underwater superhydrophobic membrane was fabricated by the multilayer deposition of AAg-PVDF membranes [74]. The same method can be applied for the fabrication of polymer nanoparticle multilayered films.

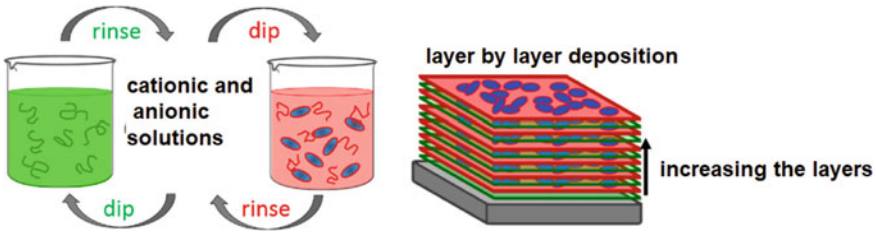

Fig. 7 Graphical representation of layer by the layer deposition technique

2.5 *Electrospinning*

The electrospinning technique has been applied for the development of superhydrophobic and omniphobic surfaces. In this technique, the superhydrophobic polymer solutions (Fig. 8), such as polystyrene (PS), polyvinylidene fluoride (PVDF), fluoroalkyl polyhedral oligometric silsesquioxane (POSS), and the nanofibers interweave into a membrane with the desired roughness to create chemical hydrophobicity, and omniphobicity [75]. By adjusting the applied voltage and flow rate of the solution, the roughness of the nanofiber membrane can be computed. Due to the cationic nature of electrical instability, the deposition and alignment of the electrospin nanofibers are challenging. The electrospinning technique can be classified as a method for developing surfaces with random roughness, i.e., the average roughness can be modified or tuned as per the requirements. The increase in the concentration of the polymer solution, the resultant structure on a substrate can lead to bead formation. In polymer materials, the beads on the string fiber surface and the straight fiber surface exhibits omniphobic character, and the hysteresis value of the beads on the string fiber surface is marginally lower than that of the straight fiber surface [76]. The hybrid solutions of polymers and nanoparticles would also be electrospined with nanoprotrusions to enhance the superhydrophobic structures. These nanostructures can be formed by nanoparticles, and several groove-like structure can be created from nanofibers [77]. For nonspinnable materials, the coaxial electrospinning method can be applied. The electrospinning approach can produce omniphobic surfaces. A light

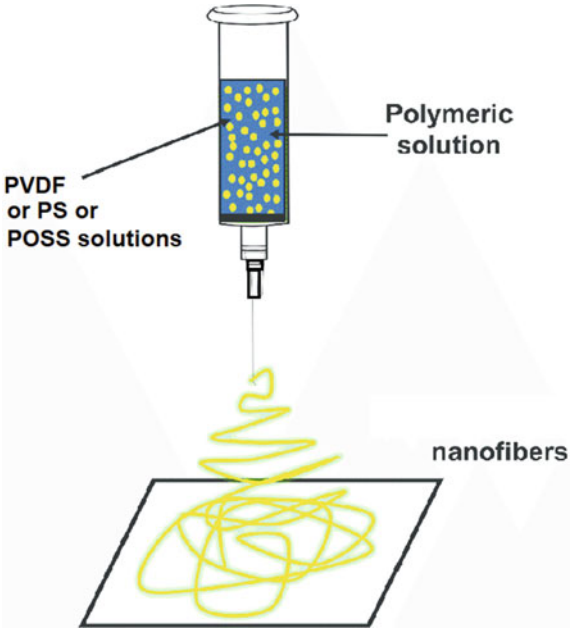

Fig. 8 Graphical illustration of electrospinning

superwettable surface can also be obtained by electrospinning, by incorporating photo responsive titanium dioxide nanoparticles and thermos-responsive polymers like poly-*N*-isopropylacrylamide [78].

2.6 *Photolithography*

Photolithography is one of the prime techniques used for micro and nanofabrication, which caters to the production of microarray kind of surfaces with predetermined geometries [79]. The sequential order of the technique is explained in Fig. 9. An inverse trapezoidal microstructured surface of polydimethylsiloxane (PDMS) was prepared by combining diffuser lithography and replication technique. The hydrophobicity and the transiency were enhanced by coating the surface with a fluoropolymer layer [80]. Two steps lithography has been applied to create overhanging microdisks patterns on polymer film. The void between the microdisks favors the air mat under the disk, thus improving the omniphobic characteristic of the patterns [81]. The mushroom-like microarrays can be generated from the straight micropillars, for example, spray coating can be applied on the straight pillars with blends of PDMS and fluoropolymers. The sprayed blend is created and generates a rough cap that has a radius bigger than the pillar. Spraying of low surface energy polymers can lead to a re-entrant structure with oleophobic properties [82]. Apart from the reentrant surfaces for omniphobicity, microgroove surface structures can also be easily developed by lithography-based methods for directional liquid spreading and transportation.

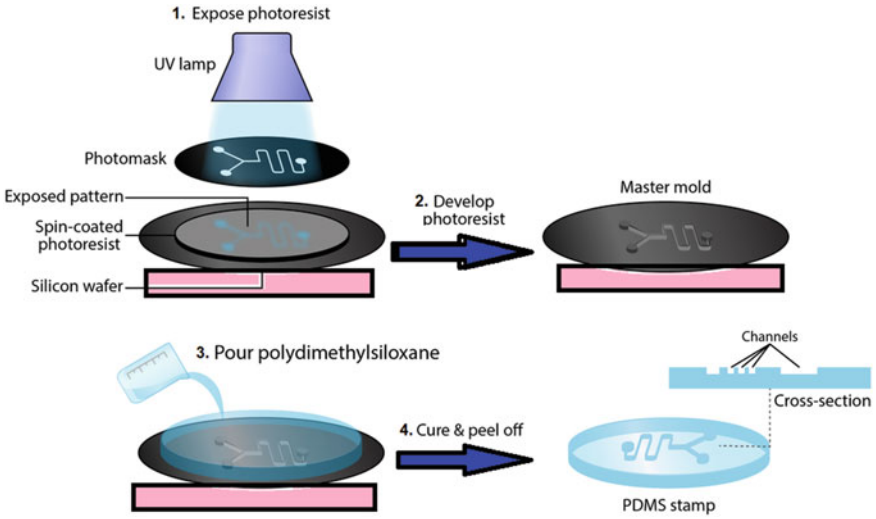

Fig. 9 The sequential order of the photolithography technique

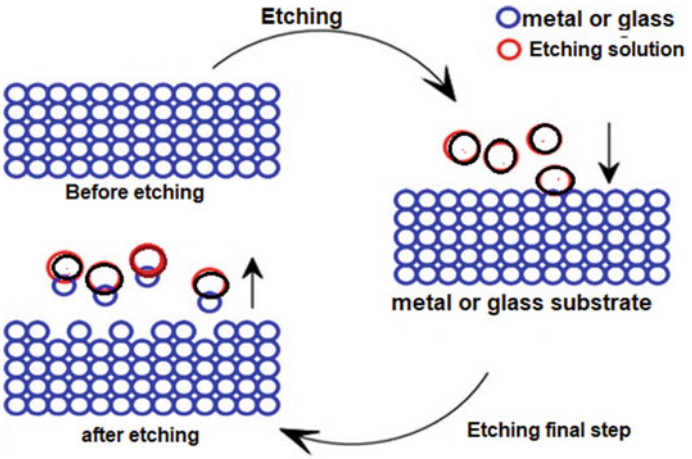

Fig. 10 Graphical illustration of wet etching process

2.7 Etching

Etching is a material removal mechanism used to remove material removal selectively to create desired surface geometry. The wet etching mechanism is illustrated in Fig. 10. Etching can be classified as wet etching and dry etching, based on the phase of the etchant, for eg. solution or reactive gas. Etching is a powerful micro/nanofabrication technique that supports the production of complicated 3D microstructures. Application of this technique removes surface materials by an etchant solution for the case of wet etching and for the dry etching, the reactive ion is used for the dry etching. The dry etching technique can be used to anisotropically remove material and it is capable of fabricating surface structures with high resolution, good aspect ratios and high fidelity. The etching technique is widely adopted to fabricate 3D micro/nanostructures with a high level of complexity, however, the major drawback is mainly on the contamination is due to chemicals.

The superomniphobic surfaces are fabricated by anisotropically etching hydrophilic silica substrate, and well crafted doubly reentrant serif-T-shaped microarrays for repelling all kinds of liquids, including perfluorohexane ($\gamma = 10$ mN m^{-1}) [83]. The omniphobic surfaces are capable of repelling fluorinated oils with surface energies <20 mN m^{-1}.

3 Direct Laser Writing

Inspired by the hierarchical surface structures of the lotus leaf, several techniques such as lithography, spin coating, etching technique, electrochemical deposition, electrospinning, vertically aligned carbon nanotubes, natural oxidation, and laser

surface patterning have been adopted for the development of hydrophobic or superhydrophobic surfaces.

Among these surface manipulation techniques, laser patterning can modify the superficial layer of material without compromising the bulk material property. Further, it is a non-contact method and a variety of materials can be processed [59, 63, 84–88]. The non-contact process is advantageous to create complex geometry and the scale of geometry can vary from nano to microscale or in some cases, it can be hierarchical surface structures with dual scale (nano and micro-scale) [63, 89]. The application of ultrashort laser pulses onto the metals causes ripples kind of structures at certain processing conditions. In case, the laser energy is near the ablation threshold and below the melting point of the material, Laser-induced Periodic Surface Structures (LIPSS) would be created. The LIPSS has been reported since the late 1960s on all varieties of materials. Such LIPSS is generally referred as 'ripples' and consists of undulating surfaces with periodicity and amplitude equal or smaller than the wavelength of the laser beam used for the laser irradiation. The LIPSS is the result of laser surface patterning with pulse energy or fluence near the ablation threshold. The ultrafast laser ablation leads to two kinds of ripples such as regular ripples and secondary ripples. In common, the orientation of regular ripples is found to be perpendicular to the polarization direction of the incident laser beam [90]. Kietzig et al. [91] investigated the aging process or the time dependency of laser machined metals and alloys for the wetting property transformation. The laser processed dual-scale surface roughness plays a substantial role in the wetting property transformation. Therefore, it is apparent that the surfaces with dual scale structures have higher apparent contact angles for water droplets. Nevertheless, there are many reports available for the wetting property transformation with microscale structures [61, 63, 85].

The most observed LIPSS has a periodicity that is equal or smaller than the wavelength of the laser applied for structuration. This effect has been explained on the basis of interference of incident and scattered laser beam or excited surface waves [92]. The formation of sub-wavelength or secondary ripple structures can be related to the relaxation of highly excited unstable surface layers [93]. The physical phenomenon about the ripple initiation, development and evaluation towards other patterns are still a matter of debate.

The wetting properties of metals have been transformed by applying a two-step process, (i) manipulation of surface morphology, (ii) modification of surface chemistry. The process of applying fluorosilane coating on a laser textured metals and semiconductor for the wetting property transformation has been successfully demonstrated [60, 94]. Moreover, laser processed hydrophobic metal surfaces were also being demonstrated without any chemical coating on the surface [95] through aging process [61] or vacuum treatment [85]. Clustered-copper nanowires were developed for the extreme water repellence property without and additional coatings. The wetting property transformation is related to the geometrical phenomenon connected to the nature of clustering [96]. The reported research findings dictate the importance of surface manipulation in the enhancement of water deadhesion.

3.1 Laser Processed Surface Structures

Micromachining by ultra-short laser pulses is a flexible technique, that has a plethora of advantages compared to other conventional techniques: (i) it can be applied to metals, ceramics, semiconductors and polymers; (ii) difficult geometries can be created with controllable patterning of structures; (iii) the patterning area can be in the range of few microns to several centimeters under controllable or in normal atmospheric conditions, thereby eliminating the need of cleanroom environment. In laser processing, the material removal mechanisms are based on ablation. Laser patterned surfaces by ablation have been investigated to a larger extent due to their caliber to create periodic structures from nanometer (nm) [97] to micrometers and the combination of both [60] (i.e., dual scale microstructures comprising features of both nano and micron-scale). The energy transfer process during the light-matter interaction has been extensively studied [98–100]. The ultra-short laser pulses with the energy higher than the ablation threshold of the metals follow the sequential process:

(a) The photon energy from the laser is absorbed by the free electrons due to inverse bremsstrahlung within several tens of nanometers. However, the depth of the optical penetration is governed by the wavelength and the physical properties of the material. The thermal equilibrium of excited electrons is governed by the electron–electron interaction time.
(b) The thermal energy transfer into the metals is explained by the two temperature diffusion model [101] (temperature of the excited electrons, (T_e) and the lattice temperature, (T_l)). Thermal equilibrium between the two sub-systems would be reached in few picoseconds by electron–phonon interactions.
(c) Melting and ablation starts, provided the lattice temperature exceeds the specific threshold value of the material. The time required for the initiation of the melting process is in the range of few to several hundred picoseconds, and ablation requires few tens of picoseconds to several nanoseconds.
(d) The cooling rate of the laser-ablated surface structure is about 10^{13}–10^{15} K/s. The physical parameters and the morphology of laser processed surface structure depend on the process parameters and the material properties.

The ablation regimes can be classified as “gentle” and “strong” are observed for the pulse duration shorter than 1 ps [102]. If the laser fluence is higher than the ablation threshold, the rate of ablation is estimated by optical penetration depth and the average ablation rate is expected to be low (13 nm for copper [102]). In a gentle ablation regime, as a very little volume of material is removed from the surface, the laser-ablated crater is largely smooth with roughness in nm scale. A strong ablation threshold is observed for the higher laser fluence, e.g., 0.7 J/cm^2 for copper, there is a strong increase in the optical penetration such as 80 nm (for copper). As a consequence of strong optical penetration, the ablation rate has been increased, as well as the roughness of surface features, in the range of micrometers (μm). The depth of the crater formed due to the ablation of the laser pulse can be explained by

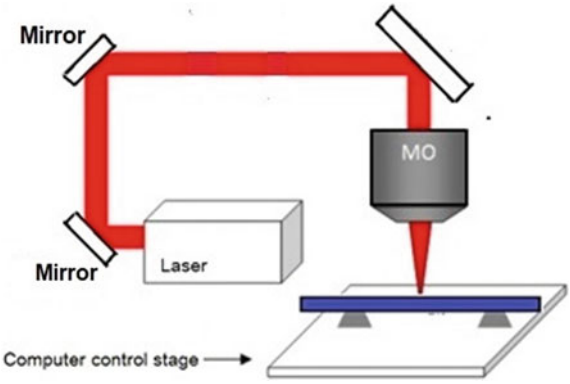

Fig. 11 Basic laser direct laser setup

logarithmic law

$$L = \lambda \ln(F/F\text{th}) \tag{5}$$

where, $\lambda = \alpha^{-1}$ is the optical penetration depth, and Fth refers to the ablation threshold fluence. However, the threshold value is an extrapolation of the ablation data and may be different from the experimental values.

Figure 11 shows the basic setup used for the laser direct-write technique for the micromanipulation of surface topography of materials. The setup has a laser source and folding mirrors to guide the laser beam to the sample surface. The beam path has a Galvo scanner, which is primarily used for the moment of the laser beam over the sample as per the required geometry. The work station may be equipped computer-controlled stage with a X–Y axis for the moment of sample, where the laser beam would be kept stationary.

Ultrashort laser pulses were applied to create superhydrophobic properties on Ti–6Al–4V surface [60]. It is noteworthy to understand the fact about the surface chemistry of laser processed surface structures. In most cases, more precisely on the metal surface, the laser processed surface structures are composed of metal oxides [85, 103] and it has high surface energy, which attracts the water droplets. Therefore, all the freshly laser processed surfaces would be hydrophilic and the surface energy can be reduced by aging process [61, 91], chemical coatings [60] or vacuum process [63, 85, 103] or low-temperature annealing [59]. The nanostructures (Fig. 12) induced by a picosecond laser on Ti–6Al–4V were hydrophilic and transformed to superhydrophobic after the chemical treatment. The figure clearly shows the regular ripple structure and broken ripples which are transformed into the cluster of nano mound structures. As the number of laser pulses per spot increases, the spot would experience a higher temperature at the center of the laser spot compared to the peripheral area for the case of Gaussian beam profiles. It eventually leads to breaking of LIPPS and transforms into clusters of nanoscale structures [60]. In general the regular ripple are normal to the polarization angle of the laser beam whereas the secondary

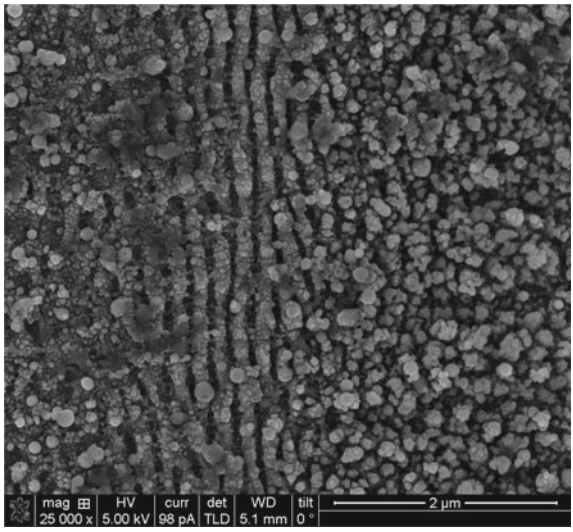

Fig. 12 Scanning electron micrographs of the Ti–6Al–4V sample after 48 laser pulses per spot. Reprinted (adopted) with ©permission [60]. Copyright (2014) American chemical society

ripples are along the direction of the polarization angle. The secondary ripples would be formed as bridges between the regular ripples as shown in Fig. 12. Furthermore, the Fig. 13 also witnesses the cauliflower-like white structures, which are the results of resolidification of metal vapors, caused during the ablation process. Apart from the LIPSS structures, the surface has the presence of nanoscale protrusion.

The surface energy of the laser patterned surfaces was hydrophilic, and the surface energy has been reduced by SAM based on perfluorinated octyl trichlorosilane (FOTS) coatings. The chemical treated surface shows superhydrophobic (CA $\geq$ 150°)

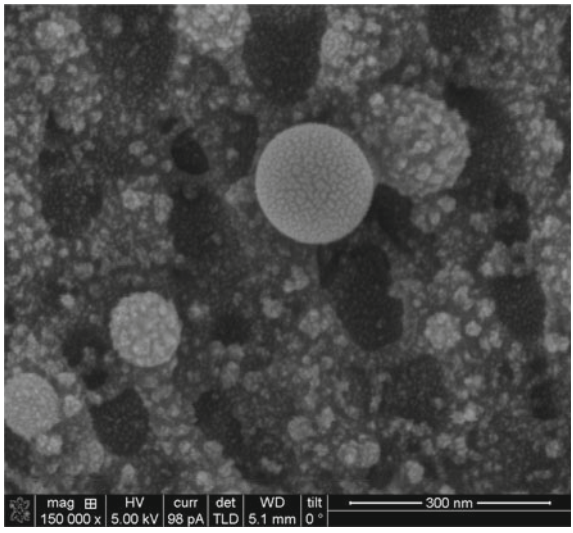

Fig. 13 Scanning electron micrographs of the Ti–6Al–4V showing the cauliflower (ball-like white structure) kind structure of the resolidified metal vapor. Reprinted (adopted) with ©permission [60]. Copyright (2014) American chemical society

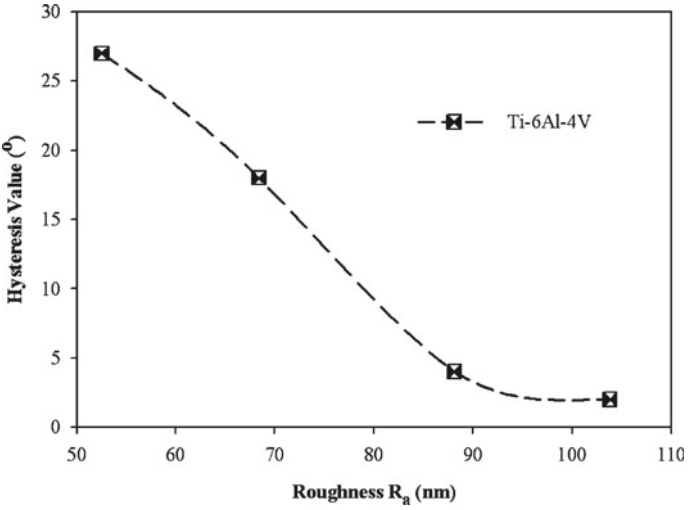

Fig. 14 Hysteresis as a function of surface roughness Reprinted (adopted) with ©permission [60]. Copyright (2014) American chemical society

property and the water repellency was found to be a function of surface roughness [60]. The wetting property, specifically the superhydrophobic property is evaluated on basis on static contact angle as well as the hysteresis (difference between the advancing and receding contact angle) of a water droplet on the surface or the sliding angle of the water droplet.

To qualify as superhydrophobic surface, the hysterics must be <5°, and the sliding angle must be <10°. Figure 14 shows the hysteresis measured for Ti–6Al–4V as a function of surface roughness.

The wetting property of the laser processed metal surface can be modified by vacuum process [63, 85, 103, 104] without any additional chemical coatings.

Lamellar structures were fabricated by Jagdheesh et al. to transform the wetting property of aerospace alloy Al7075by vacuum process [104]. Figure 14 show the lamella structures processed with two different flunce such as 0.21 J/cm^2 and of 0.43 J/cm^2 at various pulses/spot. It is found that the top surface of the lamella structures was covered with random nanoscale protrusions and nanowiresFig. 15.

The periodicity of the lamella structures is comparable with the wavelength of the incident laser beam 1030 nm. Figure 16 depicts the static contact angle measurements made for the lamella as well as the lotus leaf papillae structures. The wetting property evaluation was found to be near superhydrophobic for the lamellar structures and superhydrophobic for the lotus leaf papillae structures [104]. The laser surface patterning in open atmospheric conditions can create a considerable amount of coordinately unsaturated Al–OH reaction sites, which supports the carboxylation by effective adsorption of airborne C–C(H) at a short span of time at very low water vapor pressure inside the vacuum chamber. The chemical analysis of the structures found to contain a large amount non-polar chain of C–C(H) as the first layer of

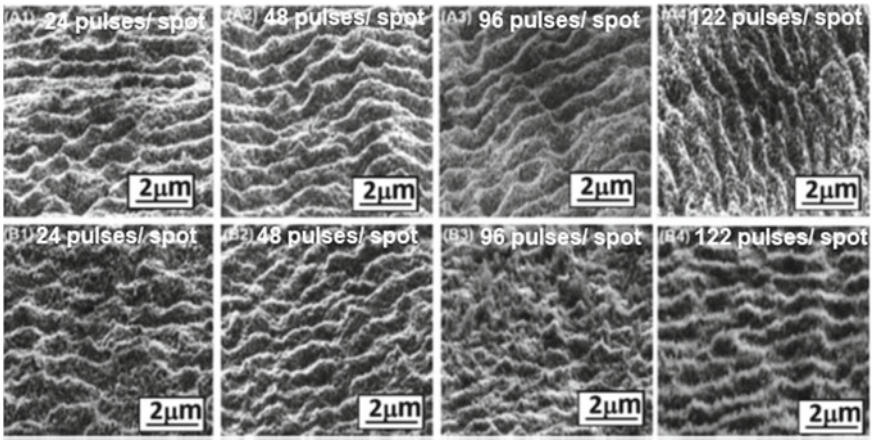

Fig. 15 SEM of lamella structures fabricated by ps laser at different fluences and pulse/unit area. A1–A4: processed with the fluence of 0.21 J/cm^2; B1–B4: processed with the fluence of 0.43 J/cm^2 [104]

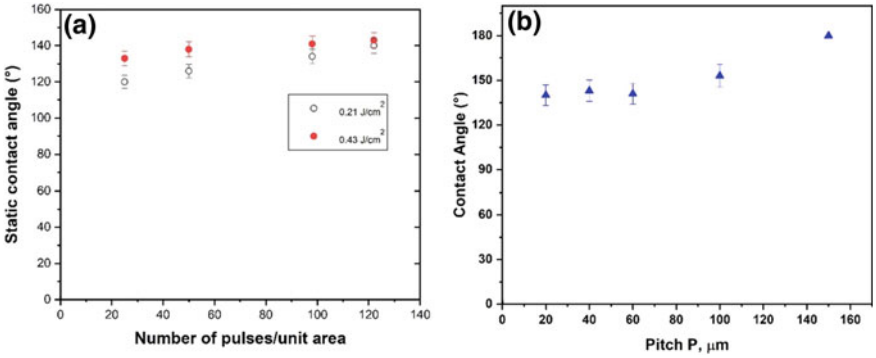

Fig. 16 **a** Static contact angle measurement (SCA) lamellar structures. **b** Lotus leaf papillae structures [104]

defense and thus the layer has a low affinity towards the polar water droplet. The lower contact angle observed for the lamella structure may be the result of random distribution of nanoscale structures, which is prone to the partial penetration bigger volume of the droplet (8 μL). For this kind of structure, the surface may exhibit Wenzel [50] state rather than Baxter [51] state of wetting. The development of superhydrophobic surface structures can also improve the wetting property of metals in an aqueous solution of NaCl 0.5 M [53]. The best anti-corrosion property was observed for the highly water repellant surface.

A cost-effective nanosecond laser source has also been used to create the superhydrophobic surface. The major difference between applying picosecond/femtosecond laser source and nanosecond (ns) laser source is the predominant presence of

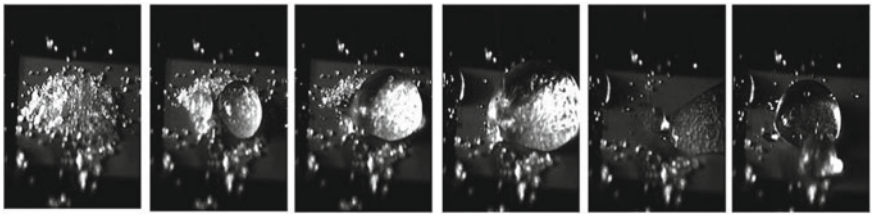

Fig. 17 Self cleaning of sugar particle on the laser processed surface [61]

nanoscale structures. The structures created by the ns laser source have proved to be ultra hydrophobic even without the predominant presence of nanostrustures [61, 63, 85]. Therefore, to fabricate perfect water-repelling or self-cleaning surface structures, it is essential to have appropriate surface geometry with sufficiently low surface energy material over the surface structures. The combination of appropriate surface geometry and predominant presence low surface energy material can be a good candididate for the self cleaning of surface as shown in Fig. 17.

Based on short and ultrashort laser processing, it is understood that since the discovery of micro or hierarchical surface structures, there has been a significant development in the micro-fabrication technology and theoretical research of superhydrophobic coatings. However, there is a lack of detailed analysis or understanding of size effect and the energy modification in the model transition process of super/hydrophobic surface, more precisely, for the nanostructures wetting model mechanism [105, 106]. The research concentrates on the performance analysis of superhydrophobic coatings, for example, the anti-icing application, development of self-cleaning surfaces, water repellent coatings is still emphases on analysis of the laboratory-based results [61, 84, 88, 106, 107]. Furthermore, there is a lack of comprehensive understanding of the physical mechanism which prevents the icing nucleation process on the superhydrophobic surfaces. In most of the cases, the fabrication of superhydrophobic surfaces try to address the icing of static droplet and icing process of the dynamic droplets have not been investigated in detail. It is difficult to avoid the icing of the superhydrophobic surface beyond –50 °C and it requires a de-icing technology to remove the ice on the surface.

4 Applications of Superhydrophobic Surface in the Industry

Biomimetic superhydrophobic structures have found excellent applications, for eg. antifogging, antireflection, anti-icing, and self-cleaning. The water repellency character has been exploited in plethora of applications such as photovoltaics, cell capture organic light-emitting diodes (OLEDs), and lab-on-chip devices including

emerging applications like topological textured surfaces, droplet manipulation, optoelectronics, medical coatings and micro-reactor biochemical assays [13, 108–112]. Photovoltaics cells are prone to the accumulation of dirt and dust particle from the open environment and it prevents the device from absorbing sunlight [113]. Bioinspired anti-reflective and superhydrophobic meso-scale structures were fabricated for optoelectronic applications. The transparent structured surface eliminates the dust deposition and enhances the efficiency of the optoelectronic device due to the reduced light reflection [108–110].

The efficiency of condensation can be improved by a superhydrophobic surface. The water droplets falling onto the superhydrophobic surface bounces and roll out quickly without adhesion to the surface. The bouncing and rolling of water droplets can be used to remove the condensed water droplets, which acts as a thermal barrier to heat transfer which results in improved efficiency of condensation [114]. The superhydrophobic surface can be applied for the cell culture and patterning, lab on chips devices, medical instruments.

5 Conclusion and Perspective

In summary, the chapter gives an overview of the biological systems and the plethora of techniques adopted to fabricate biomimetic surface structures. Different state-of-the-art techniques adopted for the development of superwettable architecture, different wetting mechanisms and evolving applications of the superhydrophobic surface have been presented. An effort has been made to address the laser direct writing method to develop biomimetic surface on metals. A genuine attempt has been made to understand the transformation of laser processed hydrophilic metal oxide surface to superhydrophobic self-cleaning surface. Different post-processing of laser fabricated surface structure such as aging, chemical treatment, vacuum processing, and low-temperature annealing process has been briefly addressed. Even though, there are fruitful developments in fabricating superwettable solid surfaces, several issues remain unaddressed, more specifically about the mechanical and chemical stability of the surfaces against harsh environments. Moreover, there is a huge demand from the industries to develop a low-cost and environmentally friendly and easily scalable technique.

References

1. Gu, Z.-Z., Uetsuka, H., Takahashi, K., Nakajima, R., Onishi, H., Fujishima, A., Sato, O.: Structural color and the lotus effect. Angew. Chem. Int. Ed. **42**(8), 894–897 (2003)
2. Sun, T., Feng, L., Gao, X., Jiang, L.: Bioinspired surfaces with special wettability. Acc. Chem. Res. **38**(8), 644–652 (2005)
3. Cheng, Y.T., Rodak, D.E., Wong, C.A., Hayden, C.A.: Effects of micro- and nano-structures on the self-cleaning behaviour of lotus leaves. Nanotechnology **17**(5), 1359–1362 (2006)

4. Quéré, D.: Wetting and roughness. Annu. Rev. Mater. Res. **38**(1), 71–99 (2008)
5. Dorrer, C., Rühe, J.: Wetting of silicon nanograss: from superhydrophilic to superhydrophobic surfaces. Adv. Mater. **20**(1), 159–163 (2008)
6. Zan, G., Wu, Q.: Biomimetic and bioinspired synthesis of nanomaterials/nanostructures. Adv. Mater. **28**(11), 2099–2147 (2016)
7. Hancock, M.J., Sekeroglu, K., Demirel, M.C.: Bioinspired directional surfaces for adhesion, wetting, and transport. Adv. Funct. Mater. **22**(11), 2223–2234 (2012)
8. Liu, K., Jiang, L.: Bio-inspired design of multiscale structures for function integration. Nano Today **6**(2), 155–175 (2011)
9. Liu, K., Tian, Y., Jiang, L.: Bio-inspired superoleophobic and smart materials: design, fabrication, and application. Prog. Mater. Sci. **58**(4), 503–564 (2013)
10. Liu, H., Wang, Y., Huang, J., Chen, Z., Chen, G., Lai, Y.: Bioinspired surfaces with superamphiphobic properties: concepts, synthesis, and applications. Adv. Funct. Mater. **28**(19), 1707415 (2018)
11. Chen, P.-Y., McKittrick, J., Meyers, M.A.: Biological materials: functional adaptations and bioinspired designs. Prog. Mater. Sci. **57**(8), 1492–1704 (2012)
12. Zhao, N., Wang, Z., Cai, C., Shen, H., Liang, F., Wang, D., Wang, C., Zhu, T., Guo, J., Wang, Y., Liu, X., Duan, C., Wang, H., Mao, Y., Jia, X., Dong, H., Zhang, X., Xu, J.: Bioinspired materials: from low to high dimensional structure. Adv. Mater. **26**(41), 6994–7017 (2014)
13. Liu, Y., Wang, X., Fei, B., Hu, H., Lai, C., Xin, J.H.: Bioinspired, stimuli-responsive, multifunctional superhydrophobic surface with directional wetting, adhesion, and transport of water. Adv. Funct. Mater. **25**(31), 5047–5056 (2015)
14. Liu, K., Jiang, L.: Multifunctional integration: from biological to bio-inspired materials. ACS Nano **5**(9), 6786–6790 (2011)
15. Wen, L., Tian, Y., Jiang, L.: Bioinspired super-wettability from fundamental research to practical applications. Angew. Chem. Int. Ed. **54**(11), 3387–3399 (2015)
16. Zhang, Q., Yang, X., Li, P., Huang, G., Feng, S., Shen, C., Han, B., Zhang, X., Jin, F., Xu, F., Lu, T.J.: Bioinspired engineering of honeycomb structure—Using nature to inspire human innovation. Prog. Mater. Sci. **74**, 332–400 (2015)
17. Sun, Y., Guo, Z.: Recent advances of bioinspired functional materials with specific wettability: from nature and beyond nature. Nanoscale Horizons **4**(1), 52–76 (2019)
18. Wang, B., Prinsen, P., Wang, H., Bai, Z., Wang, H., Luque, R., Xuan, J.: Macroporous materials: microfluidic fabrication, functionalization and applications. Chem. Soc. Rev. **46**(3), 855–914 (2017)
19. Feng, L., Li, S., Li, Y., Li, H., Zhang, L., Zhai, J., Song, Y., Liu, B., Jiang, L., Zhu, D.: Super-hydrophobic surfaces: from natural to artificial. Adv. Mater. **14**(24), 1857–1860 (2002)
20. Parker, A.R., Lawrence, C.R.: Water capture by a desert beetle. Nature **414**(6859), 33–34 (2001)
21. Srinivasarao, M.: Nano-optics in the biological world: beetles, butterflies, birds, and moths. Chem. Rev. **99**(7), 1935–1962 (1999)
22. Park, K.-C., Kim, P., Grinthal, A., He, N., Fox, D., Weaver, J.C., Aizenberg, J.: Condensation on slippery asymmetric bumps. Nature **531**(7592), 78–82 (2016)
23. Yu, Z., Yun, F.F., Wang, Y., Yao, L., Dou, S., Liu, K., Jiang, L., Wang, X.: Desert beetle-inspired superwettable patterned surfaces for water harvesting. Small **13**(36), 1701403 (2017)
24. Nosonovsky, M.: Slippery when wetted. Nature **477**(7365), 412–413 (2011)
25. Chen, H., Zhang, P., Zhang, L., Liu, H., Jiang, Y., Zhang, D., Han, Z., Jiang, L.: Continuous directional water transport on the peristome surface of nepenthes alata. Nature **532**(7597), 85–89 (2016)
26. Bohn, H.F., Federle, W.: Insect aquaplaning: Nepenthes pitcher plants capture prey with the peristome, a fully wettable water-lubricated anisotropic surface. Proc. Natl. Acad. Sci. U.S.A. **101**(39), 14138–14143 (2004)
27. Gao, X., Jiang, L.: Water-repellent legs of water striders. Nature **432**(7013), 36–36 (2004)
28. Hu, D.L., Chan, B., Bush, J.W.M.: The hydrodynamics of water strider locomotion. Nature **424**(6949), 663–666 (2003)

29. Bush, J.W.M., Hu, D.L., Prakash, M.: The integument of water-walking arthropods: form and function. In: Casas, J., Simpson, S.J., (eds) Advances in Insect Physiology, vol. 34. Academic Press, pp. 117–192 (2007)
30. Kota, A.K., Kwon, G., Tuteja, A.: The design and applications of superomniphobic surfaces. NPG Asia Mater. **6**(7), e109–e109 (2014)
31. Yao, X., Song, Y., Jiang, L.: Applications of bio-inspired special wettable surfaces. Adv. Mater. **23**(6), 719–734 (2011)
32. Zhang, C., McAdams Ii, D.A., Grunlan, J.C.: Nano/Micro-manufacturing of bioinspired materials: a review of methods to mimic natural structures. Adv. Mater. **28**(30), 6292–6321 (2016)
33. Kuang, M., Wang, J., Jiang, L.: Bio-inspired photonic crystals with superwettability. Chem. Soc. Rev. **45**(24), 6833–6854 (2016)
34. Jiang, T., Guo, Z., Liu, W.: Biomimetic superoleophobic surfaces: focusing on their fabrication and applications. J. Mater. Chem. A **3**(5), 1811–1827 (2015)
35. Li, S., Huang, J., Chen, Z., Chen, G., Lai, Y.: A review on special wettability textiles: theoretical models, fabrication technologies and multifunctional applications. J. Mater. Chem. A **5**(1), 31–55 (2017)
36. Tie, L., Li, J., Liu, M., Guo, Z., Liang, Y., Liu, W.: Facile fabrication of superhydrophobic and underwater superoleophobic coatings. ACS Appl. Nano Mater. **1**(9), 4894–4899 (2018)
37. Yong, J., Huo, J., Yang, Q., Chen, F., Fang, Y., Wu, X., Liu, L., Lu, X., Zhang, J., Hou, X.: Femtosecond laser direct writing of porous network microstructures for fabricating super-slippery surfaces with excellent liquid repellence and anti-cell proliferation. Adv. Mater. Interfaces **5**(7), 1701479 (2018)
38. Bachus, K.J., Mats, L., Choi, H.W., Gibson, G.T.T., Oleschuk, R.D.: Fabrication of patterned superhydrophobic/hydrophilic substrates by laser micromachining for small volume deposition and droplet-based fluorescence. ACS Appl. Mater. Interfaces **9**(8), 7629–7636 (2017)
39. Wang, X., Ding, B., Yu, J., Wang, M.: Engineering biomimetic superhydrophobic surfaces of electrospun nanomaterials. Nano Today **6**(5), 510–530 (2011)
40. Xia, D., Johnson, L.M., López, G.P.: Anisotropic wetting surfaces with one-dimesional and directional structures: fabrication approaches, wetting properties and potential applications. Adv. Mater. **24**(10), 1287–1302 (2012)
41. Hong, S.-H., Hwang, J., Lee, H.: Replication of cicada wing's nano-patterns by hot embossing and UV nanoimprinting. Nanotechnology **20**(38), 385303 (2009)
42. Ju, J., Yao, X., Yang, S., Wang, L., Sun, R., He, Y., Jiang, L.: Cactus stem inspired cone-arrayed surfaces for efficient fog collection. Adv. Funct. Mater. **24**(44), 6933–6938 (2014)
43. Tricinci, O., Terencio, T., Mazzolai, B., Pugno, N.M., Greco, F., Mattoli, V.: 3D Micropatterned surface inspired by salvinia molesta via direct laser lithography. ACS Appl. Mater. Interfaces **7**(46), 25560–25567 (2015)
44. Barthlott, W., Mail, M., Bhushan, B., Koch, K.: Plant surfaces: structures and functions for biomimetic innovations. Nano-Micro Lett. **9**(2), 23 (2017)
45. Gao, L., McCarthy, T.J.: Contact angle hysteresis explained. Langmuir **22**(14), 6234–6237 (2006)
46. McHale, G., Shirtcliffe, N.J., Newton, M.I.: Contact-angle hysteresis on super-hydrophobic surfaces. Langmuir **20**(23), 10146–10149 (2004)
47. Whyman, G., Bormashenko, E., Stein, T.: The rigorous derivation of Young, Cassie-Baxter and Wenzel equations and the analysis of the contact angle hysteresis phenomenon. Chem. Phys. Lett. **450**(4), 355–359 (2008)
48. Kulinich, S.A., Farzaneh, M.: Effect of contact angle hysteresis on water droplet evaporation from super-hydrophobic surfaces. Appl. Surf. Sci. **255**(7), 4056–4060 (2009)
49. Debuisson, D., Senez, V., Arscott, S.: Tunable contact angle hysteresis by micropatterning surfaces. Appl. Phys. Lett. **98**(18), 184101 (2011)
50. Wenzel, R.N.: Resistance of solid surfaces to wetting by water. Ind. Eng. Chem. Res. **28**(8), 988–994 (1936)

51. Cassie, A.B.D., Baxter, S.: Wettability of porous surfaces. Trans. Faraday Soc. **40**, 546–551 (1944)
52. Jenner, E., D'Urso, B.: Wetting states on structured immiscible liquid coated surfaces. Appl. Phys. Lett. **103**(25), 251606 (2013)
53. de Lara, L.R., Jagdheesh, R., Ocaña, J.L.: Corrosion resistance of laser patterned ultrahydrophobic aluminium surface. Mater. Lett. **184**, 100–103 (2016)
54. Sun, T., Qing, G.: Biomimetic smart interface materials for biological applications. Adv. Mater. **23**(12), H57–H77 (2011)
55. Jiang, T., Koch, J., Unger, C., Fadeeva, E., Koroleva, A., Zhao, Q., Chichkov, B.N.: Ultrashort picosecond laser processing of micro-molds for fabricating plastic parts with superhydrophobic surfaces. Appl. Phys. A **108**(4), 863–869 (2012)
56. Koch, K., Hartmann, K.D., Schreiber, L., Barthlott, W., Neinhuis, C.: Influences of air humidity during the cultivation of plants on wax chemical composition, morphology and leaf surface wettability. Environ. Exp. Bot. **56**(1), 1–9 (2006)
57. Shepherd, T., Wynne Griffiths, D.: The effects of stress on plant cuticular waxes. New Phytol. **171**(3), 469–499 (2006)
58. Jagdheesh, R., García-Ballesteros, J.J., Ocaña, J.L.: One-step fabrication of near superhydrophobic aluminum surface by nanosecond laser ablation. Appl. Surf. Sci. **374**, 2–11 (2016)
59. Jagdheesh, R., Kopeček, J., Brajer, J., Mocek, T.: Superhydrophobic microspiked surface structures by ultrashort laser patterning. Surf. Eng. **37**(10), 1266–1276 (2021)
60. Jagdheesh, R., Pathiraj, B., Karatay, E., Römer, G.R.B.E., Huis in't Veld, A.J.: Laser-induced nanoscale superhydrophobic structures on metal surfaces. Langmuir **27**(13), 8464–8469 (2011)
61. Jagdheesh, R., Diaz, M., Ocaña, J.L.: Bio inspired self-cleaning ultrahydrophobic aluminium surface by laser processing. RSC Adv. **6**(77), 72933–72941 (2016)
62. Extrand, C.W.: Origins of wetting. Langmuir **32**(31), 7697–7706 (2016)
63. Jagdheesh, R., Diaz, M., Marimuthu, S., Ocaña, J.L.: Hybrid laser and vacuum process for rapid ultrahydrophobic Ti–6Al–4V surface formation. Appl. Surf. Sci. **471**, 759–766 (2019)
64. Lu, Y., Sathasivam, S., Song, J., Crick, C.R., Carmalt, C.J., Parkin, I.P.: Robust self-cleaning surfaces that function when exposed to either air or oil. Science **347**(6226), 1132–1135 (2015)
65. Chen, B., Qiu, J., Sakai, E., Kanazawa, N., Liang, R., Feng, H.: Robust and superhydrophobic surface modification by a "Paint + Adhesive" method: applications in self-cleaning after oil contamination and oil-water separation. ACS Appl. Mater. Interfaces **8**(27), 17659–17667 (2016)
66. Nine, M.J., Cole, M.A., Johnson, L., Tran, D.N.H., Losic, D.: Robust superhydrophobic graphene-based composite coatings with self-cleaning and corrosion barrier properties. ACS Appl. Mater. Interfaces **7**(51), 28482–28493 (2015)
67. Faustini, M., Capobianchi, A., Varvaro, G., Grosso, D.: Highly controlled Dip-coating deposition of fct FePt nanoparticles from layered salt precursor into nanostructured thin films: an easy way to tune magnetic and optical properties. Chem. Mater. **24**(6), 1072–1079 (2012)
68. Wang, S., Feng, L., Jiang, L.: One-step solution-immersion process for the fabrication of stable bionic superhydrophobic surfaces. Adv. Mater. **18**(6), 767–770 (2006)
69. Rangel, T.C., Michels, A.F., Horowitz, F., Weibel, D.E.: Superomniphobic and easily repairable coatings on copper substrates based on simple immersion or spray processes. Langmuir **31**(11), 3465–3472 (2015)
70. Cheng, Q., Huang, C., Tomsia, A.P.: Freeze casting for assembling bioinspired structural materials. Adv. Mater. **29**(45), 1703155 (2017)
71. Wang, J., Sun, L., Zou, M., Gao, W., Liu, C., Shang, L., Gu, Z., Zhao, Y.: Bioinspired shape-memory graphene film with tunable wettability. Sci. Adv. **3**(6), e1700004 (2017)
72. Richardson, J.J., Björnmalm, M., Caruso, F.: Multilayer assembly. Technology-driven layer-by-layer assembly of nanofilms. Science **348**(6233), aaa2491 (2015)
73. Manabe, K., Tanaka, C., Moriyama, Y., Tenjimbayashi, M., Nakamura, C., Tokura, Y., Matsubayashi, T., Kyung, K.-H., Shiratori, S.: Chitin nanofibers extracted from crab shells in

broadband visible antireflection coatings with controlling layer-by-layer deposition and the application for durable antifog surfaces. ACS Appl. Mater. Interfaces **8**(46), 31951–31958 (2016)
74. Gao, S., Zhu, Y., Wang, J., Zhang, F., Li, J., Jin, J.: Layer-by-layer construction of Cu^{2+}/alginate multilayer modified ultrafiltration membrane with bioinspired superwetting property for high-efficient crude-oil-in-water emulsion separation. Adv. Funct. Mater. **28**(49), 1801944 (2018)
75. Li, X., Wang, M., Wang, C., Cheng, C., Wang, X.: Facile immobilization of Ag nanocluster on nanofibrous membrane for oil/water separation. ACS Appl. Mater. Interfaces **6**(17), 15272–15282 (2014)
76. Tuteja, A., Choi, W., Mabry, J.M., McKinley, G.H., Cohen, R.E.: Robust omniphobic surfaces. Proc. Natl. Acad. Sci. **105**(47), 18200–18205 (2008)
77. Hou, J., Sun, Y., Wu, Y., Cao, S., Sun, L.: Promoting active sites in core-shell nanowire array as mott-schottky electrocatalysts for efficient and stable overall water splitting. Adv. Funct. Mater. **28**(4), 1704447 (2018)
78. Yu, H.R., Hu, J.Q., Liu, Z., Ju, X.J., Xie, R., Wang, W., Chu, L.Y.: Ion-recognizable hydrogels for efficient removal of cesium ions from aqueous environment. J. Hazard. Mater. **323**(Pt B), 632–640 (2017)
79. Shao, D.B., Chen, S.C.: Surface-plasmon-assisted nanoscale photolithography by polarized light. Appl. Phys. Lett. **86**(25), 253107 (2005)
80. Im, M., Im, H., Lee, J.-H., Yoon, J.-B., Choi, Y.-K.: A robust superhydrophobic and super-oleophobic surface with inverse-trapezoidal microstructures on a large transparent flexible substrate. Soft Matter. **6**(7), 1401–1404 (2010)
81. Kim, J.H., Shim, T.S., Kim, S.-H.: Lithographic design of overhanging microdisk arrays toward omniphobic surfaces. Adv. Mater. **28**(2), 291–298 (2016)
82. Srinivasan, S., Choi, W., Park, K.-C., Chhatre, S.S., Cohen, R.E., McKinley, G.H.: Drag reduction for viscous laminar flow on spray-coated non-wetting surfaces. Soft Matter. **9**(24), 5691–5702 (2013)
83. Liu, T.L., Kim, C.J.: Repellent surfaces. Turning a surface superrepellent even to completely wetting liquids. Science **346**(6213), 1096–1100 (2014)
84. Jagdheesh, R.: Fabrication of a superhydrophobic Al_2O_3 surface using picosecond laser pulses. Langmuir **30**(40), 12067–12073 (2014)
85. Jagdheesh, R., Diaz, M., Marimuthu, S., Ocana, J.L.: Robust fabrication of μ-patterns with tunable and durable wetting properties: hydrophilic to ultrahydrophobic via a vacuum process. J. Mater. Chem. A **5**(15), 7125–7136 (2017)
86. Jagdheesh, R., Valarmathi, A., Sivakumar, M.: Influence of laser beam polarization on micro-machining of crystalline silicon using ultrafast laser pulses. Lasers Eng. **32**(1–2), 19–35 (2015)
87. Jagdheesh, R., Tur, A., Ocaña, J.L.: The effects of pulse period on nanosecond laser microfabrication. Lasers Eng. **37**(4–6), 333–343 (2017)
88. Jagdheesh, R., BičišŤová, R., Brajer, J., Mocek, T.: Laser-induced superhydrophobic and oleophobic surface structures on float glass. Lasers Eng. **50**, 289–298 (2021)
89. Huerta-Murillo, D., Aguilar-Morales, A.I., Alamri, S., Cardoso, J.T., Jagdheesh, R., Lasagni, A.F., Ocaña, J.L.: Fabrication of multi-scale periodic surface structures on Ti–6Al–4V by direct laser writing and direct laser interference patterning for modified wettability applications. Opt. Lasers Eng. **98**, 134–142 (2017)
90. Guosheng, Z., Fauchet, P.M., Siegman, A.E.: Growth of spontaneous periodic surface structures on solids during laser illumination. Phys. Rev. B **26**(10), 5366–5381 (1982)
91. Kietzig, A.-M., Hatzikiriakos, S.G., Englezos, P.: Patterned superhydrophobic metallic surfaces. Langmuir **25**(8), 4821–4827 (2009)
92. Emmony, D.C., Howson, R.P., Willis, L.J.: Laser mirror damage in germanium at 10.6 μm. Appl. Phys. Lett. **23**(11), 598–600 (1973)
93. Varlamova, O., Costache, F., Reif, J., Bestehorn, M.: Self-organized pattern formation upon femtosecond laser ablation by circularly polarized light. Appl. Surf. Sci. **252**(13), 4702–4706 (2006)

94. Baldacchini, T., Carey, J.E., Zhou, M., Mazur, E.: Superhydrophobic surfaces prepared by microstructuring of silicon using a femtosecond laser. Langmuir **22**(11), 4917–4919 (2006)
95. Barberoglou, M., Tzanetakis, P., Fotakis, C., Stratakis, E., Spanakis, E., Zorba, V., Rhizopoulou, S., Anastasiadis, S.: Laser structuring of water-repellent biomimetic surfaces. SPIE (2009)
96. Priyanka, B., Smita, G., Javed, M., Shankar, G., Pushan, A.: Universal, geometry-driven hydrophobic behaviour of bare metal nanowire clusters. Nanotechnology **19**(7), 075709 (2008)
97. Vorobyev, A.Y., Guo, C.: Femtosecond laser nanostructuring of metals. Opt. Express **14**(6), 2164–2169 (2006)
98. von der Linde, D., Sokolowski-Tinten, K.: The physical mechanisms of short-pulse laser ablation. Appl. Surf. Sci. **154–155**, 1–10 (2000)
99. Hohlfeld, J., Wellershoff, S.S., Güdde, J., Conrad, U., Jähnke, V., Matthias, E.: Electron and lattice dynamics following optical excitation of metals. Chem. Phys. **251**(1–3), 237–258 (2000)
100. Rethfeld, B., Sokolowski-Tinten, K., von der Linde, D., Anisimov, S.I.: Timescales in the response of materials to femtosecond laser excitation. Appl. Phys. A **79**(4), 767–769 (2004)
101. Anisimov, S.I., Kapeliovich, B.L., Perel'man, T.L.: Electron emission from metal surfaces exposed to ultrashort laser pulses. Sov. Phys. JETP **375**, 375–377 (1974)
102. Nolte, S., Momma, C., Jacobs, H., Tünnermann, A.: Ablation of metals by ultrashort laser pulses. J. Opt. Soc. Am. B **14**(10), 2716–2722 (1997)
103. Jagdheesh, R., Ocaña, J.L.: Laser machined ultralow water adhesion surface by low pressure processing. Mater. Lett. **270**, 127721 (2020)
104. Jagdheesh, R., Hauschwitz, P., Mužík, J., Brajer, J., Rostohar, D., Jiříček, P., Kopeček, J., Mocek, T.: Non-fluorinated superhydrophobic Al7075 aerospace alloy by ps laser processing. Appl. Surf. Sci. **493**, 287–293 (2019)
105. Liu, Y., Whyman, G., Bormashenko, E., Hao, C., Wang, Z.: Controlling drop bouncing using surfaces with gradient features. Appl. Phys. Lett. **107**(5), 051604 (2015)
106. Kim, P., Wong, T.-S., Alvarenga, J., Kreder, M.J., Adorno-Martinez, W.E., Aizenberg, J.: Liquid-infused nanostructured surfaces with extreme anti-ice and anti-frost performance. ACS Nano **6**(8), 6569–6577 (2012)
107. Cardoso, J.T., Garcia-Girón, A., Romano, J.M., Huerta-Murillo, D., Jagdheesh, R., Walker, M., Dimov, S.S., Ocaña, J.L.: Influence of ambient conditions on the evolution of wettability properties of an IR-, ns-laser textured aluminium alloy. RSC Adv. **7**(63), 39617–39627 (2017)
108. Zhang, Y.-L., Xia, H., Kim, E., Sun, H.-B.: Recent developments in superhydrophobic surfaces with unique structural and functional properties. Soft Matter. **8**(44), 11217–11231 (2012)
109. Leem, Y.-C., Park, J.S., Kim, J.H., Myoung, N., Yim, S.-Y., Jeong, S., Lim, W., Kim, S.-T., Park, S.-J.: Light-emitting diodes with hierarchical and multifunctional surface structures for high light extraction and an antifouling effect. Small **12**(2), 161–168 (2016)
110. Kim, J.-J., Lee, J., Yang, S.-P., Kim, H.G., Kweon, H.-S., Yoo, S., Jeong, K.-H.: Biologically inspired organic light-emitting diodes. Nano Lett. **16**(5), 2994–3000 (2016)
111. Wu, D., Zhao, Y.-B., Wu, S.-Z., Liu, Y.-F., Zhang, H., Zhao, S., Feng, J., Chen, Q.-D., Ma, D.-G., Sun, H.-B.: Simultaneous efficiency enhancement and self-cleaning effect of white organic light-emitting devices by flexible antireflective films. Opt. Lett. **36**(14), 2635–2637 (2011)
112. Wang, Y., Ma, K., Xin, J.H.: Stimuli-responsive bioinspired materials for controllable liquid manipulation: principles, fabrication, and applications. Adv. Funct. Mater. **28**(6), 1705128 (2018)
113. Vüllers, F., Gomard, G., Preinfalk, J.B., Klampaftis, E., Worgull, M., Richards, B., Hölscher, H., Kavalenka, M.N.: Bioinspired superhydrophobic highly transmissive films for optical applications. Small **12**(44), 6144–6152 (2016)
114. Miljkovic, N., Enright, R., Nam, Y., Lopez, K., Dou, N., Sack, J., Wang, E.N.: Jumping-droplet-enhanced condensation on scalable superhydrophobic nanostructured surfaces. Nano Lett. **13**(1), 179–187 (2013)

Index

J. Radhakrishnan and S. Pathak (eds.), *Advanced Engineering of Materials Through Lasers*, Advances in Material Research and Technology,
https://doi.org/10.1007/978-3-031-03830-3